

THÈSE

Pour obtenir le grade de
Docteur

**Délivré par l'École Nationale Supérieure de
Chimie de Montpellier**

**Préparée au sein de l'école doctorale Sciences
Chimiques Balard
Et de l'unité de recherche Institut Charles Gerhardt**

Spécialité : Physico-Chimie des Matériaux

Présentée par Achraf NOUREDDINE

Approches Click en Chimie Sol-Gel

Soutenue le 26 septembre 2014 devant le jury composé de

M. Philippe TRENS, Professeur, Ecole Nationale Supérieure de Chimie de Montpellier	Président du jury
Mme Florence BABONNEAU, Directrice de Recherche CNRS-Université Pierre et Marie Curie Paris	Rapporteur
Mme Céline CROUTXÉ-BARGHORN, Professeure, Université de Haute-Alsace, Mulhouse	Rapporteur
M. Miquel A. PERICÀS, Professeur, ICIQ et Université de Barcelone, Espagne	Examineur
M. Xavier CATTOËN, Chargé de Recherche CNRS, ENSCM et Université Grenoble Alpes	Directeur de thèse
M. Michel WONG CHI MAN, Directeur de Recherche CNRS-Ecole Nationale Supérieure de Chimie de Montpellier	Directeur de thèse

*A toi, mon grand père, jeddo,
A toi, Mohamad Ali Karaki, Abou Kassem,
Toi, qui m'as quitté il y a dix ans,
Toi, qui aurait adoré me voir en ce moment,
Toi, qui aurais versé des larmes à cet instant,
A ta mémoire, je dédie cette thèse,
En versant des petites larmes,
En te disant,
Jeddo, tu me manques...*

~~~~~Remerciements~~~~~

Contrairement à ce l'on peut parfois croire, ces mots qui vont suivre ne sont pas un « devoir » mais ils constituent la crème d'une expérience de savoir.

Quelques petites expressions de reconnaissance, mais surtout pour que l'histoire grave les noms des personnes qui ont contribué d'une façon ou d'autre, et qui ont aidé matériellement ou moralement à me faire déposer une brique dans le gratte-ciel de la science.

Pour commencer, je voudrais tout d'abord remercier les membres du jury qui m'ont fait l'honneur d'accepter d'examiner minutieusement ce manuscrit de thèse qui, grâce à leurs commentaires et suggestions, est devenu plus riche. Monsieur le Professeur Philippe Trens, Madame la Directrice de Recherche Florence Babonneau, Madame la Professeure Céline Croutxé-Barghorn, Monsieur le Professeur Miquel Pericàs, veuillez accepter toute ma gratitude !

Monsieur le Directeur de Recherche Michel Wong Chi Man et Monsieur le Chargé de Recherche Xavier Cattoën, ou tout simplement, Michel et Xavier : deux noms qui reviendront souvent à mon esprit. Deux personnes à qui j'ai toute ma reconnaissance et mon respect. Ils étaient d'exceptionnels directeurs, et ils le resteront. Vous êtes mes instituteurs à la vie de recherche ! L'ambiance de respect et d'estime mutuels que l'on vivait m'a rendu fructueux et heureux.. des moments que je n'oublierai jamais. Michel et Xavier, merci !

Tous mes amis et collègues du labo : Simon, François (soirées saumon PS3), Christophe (énergie vs radio classic :D) , Ana, Philippe, Camille, Alexandra, Jonas (Mr. Super papers ☺), Doria, Romain, Gilles, Claude, Noaki, Yutaka, Chiara, Vania, Kristyna, Samir, vous étiez charmant, chacun à son style, merci pour chaque mot, chaque discussion, chaque encouragement, chaque...cadeau que vous m'auriez offert le 26/09/2014 (c'est bien d'anticiper !)

Dr. Jean-Olivier Durand, avec qui j'ai commencé les essais de fabrication de nanoparticules, et qui n'a pas hésité tout au long de ma thèse à donner les conseils et les orientations (surtout pour le mois suivant ma soutenance ;-))

Professeur Jeffrey Zink et toute son équipe de UCLA qui m'a très chaleureusement accueilli pendant mon séjour au sein de son laboratoire. J'ai apprécié chaque instant avec eux !

Professeur Philippe Trens, ici non pas le président du jury mais notre collègue, avec qui le travail est toujours agréable, pour ses aides dans l'interprétation des analyses de physisorption de gaz, pour les cours d'analyse texturale et bien sûr dans tout le travail que nous avons effectué ensemble.

Docteur Guillaume Toquer pour sa sympathie tout en performant nos analyses structurales, pour sa disponibilité, sa motivation et sa large coopération.

Merci à Docteur Magali Gary-Bobo pour les tests *in vitro* et pour sa grande sympathie, dommage que l'on s'est connu juste avant que je termine ma thèse !

Merci à Mme Yvette Odile, Mme Pascale Guiffrey et M. Lionel Sauvigné pour leur soutien et pour le délicat soin qu'ils prennent de la vie de chaque jour dans notre laboratoire.

Je remercie également M. Franck Godiard, M. Didier Cot, Mme Dominique Granier, M. David Bourgogne, Mme Christine Biolley pour les analyses des matériaux.

Merci aussi à Mme Sylvie Condom, ma tutrice pendant le monitorat, qui était d'extrême gentillesse mais aussi une superbe formatrice.

Un merci particulier à mon ami Eddy avec qui j'ai passé de très bons moments pendant les weekends et pour nos riches discussions pendant les déjeuners à Boutonnet ☺.

Pour terminer, j'arrive à ceux qui m'ont accompagné pas seulement durant la thèse mais depuis bien avant. J'arrive à ceux qui occupent mes pensées et qui ne cessent de penser à moi dans chaque pas. J'arrive à ceux qui méritent le plus profond et respectueux merci du monde. J'arrive à ma famille.

Mon père Mourtada, ma mère Najwa, ma grand-mère Siham, mes frères Hussein et Ahmad, ma sœur Siham. Merci pour chaque moment.. sans votre chaleur tout aurait été différent..

Mon oncle Kassem, avec qui j'ai commencé mon séjour en France, peu de mots peuvent te donner la vraie valeur de ta contribution dans mon parcours, ta présence à mes côtés m'a été d'importance cruciale. Merci pour tout khal..

Eliane, ma chérie, depuis huit ans et tu es l'étoile qui illumine mon chemin, merci pour ton indéfectible support, ta grande compréhension et tes encouragements. Tout simplement, merci pour ta présence..

Avant-Propos

Cette thèse a bénéficié d'un financement du Ministère de l'Education Nationale, de l'Enseignement Supérieur et de la Recherche. Le travail a été réalisé dans le laboratoire Architectures Moléculaires et Matériaux Nanostructurés (AM2N) de l'Institut Charles Gerhardt Montpellier (ICGM, UMR 5253), localisé à l'École Nationale Supérieure de Chimie de Montpellier sous la direction de Dr. Michel Wong Chi Man et Dr. Xavier Cattoën.

La première partie du chapitre 2 s'inscrit dans la continuité des travaux initiés par Dr. Nirmalya Moitra et Dr. Kristýna Bürglová. La deuxième partie de ce chapitre a été réalisée en étroite collaboration avec Prof. Philippe Trens de l'équipe Matériaux Avancés pour la Catalyse et la Santé (MACS) de l'ICGM et du Dr. Guillaume Toquer du Laboratoire de Nanomatériaux pour l'Energie et le Recyclage (LNER) de l'Institut de Chimie Séparative de Marcoule (ICSM).

Les études décrites au chapitre 3 ont été menées dans le cadre d'une collaboration avec Dr. Jean-Olivier Durand et Jonas Croissant (projet ANR MECHANANO) ainsi qu'avec Prof. Jeffrey I. Zink de l'Université de Californie à Los Angeles (UCLA) qui m'a accueilli dans son laboratoire durant un trimestre pour développer les études sur les nanomachines multifonctionnelles. Les études *in vitro* sont faites par Dr. Magali Gary-Bobo de l'Institut des Biomolécules Max-Mousseron (IBMM).

Pour ce qui suit, la langue d'expression sera l'anglais. Un résumé de 12 pages en français est donné à la fin de ce manuscrit.

This page was intentionally left blank

Abbreviations

2D: Two dimensional	Laser: Light Amplification by Stimulated Emission of Radiation
AHQI: Ammonium Hydroxyquinolinium Iodide	m: Multiplet
ATR: Attenuated Total Reflectance	MAS: Magic Angle Spinning
a.u.: Arbitrary Unit	MeOH: Methanol
AzPTES: (3-Azidopropyl)triethoxysilane	MHz: MegaHertz
BET: Brunauer; Emmett and Teller	Na-Asc: Sodium Ascorbate
BJH: Barret-Joyner and Halenda	NMR: Nuclear Magnetic Resonance
Br: Broad	O/I: Organic/Inorganic
BS: Bridged Silsesquioxane	Op: One pot
BTME: Bis(trimethoxysilyl)ethane	p-: para-
CD: Cyclodextrin	P: Power
cmc: Critical Micellar Concentration	PEG: Polyethyleneglycol
Cu: Copper	Ph: Phenyl
CuAAC: Copper-Catalyzed Azide-Alkyne Cycloaddition	PFOA: Perfluorooctanoic Acid
CTABr: Cetyl trimethyl Ammonium Bromide	PMO: Periodic Mesoporous Organosilica
CP: Cross Polarization	ppm: Part Per Million
DCM: Dichloromethane	Prec: Precursor
DMF: <i>N,N</i> -Dimethylformamide	PXRD: Powder X-ray Diffraction
EtOH: Ethanol	q: Quadruplet
EtOEt: Diethylether	RT: Room Temperature
ESI: Electrospray Ionization	s: Singlet
Et₃N: Triethylamine	SAXS: Small Angle X-ray Scattering
FA: Folic Acid	SEM: Scanning Electron Microscopy
FFT: Fast Fourier Transform	SHS: Sodium Hexadecylsulphate
FRET: Förster Resonance Energy Transfer	SN: Nucleophilic Substitution
FTIR: Fourier-transformed InfraRed	t: Triplet
HRMS: High Resolution Mass Spectrometry	TBABr: Tetrabutylammonium Bromide
TEM: Transmission Electron Microscopy	UV: Ultraviolet
THF: Tetrahydrofuran	Vis: Visible
Thy: Thymine	WAXS: Wide Angle X-ray Scattering
TEOS: Tetraethylorthosilicate	XRD: X-ray Diffraction
TGA: Thermogravimetric Analysis	
TLC: Thin Layer Chromatography	
TMOS: Tetramethylorthosilicate	
TMS: Trimethylsilyl	

Table of Contents

General Introduction.....	11
CHAPTER I : BIBLIOGRAPHIC STUDY.....	12
1. The Sol-Gel Process	14
1.1. Physical point of view	14
1.2. Chemical point of view.....	15
1.2.1. Reactions involved.....	15
1.2.2. Control of kinetics.....	16
1.2.3. Catalysis of the sol-gel process	17
2. Ordered Porous Materials.....	19
2.1. Synthetic approaches to mesostructured materials	20
2.2. From bulk materials to nanoparticles	22
3. Hybrid Functional Mesoporous Silica.....	24
3.1. <i>Class I</i>	24
3.2. <i>Class II</i>	24
3.2.1. Conventional post-modification.....	25
3.2.2. Co-condensation	26
3.2.3. Hydrolysis-condensation of poly-silylated precursors.....	26
3.2.4. Click-grafting on functionalizable organosilicas	27
4. Click Chemistry.....	28
4.1. Definition.....	28
4.2. Reactions	28
4.3. Copper Catalyzed Azide-Alkyne Cycloaddition (CuAAC)	29
4.3.1. Mechanism and kinetics of the CuAAC reaction	31
4.3.2. CuAAC reaction conditions	32
4.3.3. Effect of ligands	33
4.4. CuAAC chemistry on hybrid silica materials.....	33
4.4.1. CuAAC on mesoporous bulk materials	33
4.4.2. CuAAC on hybrid thin films.....	34
4.4.3. CuAAC on Silica Mesoporous Microdots Arrays	35
4.4.4. CuAAC on mesoporous silica nanoparticles	36
4.4.5. Click on PMOs.....	37
5. Conclusion/ Objectives of the present work	37

CHAPTER II: Periodic Mesoporous Organosilica and Bridged Silsesquioxane Functionalized by CuAAC Click Reaction.....	38
1. Introduction	40
2. Functional PMOs and Bridged Silsesquioxane by CuAAC grafting	42
2.1. Interaction Organic fragment- Surfactant.....	44
2.1.1. Synthesis of Clickable Periodic Mesoporous Organosilicas M1 and M2.....	44
2.2. CuAAC Click Reactions on PMOs	51
2.2.1. Click reaction influence on textural properties of PMOs	53
2.3. Interaction Silicates-Surfactant.....	55
2.3.1. Synthesis of materials M3 and M4	56
2.3.2. Characterization of M3 and M4.....	56
2.4. CuAAC reaction on Mesoporous Materials M3 and M4	59
3. Functional Bridged Organosilane from functional organosilane block-built by CuAAC reaction	67
3.1. Synthesis of material M-Thy	67
3.2. Characterization of M-Thy	68
3.3. Conclusion	69
4. Functional Bridged Silsesquioxane by one pot pathway from clickable organosilane.....	70
4.1. Synthesis of Clickable Materials and One-Pot Functional Materials.....	70
4.2. Characterization of one-pot made materials	71
5. Tailoring the Hydrophilic/Lipophilic Balance of Clickable Mesoporous Organosilicas by CuAAC <i>Click</i> -Functionalization	76
5.1. Introduction	76
5.2. CuAAC Reaction.....	79
5.3. Characterization.....	80
5.4. Gas-sorption study	85
5.5. Conclusions	91
6. General conclusion of chapter II	92
CHAPTER III: Multiclickable Mesoporous Silica Nanoparticles for Controlled Release of Cargo Molecules.....	92
1. From a normal cell to a cancer cell	94
2. Hybrid Mesoporous Silica Nanoparticles (MSNs).....	95
2.1. Biocompatibility and morphology of MSNs	96
2.2. Morphology	96

2.3. Cytotoxicity	96
2.4. Targeting.....	98
2.5. Controlled release of cargo molecules.....	98
3. Monoclickable Mesoporous Silica Nanoparticles: Light-triggered clicked nanoimpeller for controlled release of cargo molecules	102
3.1. Concept of Nanoimpeller.....	102
3.2. Photochemical properties of azobenzene derivatives	102
3.3. Photoisomerization of azobenzene	103
3.3.1. Mechanism	103
3.3.2. Spectral properties of azobenzene	104
3.4. Synthesis of Monoclickable Mesoporous Silica Nanoparticles	105
3.4.1. Characterization	106
3.5. CuAAC reaction on monoclickable nanoparticles	109
3.6. Cargo loading	114
3.7. Release experiments	114
3.8. Conclusion	117
4. Bisclickable Mesoporous Silica Nanoparticles: A multifunctional platform for selected applications in cancer cell treatment	118
4.1. Synthesis of the bisclickable nanoparticles	118
4.2. Characterization of the nanoparticles	119
5. CuAAC on bisclickable nanoparticles: Light triggered controlled cargo release from a targeting nanocarrier	124
5.1. Characterization of bisclicked nanoparticles	125
5.2 Release profile	129
5.3. In vitro preliminary essays:	130
6. Double click reaction (CuAAC) on mesoporous silica nanoparticles: probing the proximity of functions by Förster Resonance Energy Transfer (FRET)	132
6.1. Introduction	132
6.2. FRET on the mesoporous silica nanoparticles	134
6.2.1. Ro calculation	136
6.2.3. CuAAC Click reactions	137
6.2.4. Characterization of the CuAAC functionalization.....	138
6.2.5. FRET effect.....	140

7. Activation of pH-Responsive Nanomachines through Photo-Responsive Proton Transfer	143
7.1. Characterization of the nanoparticles	145
7.2. Release tests and photoacid effect control.....	149
7.3. Conclusion	152
8. General conclusion of chapter III.....	153
General Conclusion of the thesis.....	155
Outlooks	156
Experimental Section	158
Supporting Information.....	176
Résumé en français.....	190
References	203

General Introduction

Hybrid silicas are materials that contain organic moieties and siloxane networks intimately mixed at the nanometer scale, which can confer them synergistic properties. They are of central importance in nowadays research since they offer a wide range of possible applications (nanomedicine, coatings, catalysis, adsorption,...). The sol-gel process offers the ability to engineer, by different smart processing approaches, the morphological and the structural properties of the materials according to their targeted application (size, shape, porosity, structuring). The amount and the spatial distribution of the organic fragments incorporated within the material play a key role to fine-tune its properties and the application range. In this work, we aim to develop a methodology for materials functionalization using click chemistry, which has enabled great advances in biological engineering and polymers modification. Click chemistry, in particular the copper-catalyzed azide-alkyne cycloaddition reaction (CuAAC) has a high potential in assembling small fragments by covalent linkage (*Lego* synthesis) with high conversions and excellent tolerance for functional groups. These features make it very attractive for materials functionalization since it considerably broadens the scope of possible functionalities incorporated. After a bibliographic introduction presenting the synthesis of silica materials by the sol-gel process and the mechanism and applications of the CuAAC reaction, the manuscript will be divided in two main sections describing:

- The synthesis of a series of clickable PMOs and bridged silsesquioxanes which inherently exhibit a maximal amount of clickable organic fragments, leading to high extents of grafted functional groups by the CuAAC reaction. These materials will then be derivatized with various organic fragments in order to tune the hydrophilic/lipophilic balance of the surface via CuAAC reactions. Alternative approaches based on the CuAAC click chemistry for the synthesis of functional hybrid bridged silsesquioxanes will also be discussed.
- The synthesis of multifunctional mesoporous silica nanoparticles to be used in the controlled release of cargo molecules. CuAAC reactions will be carried out in order to provide a simplified and controlled synthesis of nanomachines. In particular, we will focus on the targeting of cancer cells, on the communication between two fluorophores by energy transfer, and on the formation of a new type of nanomachine based on a photoacid-mediated gate-opening.

CHAPTER I

BIBLIOGRAPHIC STUDY

CHAPTER I: Bibliographic Study

In this chapter, we will highlight the importance of the sol-gel process for the preparation of silica-based functional porous materials under mild conditions, suitable to incorporate organic functionalities in the materials. Afterwards, the recent studies devoted to click chemistry in materials science will be discussed based on recent examples from the literature. Finally, the opportunities brought by the CuAAC click reaction for the functionalization of sol-gel materials will be outlined.

1. The Sol-Gel Process^{1,2}

The sol-gel process is a bottom-up approach for the synthesis of (nano)materials. It is widely used as a soft chemical process purposing the design of solid materials from molecular precursors in solution. This process typically concerns the formation of metal oxide-based solid materials from metal alkoxide $M(OR)_n$ precursors (M = Metal atom, R = alkyl group) under mild conditions (conventional solvents, low temperature and pressure).

1.1. Physical point of view

The soluble metal alkoxides species are hydrolyzed into $M(OR)_{n-x}(OH)_x$ and the obtained metal hydroxide condense to give at first a *sol*, which is a colloidal suspension formed by the primary inorganic oligomers, that undergoes further cross-linking to form a *gel*, an advanced condensed tridimensional metal oxide network entrapping the solvent. The sol-to-gel transition is characterized by a dramatic increase of the viscosity of the mixture. A sol can easily be processed to obtain materials under different shapes: nanoparticles, thin films, fibers or microdots arrays can be prepared following different processing methods (Figure 1). The *gel* can be subjected to an appropriate mechanical and/or thermal treatment to afford a dry solid with robust mechanical properties. For example, supercritical drying affords an aerogel, which is composed of about 90 to 99% air and can be used for its insulation properties. A conventional drying by thermal evaporation yields a xerogel.

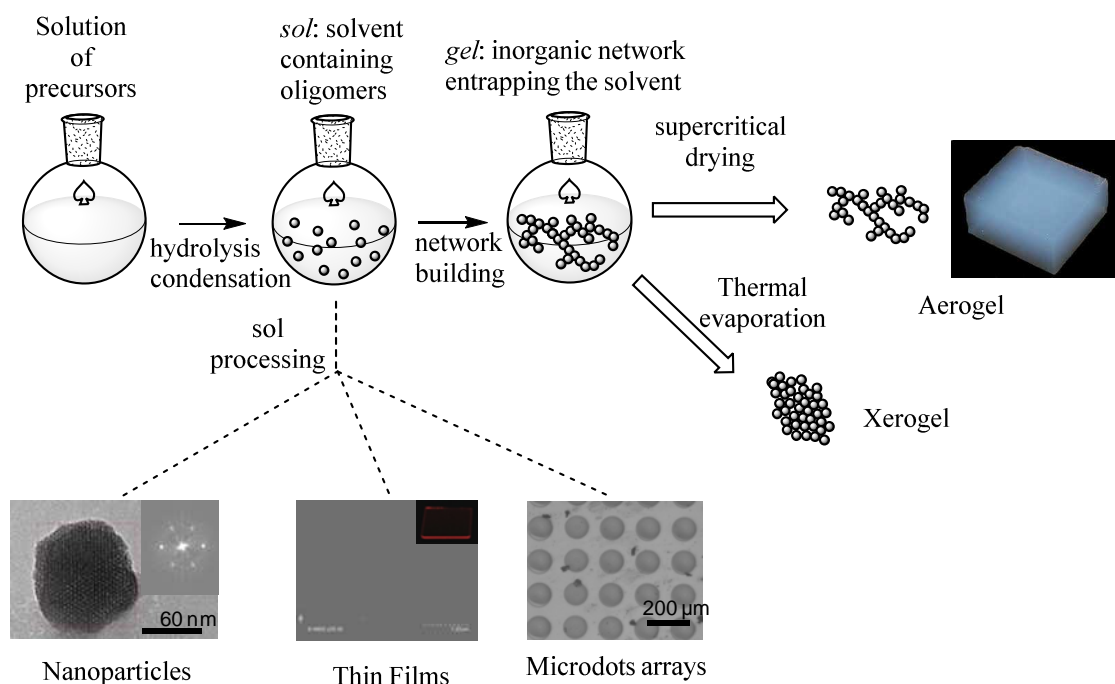


Figure 1: physical transitions occurring during the sol-gel process

1.2. Chemical point of view

The sol-gel process can be used with a variety of metal alkoxides³, especially silicon, aluminium, boron and transition metals such as vanadium, titanium, zirconium or hafnium.

Regarding our group's expertise and the application in nanomedicine intended from this thesis, we will focus on siliceous materials in the following discussions.

Siliceous materials have proven to be of central importance in nowadays research. They expand their roots in almost all the fields of applied chemistry as well as in physics, biology and medicine. A good understanding of the chemical processes governing the formation of these materials is compulsory to design new materials for these applications.

1.2.1. Reactions involved¹⁻³

Two main reactions are involved in the sol-gel process: hydrolysis and polycondensation. The following mechanism is typical for a silicate sol-gel preparation in water without any external agent.

-Hydrolysis: water molecules react with alkoxysilane functions Si-OR producing silanol groups (Si-OH) and the corresponding alcohol (R-OH) thus making the elemental entities that will be involved in the condensation.

-Condensation: the condensation is the step of block building via siloxanes links (Si-O-Si). This reaction occurs either by the coupling of two silanol groups with formation of water molecules or by condensation between silanols and alkoxy groups, with formation of alcohol molecules.

The first steps of hydrolysis and condensation lead to a colloidal suspension of inorganic oligomers, the *sol*, which cross-linking through sequences of hydrolysis and condensation reactions leads to the *gel*, formed by a 3D inorganic network entrapping the remaining solution. The hydrolysis and condensation reactions are depicted in Figure 2.

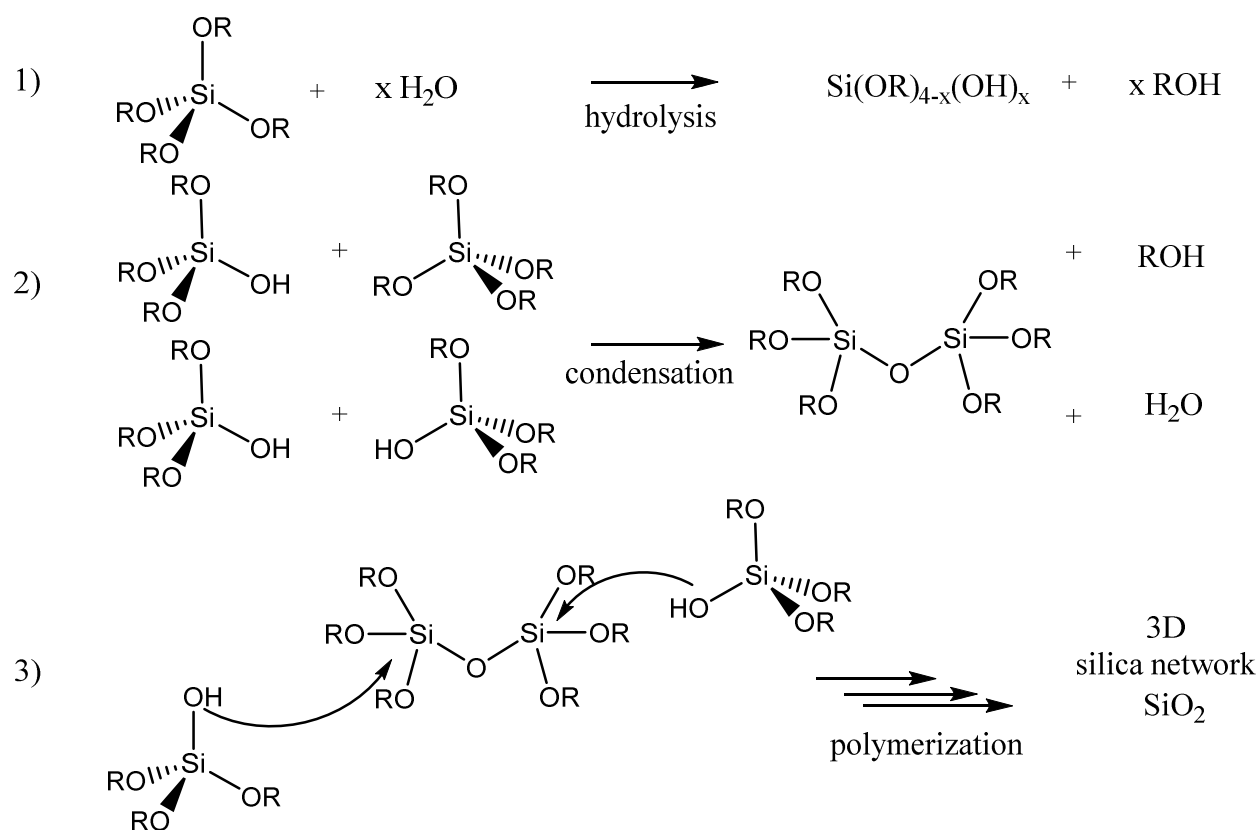


Figure 2: Reactions involved in the formation of silica from a tetraalkoxysilane

1.2.2. Control of kinetics

The rate of the sol-gel transformation can be drastically enhanced by using appropriate catalysts (see below). Different factors can also be tuned in order to improve the reaction rate or to control the morphology of the obtained solid material.

-Temperature and solvent⁴: Metal alkoxides are poorly soluble in water at low temperature. This can inhibit the initiation of the hydrolysis process or strongly decrease the transformation rate. Working at higher temperature and using, in addition to water, a common solvent for the reaction mixture (ideally the alcohol corresponding to the alkoxides to prevent any perturbation in the reaction due to the different compounds formed) may increase the homogeneity of the mixture and therefore the rate of the transformation.

-Concentration in alkoxides⁵: The concentration of the metal alkoxides in the reaction mixture also plays a crucial role in the reaction rate especially during the condensation process where the probability of the cross-linking between the precursors decreases when lower quantity of metal alkoxide is involved. This feature is used to control the size of the obtained material.

-pH change: The pH has the most important effect on the course of the sol-gel reaction. While the choice of the pH is essentially used to control the rate of the transformation^{6,7}, it can be used to modify the shape and the size of the obtained solid material⁸.

1.2.3. Catalysis of the sol-gel process²:

-Acidic catalysis (Figure 3): at low pH, the alkoxy groups on the silicon atom get protonated (Si-O(R)H^+), thus rendering the silicon atom more electrophilic and prone to nucleophilic attack. A pentacoordinated silicon intermediate is involved in this step.

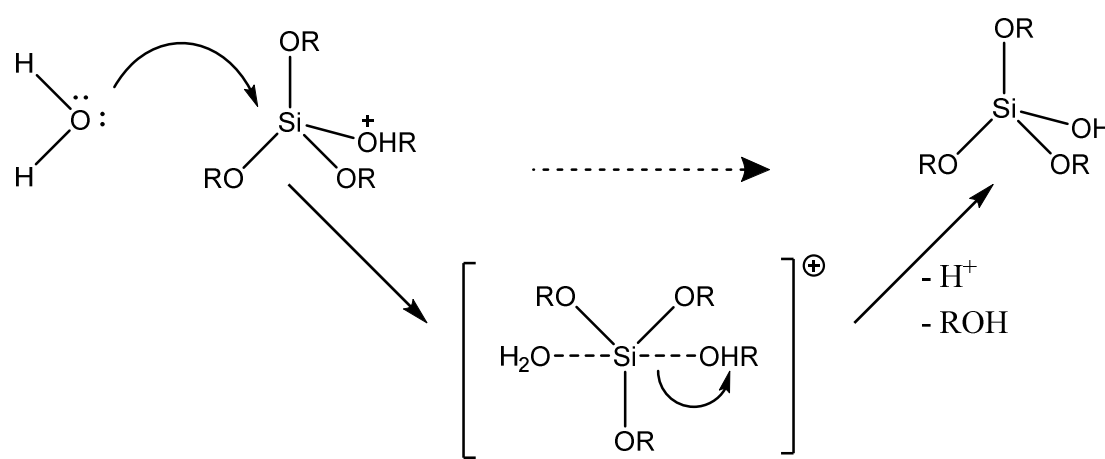


Figure 3: acid-catalyzed hydrolysis

-Basic catalysis (Figure 4): Hydroxide ions are more nucleophilic than water and can directly attack the silicon atom, through an addition-elimination mechanism.

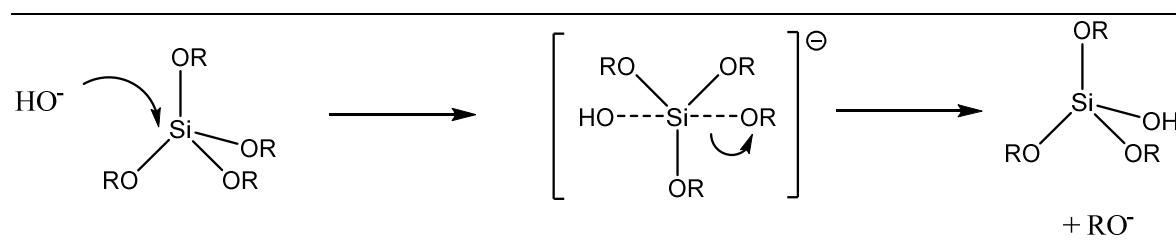


Figure 4: base-catalyzed hydrolysis

Nucleophilic catalysis (Figure 5): This catalytic route usually involves fluoride ions (NH_4F , NaF , TBAF ...) under neutral conditions. It is specific to silicate chemistry, owing to the high affinity between silicon and fluoride. The fluoride ions reversibly add to the silicon center, forming pentacoordinated intermediates in which the silicon-oxygen bonds are weakened. The preferential hydrolysis of the Si-F bonds and the departure of alcohol molecules afford silanol functions. It is noteworthy that the features of the gels obtained through fluoride catalysis are mostly similar to those obtained under basic catalysis².

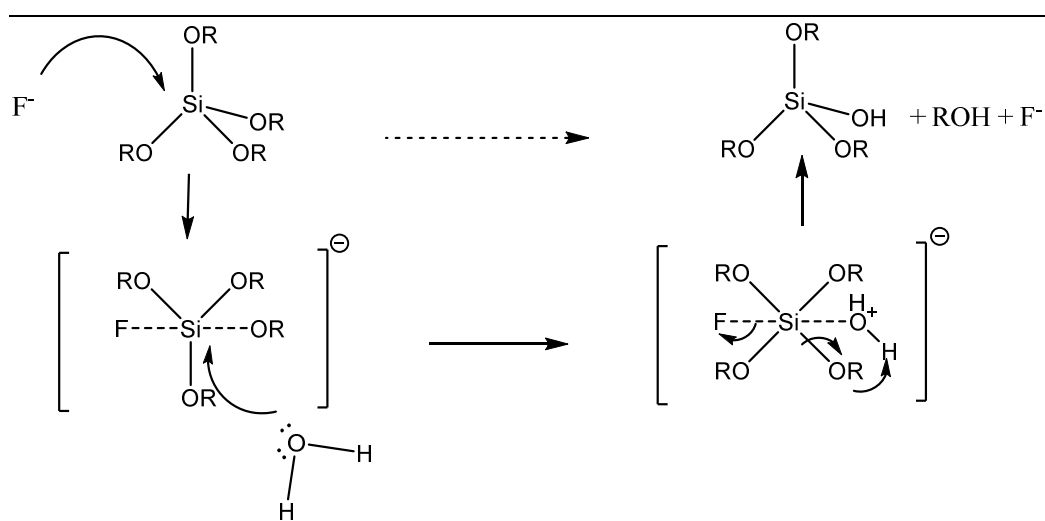


Figure 5: nucleophilic catalysis of hydrolysis mechanism by fluoride ions

Owing to the intermediates involved under basic, nucleophilic or acidic catalysis, electron-donating groups (alkyl, alkoxy) accelerate the hydrolysis reactions performed under acidic catalysis, while electron withdrawing groups accelerate the nucleophile- or base-catalyzed hydrolysis. This holds also true for the condensation reactions that follow similar mechanisms. O-Si groups being more electron-withdrawing than -OR groups, condensation at

the end of the chains will be favored under acidic catalysis, with the formation of chain-like oligomers, while ramifications will be favored under basic or nucleophilic catalysis, with the isotropic growth of the silicate clusters leading to spherical morphologies (Figure 6).

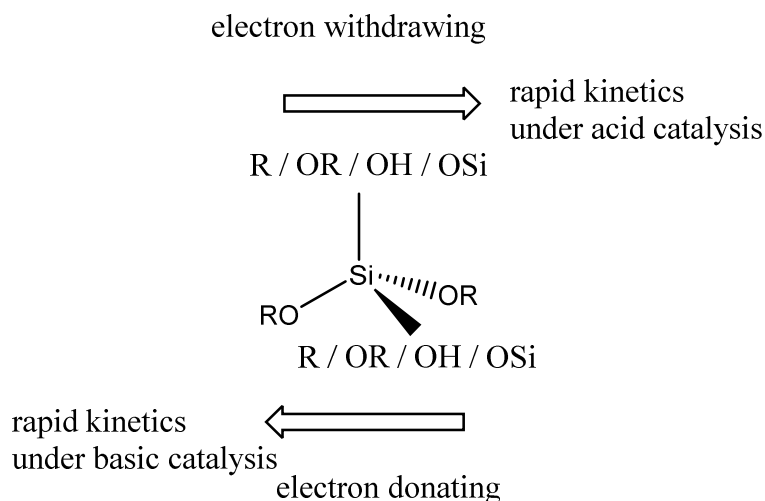


Figure 6: influence of silicon substituent on reaction kinetics. Adapted from ref²

The robustness of the sol-gel process has enabled the development of new categories of highly useful materials and has opened doors to materials engineering with countless research fields and corresponding applications. In particular, porous materials which are divided solids containing accessible cavities (pores), are attracting considerable attention as they can be used as mini reactors or for storing molecules or salts.

2. Ordered Porous Materials

According to the pore size, the IUPAC classified the materials into 3 groups: microporous (pore diameter < 2 nm), mesoporous (2 nm < pore size < 50 nm) and macroporous materials for pores larger than 50 nm.

Zeolites were the first known useful porous materials⁹. Naturally- or artificially-made zeolites have found wide applications in refining and petrochemical processes especially owing to their stability, ability to hold acidic, basic, redox sites and to replace the toxic liquid catalysts⁹ previously used. Despite the great advantages they offer such as cristallinity, ionic exchange ability, reproducibility, zeolites are essentially microporous and this can strongly limit their field of application when voluminous molecules are involved as it is the case for fine chemicals⁹. The quest of new types of sieves to get rid of these diffusion limitations led the

researchers of the Mobil Corporation in the early 1990s to implement a novel type of ordered mesoporous silica materials known as M41S, following earlier work of Kuroda¹⁰. These materials were prepared in basic medium at relatively low temperature and using a cationic structure directing agent (CTAB) forming micelles around which the negatively charged silica source can condense. The surfactant can then be removed giving place to accessible pores. The generated famous MCM-41 material (which stands for Mobil Composition of Matter n° 41) exhibit very high surface area along with an ordered 2D-hexagonal pore arrangement with very narrow size distribution^{11,12}. Related materials such as cubic MCM-48 and lamellar MCM-50 were also reported by varying the relative amounts of surfactant and silica source¹². The discovery of M41S materials has been a breakthrough, which has led to unprecedented progress in the design of materials by modulating the reaction conditions.

2.1. Synthetic approaches to mesostructured materials

Depending on the synthesis conditions (especially the pH), the silica source and the surfactant nature, mesoporous materials can be obtained according to two main approaches (Figure 8):

- True liquid crystal templating^{12,13} in which the silica condenses around a preformed surfactant mesophase. The inorganic phase grows in the intermicellar space, keeping the same ordered structure. This mechanism requires high surfactant concentration¹⁴.
- Cooperative self-assembly: the interactions between the surfactant and the inorganic precursor lead to a mesostructured material. This mechanism involves “hybrid” micelles that are the nuclei of the final material. Cooperative self-assembly mechanism occurs at the critical micellar concentration (cmc) in water (and < cmc when working under catalytic conditions).

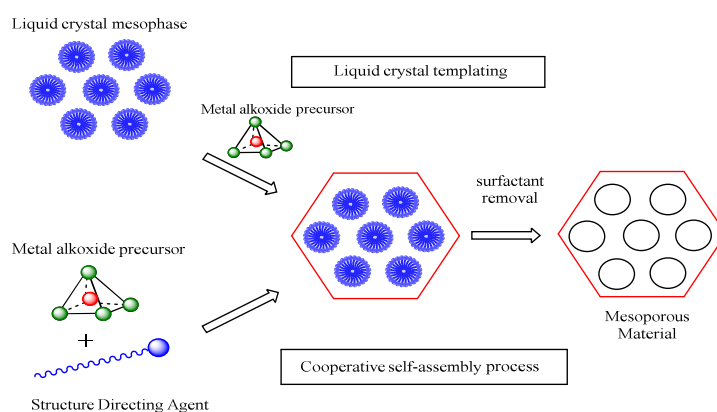


Figure 7: main synthetic approaches to mesostructured structures

The cooperative assembly mechanism was outlined in details in several works^{15–17} and extended to a series of interactions between the inorganic precursor and the selected surfactant depending on the pH (Figure 9).

Indeed, the charge of the silica surface plays a key role in the interaction with the surfactants. The isoelectric point (when the surface charge is null) of the silicates is found to be around $\text{pH} = 2\text{--}4.5$ ². Above this pH, (Si-O^-) entities are dominant but below, (Si-OH_2^+) are the present species¹⁸. In the first case, the use of surfactant with opposite charge leads to a direct interaction (I^+S^- e.g. MCM-41, MCM-48) while similarly charged surfactants involve counterions (halogenide anions X^- or alkaline metals X^+ mainly coming from the solvent) as intermediate species resulting in an indirect interaction $\text{I}^+\text{X}^-\text{S}^+$ (SBA-2, SBA-3). The literature hasn't mentioned any example of direct or mediated interaction between positively charged silica and ionic surfactant. This kind of interaction is only devoted for other metal oxides (aluminum, tin, titanium)¹⁹. In the case of non-ionic surfactants, the mesophase is governed by dipolar interaction or H-bonding giving place to interactions either by neutral silica surface such as MSU, HMS or neutral association between the silica surface and a counterion such as SBA-15.

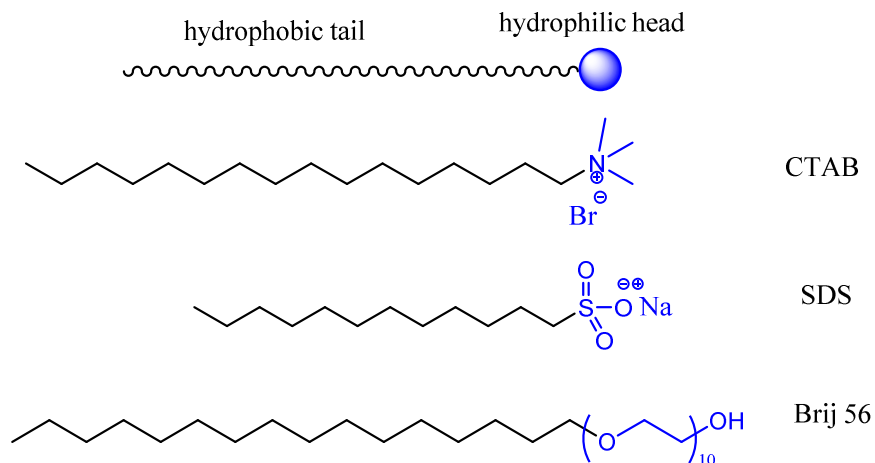


Figure 8: examples of amphiphilic surfactants used in ordered materials synthesis

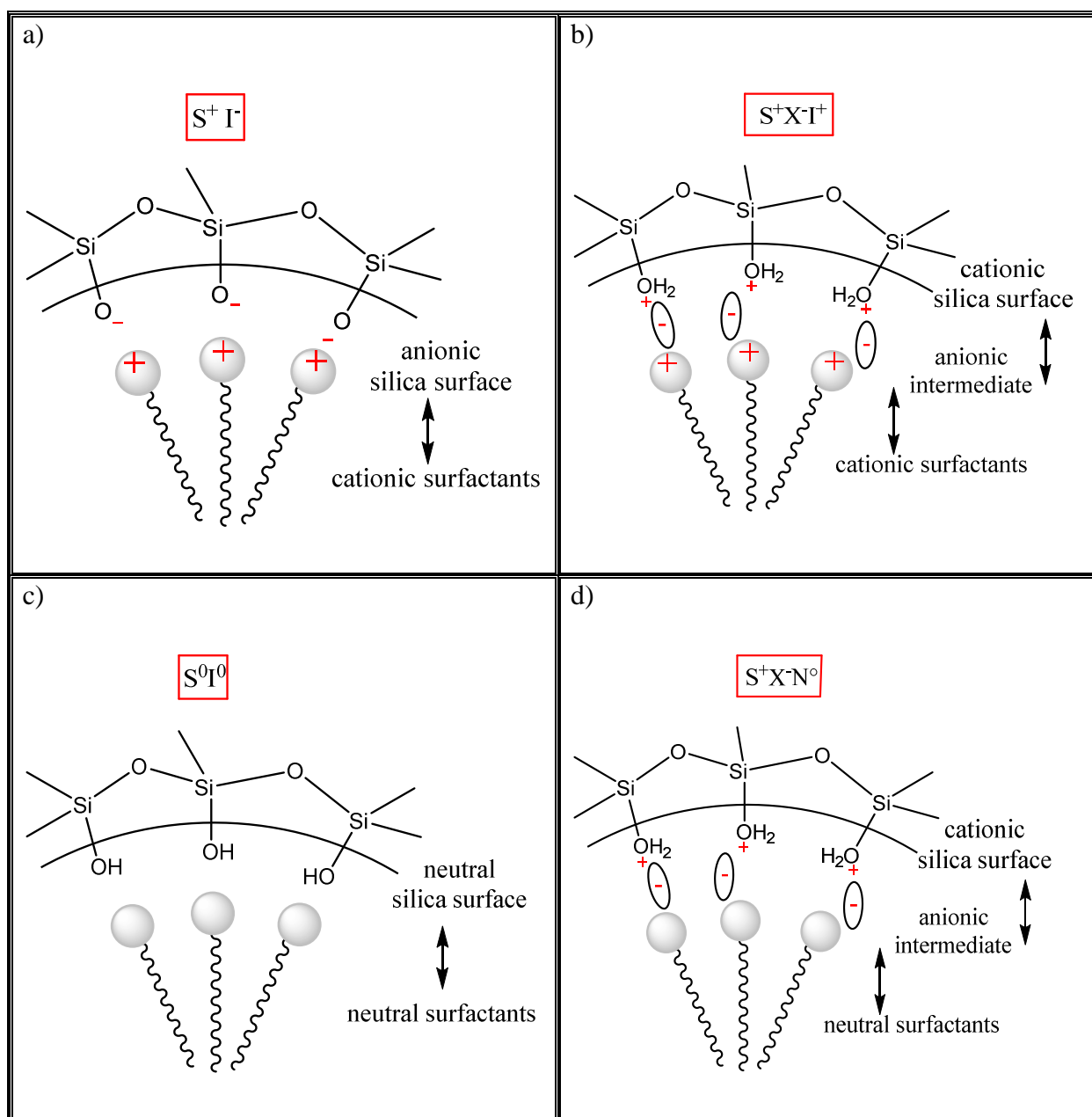


Figure 9: different possible interactions between silicates and surfactants. I is the inorganic specie, S is the surfactant and X is a mediator counter ion

2.2. From bulk materials to nanoparticles

Typical syntheses of mesoporous materials lead to particles on the micrometer-scale²⁰ (0.5 μm to several μms) not necessarily with defined shapes. However, emerging applications as polymers filling, chemical sensors and especially drug delivery²¹ impose smaller particles sizes and well-defined shapes. Thus, the synthesis of mesoporous silica nanoparticles (MSN), with diameters from 50 to 400 nm has recently attracted considerable attention.

Although several works were carried out in order to prepare silica nanoparticles, the latter were dense²², agglomerated²³ or fused²⁴ particles which strongly limits their usefulness. Two main routes are commonly used to prepare stable nanosized silica particles:

-High dilutions (Figure 10): This route consists in using a very low concentration of silica precursor in order to decrease the cross-linking kinetics of the precursors and hence inhibit their growth. The pH used in this route is highly basic and the hydroxide ions act as nucleation sites. This method has shown good success in making stable colloidal mesoporous nanoparticles by several research groups^{25,26}.

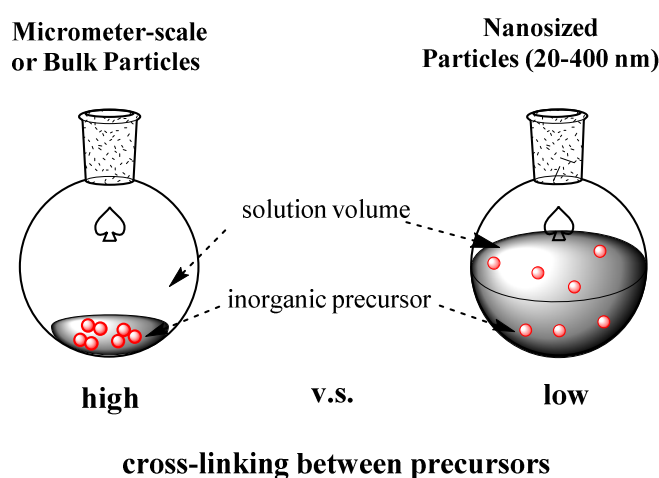


Figure 10: difference of interaction between inorganic precursors by using high water dilutions

-Atrane route (Figure 11): The use of triethanol amine TEOA as a hydrolysis-retarding agent was outlined in the early 2000s¹⁴. In the absence of water, TEOA forms a stable amine trialkoxo complex with the alkoxysilane by acting as an anionic tetradentate ligand $N(CH_2CH_2O)_3Si$. Once exposed to water, the as-made complex can stay relatively stable towards hydrolysis presumably due to a combination of electronic, steric and thermodynamic factors¹⁴. The obtained atrane complex is then subjected to surfactant addition followed by water along with controlling the temperature to initiate the hydrolysis-condensation process. The atrane complex prevents the rapid cross-linking between the alkoxysilanes making possible the control of the particles size by the time. It is noteworthy that so far, this route was used only for materials made using the conventional silica source (TEOS, TMOS).

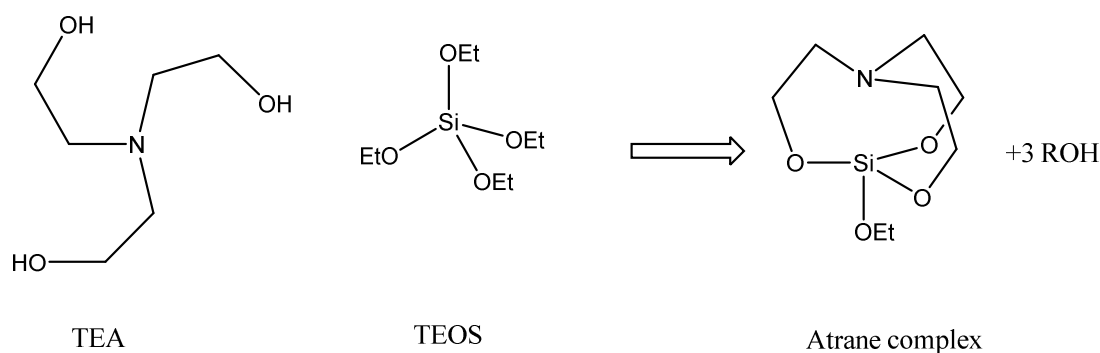


Figure 11: atrane complex formation by addition of TEOA to the silica source

In order to extend the application field of mesoporous silica materials²⁷, the mild conditions of the sol-gel process combined with the high accessible surface area obtained by templating mechanisms allowed incorporating organic functional groups. These hybrid organic/inorganic frame works combine the robustness of the silica skeleton and the versatility of organic functional groups thus renders possible a great number of chemical transformations at the surface. This makes the functional hybrid materials of central importance in soft chemistry with widespread applications^{15,19,28–31} regrouping catalysis, sorption, separation, sensing, optics or drug delivery.

3. Hybrid Functional Mesoporous Silica

Hybrid functional materials synergistically combine organic and inorganic fragments at the nanoscale, offering interactive properties from the inorganic skeleton and the active organic moieties. Depending on the link between the two components, hybrid materials can be divided into two classes^{32–35} (Figure 12):

3.1. Class I: Weak interactions dominate the linkage between the inorganic skeleton and the organic phase. This can be originated from hydrogen bonds, van der Waals or electrostatic interactions. However, the non-covalent interactions between the silica and the organic fragments allows the latter to leach out of the pores during the treatment steps thus resulting in low organic loading³⁶.

3.2. Class II: The organic phase is strongly linked (by covalent bonds) to the inorganic matrix. Obviously, the covalent linkage in *class II* materials can be widely exploited since it offers a wide tunable range of chemical properties and synthesis conditions.

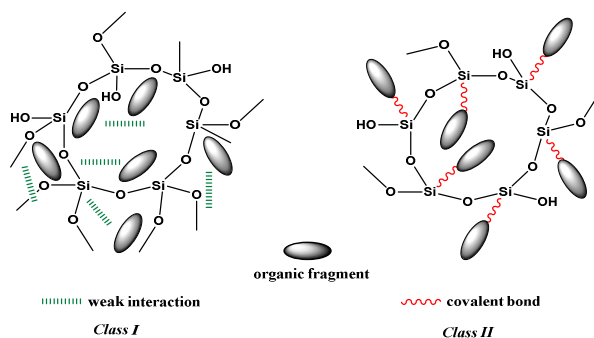


Figure 12: Structural difference between *class I* and *class II* hybrid silica materials

Class II hybrid silica materials are prepared by incorporating organic groups into the silica matrix during the synthesis process (co-condensation) or afterwards (post-functionalization). In both cases, the organic fragments must be previously derivatized with at least one trialkoxysilyl group (Figure 13).

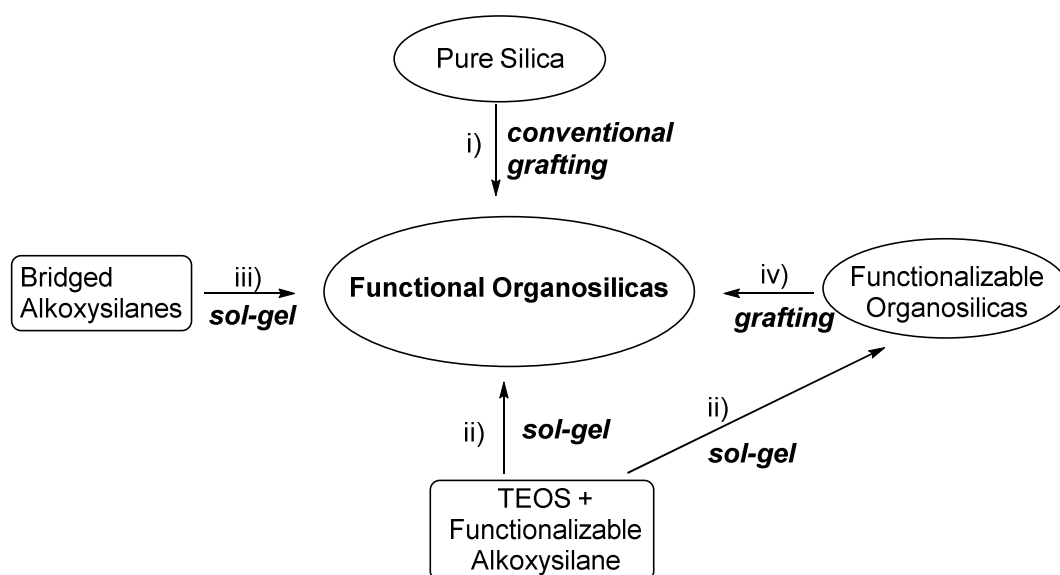


Figure 13: different functionalization routes for *class II* hybrid materials.

3.2.1. Conventional post-modification (or *grafting*)^{37,38} consists in anchoring the desired organic (active) function bearing a trialkoxysilyl group on the surface silanols. This route is simple, highly dependent on the condensation degree of the material and its efficiency may vary from a batch to another depending on external conditions. Furthermore, the density of grafted functions is highly heterogeneous, the external surface and the entrance of the pores being more easily functionalized. The main advantage lies in the preservation of the texture of the original silica material.

3.2.2. Co-condensation^{39–41} of an organo(trialkoxo)silane with a silica source (TEOS, TMOS,...) can be performed by the sol-gel process. The advantage of this route is the homogeneous distribution of the active functions within the whole material⁴². However, the creation of an organized porosity using surfactants shows strong limitations when voluminous organic groups are inserted, as the interactions between the template and the growing organosilica clusters gets altered.

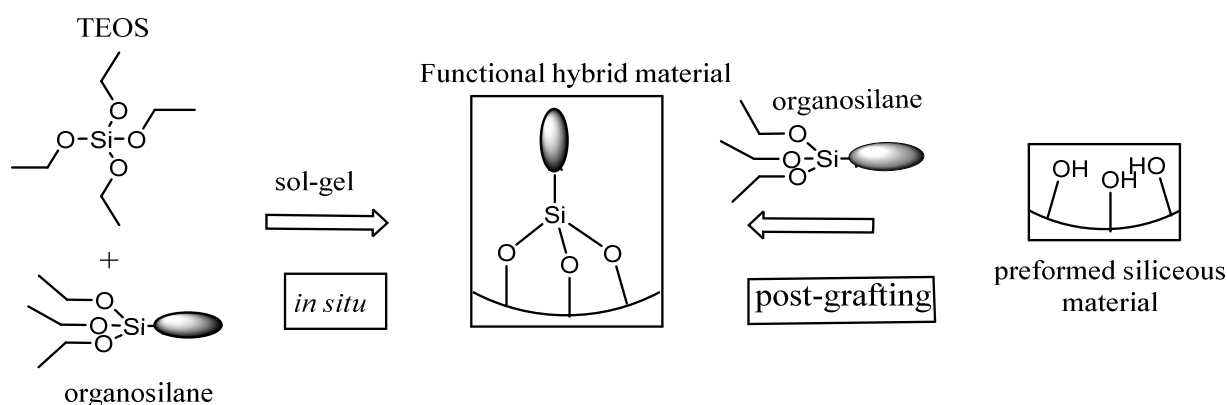


Figure 14: functional silica synthesis by the co-condensation and grafting methods

3.2.3. Hydrolysis-condensation of poly-silylated precursors: Without the use of any silica source, poly-silylated precursors lead to *bridged silsesquioxanes* (or *Periodic Mesoporous Organosilica* (PMOs) when a structure directing agent is used).

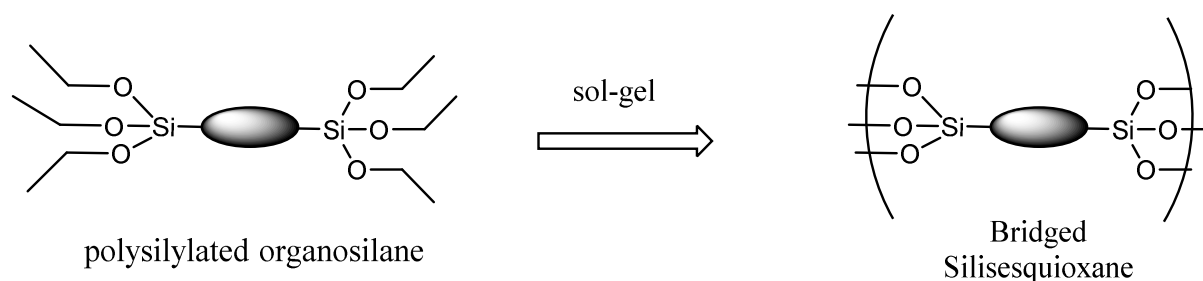


Figure 15: formation of pure organosilica by sol-gel process

This route is attracting increased interest since it provides materials with a high loading of functional groups inherently homogenously distributed and may offer new widespread applications^{43–48}. Moreover, a chain-like organosilica mainly constitutes the walls of the PMO while introducing monosilylated organosilanes affords pending functionalities on the internal and external surfaces (Figure 16). However, the formation of PMOs is strongly dependent on the structure of the precursor. PMOs can be produced from organosilanes with small organic fragments. Only few examples rule out this observation when the condensable fragments (alkoxysilanes) are dominant^{49–52} or when assisted by other interaction (e.g. π -stacking)⁵².

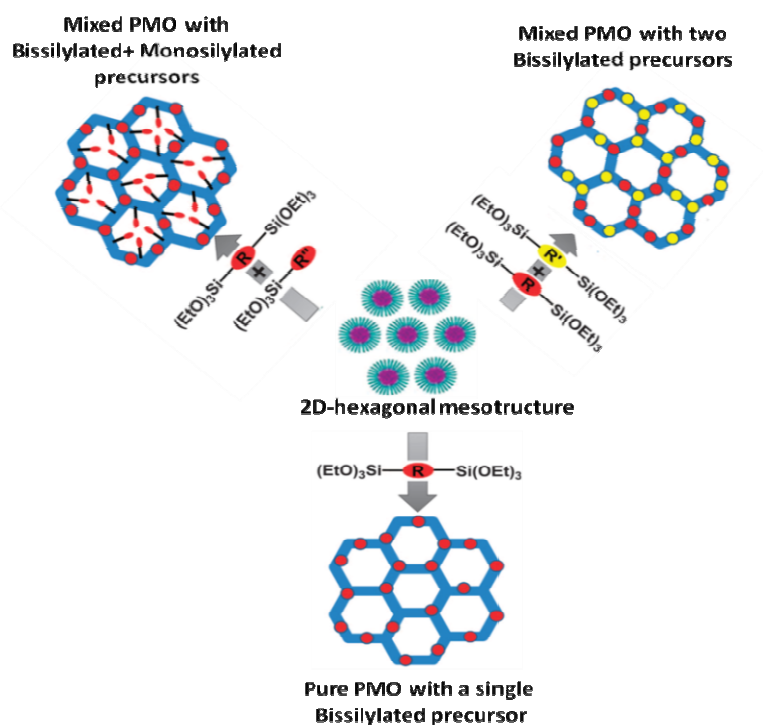


Figure 16: preparation of PMOs with organic moieties in their frameworks. adapted from ref⁴⁴

3.2.4. Click-grafting on functionalizable organosilicas

To circumvent the issues associated with the conventional grafting (use of moisture-sensitive reagents, heterogeneous functionalization) and the co-condensation methods (dependence of the texture on the organic fragments introduced), the chemical modification of organosilicas containing functionalizable groups appears as a promising strategy, which can also be applied to PMO materials, as functionalizable PMOs can be made with small organosilanes which are able to undergo further reactions; this can be very useful to make highly functional materials with robust features in a convenient route.

The reactions able to perform such chemical post-modifications with high conversions for a wide scope of organic functionalities have been classified as *Click* reactions.

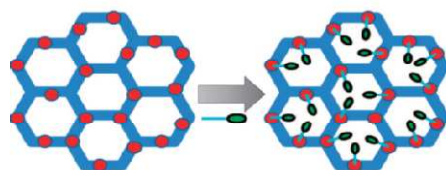


Figure 17: post-grafting on a pre-synthesized organosilica (PMO) bearing functionalizable groups. Adapted from ref⁴⁴

4. Click Chemistry

4.1. Definition

As it was introduced in 2001 by Sharpless, Click Chemistry is defined as a “set of powerful, highly reliable, and selective reactions for the rapid synthesis of useful new compounds and combinatorial libraries”⁵³. It consists of joining small units (molecules) together with the formation of carbon-heteroatom bonds in order to obtain new, complex and useful compounds.

Click Chemistry is not limited to a single type of reactions, but it is considered as a synthetic strategy. This gathers a wide range of already existing transformations that fulfill the “Click” criteria: the click reactions should be modular, wide in scope, high yielding, need simple work up and require benign reaction conditions^{54,55}.

Click reactions have a high thermodynamic driving force, leading to a rapid completion of the reaction and to a high selectivity towards one product. This feature can be exploited in many research areas making the click chemistry one of the most valuable approaches in molecular synthesis as well as in materials and polymers functionalization.

4.2. Reactions: This list shows the most frequently encountered examples of chemical transformations falling within the framework of the click chemistry:

a) Cycloaddition of unsaturated species:

- 1,3-dipolar cycloaddition: Copper catalyzed or strain promoted azide-alkyne cycloaddition.

- [4+2] cycloaddition: Diels-Alder.

b) Addition to carbon-carbon multiple bonds:

-Thiol-ene reaction (more generally Michael addition of Nu-H).

c) Non-aldolic carbonyl reactions type:

-Hydrazone and Oxime formation reactions.

Click reactions have confirmed their efficiency in many applications going from biotechnology, click modification of rotaxane, cyclodextrines, DNA, membranes, dendrimers, biomolecules (proteins, carbohydrates, oligonucleotides) conjugation⁵⁶⁻⁵⁹ to polymers and

material science such as surface modification of silicon^{60,61}, metal^{62–66}, carbon-based^{67–69} materials.

However, the Copper Catalyzed Azide-Alkyne Cycloaddition (CuAAC) remains by far the most useful and applied click reaction especially thanks to its high yield, rapid kinetics, chemo- and regio-selectivity, conferring it the most extended field of applications amongst the click reactions.

4.3. Copper Catalyzed Azide-Alkyne Cycloaddition (CuAAC)

The typical example of click chemistry is undoubtedly the CuAAC reaction which is the most encountered, useful and applied click reaction. This reaction was discovered simultaneously by the groups of Sharpless and Meldal in 2002^{70–72}. The success of this reaction is fueled by its quantitative yield, robustness and modularity. By contrast to Huisgen thermal cycloaddition which requires high temperatures and is not regioselective (thus it is not considered a click reaction), CuAAC consists of a regioselective 1,3-cycloaddition of an organic azide and a terminal alkyne using Cu(I) as a catalyst and giving place solely to a (1,4)-disubstituted triazole linker which is essentially chemically inert to reactive conditions, *e.g.* oxidation, reduction, hydrolysis. This reaction tolerates an extremely wide scope of functionalities, which makes it a unique linking method.

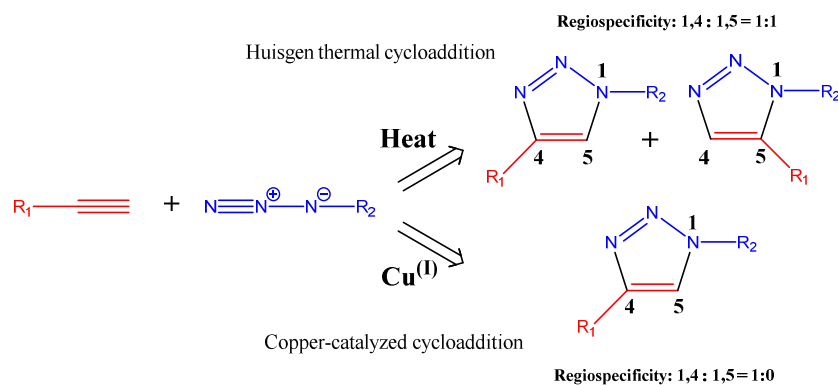


Figure 18: Cu-catalyzed vs Huisgen Azide-Alkyne cycloadditions

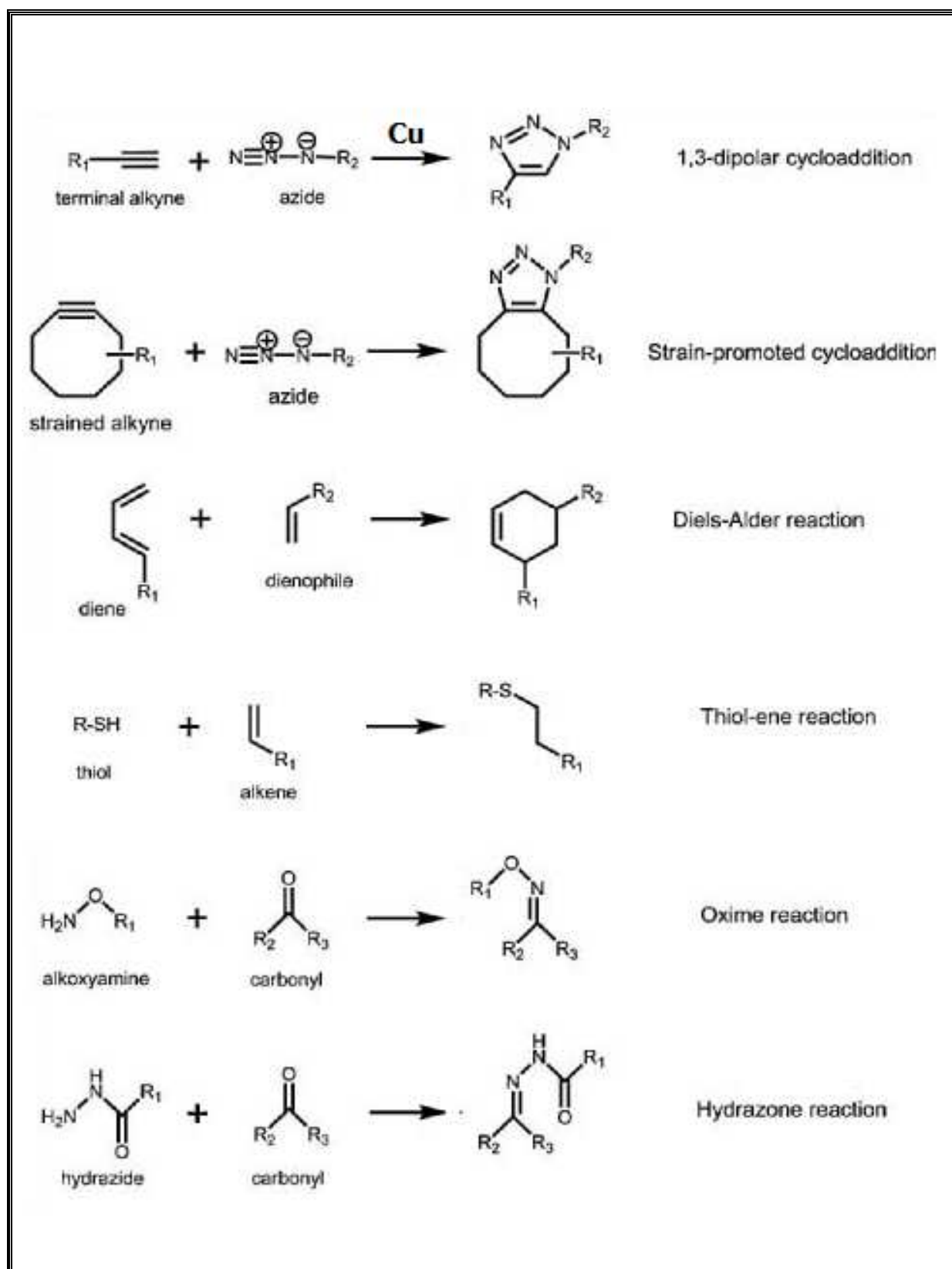


Figure 19: Most encountered click reactions. Reproduced from reference⁵⁴

4.3.1. Mechanism and kinetics of the CuAAC reaction

Any mechanistic approach of the CuAAC Click reaction should take into account the unique tolerance features of this reaction towards organic groups, solvent, pH and temperature. CuAAC reaction is driven by a high thermodynamic force ($> 20 \text{ kcal mol}^{-1}$)⁵³.

The great enhancement of the Huisgen reaction rate by using Cu(I) has shed light on the central importance of the mechanism modification induced by copper; several computational studies^{55,73,74} were made in order to probe the most plausible transitions of the this reaction.

Quantum calculations for non-catalyzed Huisgen reactions between several azides and alkynes have shown that the transition state is not polarized⁷⁵ and the alkyne remains a poor electrophile⁷⁶ by varying the adjacent group. In contrast to Huisgen thermal cycloaddition which exhibits a concerted mechanism, a stepwise mechanism in which a single Cu(I) is involved was initially suggested by DFT investigations.⁵⁵ The Cu(I) center is involved in the catalytic cycle through the coordination on the π electrons of the alkyne rendering it more acidic, followed by the exothermal formation of a copper acetylide. The mechanism proposes that Cu(I)-acetylide complex coordinates the azide inducing a rearrangement of the complex into six-membered metallocycle then into copper triazolide. The triazole is finally released after a reaction with an electrophile.

However, kinetic studies⁷⁴ confirmed a second order reaction with respect to Cu(I) concentration when the latter is lower than the concentration of the involved clickable partners. Therefore, it is very likely that more than one Cu(I) centers are involved in the transition state⁷¹. This is supported by the Cambridge Cristal Database which indicates that more than 98% of alkyne-copper complexes implicate two or three Cu atoms. In these structures, the $\text{C}\equiv\text{C}-\text{Cu}_2$ fragments strongly involve the π electrons of the alkyne in the Cu(I) coordination rendering the adjacent carbon very electropositive. The proposed mechanism is close to that involving a single metal. The copper coordination with the alkyne lowers the pKa and expels the H^+ (step 1) forming the copper-acetylide complex (step 2). In the transition state, the coordination between the azide and the acetylide does not necessarily take place on the same Cu (step 3)^{55,71,73,74} inducing the formation of the triazole-metallacycle (step 4) then releasing the triazole (step 5-6) after reaction with the H^+ liberated in step 1. Very recently, Fokin has demonstrated using isotopic enrichment of the triazolides that exactly 2 copper centers are involved in the mechanism of CuAAC⁷⁷ (Figure 20).

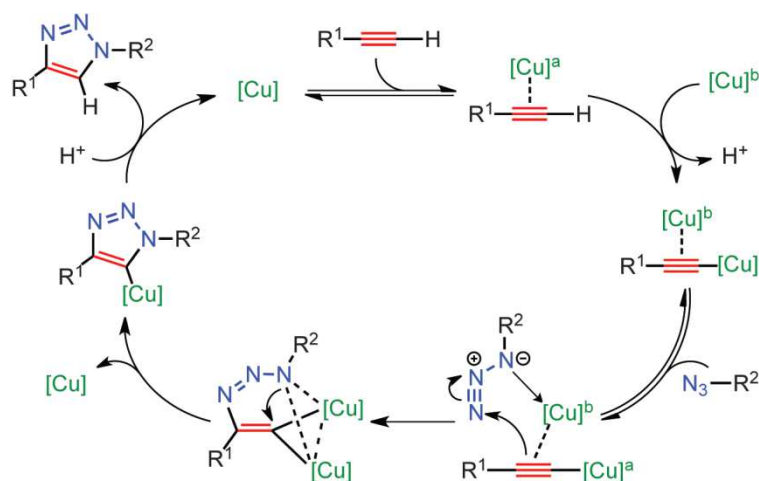


Figure 20: Proposed mechanism of the CuAAC click reaction using two copper centers. Reproduced from ref⁷⁷

4.3.2. CuAAC reaction conditions

The CuAAC reaction success as well as its extent is basically related to the mild reaction conditions which ensure the preservation of the clickable partner (organic or bio molecules). Undoubtedly, the copper center plays the central role in the reaction and it is important to keep the concentration of the copper as high as the reaction progress needs. Since most of the click reactions are carried out under air, Cu(I) may oxidize and the rate of the click reaction strongly decrease. This is the reason why Cu(II) salts with excess of reducing agent are widely used rendering the reaction less sensitive to oxygen.

The most common catalytic system is a combination of copper sulfate (0.01-0.1 molar equivalent to clickable partners) and sodium ascorbate (*ca* 4 eq/ Cu) in a water-alcohol mixture (typically tert-butanol) at room temperature. These conditions were first optimized by Sharpless⁷² and used later in a myriad of works⁷⁸⁻⁸⁴ due to their quantitative yield.

However, some organic functionalities (lysine or guanidine residues for example) are sensitive to reducing agents (even to the mild sodium ascorbate⁸⁵) or to the aqueous conditions⁸⁶. Cu(I) halides as CuBr, CuI, CuBr(PPh₃)₃ or Cu(I)-NHC complexes can be used as an alternative to the CuSO₄/Na-ascorbate system. In this case, the use of a base is often required (usually an amine such as Et₃N or DIPEA) to form the Cu-acetylide complex. Copper halides are used in solvents of intermediate polarity like THF, MeCN, and DMSO. In some cases the use of nitrogen heterocycles ligands are needed to protect the copper from oxidation.

4.3.3. Effect of ligands

Although using ligands is not a basic requirement for the catalytic effect of Cu(I) in the CuAAC reaction, they are usually employed to protect the Cu(I) from oxidation by oxygen thus to preserve the activity of the catalyst when working under air. They are also used to enhance the rate of the triazole formation, however, in some cases⁸⁷ it was found that some ligands decrease the rate of the click reaction by saturating the coordination sites of copper.

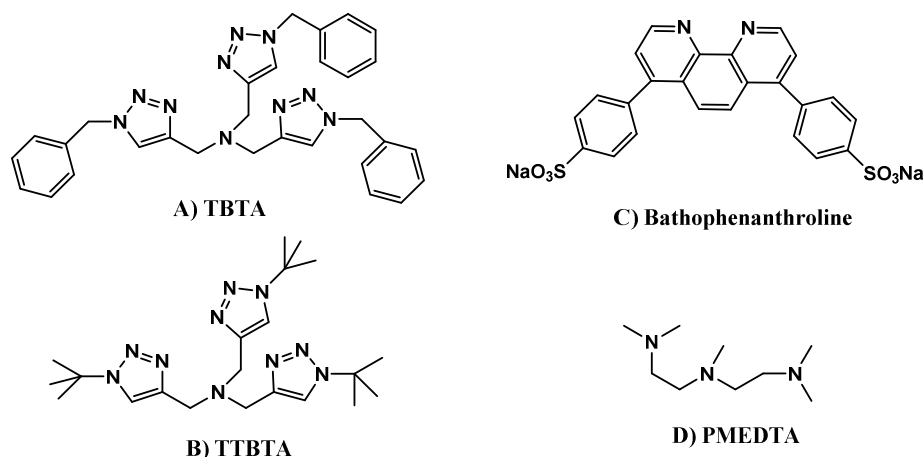


Figure 21: most popular ligands used to promote the CuAAC click reaction. A, B, C are used in molecular synthesis and materials functionalization, D is frequent in polymer chemistry.

4.4. CuAAC chemistry on hybrid silica materials

The CuAAC click chemistry is intensively exploited in molecular *Lego* construction and has recently shown a high importance in materials science since it enables a trustful tuning of the materials properties. CuAAC functionalizations have been used on silica-based materials processed as powders, nanoparticles, thin films and microdots.

4.4.1. CuAAC on mesoporous bulk materials

To the best of our knowledge, the first use of the CuAAC click reaction on mesoporous silicas was reported in 2008^{88,89}. In one example, an enzyme (trypsin) that was successfully attached on an azide-containing large-pores SBA-15 material through a NHS pentynoate linker (Figure 22) was shown to retain its catalytic activity. Azide functions were introduced by nucleophilic substitution on chloropropyl functions grafted on the SBA-15 material. Considering the difficulty to covalently incorporate biological fragments into materials, this work is considered a breakthrough and paved the way to a wide range of possible functionalizations.

Since then, the functionalization of mesoporous materials was investigated with different functions. For instance, the work was extended to several clickable functions (including mannose⁹⁰ ferrocene⁹¹ and TPA derivatives⁹²) that were anchored by CuAAC to N₃-SBA-15. Recently, adsorption of antibiotics was also achieved by clicking hydrophobic moieties on SBA-15 materials⁹³.

The loading of azide was reproducible and predictable since co-condensation method leads to a homogenous distribution of pending groups.

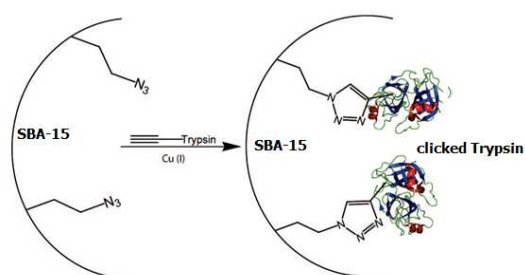


Figure 22: CuAAC-functionalized SBA-15 material with trypsin. Adapted from ref ⁸⁸

4.4.2. CuAAC on hybrid thin films

Making use of electrochemically-assisted self assembly (EASA), clickable hybrid films with ordered oriented mesopores and different extents of clickable functions were also synthesized and successfully characterized by cyclic voltammetry after CuAAC with ferrocene⁹⁴.

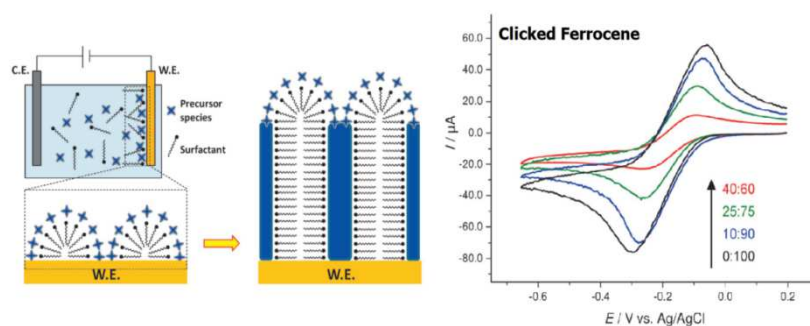


Figure 23: (left) Illustration of the EASA co-condensation process of AzPTMS and TEOS in the presence of CTAB to get vertically aligned azide-functionalized mesoporous silica film (W.E.=working electrode; C.E.=counter electrode) and (right) Cyclic voltammograms characterizing the different extent of clicked ferrocene. Adapted from ref ⁹⁴

4.4.3. CuAAC on Silica Mesoporous Microdots Arrays

Applying inkjet printing to produce microdots is promising in the field of sensing⁹⁵ and to miniaturize biochips⁹⁶. By combining this technique with evaporation induced self assembly (EISA) and the CuAAC click chemistry it was possible to form microdots arrays of clickable mesoporous silica on which sensing properties were validated by selectively clicking adenine that was recognized by a labeled thymine (Figure 24). The development of this chemistry to produce innovative biochips is underway⁹⁵.

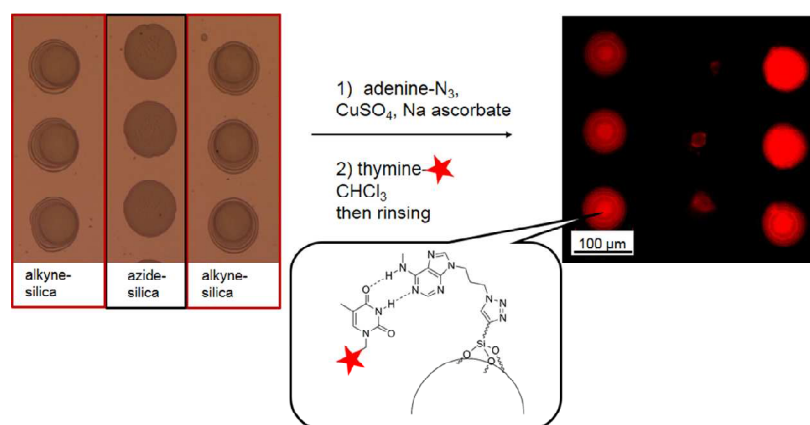


Figure 24: CuAAC covalent functionalization of alkyne derivatized silica microdots with azidopropyl-adenine and subsequent recognition with labeled thymine. The central column consists of azide-silica and serves as control. It can be further functionalized by alkyne nucleosides in the same fashion to obtain a multi-functional network. Reproduced from ref⁹⁶

4.4.4. CuAAC on mesoporous silica nanoparticles

Mesoporous silica nanoparticles (MSNs) offer a wide range of important applications in nanomedicine^{97,98}, catalysis⁹⁹ or for coatings¹⁰⁰. Nanoparticle functionalization is a step of primary importance to implement functionalities to the materials.

The first works that made use of the CuAAC reaction on mesoporous silica nanoparticles were attempting to make nanocarriers for controlled drug delivery upon specific stimuli. Hence, the pores were capped with supramolecular groups such as cyclodextrine^{101,102}, DNA¹⁰³, rotaxane⁸⁵ by anchoring them to the external surface of the nanoparticles via CuAAC click reaction. Enzymes were also imprisoned in a network of MSN via CuAAC¹⁰⁶, while a peroxidase mimic based on an iron-based voluminous group was successfully clicked and was used for biosensing (Figure 25).¹⁰⁷

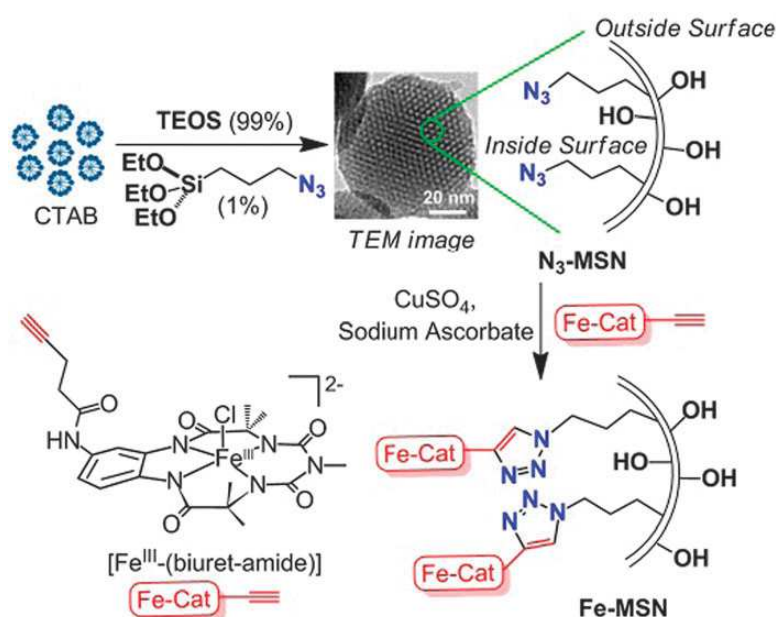


Figure 25: click reaction of [Fe^{III}(biuret-amide)] on MSN. Adapted from ref ¹⁰⁷

Click chemistry offers promising opportunities to perform multiple functionalization on silica materials^{95,108}. The first published application of dual click reactions on MSNs was highlighted in 2012 where the orthogonal CuAAC and thiol-ene reactions were used to incorporate acidic and basic sites for cooperative catalysis⁹⁹ of the Henry reaction.

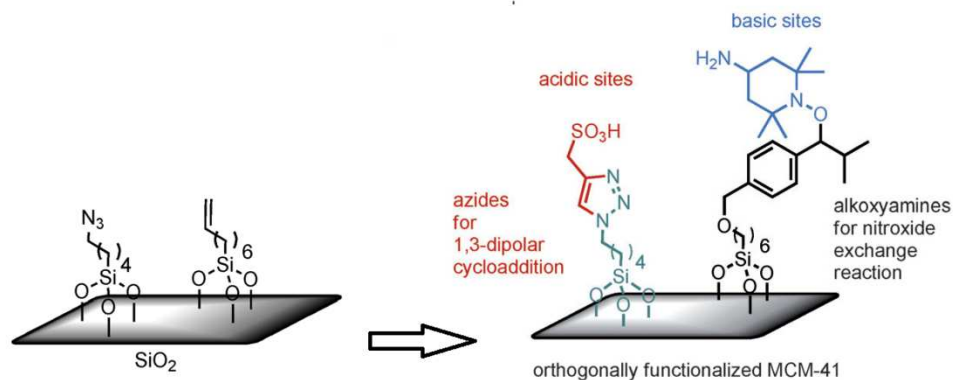


Figure 26: Azide and alkene functionalized nanoparticles ready for CuAAC and thiol-ene couplings. Adapted from ref ⁹⁹.

4.4.5. Click on PMOs

PMOs materials exhibit important features as they hold the highest amount of organic fragments. Even though several works were achieved on mesoporous silica materials (focusing on SBA-15 and MCM-41), very few results were published on clickable PMOs materials. Very recently¹⁰⁹ a clickable mixed PMO was synthesized via co-condensation of azidopropyltrimethoxysilane (AzPTMS) with 1,2-bis(trimethoxysilyl)ethane (BTME) (Figure 27), and was used as a platform to screen surface functionalities enabling efficient adsorption of antibiotics.

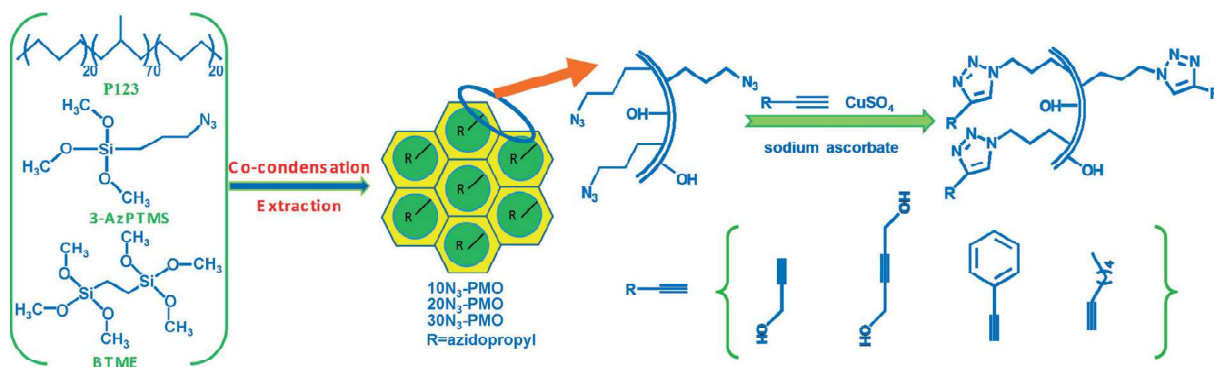


Figure 27: surface modification by CuAAC reaction on clickable mixed PMO. Adapted from ref ¹⁰⁹

5. Conclusion/ Objectives of the present work

The sol-gel process is now a widely used method to prepare silica-based materials with controlled morphology and texture (shape, porosity, size). Owing to the mild conditions used,

it is possible to introduce organic moieties in order to confer functionalities and broaden the application field of such materials. Well-documented methods have been established to incorporate organic functions and to optimize the surface properties; however, the CuAAC reaction arises as a great candidate to produce highly functional materials owing to its high conversions, exceptional functional group tolerance and to the mild conditions needed. Clickable hybrid materials, nanoparticles, thin films and mixed PMOs were recently combined to the CuAAC reaction for various unprecedented applications in nanomedicine, luminescence, catalysis or adsorption thanks to the ease of incorporation of several voluminous and functional groups.

Following this bibliographic review, it appears that clickable PMOs constitute a very interesting target as these materials might allow a maximal loading of clicked organic functionalities, ideal to drastically tune the surface properties. Furthermore, the possibility to implement multiple organic functionalities on a single piece of material in a controlled fashion should help designing multifunctional materials for applications in catalysis or nanomedicine.

The present work is part of a wider study aiming at establishing the foundations of the CuAAC functionalization methodology for silica-based materials made by the sol-gel process, following the PhD thesis of Nirmalya Moitra¹¹⁰, Kristýna Bürglová¹¹¹ and Olivia De Los Cobos¹⁰⁸. Its specificity resides in the new types of materials designed (PMOs and MSNs) and in the application foreseen in nanomedicine in collaboration with Prof. JI Zink (UCLA).

In the first part, we will use a novel approach to make fully-clickable mesoporous bridged silsesquioxanes and PMOs from clickable bridged organosilanes. CuAAC reactions will be then performed with model clickable molecules to highlight the high conversions and the wide functional tolerance offered by the CuAAC reaction. Afterwards, making benefit of this feature, we will tailor the surface properties of clickable mesoporous materials by grafting organic fragments with different hydrophilic-lipophilic characters.

The second part of this work will be devoted to apply click chemistry on multifunctionalizable mesoporous silica nanoparticles in order to design stimuli-responsive nanocarriers for controlled drug delivery. The CuAAC reaction will be performed to confer selected features to the nanoparticles such as pore gating for stimuli-responsive drug delivery, cancer cell targeting, and fluorescent tracking.

CHAPTER II

Periodic Mesoporous Organosilica and Bridged Silsesquioxane Functionalized by CuAAC Click Reaction.

CHAPTER II: Periodic Mesoporous Organosilica and Bridged Silsesquioxane Functionalized by CuAAC Click Reaction.

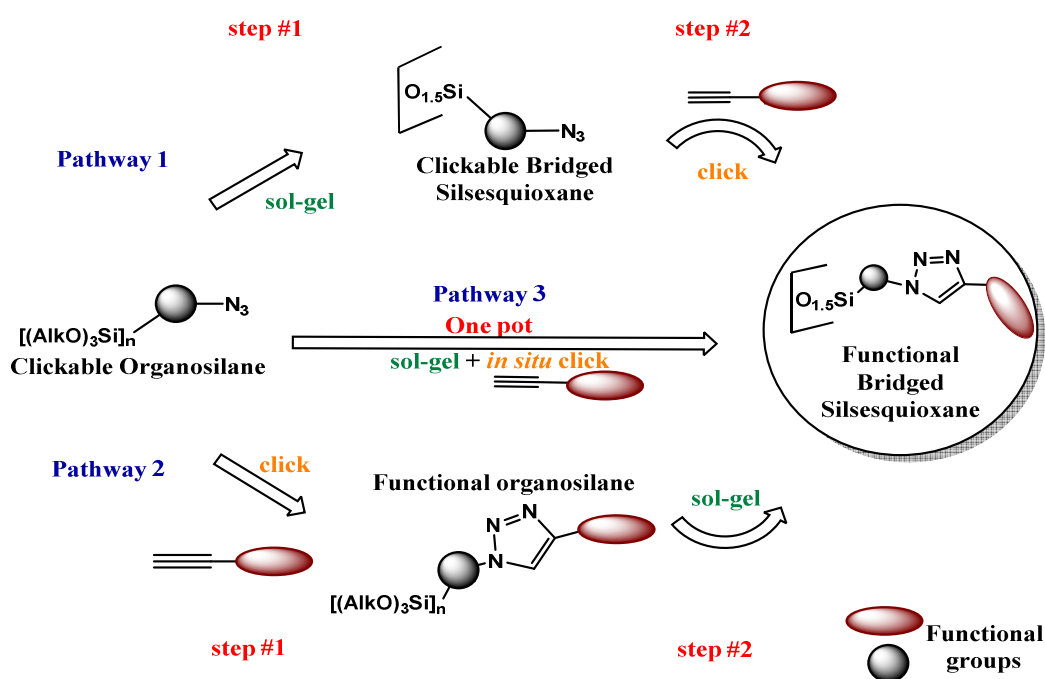
In this chapter our discussions will focus about the synthesis of new family of functional materials making benefit of the potential of the CuAAC click reaction as a gold standard in molecular *Lego* synthesis as well as in material functionalization. The second subdivision of this chapter consists of using the strength of CuAAC to tailor and investigate the hydrophobic/lipophobic induced character of the clickable bridged silsesquioxane using different clickable model molecules.

1. Introduction

Over the past years hybrid (Inorganic/Organic) siliceous materials have become a center of interest in applied chemistry² occupying the interface between the inorganic materials' input and organic functions' contributions. The combined complementary properties of the inorganic silica matrix and the organic functional groups is leading to many investments in several applications where catalysis^{112–116}, light harvesting⁴⁴, drug delivery⁴³, sensing^{36,117}, adsorption^{118–122} and microelectronics¹²³ have shown their potential.

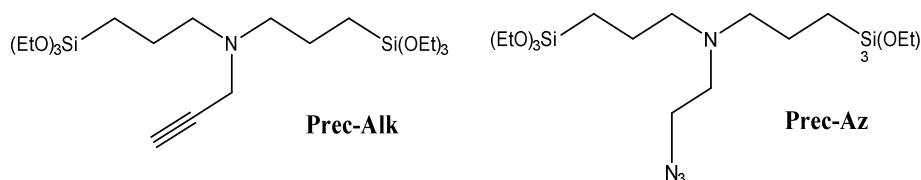
As we have shown in the first chapter, hybrid silica could be prepared according to many pathways¹²⁴. The co-condensation of an organosilane with a silica source (typically TEOS or TMOS) is the most commonly used way to get an ordered and homogeneously functionalizable material while using limited concentrations (up to 20%) of organosilane bearing small organic fractions. In this case, from 90 to 99% of the material only constitutes the skeleton, thus this reduced amount of functional groups may limit the performances of such materials. In order to obtain a maximal and regular loading of functionalities, pure polysilylated organosilanes (without added silica sources such as TEOS or TMOS) were used to make, according to three pathways (Scheme 1), bridged silsesquioxanes for which PMOs (for Periodic Mesoporous Organosilica) constitute a particular family. PMOs, which are currently being developed for demanding applications can be obtained by using structure-directing agents during the synthesis. However, their synthesis is known to be disfavoured with organo-bridged silanes bearing voluminous organic units.

In this respect, we will present here the use of a new series of clickable organo bis(triethoxysilane)s which synthesis has been recently patented by our group¹²⁵ as new sol-gel precursors to capitalize on CuAAC reactions in making functional PMOs and more generally functional bridged silsesquioxane by either grafting methods (Scheme 1, pathway 1) or direct sol-gel from a functional organosilane which is built by CuAAC from the starting organosilane (Scheme 1, pathway 2) or finally, by a single step synthesis from the starting clickable organosilane performing simultaneously the sol-gel and CuAAC reactions in a one pot strategy. (Scheme 1, pathway 3).



Scheme 1: New pathways to afford functional bridged silsesquioxanes

Novel clickable polysilylated organo-bridged silanes were synthesized by our group to be used as precursors i) for making other functional organosilanes *via* the CuAAC reaction and ii) to fabricate highly functionalizable materials *via* click grafting.



Clickable bis-silylated organosilanes used in functional material preparation

2. Functional PMOs and Bridged Silsesquioxane by CuAAC grafting

This part corresponds to pathway 1 of Scheme 1. The clickable organosilane undergoes a sol-gel polymerisation process to form a clickable material (step 1). The sol-gel reaction can be either fluoride, acid or base-catalyzed; in the two latter cases, the use of an appropriate surfactant leads to a porous and eventually structured material (PMO) that may afford important properties. The functionalization of the material is done by a grafting method (step 2); easily prepared clickable functional molecules can be incorporated by a CuAAC reaction under mild conditions (room temperature and atmospheric pressure). Although the grafting yield may vary with some conditions (size and solubility of clickable partner, diffusion into the pores, ...), the major advantage of this method is the possibility to introduce useful functions such as biocatalysts (enzymes), biomolecules (DNA strands, folic acid), on a preformed material without altering its structure to afford structured and functional materials hardly conceivable using other strategies.

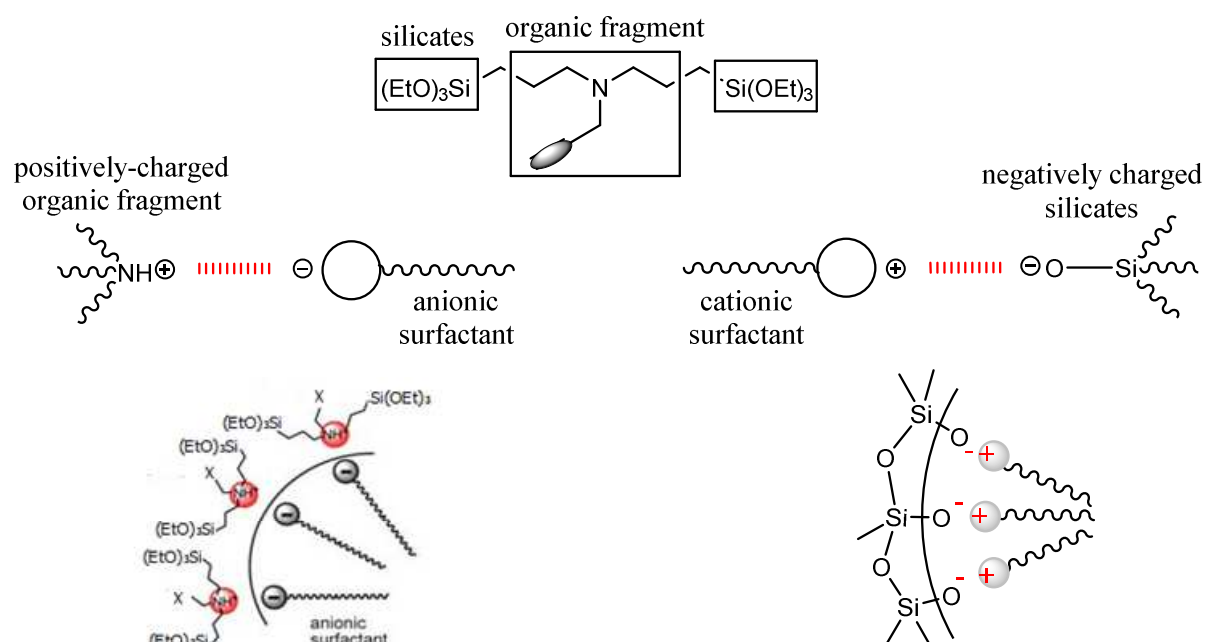
As already mentioned, making PMOs is disfavoured in the case of voluminous organic fragments that may mask the interaction between the hydrolyzed precursor and the surfactant. Few works attempting to make clickable PMOs have been done yet but with the use, in high fraction, of organosilane bearing small organic groups (ethyl, ethylene). Gao et al.¹⁰⁹ have recently developed clickable PMOs by using a maximum of 10% azidopropyltriethoxysilane AzPTES with 90% bis(trimethoxysilyl)ethane (BTME) as skeleton. At the functionalizing level, this kind of “mixed” clickable PMOs still encounters limitations close to those of materials made by co-condensation with silica source (TEOS, TMOS).

In our work, we will make use solely of **Prec-Alk** and **Prec-Az** to synthesize ordered clickable materials. As described in previous works^{126,127}, amine-containing bridged organosilanes containing three trialkoxysilane groups can be transformed into PMOs using anionic surfactants.

In the aim of obtaining PMOs material using bisilylated organosilanes, two different types of interactions between the organosilane and the surfactant were approached (scheme 1 bis):

1) Interaction between **organic fragment** and the ionic head of the surfactant: Analogously to trisilylated organosilanes, the amine propagyl group is subjected to a protonation at low pH. An electrostatic interaction with a negatively charged surfactant may take place and afford the desired PMO.

2) Interaction between the **silicates** and the hydrophilic head of the surfactant: Upon basic catalysis conditions, the silicates of the organosilane are negatively charged, an interaction with a positively charged surfactant can be brought into light in order to afford the PMO.

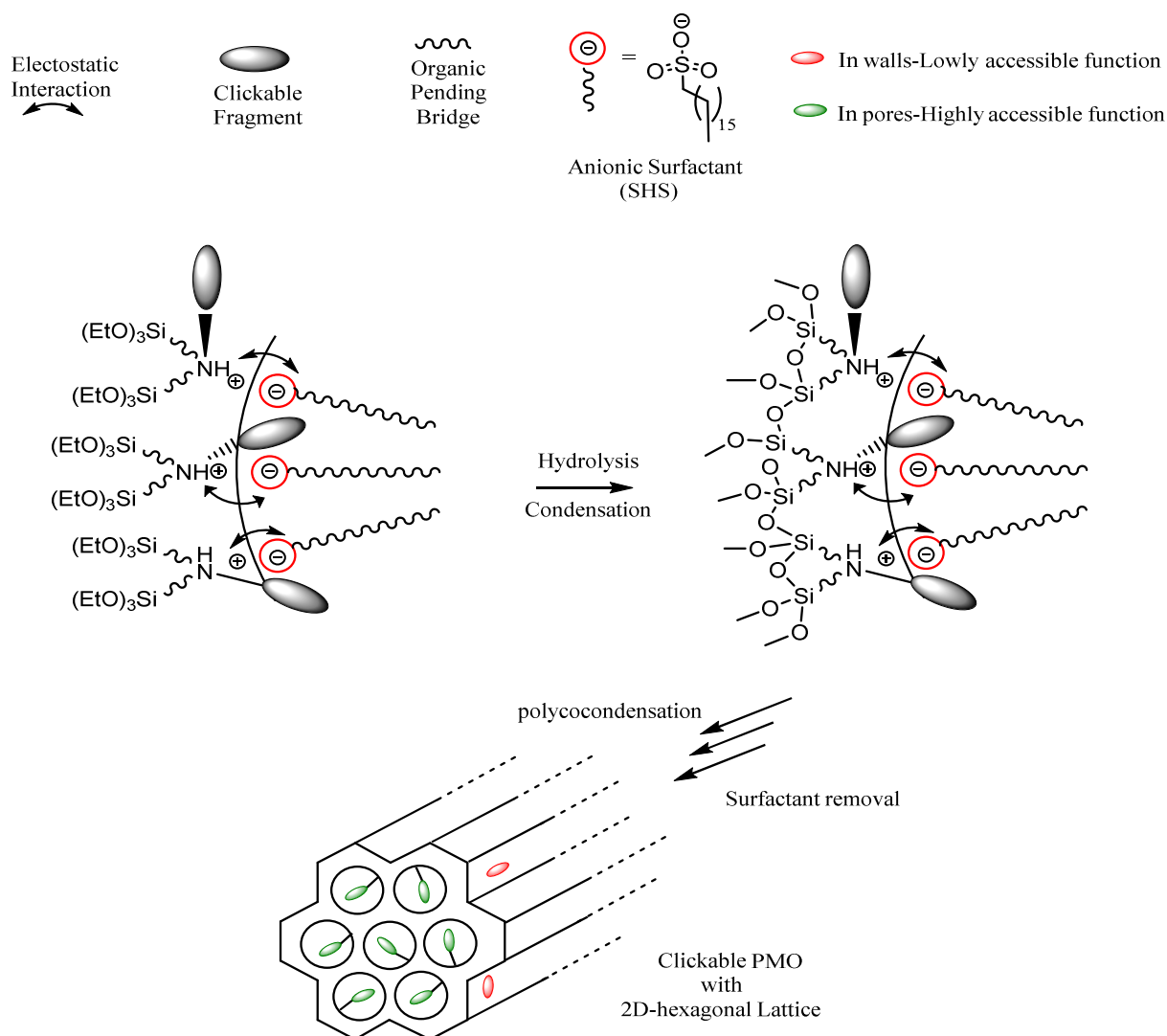


Scheme 1 bis: Two main types of interactions (organosilane-surfactant) approached in the synthesis of PMO material

2.1. Interaction Organic fragment- Surfactant

2.1.1. Synthesis of Clickable Periodic Mesoporous Organosilicas M1 and M2

PMOs **M1** and **M2** were synthesized from their respective precursors **Prec-Alk** and **Prec-Az** using sodium hexadecylsulphate (SHS) as structure-directing agent in acidic medium (60 °C over 30 min). Under acidic conditions, the electrostatic interactions between the ammonium group and the anionic head of the template lead to an organized 2D-hexagonal structure according to scheme 2. After template removal, PMOs were fully-characterized and functionalized *via* CuAAC Click Chemistry.



Scheme 2: Mechanism of PMOs formation using amine precursors under acidic conditions.

2.1.2. Clickable PMOs Characterization

Composition of the materials: Fourier-Transformed InfraRed (FTIR) and Raman spectroscopies were firstly used to characterize the synthesized materials (Figure 1). This kind of analysis is very fast and gives valuable primary information about the presence of functional groups, thus the chemical composition. For **M1** and **M2**, both FTIR spectra show vibrations typical of Si-O-Si ($1000\text{--}1100\text{ cm}^{-1}$), Si-OH (910 cm^{-1}), C-C and C-N ($1250\text{--}1470\text{ cm}^{-1}$) and CH₂ ($2800\text{--}3000\text{ cm}^{-1}$). A prominent peak corresponding to azide's N₃ stretching is seen at 2097 cm^{-1} for **M2**. In the case of **M1**, the H-C_{sp} stretching of the terminal alkyne is identified by a medium peak at 3294 cm^{-1} by FTIR and the terminal (asymmetric) C≡C vibration is only detectable, because of its polarizability, by Raman spectroscopy at about 2100 cm^{-1} .

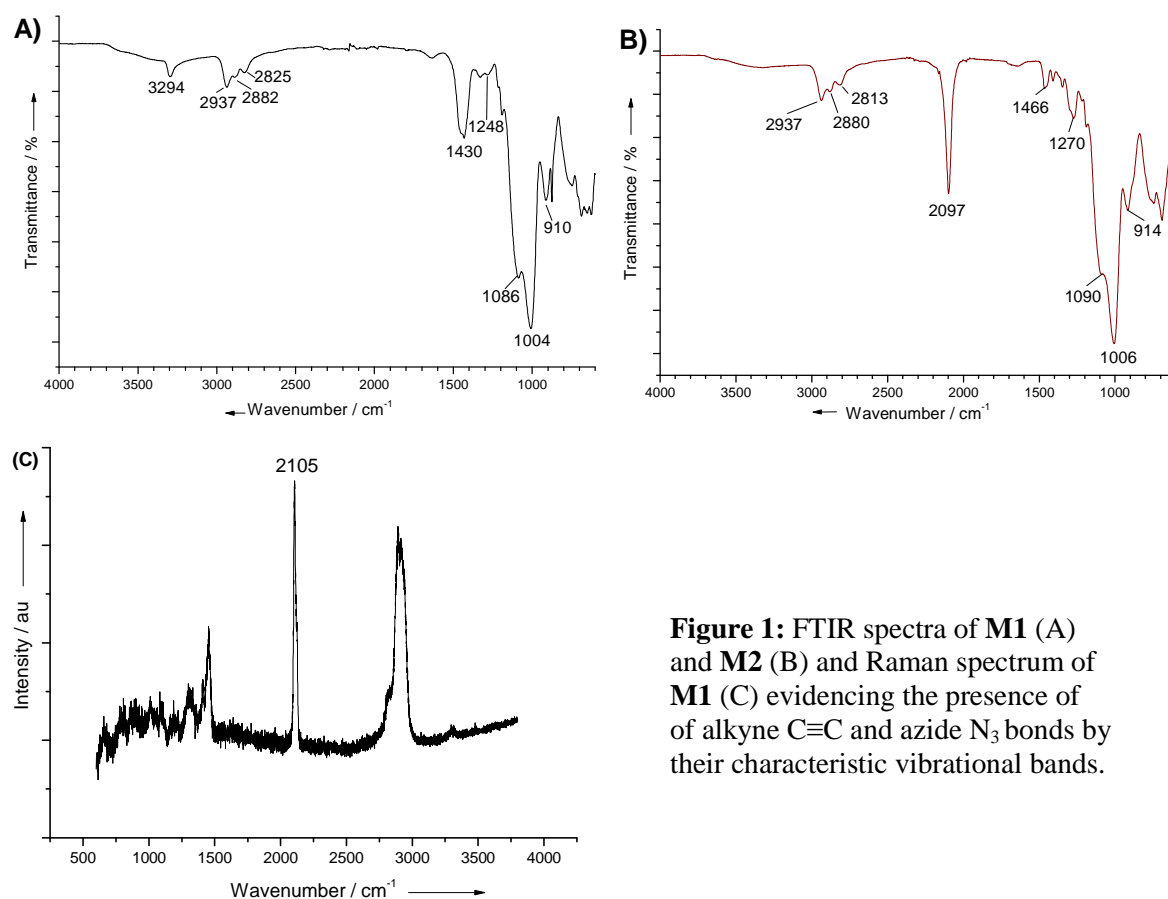


Figure 1: FTIR spectra of **M1** (A) and **M2** (B) and Raman spectrum of **M1** (C) evidencing the presence of alkyne C≡C and azide N₃ bonds by their characteristic vibrational bands.

^{13}C CP-MAS NMR spectra of **M1** and **M2** (Figure 4) display the expected signals at close positions to those of the corresponding precursors, except the signals at 18 and 58 ppm, which correspond to the ethoxy groups in the precursors which are involved in the sol-gel process. The carbons in positions 1 and 2 (in alpha and beta to silicon, respectively C1 and C2) appear at low chemical shift (δ 10-25 ppm), they are slightly shifted (from 7 to 13 ppm for C1 and 18 to 22 ppm for C2 for **M1** and **M2**) because of the modification of their chemical environment. Carbons (3, 4) in alpha to the central nitrogen atom are in the 40-55 ppm region where carbon 5 (alpha of azide) in **M2** is also seen. Typical signals of alkyne's carbons in **M1** are shown at about 70-80 ppm. ^{29}Si CP-MAS NMR shows a very high condensation degree of 88% for **M1** and 91% for **M2** with only T^2 [$\text{R-Si}(\text{OSi})_2(\text{SiOH})$] and T^3 [$\text{R-Si}(\text{OSi})_3$] signals.

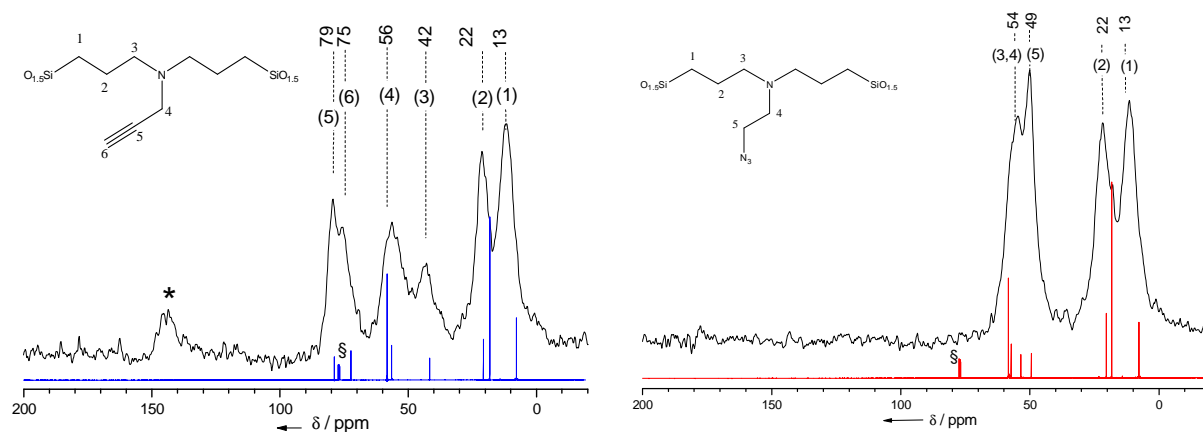


Figure 2: ^{13}C CP MAS NMR of PMOs **M1** (left) **M2** (right) + liquid ^{13}C CPD NMR of the corresponding precursor (**Prec-Alk** blue left, **Prec-Az** red right)

Elemental analyses performed on the alkyne-containing material before surfactant removal are in good agreement with the formula $[\text{O}_{1.5}\text{Si}(\text{CH}_2)_3]_2\text{NCH}_2\text{C}\equiv\text{CH}\cdot\text{C}_{16}\text{H}_{34}\text{SO}_4$ which corresponds to a 1:1 adduct between the surfactant and the fully condensed monomer (Table 1). However, whereas the extracted material does not contain any more surfactant (with no detectable sulphur), it still contains a high amount of water, as the C and N contents are far below the expected amounts (mass percentage), while their relative contents are in agreement with the theoretical ratio (Table 1). This is confirmed by TGA analyses (Figure 5) with a strong weight loss of around 17% below 100 °C.

Material	%N	Elemental analysis		
		%C	%S	N/C (th)
M1 -alk as synthesized	2.3 (2.5)	53 (53)	6.5 (5.8)	
M1	3.5 (5.8)	28 (45)	< 0.2	0.125 (0.129)
M2 -N ₃ as synthesized				
M2	17.7 (20.5)	33.97 (35.3)	< 0.2	0.52 (0.58)

Table 1: elemental analyses of **M1** and **M2** before and after template removal

Textural analyses: Scanning electron micrographs (Figure 2, A and D) indicate that the material was obtained with a curved rods structure (*ca* 70–150 nm wide and 1–5 μm long microrods). Transmission Electron Microscopy (Figure 2) clearly shows (pictures B and E) tubular pores for **M1** and **M2** with a hexagonal lattice, as seen by Fourier Transform of part of the image (insets). Furthermore, particles with hexagonal shapes are visible in micrographs C and F. In addition, **SAXS** experiments were run to confirm the mesostructure observed by TEM for materials **M1** and **M2**, as this technique is representative of the whole material, contrarily to TEM which is a local technique. SAXS profiles (Figure 3) are characteristic of cylindrical mesopores with a 2D-hexagonal arrangement of the structure (*P6mm* space group) for **M1** and **M2**. Before template extraction, both PMOs presented better resolved mesostructure with clear Bragg peak (q_0) and harmonics ($3^{1/2}q_0$ and $2q_0$) at $q = 1.5, 2.6$ and 3.0 nm^{-1} for **M1** and $q = 1.45, 2.5$ and 2.9 nm^{-1} for **M2** corresponding to inter-reticular distances of d_{10}, d_{11} and d_{20} plans respectively. The cell parameter “*a*” indicating the distance between the axes of two neighbouring cylindrical pores is calculated as $a = 2d_{10}/3^{1/2}$ while $d_{10} = 2\pi/q_0$. Therefore, **M1** and **M2** display very close interpore distances of (4.8 and 5.0 nm). According to results previously published by Hesemann¹²⁷ on a related material synthesized under similar conditions with the same surfactant, the pores are expected to have a diameter of 2.0 nm thus the wall thickness is calculated at $3.0 \pm 0.3 \text{ nm}$ for both PMOs. After template removal, for **M1** as well as for **M2**, the harmonics corresponding to d_{11} and d_{20} plans tend to disappear, which means that the long-range mesostructure order is partially lost. No change in d_{10} was observed for **M1**. However, the Bragg peak in **M2** is slightly shifted towards higher q values (from 1.45 to 1.6 nm^{-1}) indicating a lattice compaction of 4 Å (*i.e.* inter-reticular distance reduction).

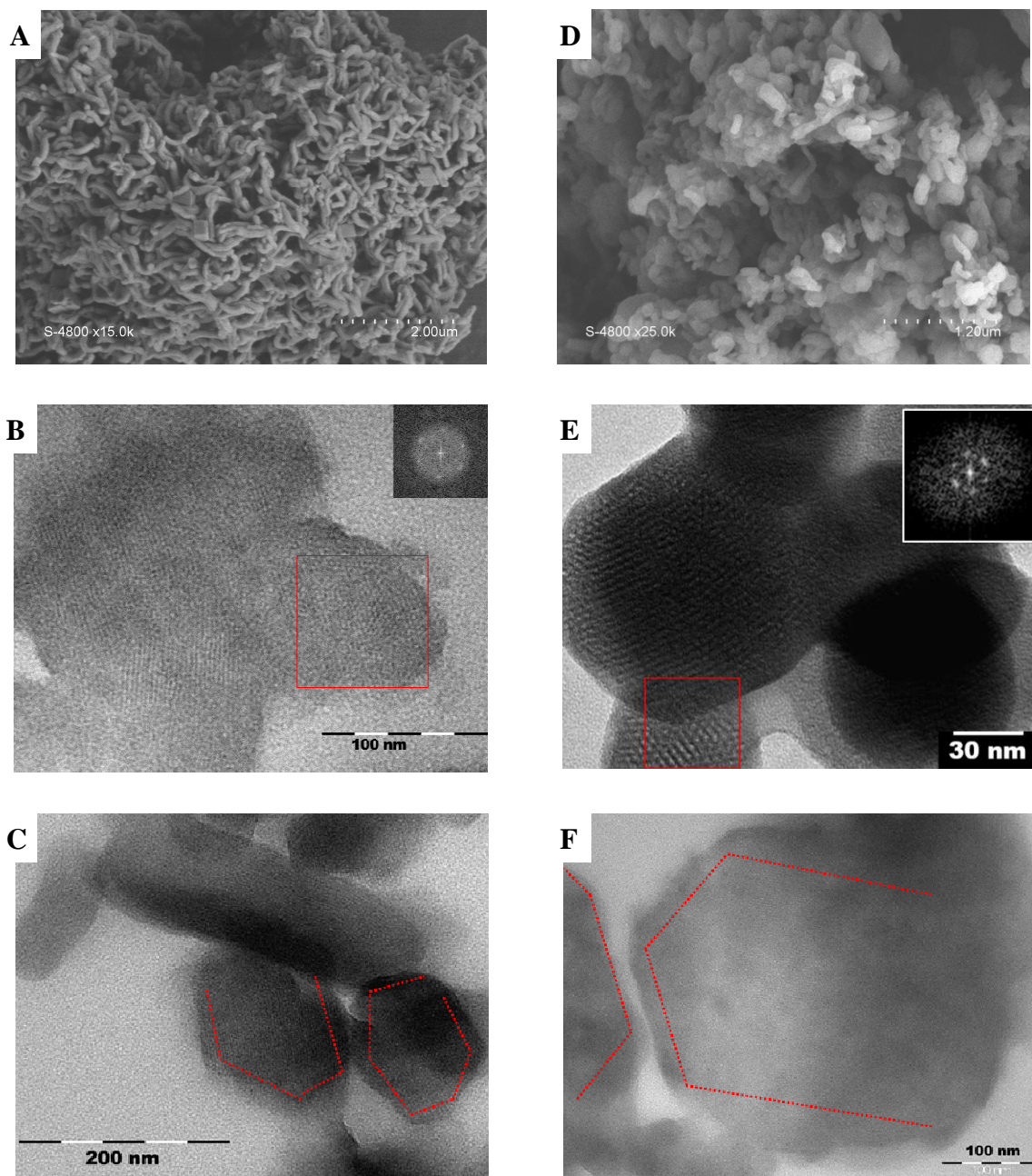


Figure 3: SEM and TEM micrographs of **M1** (A, B, C) and **M2** (D, E, F). The insets represent the FFT of the zones delimited by the red square

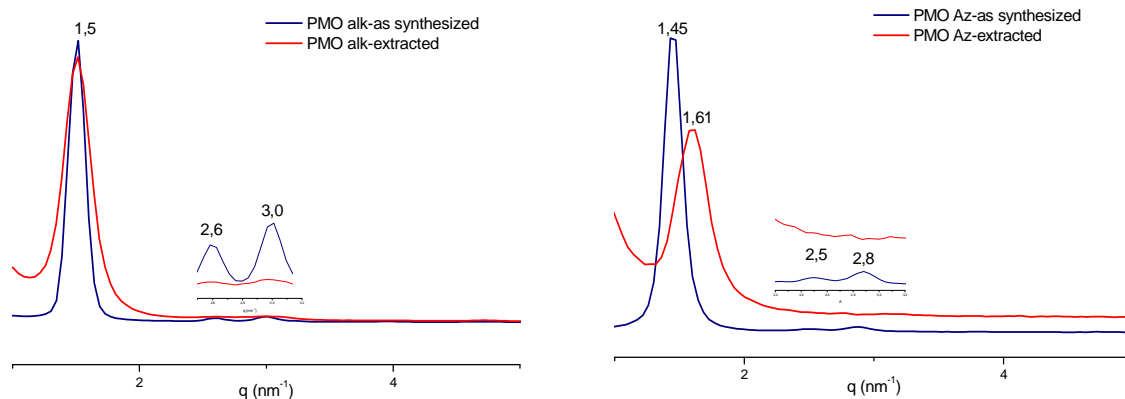


Figure 4: SAXS analyses of **M1** and **M2** before and after template removal

Thermal analysis:

Thermal stability of the PMOs is investigated by thermogravimetric analysis (TGA). The TGA curve of **M1** presents (Figure 5) a weight loss between 200 and 300 °C of 14%, most presumably arising from the decomposition of the propargyl pending groups. Indeed, the decomposition into acetylene would yield to a weight loss of 11% according to the formula $C_9H_{15}NO_3Si_2$. However, the thermal stability of **M2** is slightly lower than for **M1**, with a weight loss of 15% starting at 180 °C. According to the ideal formula $C_8H_{16}N_4O_3Si_2$, the loss of a nitrogen molecule would result in a weight loss of 10%. This difference could be due either to the desorption of a confined solvent or to the overlap with the other decomposition fringe seen at about 260°C.

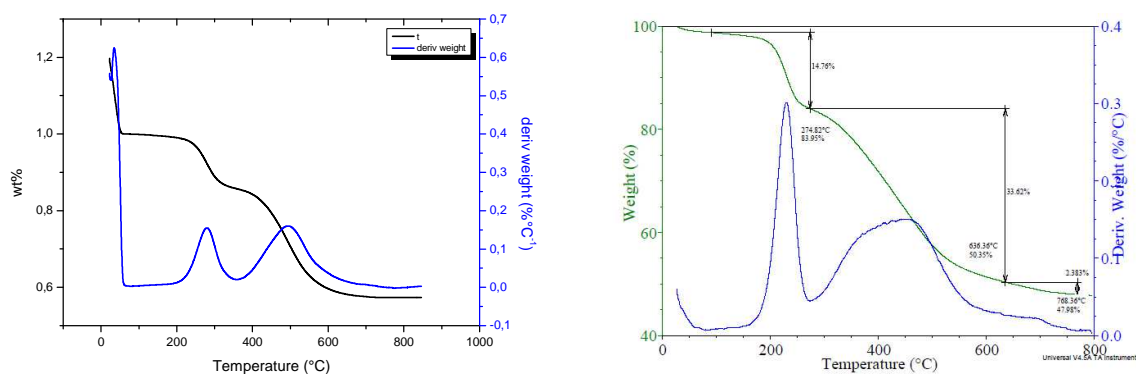


Figure 5: Thermogravimetric analyses ($10\text{ }^{\circ}\text{C min}^{-1}$, under air) of materials **M1** (left) and **M2** (right).

N₂ sorption analyses: To evaluate the porosity of the material, N₂-sorption experiments were run after outgassing the samples at low temperature (40°C) under a pressure of 10 μmHg. Under these standard conditions for O/I hybrid samples, we were surprised that PMOs **M1** and **M2** did not show any adsorption of nitrogen. Indeed, the recorded adsorbed amounts lie under the analytical limit of our equipment, with even negative values of adsorbed amounts being displayed. Recent studies¹²⁸ have also mentioned that the use of bisilylated silica precursor (instead of trisilylated precursor) have led to compact material without surface nor ordered mesoporosity. After several unsuccessful attempts, we decided to investigate if any structural change would have occurred during outgassing. In order to probe the possible structural changes, complementary SAXS studies (Figure 6) were done on the same batch (**M2**) before and after template extraction and especially after degassing overnight at 40°C under strong vacuum. Although the thermal stability of PMO materials is close to 200°C at atmospheric pressure (TGA, figure 5), SAXS studies showed a sharp decrease in the intensity upon outgassing, which suggests either a partial pore collapse or a partial pore obstruction phenomena resulting from a contrast in lower electronic density. It is noteworthy that the FTIR spectra of the materials before and after outgassing remained mostly unchanged, which proves that the fragile clickable functions were not altered.

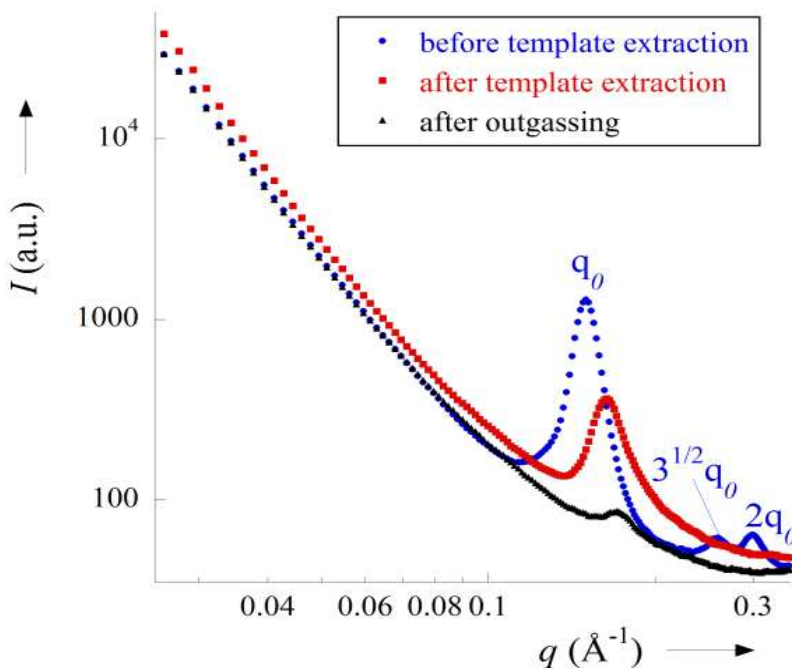


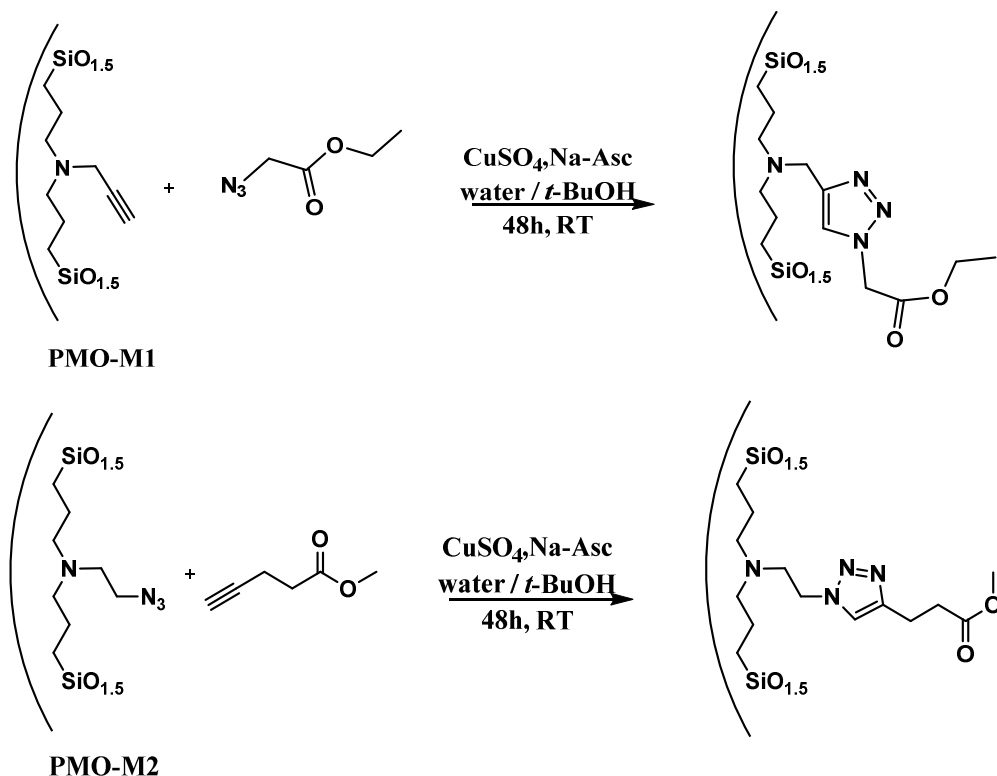
Figure 6: SAXS study of **M2** before and after template removal and after degassing 40°C/ overnight

Despite the undetectable surface area, we decided to perform CuAAC click reaction on both PMOs, resulting in high conversions as shown in the following results.

2.2. CuAAC Click Reactions on PMOs

In order to check the reactivity of prepared clickable PMOs, they were reacted under the CuAAC conditions with molecules possessing a footprint in an easily accessible analytical method, as it is the case for the ester function in FTIR.

Therefore, clickable esters (ethyl 2-azidoacetate and methylpent-4-ynoate) were reacted with the corresponding PMO using the classical copper sulphate-sodium ascorbate catalytic system in a mixture of water and *tert*-butanol over 48 h at room temperature (Scheme 3).



Scheme 3: CuAAC reactions between model molecules and PMOs **M1** and **M2**

This reaction was first monitored by FTIR (Figure 7), while no major change have occurred in the siloxane bands ($1000\text{--}1100\text{ cm}^{-1}$) the spectra reveal interesting results:

-For the reaction between ethyl 2-azidoacetate and **M1**, the H-C_{sp} band at 3294 cm^{-1} fade out and a weak band at 3144 cm^{-1} , attributable to H-C_{sp^2} stretching vibrations in the triazole fragment appears along with a prominent band at 1745 cm^{-1} corresponding to the ester group.

-In the case of **M2** reacting with methyl pent-4-ynoate, a conversion of *ca* 60 % was attained (calculated as the surface ratio between the azide peak at 2097 cm^{-1} and the siloxane broad band before and after click reaction). The presence of the ester group is confirmed by a clear C=O band 1735 cm^{-1} .

In both cases, a high conversion is deduced from the spectra. Solid-state NMR analyses were then performed to clearly confirm the formation of the triazole linker and thus the success of the CuAAC reaction.

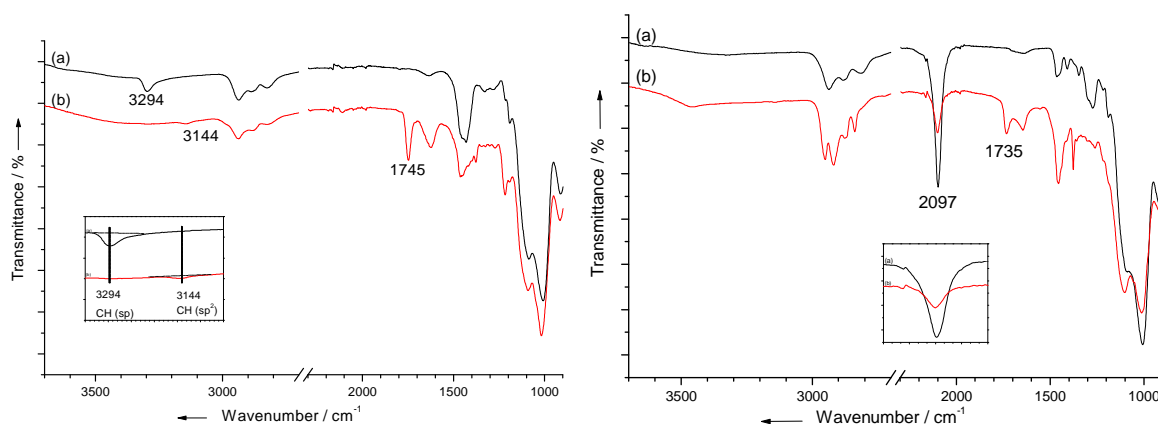


Figure 7: FTIR spectra of PMO materials before (a, black) and after (b, red) CuAAC functionalization: (left) alkyne-containing PMO reacting with ethyl 2-azidoacetate. Inset: zoom on the $\nu(\text{CH})$ bands; (right) azide-containing PMO reacting with methyl pent-4-ynoate. Inset: zoom on the azide band.

^{13}C CP-MAS NMR analyses (Figure 8) clearly evidence the formation of the triazole fragment, with prominent signals at δ 125 (CH) and δ 146 ppm (Cq), and the presence of the ester functions (δ 168 ppm). Furthermore, the total vanishing of the $\text{C}\equiv\text{C}$ carbon signals for **M1** confirms the high conversion of the terminal alkyne suggested by the FTIR analysis. It is noteworthy that these positions of the different signal match those of the molecular analogues **Prec A** and **Prec B** synthesized for comparison. (**Prec A** and **Prec B**: made by CuAAC between **Prec-Alk** or **Prec-Az** and the functional clickable molecule ester 1 and ester 2 respectively, under anhydrous conditions without being involved in any hydrolysis-condensation reaction).

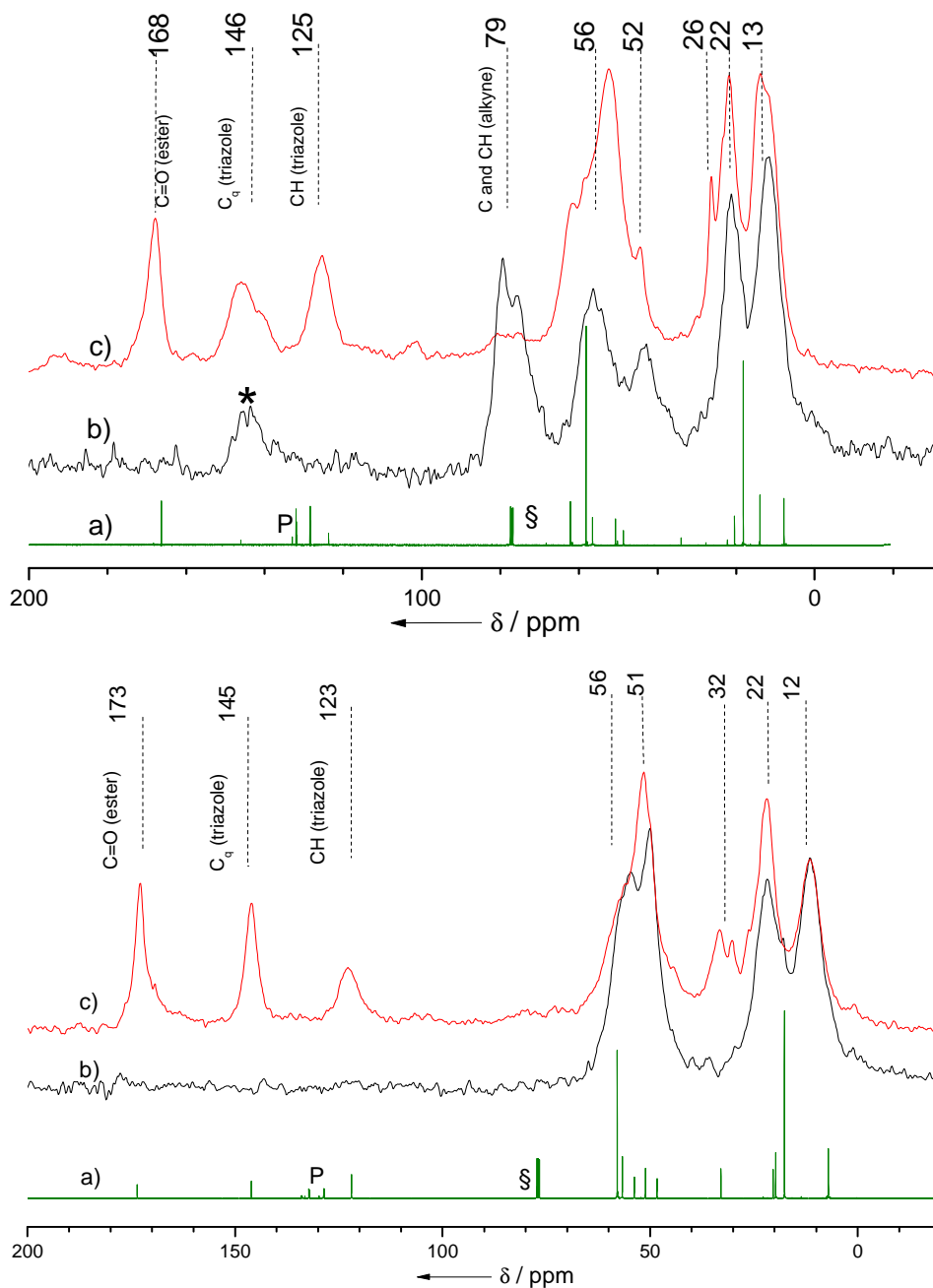


Figure 8: ^{13}C NMR spectra of precursors and PMO materials (up): solution NMR of **A** (a, green) CP-MAS NMR of **M1** before (b, black) and after (c, red) CuAAC functionalization with ethyl 2-azidoacetate; (down) solution NMR of **B** (a, green) CP-MAS NMR of **M2** before (b, black) and after (c, red) CuAAC functionalization with methyl pent-4-ynoate. The *, P and § symbols denote spinning side bands, triphenylphosphine oxide (130-140 ppm) and CDCl_3 signals (77 ppm) respectively.

2.2.1. Click reaction influence on textural properties of PMOs

After click reaction, the external texture of clicked **M1** and **M2** shows no major modification in SEM micrographs (Figure 9) with the preservation of the microrod structure. In addition,

^{29}Si CP-MAS NMR (Figure 10) shows a slight decrease in the T2 signal after CuAAC reaction. For **M1** and **M2** it is presumably that the condensation of the silica network pursued during the click reaction and some of the silanols have cocondensed together resulting in decrease of the signal $[\text{Si}(\text{OH})(\text{OSi})_2(\text{OR})]$ for $[\text{Si}(\text{OSi})_3(\text{OR})]$. SAXS study (Figure 11) was performed for one batch (**M1** reacted with ethyl 2-azidoacetate) before and after template removal, and after CuAAC reaction to probe the evolution of the mesoporous structure. It shows a decrease of the first peak (Bragg peak) and a vanishing of the harmonics when the material **M1** is reacted in solution. This behaviour is most likely due to the relatively thin walls of the material which lead to a fragile structure whose consequence is the partial loss of the ordered structure with time when it is kept in solution.

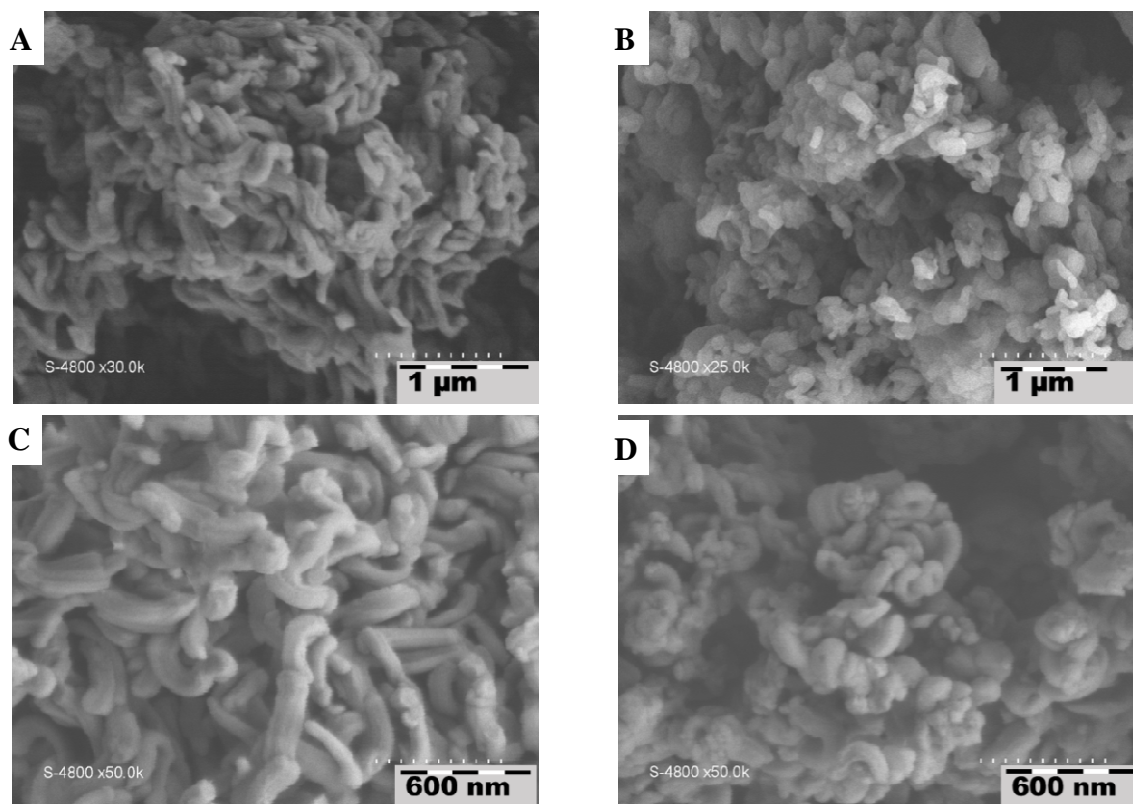


Figure 9: SEM micrographs of **M1** before (A) and after (B) CuAAC reaction with ethyl azidoacetate and of **M2** before (C) and after (D) CuAAC with methyl pent-4-ynoate.

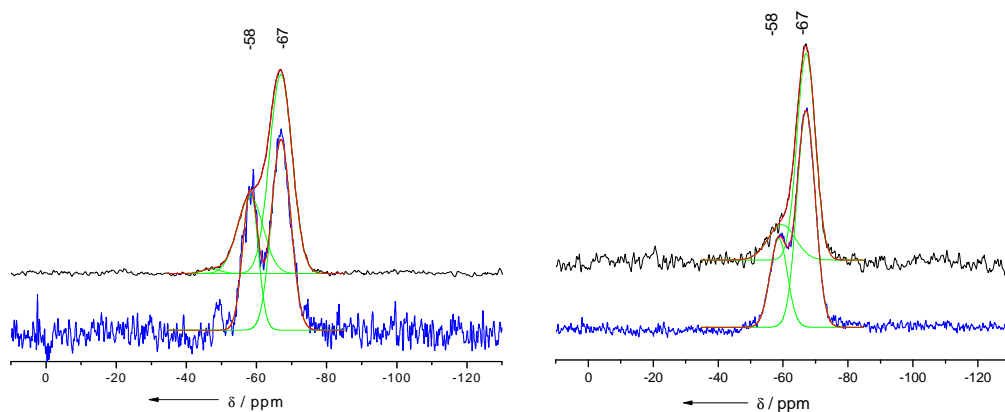


Figure 10: ^{29}Si CP-MAS NMR spectra of PMO materials before (blue) and after (black) CuAAC reaction: (left) **M1**; (right) **M2**.

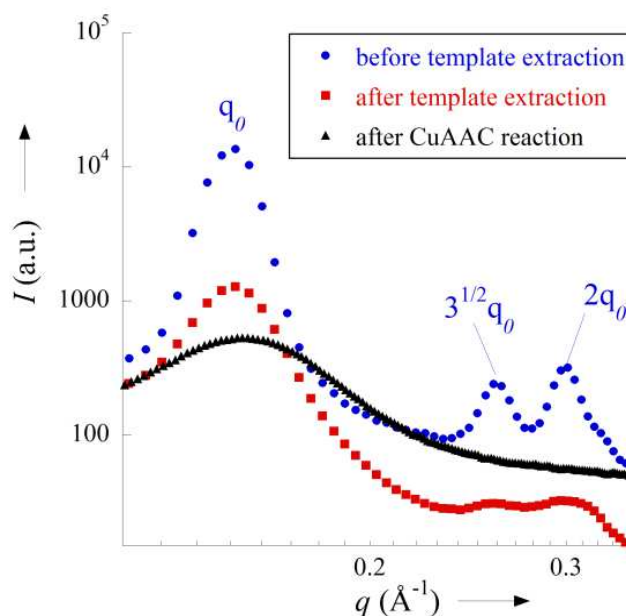
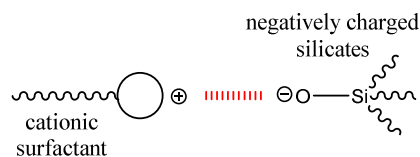


Figure 11: SAXS profile of **M1** before and after template removal and after CuAAC reaction

2.3. Interaction Silicates-Surfactant

The first type of interaction (organic fragment-surfactant) has afforded **M1** and **M2** PMO materials with accessible functionalities but it was unfortunately too fragile under degassing conditions (ultravacuum). In this part, we will check to feasibility of PMO materials using silicates-surfactant interaction in order to have structurally more stable materials, with both high reactivity and easily-probed surfaces.

The new materials made with this type of interaction are denoted **M3** and **M4** respectively for alkyne and azide-bearing materials (Scheme 1 bis).



2.3.1. Synthesis of materials **M3** and **M4**

Materials **M3** and **M4** were synthesized from their respective precursors (**Prec-Alk** and **Prec-Az**) using CTAB as surfactant and PFOA as co-surfactant in basic conditions. The use of PFOA has led to a more reproducible material and a higher specific surface area (especially for **M4**) while making the synthesis at higher scale than our first works¹²⁹. After surfactant removal, the chemical and textural compositions were characterized.

2.3.2. Characterization of **M3** and **M4**

The chemical composition of the materials was characterized by vibrational spectroscopy. The FTIR spectra of **M3** and **M4** (Figure 12) are essentially similar to those of **M1** and **M2**, and show the existing typical bands of the clickable functions: terminal alkyne's H-C_{sp} stretching at 3302 cm⁻¹ for **M3** and azide group which peak appears at 2107 cm⁻¹ for **M4**.

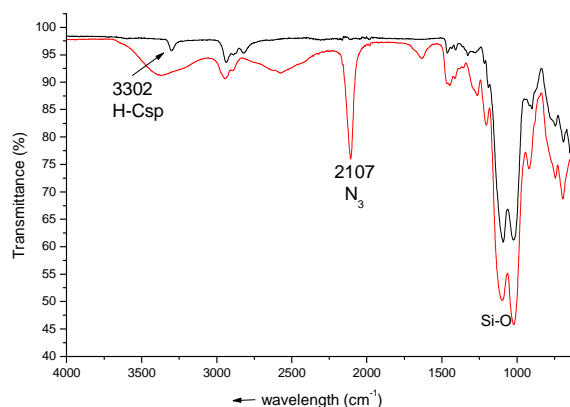


Figure 12: FTIR spectra of **M3** and **M4** materials after template removal

¹³C CPMAS NMR (Figure 17) confirms the expected chemical structure of synthesized materials where the signals correspond to those of the molecular precursor except the signals at 18 and 58 ppm, which correspond to the ethoxy groups in the precursors which are involved in the sol-gel process. The carbons in positions 1 and 2 (in alpha and beta to silicon, respectively C1 and C2) appear at low chemical shift (δ 10-25 ppm), they are slightly shifted

(from 7 to 11 ppm for C1 and 18 to 22 ppm for C2 for **M3** and **M4**) because of the modification of their chemical environment. Carbons (3, 4) in proximity to the central nitrogen atom are in the 40-55 ppm region where carbon 5 (alpha of azide) in **M4** is also seen. Typical signals of alkyne's carbons in **M3** are shown at about 70-80 ppm.

^{29}Si CP-MAS NMR (Figure 21) shows only T² and T³ signals, with even higher condensation degrees than for **M1** and **M2** (*ca* 95%).

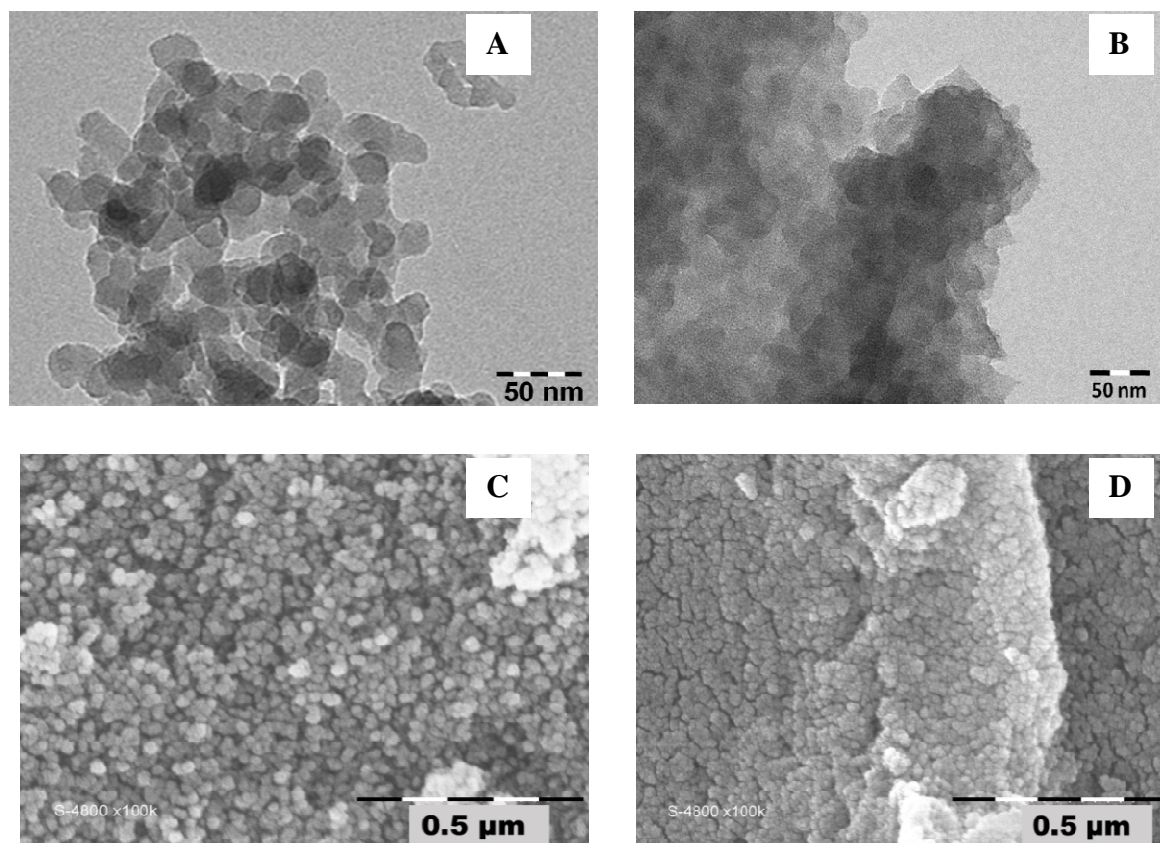


Figure 13: TEM and SEM micrographs of raw mesoporous materials **M3** (A,C) and **M4** (B,D)

TEM and SEM micrographs (Figure 13) show that **M3** and **M4** consist of aggregated nanoparticles of 20-30 nm in diameter. Clearly, **M4** is more compact than **M3**. In addition, SAXS (Figure 14) of mesoporous materials **M3** and **M4** after template extraction exhibit similar behaviours. At intermediate q values ($0.2\text{-}0.3\text{ \AA}^{-1}$), a non-Porod regime ($I(q) \propto q^{-3}$) is shown, suggesting that the nanospheres have rough surfaces. The broad peak around 0.5 \AA^{-1} might correspond to the approximate distance between holes-like of 1.3 nm. N₂-sorption experiments (Figure 14) display an overall close behavior for **M3** and **M4**. Looking at the adsorption branch, at very low relative pressure ($p/p^\circ < 0.1$) **M3** exhibits more affinity towards adsorbent and hosts more nitrogen than **M4**. In addition, a high

increase of the adsorbed amount in function of pressure is observed for **M3**, to reach a plateau at $p/p^\circ = 0.85$, while the increase in the case of **M4** is slower and a quasi-plateau is seen at lower pressure ($p/p^\circ = 0.75$) followed by a slight increase that may corresponds to non-porous punctual zones.

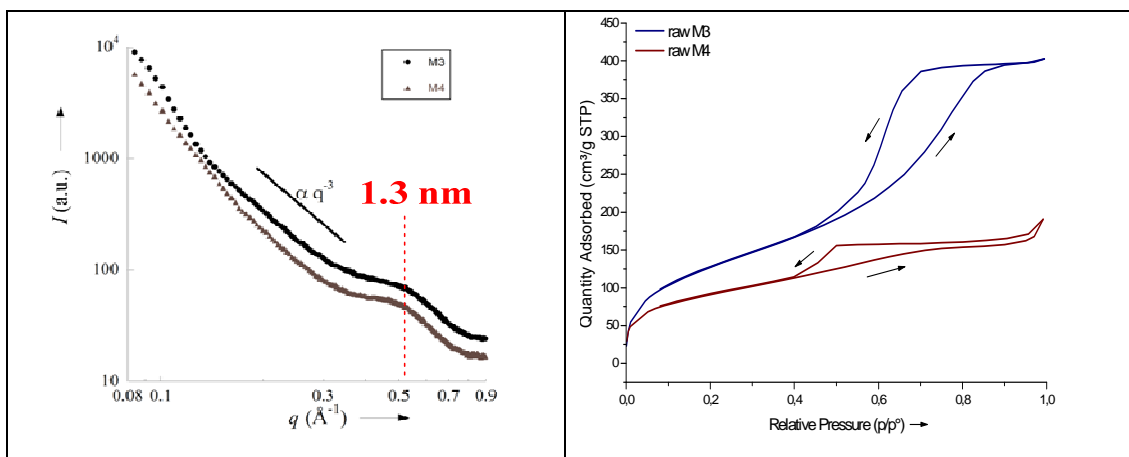


Figure 14: SAXS of raw mesoporous materials **M3** and **M4** after template extraction. N_2 sorption isotherms for **M3** (blue) and **M4** (brown)

Those plateaus correspond to a saturation of the mesoporosity. Both materials present a type II hysteresis loop with a brutal desorption starting at ($p/p^\circ = 0.7$) for **M3** but lower ($p/p^\circ = 0.5$) for **M4** (this lowering is presumably coming from the difference of structure compaction) and typical for inter-particle voids constituting the mesopores. The less compact structure of **M3** is outlined by the higher BET specific area ($471 \text{ m}^2 \text{ g}^{-1}$) and uptake at saturation ($395 \text{ cm}^3 \text{ g}^{-1}$) than in the case of **M4** ($321 \text{ m}^2 \text{ g}^{-1}$ and $162 \text{ cm}^3 \text{ g}^{-1}$). The t-plots of **M3** and **M4** shown in figure 15 demonstrate that no microporosity is detectable by nitrogen sorption (Y-intercept < 0 giving a negative pore volume which physically means that microporosity does not exist).

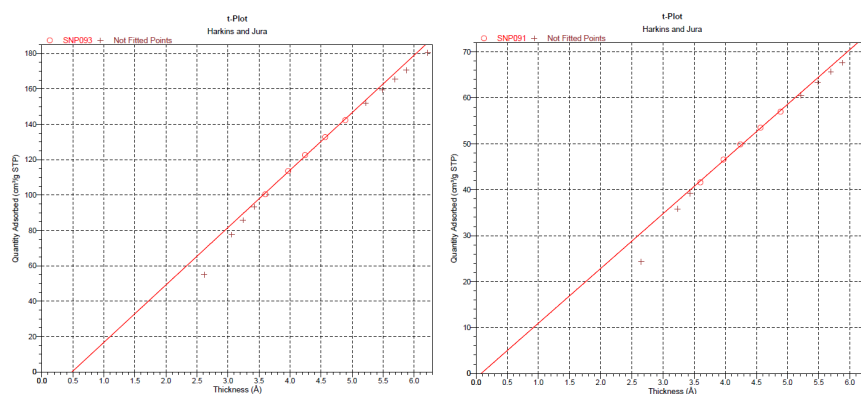
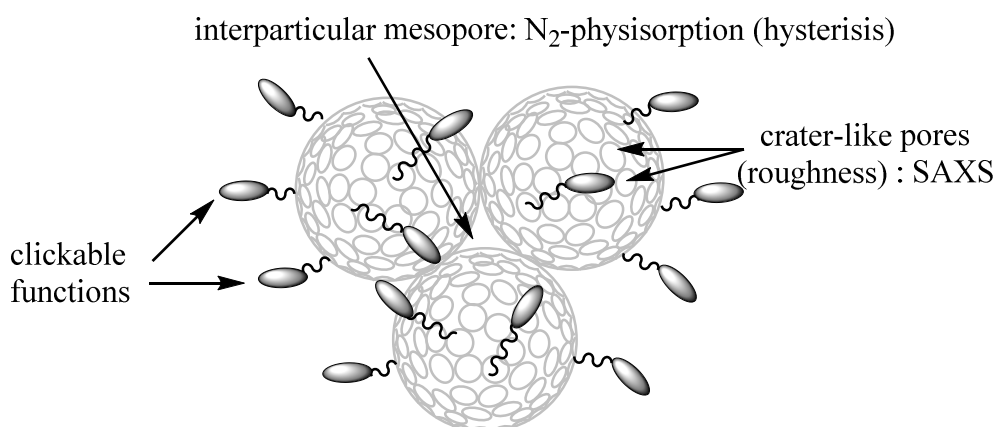


Figure 15 : Harkins and Jura's t-plot for (left) **M3** and (right) **M4**

Consequently, by combining the following results of the textural analyses:

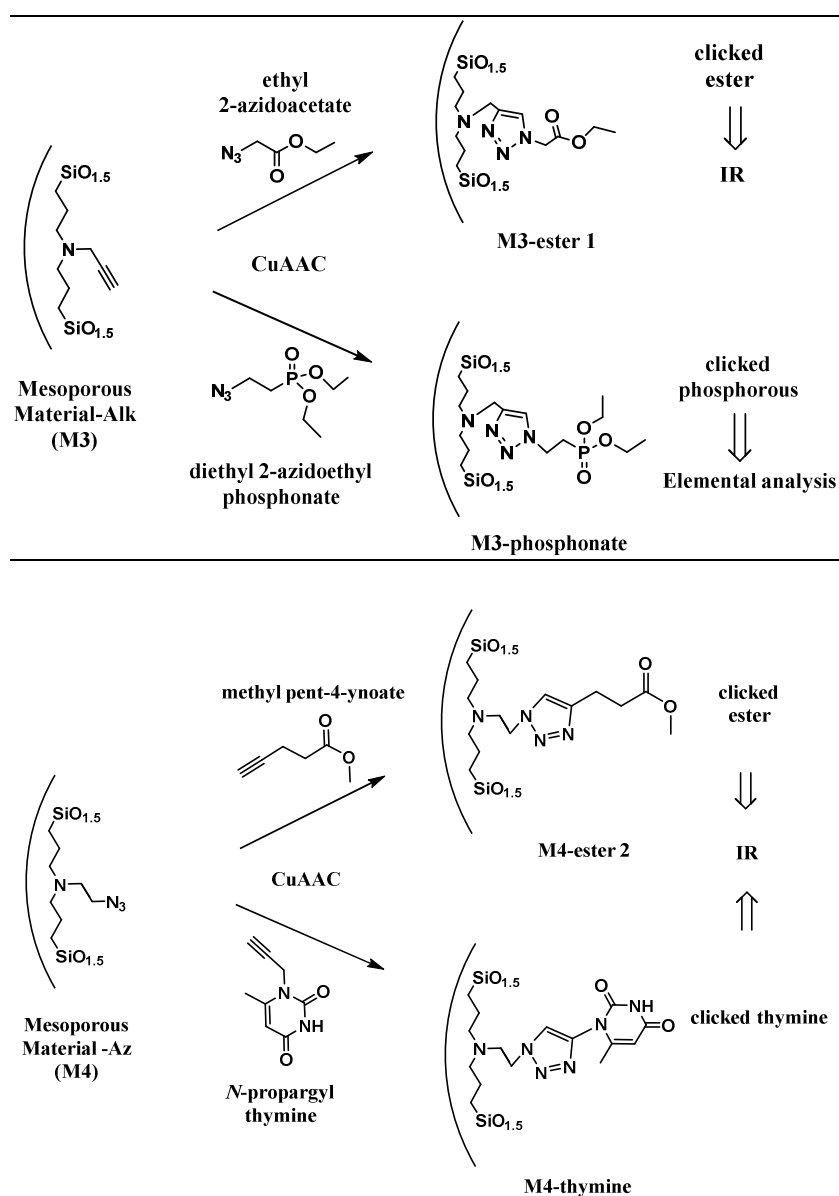
- Assemblies of nanospheres of 20-30 nm diameter (Electron microscopy)
- No structured porosity and surface roughness does exist (SAXS). This roughness is repetiting at 1.3 nm suggesting crater-like pores on the surface of the nanospheres.
- Nitrogen sorption indicated that the material is only mesoporous. However this mesoporosity is constituted by the void between the aggregated nanoparticles.

We can conclude that the obtained material can not be considered as a PMO but a mesoporous assembly of golf-ball like nanoparticles with the following suggested morphology for **M3** and **M4**:



2.4. CuAAC reaction on Mesoporous Materials M3 and M4

The reactivity of these mesoporous organosilicas was checked using model alkynes and azides bearing functions that can be easily probed by FTIR (C=O) or quantified by elemental analysis such as phosphorous (Scheme 4). Thus, ethyl 2-azidoacetate and diethyl 2-azidoethylphosphonate were clicked on **M3** (afforded materials were denoted **M3-ester 1** and **M3-phosphonate**, respectively) and methyl pent-4-ynoate and *N*-propargylthymine were clicked on **M4** (afforded materials were denoted **M4-ester 2** and **M4-thymine**, respectively).



Scheme 4: Typical CuAAC click reaction on **M3** and **M4** using model molecules

The reactivity of the alkyne-material **M3** towards organic azides was probed by FTIR (Figure 16). In all cases, an important decrease of the FTIR $\text{C}_{(\text{sp})}\text{-H}$ peak at 3294 cm^{-1} and the concomitant formation of the triazole ring ($\text{C}_{(\text{sp}^2)}\text{-H}$ band at 3140 cm^{-1}) were observed, while no trace of remaining adsorbed organic azide (that would absorb at 2100 cm^{-1}) was detected.

Clicked azidoacetate's footprint is outlined by the ester $\text{C}=\text{O}$ band at 1749 cm^{-1} . In addition, by using organic fragments containing phosphorus, it was possible to determine the extent of click-grafting. Indeed, the P content after grafting diethyl 2-azidoethyl

phosphonate on **M3** was 4.7%, with N/P and P/Si molar ratios of 4.5 and 0.17. From the latter value, a conversion of *ca*35% can be calculated for this reaction. Furthermore, the presence of the phosphonated fragment was evidenced in the FTIR spectrum by strong peaks in the 950-1050 cm⁻¹ region (corresponding to P=O and P-O-C₂H₅ vibrations).

On the other side, the azide-functionalized material **M4** was almost quantitatively converted ($89 \pm 10\%$) when reacted with methyl pent-4-ynoate using the CuAAC-sodium ascorbate catalytic system, with a nearly complete disappearance of the N₃-absorption band at 2100 cm⁻¹ (Figure 16) and a sharp and intense peak appearing at 1731 cm⁻¹ corresponding to the clicked ester functionality. A weak band (C_(sp2)-H stretching) can also be distinguished at 3140 cm⁻¹, which highlights the formation of the triazole ring. In addition, clickable material **M4** was functionalized using propargylthymine. As observed by FTIR, a high conversion of *ca* 78% was achieved, as deduced from the ratio of the peak areas between the azide and siloxane absorptions, while the band at 1680 cm⁻¹ corresponds the amide functions of the thymine.

Furthermore, a control experiment was performed by stirring separately **M3** and **M4** in a solution of copper (II) sulphate and sodium ascorbate in a water/*t*-butanol mixture in the absence of any clickable partner. After a prolonged stirring (65 h instead of 48 h for the CuAAC reactions), the band at 3140 cm⁻¹ shows no detectable decrease while a 32% decrease of the azide IR band at 2100 cm⁻¹ was observed (Figure 16). This is much less than for the corresponding CuAAC experiments in the presence of methylpent-4-ynoate (89%) and propargylthymine (78%), for a significantly longer reaction time, indicating that CuAAC occurs successfully and with high conversion on the prepared clickable mesoporous material.

At first sight, this very high yield of functionalization for **M4** seems counterintuitive as the materials are composed of dense nanospheres. However, the flexible nature of the organic fragments should favour the diffusion of small reactants within the structure, which is supported by SAXS analysis.

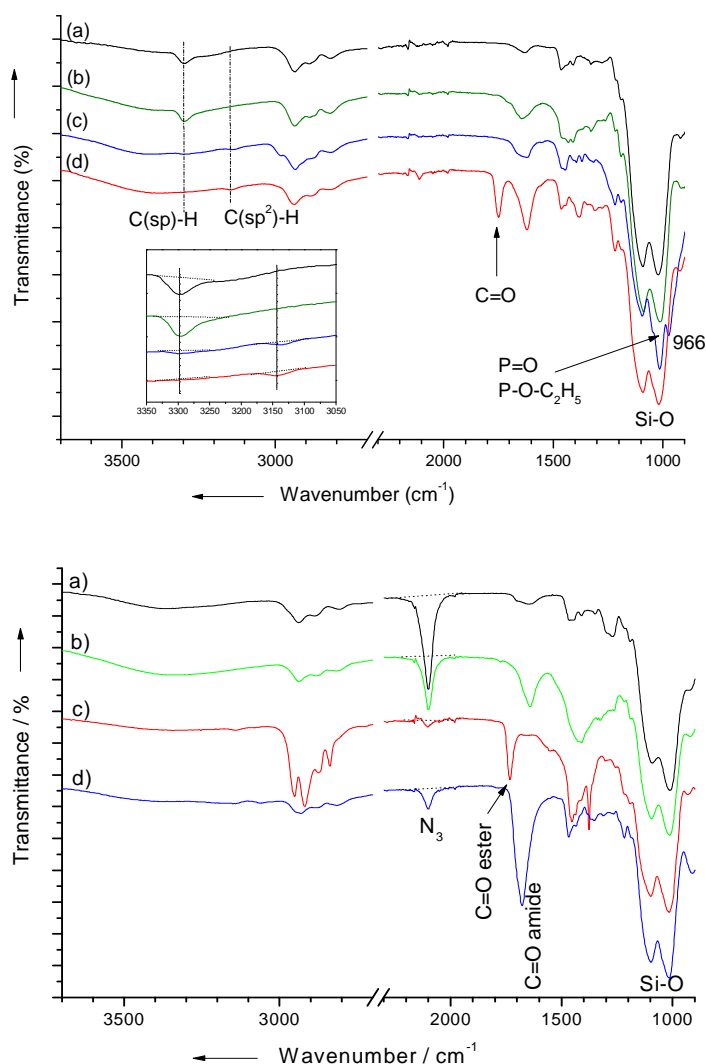


Figure 16: FT-IR spectra of (up) mesoporous material **M3** (a, black), **M3** after exposure to click conditions (b, green) and after CuAAC-functionalization with (c, blue) diethyl 2-azidoethylphosphonate (**M3-phosphonate**) and (d, red) ethyl 2-azidoacetate (**M3-ester 1**). Inset: zoom on the 3050-3350 cm⁻¹ region; (down) mesoporous material **M4** (a, black) **M4** after exposure to CuAAC conditions (b, green), and after CuAAC-functionalization with (c, red) methyl pent-4-ynoate (**M4-ester 2**), (d, blue) propargylthymine (**M4-thymine**)

¹³C CP-MAS NMR spectra (Figure 17) were recorded for the click reaction of ethyl 2-azidoacetate on **M3** and methylpent-4-ynoate on **M4**. They highlight the covalent anchoring of the functional moieties *via* a triazole ring whose typical bands appear at 125 ppm and 145 ppm for both click reactions along with the 172 ppm signal corresponding to C=O ester carbons. In **M3-ester 1**, the quasi-complete vanishing of the alkyne's signals at 70-80 ppm also confirms the CuAAC reaction. As for **M4-ester 2**, the appearance of new bands (for instance, $\delta = 26, 33, 44$ ppm) corresponding to carbons of the anchored pentynoate is also a proof of the success of the incorporation of the organic molecule. For

comparison, the spectra are superimposed with the ^{13}C liquid NMR spectra of the molecular analogues (**Prec A** and **Prec B**: made by CuAAC between **Prec-Alk** or **Prec-Az** and the functional clickable molecule under anhydrous conditions without being involved in any hydrolysis-condensation reaction).

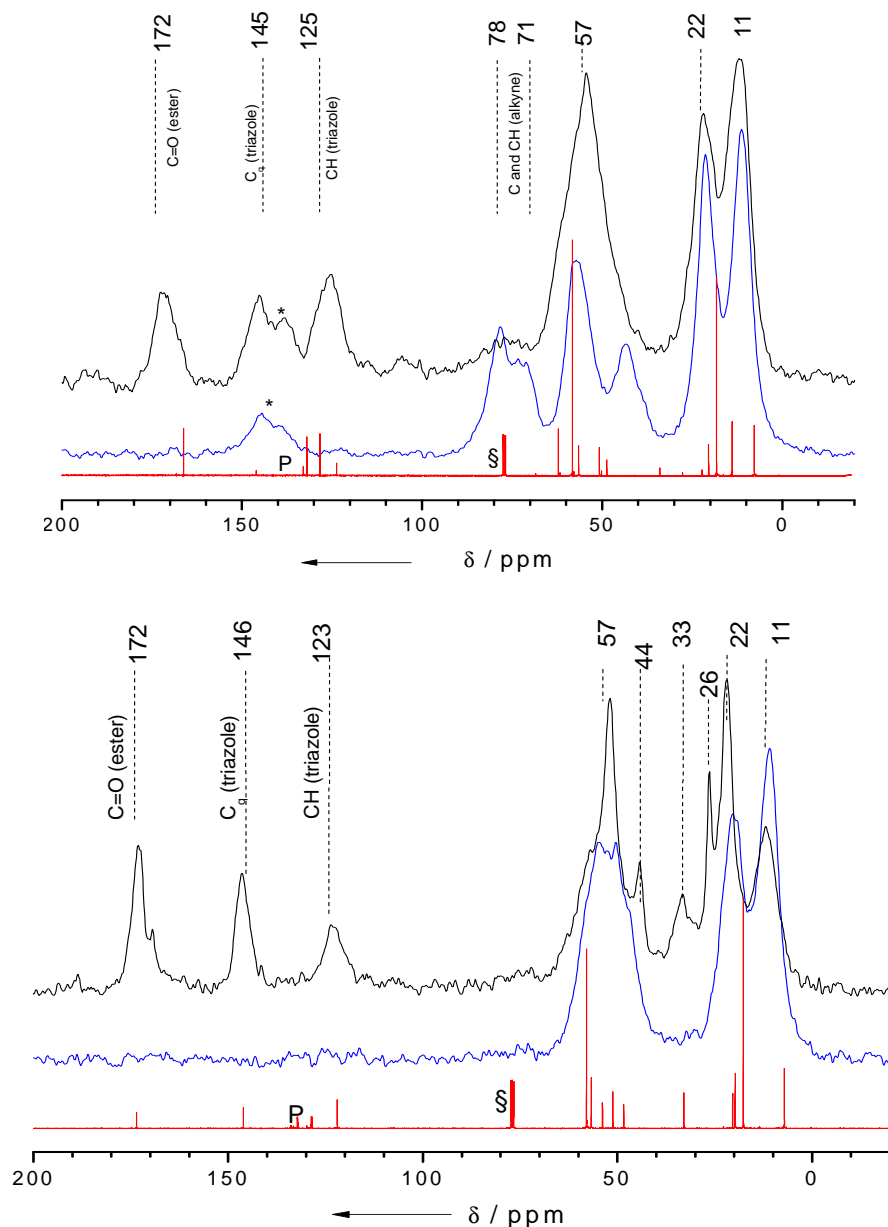


Figure 17: ^{13}C NMR spectra of mesoporous materials before (blue) and after (black) CuAAC reaction, together with the corresponding molecular analogues in solution (red): (up) **M3-ester 1**, precursor **A**; (down) **M4-ester 2**, precursor **B**. The *, P and § symbols denote spinning side bands, triphenylphosphine oxide (130-140 ppm) and CDCl_3 signals (77 ppm) respectively.

After CuAAC reaction, the N_2 -sorption isotherms of the materials derived from **M3** and **M4** (Figures 18, 19) show an evident decrease in specific surface area while keeping the

same sorption behaviour than the parent materials. BET surface area of the mesoporous materials are compiled in the following table:

Sample	BET Surface Area (m ² /g)
M3	475
M3-ester 1	187
M3-phosphonate	54
M4	320
M4-ester 2	12
M4-thymine	38

Table 2: BET specific surface areas of different raw and clicked mesoporous material.

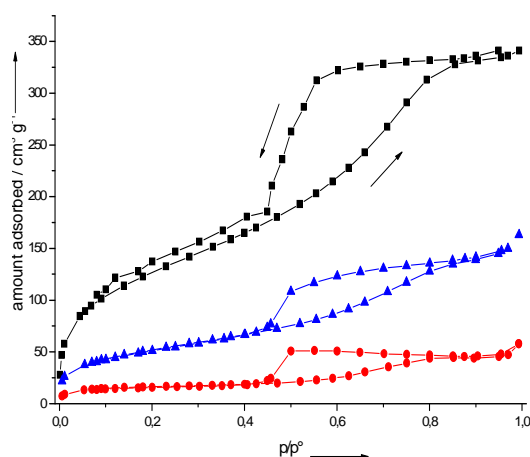


Figure 18: N₂-sorption isotherms of raw mesoporous material **M3** (black squares) and after CuAAC-functionalization: **M3-ester 1** (blue triangles) and (red spheres) **M3-phosphonate**.

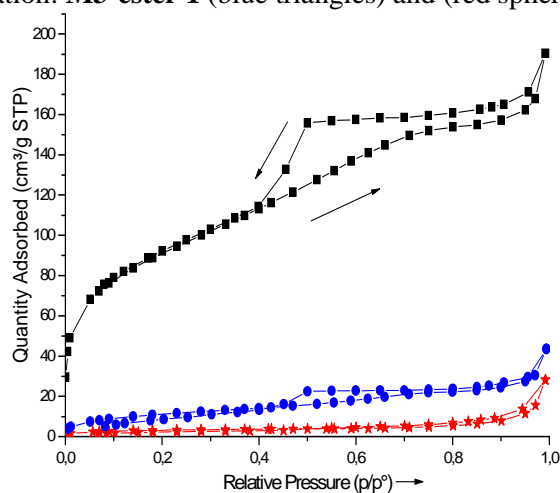


Figure 19: N₂-sorption isotherms of raw mesoporous material **M4** (black squares) and after CuAAC-functionalization: (blue spheres) **M4-thymine** and (red stars) **M4-ester 2**

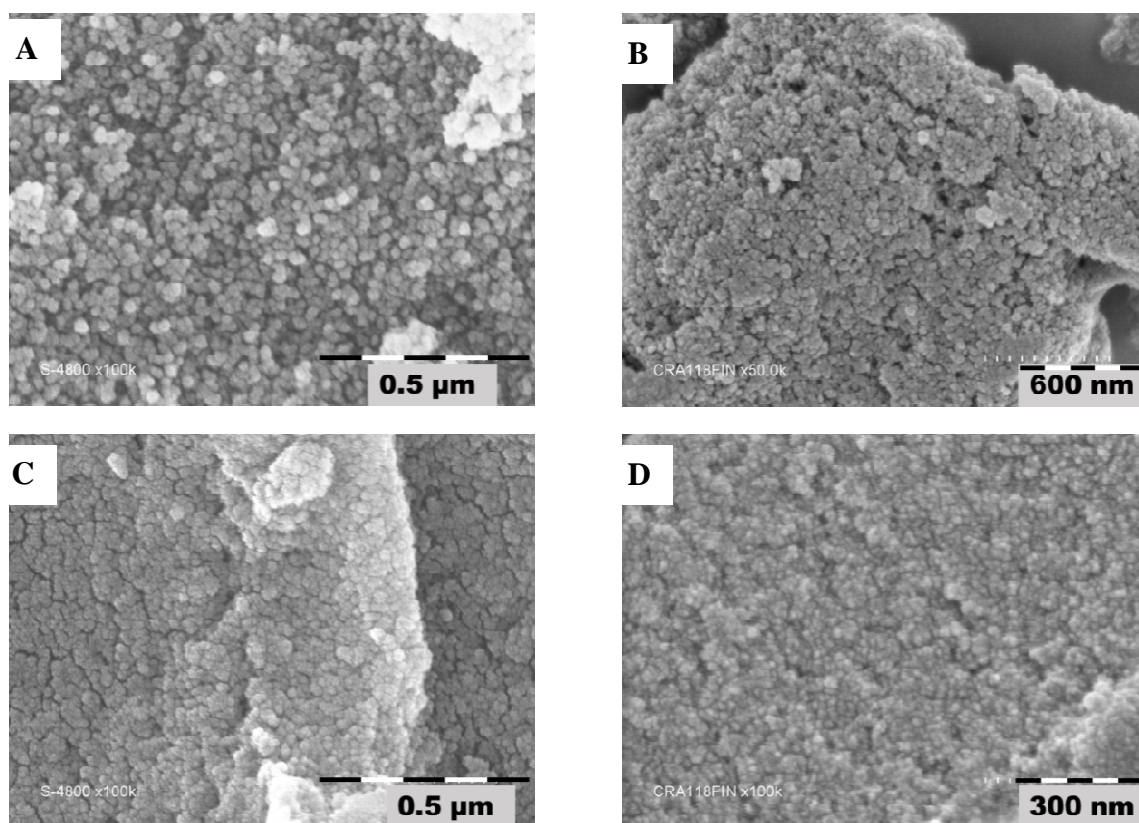
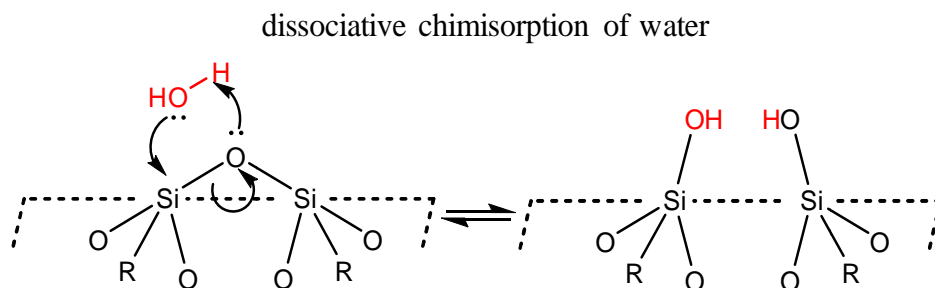


Figure 20: SEM micrographs of **M3** before (A) and after (B) CuAAC reaction for **M3-ester 1**, of **M4** before (C) and after (D) CuAAC reaction of **M4-ester 2**.

After click reaction, ^{29}Si CP-MAS NMR shows a slight decrease of the condensation degree. It is clearly seen that the T^2 (δ -58 ppm) signal increases in the case of clicked ethyl 2-azidoacetate on **M3** and methyl pent-4-ynoate on **M4**. In the first case, even some T^1 species $[\text{R-Si}-(\text{OSi})(\text{SiOH})_2]$ are detected at $\delta = -51$ ppm. Most presumably, a dissociative chemisorption of water occurs by cleaving some siloxanes bonds (Si-O-Si) and giving silanols groups (Si-OH). This phenomenon probably may be due to the CuAAC reaction conditions (Scheme 5).



Scheme 5: siloxane bond hydrolysis by dissociative chemisorption of water (adapted from ref ¹³⁰)

Interestingly, this phenomenon is in contrast with what happened to **M1** and **M2** (decrease of T^2). The origin of this, is presumably the difference in the structural properties between the two families (**M1**, **M2** and **M3**, **M4**)

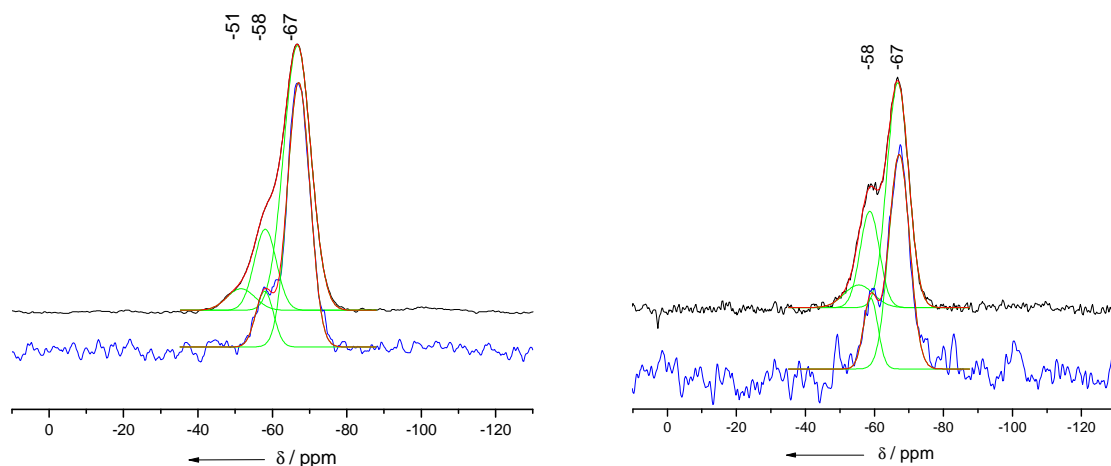


Figure 21. ^{29}Si CP-MAS NMR spectra of mesoporous materials before (blue) and after (black) CuAAC reaction with the corresponding ester: (left) **M3**; (right) **M4**.

SEM micrographs (Figure 20) show a preservation of the granular structure of the materials after click reaction with a narrow size of the particles. However, SAXS experiments show that in the zone ranging from $q = 0.2$ to 0.3 \AA^{-1} the slope of $I(q) \propto q^{-n}$ (with $n=3$ in the case of **M3** and **M4**) decreases slightly indicating that the roughness was reduced because $I(q) \propto q^{-n}$ (with $3 < n < 4$ in the case of **M3-ester 1** and **M4-ester 2**). A slight shift towards higher wavevectors after click reaction is also seen, hence reducing the pores size from 1.5 nm in raw material **M3** and **M4** to about 1.1 nm in both clicked materials **M3-ester 1** and **M4-ester 2**.

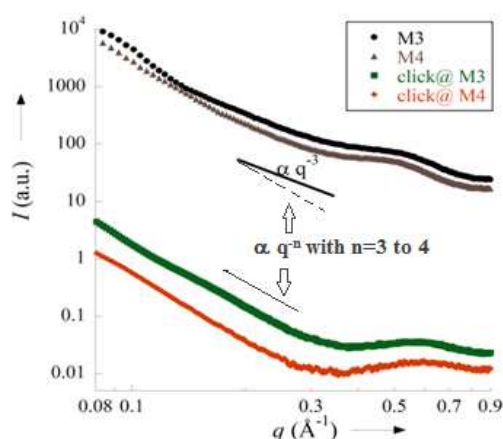


Figure 22: SAXS profiles of **M3-ester 1** and **M4-ester 2** (after click reaction, compared to those before CuAAC)

In conclusion, using solely clickable organosilane we were able to synthesize at first one PMO material (**M1** and **M2**) bearing either alkyne or azide groups, using an interaction between the organic fragment of the organosilane and the surfactant. The high reactivity towards CuAAC click reactions was probed with different techniques but this family of materials was dropped since it was too fragile to probe the evolution of its surface area. On the other hand, the interaction between the silicates part of the organosilane with the surfactant has led to a family of materials (**M3** and **M4**) which cannot be considered as PMO but as a mesoporous assembly of nanoparticles. This family was also highly reactive towards CuAAC clickable molecules and easily probed by gas-sorption experiments.

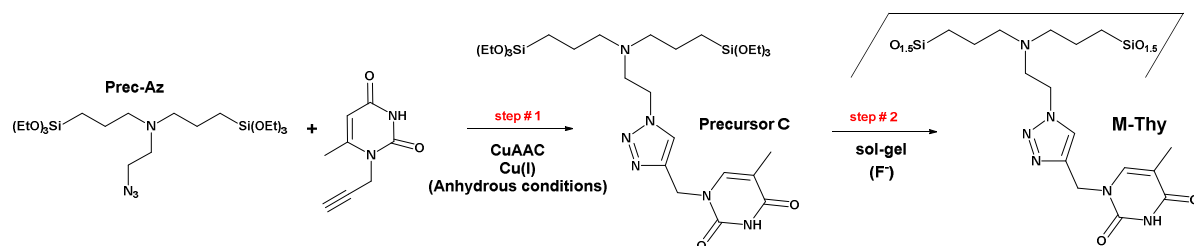
3. Functional Bridged Organosilane from functional organosilane block-built by CuAAC reaction

For this method, we have used the reverse order of CuAAC and sol-gel reactions compared to pathway 1 (Scheme 1). After forming a multifunctional organosilane by attaching a clickable organosilane to a complementary clickable functional unit (step 1), the sol gel process is led off (step 2). The final material contains a very high (close to 100%) concentration in desired functions if the condensation was complete. Nevertheless, a structured material is very difficult to make from this kind of precursors solely, since the organic fraction is highly present and may alter any recognition with structure-directing agents. Merely small polysilylated compounds are currently known to produce PMOs so far. Only the rigid aromatic systems rule out this observation and even in this case, a small amount of added TEOS may be required to stabilize the PMO framework after the removal of the surfactant⁵². The PMO based on voluminous groups could be made by introducing small organosilane in high concentration and with dominant fraction along with the desired function.

3.1. Synthesis of material M-Thy

Prec C was synthesized by CuAAC reaction between *N*-propargylthymine and the **Prec-Az** by microwave at 100°C for 5 min irradiation under inert atmosphere.

M-Thy is synthesized from the **Prec C** via a nucleophilic catalysis (NH₄F) in a mixture of water-ethanol and without the use of template.



Scheme 6: 2 steps synthesis of **M-Thy** from (**Prec-Az**) according to pathway 2

3.2. Characterization of **M-Thy**

Chemical composition and textural properties were probed by vibrational spectroscopy and electron microscopy in addition to nitrogen sorption experiments.

FTIR spectra (Figure 23) display very close profiles for the material **M-Thy** and its precursor **Prec-C**. The main difference lies in the 1000-1200 cm^{-1} region, where the Si-O-Et band of the precursor at 1070 cm^{-1} is transformed into a broad Si-O-Si siloxane band (1010-1100 cm^{-1}) for **M-Thy**, which shows the success of the sol-gel reaction. The important peaks at 1677 cm^{-1} (C=O amide) and 3145 cm^{-1} (triazole H-C_(sp) stretching) are still prominently displayed.

TGA analysis (Figure 23) shows a strong weight loss between 200 °C and 700 °C corresponding to the weight loss of organic fragments with respect to the formula $\text{C}_{15}\text{H}_{22}\text{N}_6\text{O}_5\text{Si}_2$.

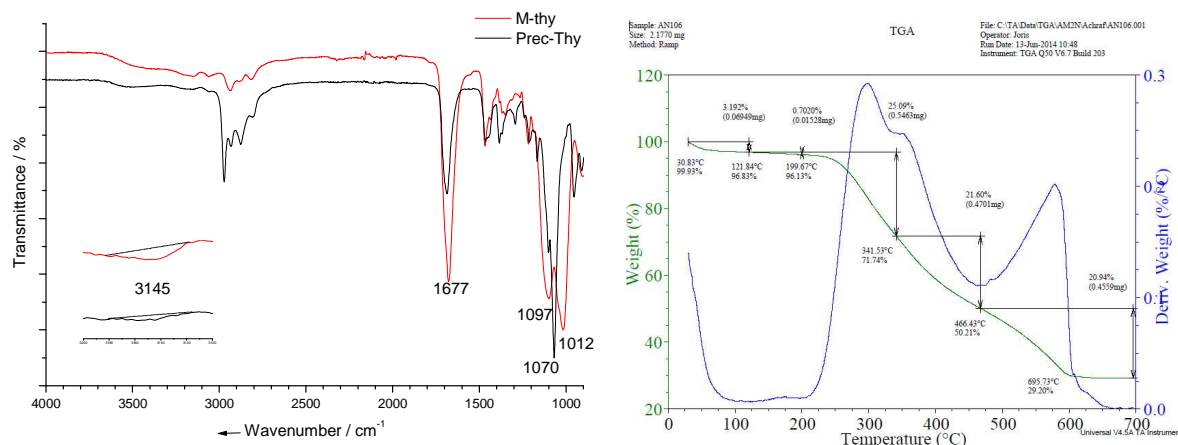


Figure 23: (Left) FTIR spectra of **M-Thy** and its precursor (**Precursor C**) and (right) thermogravimetric analysis of **M-Thy** (10 °C min⁻¹, under air)

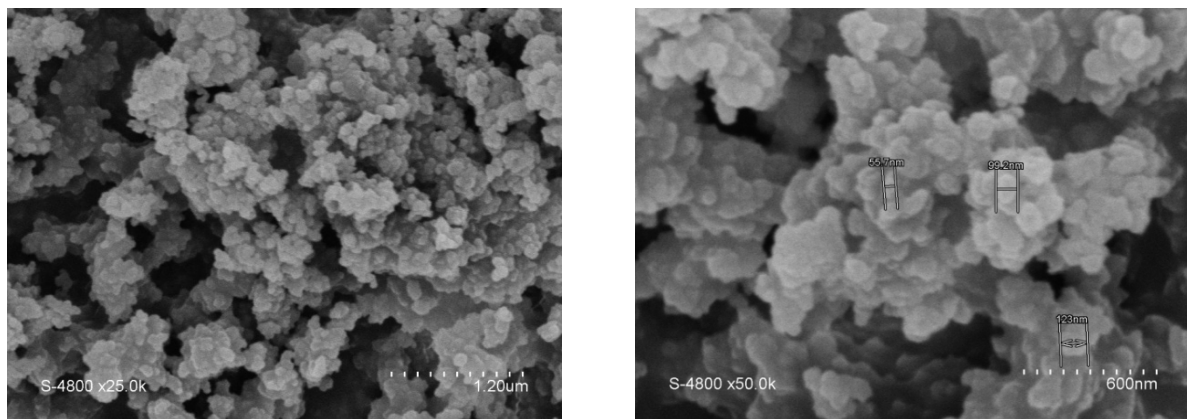


Figure 24: SEM micrographs of **M-Thy**

SEM micrographs show that **M-Thy** consists of agglomerated nanoparticles with diameters ranging from 30 to 90 nm. The interstitial space constitutes the main accessible area which is given by BET method as $33 \text{ m}^2 \text{ g}^{-1}$. The N_2 -sorption isotherm is typical of a lowly porous material (IUPAC type II). At the first edge, no microporosity is identified and the adsorbed quantity increases very slowly (multimolecular adsorption) until it reaches a high relative pressure ($p/p^\circ = 0.9$) and gets close to a maximum of $160 \text{ cm}^3 \text{ g}^{-1}$. The hysteresis that takes place from $p/p^\circ = 1$ to 0.7 is close to a type III and it is characteristic of aggregates having no definite porosity as it is seen in SEM images of this material.

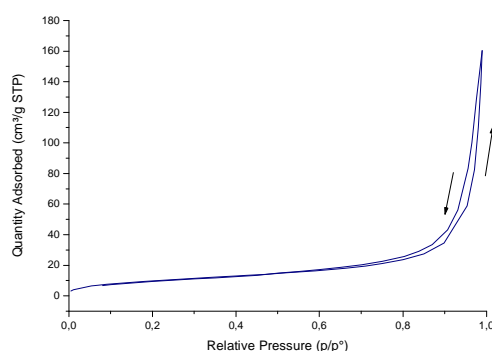


Figure 25: N_2 -sorption isotherm of **M-Thy**

3.3. Conclusion

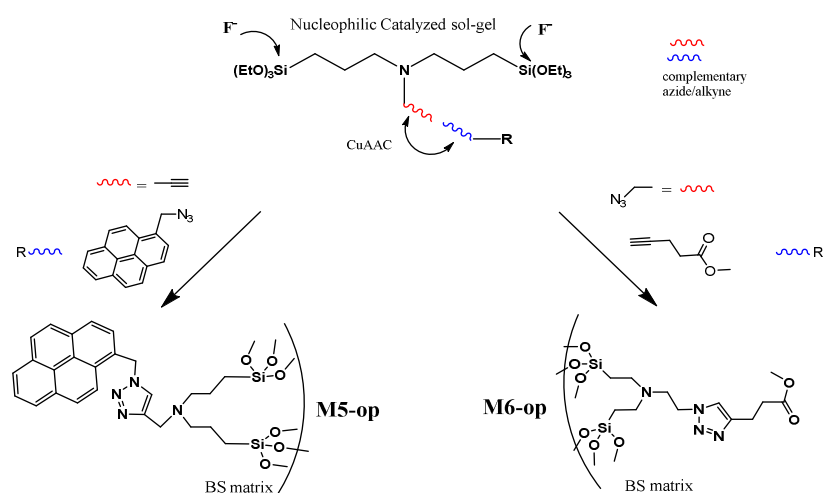
This work has showed that bissilylated organosilane with a voluminous pending fragment are very promising to prepare solid materials bearing high capacity of functional groups which is hardly conceivable with a monosilylated organosilane. The high organic fraction may alter the specific interaction with a surfactant and then, a structured material made purely by a voluminous group is not reachable yet.

4. Functional Bridged Silsesquioxane by one pot pathway from clickable organosilane

In this division, we will show that a click reaction can be performed simultaneously with the sol-gel process since both operations exhibit similar kinetics. While no material structuring is needed, the addition of components of the click reaction along with the sol-gel catalyst is convenient to one-step synthesis of functionalized material from an organosilane. In this prospect, we made use of clickable bissilylated precursors (bearing azide and alkyne functions) to prepare at first a clickable material as a “blank” and most importantly a functional material with an *in situ* click reaction (one pot material synthesis).

4.1. Synthesis of Clickable Materials and One-Pot Functional Materials

Clickable materials were made from the key-clickable precursors **Prec-Alk** and **Prec-Az** in a water-ethanol solvents mixture and *via* a nucleophilic catalysis (fluoride). These materials were made to serve as a blank for the one-pot functional materials and denoted (**M5** and **M6**, respectively). One-pot materials were synthesized by using the same abovementioned conditions for the precursor (**Prec-Alk** or **Prec-Az**) but with adding *in situ* the corresponding clickable partner (20% molar equivalent of Prec-Alk or Prec-Az) in an appropriate solvent (THF) and with the copper (I) catalyst. The clickable partner involved in the reaction was 1-azidomethylpyrene (for **Prec-Alk**) and methylpent-4-ynoate (for **prec-Az**). The *in situ* pyrene and pentynoate clicked materials are denoted **M5-op** and **M6-op** respectively (op: one pot).



Scheme 7: Schematic synthesis of **M5-op** and **M6-op** with a sol-gel process and an *in situ* CuAAC reaction.

4.2. Characterization of one-pot made materials

Solid-state ^{13}C CP-MAS NMR suggests the success of the CuAAC reaction by the signal at 145 ppm corresponding to triazole while the expected second signal at 125 ppm may be masked by the strong signal (δ 120-135 ppm) corresponding to pyrene aromatic carbons anchored after CuAAC reaction. In addition, the intensity of $\text{C}\equiv\text{C}$ signal decreases from **M5** to **M5-op** (relatively to the band on 11 ppm corresponding to C in alpha to Si nucleus, which has not to be affected by the click reaction) meaning that some of the alkynes were converted.

The click reaction was also revealed on **M6** by the triazole's inherent signature (δ 123 and 146 ppm) and the ester carbon of the clicked methyl pent-4-ynoate which appears at 172 ppm.

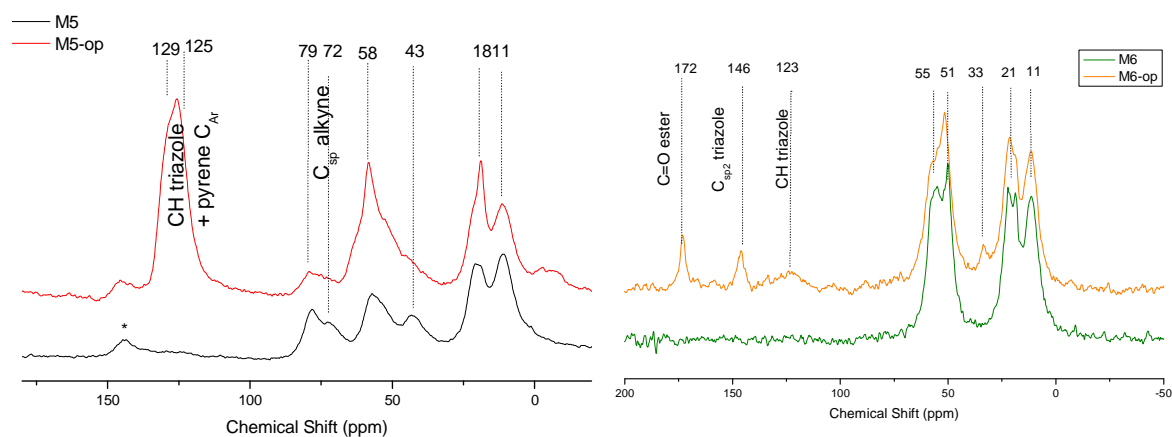


Figure 26: ^{13}C CP-MAS NMR spectra of (left) **M5** (black) and **M5-op** (red) and (right) **M6** (green) and **M6-op** (orange)

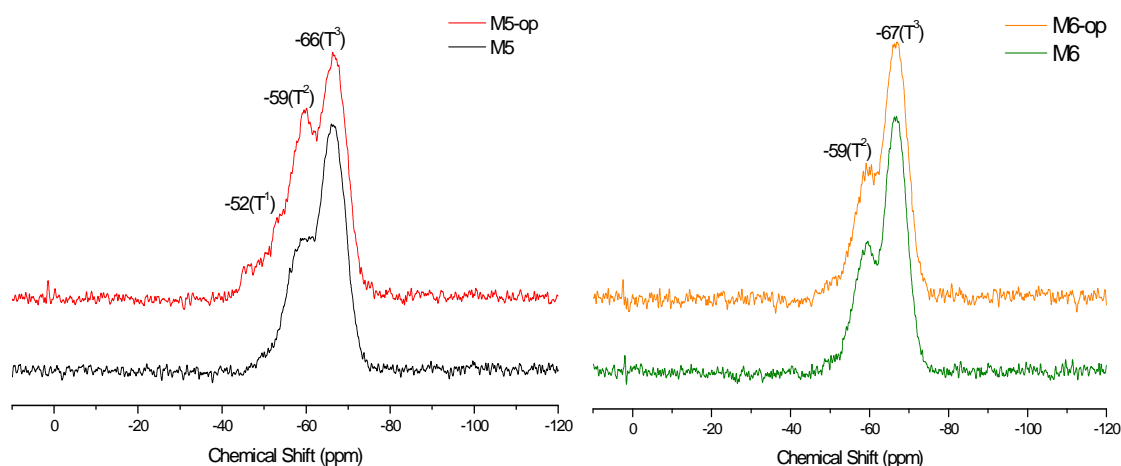


Figure 27: ^{29}Si NMR spectra of (left) **M5** (black) and **M5-op** (red) and (right) **M6** (green) and **M6-op** (orange)

^{29}Si solid state CP-MAS NMR of **M5** shows only T^3 and T^2 signals (δ -66 and -59 ppm) indicating a high condensation degree. In the **M5-op** spectra, T^1 signal appears in addition to a

higher T^2/T^3 ratio. On the other hand, the *in situ* click has no effect on the condensation degree of **M6-op**. Indeed, the small flexible chain of the methyl pent-4-ynoate can be incorporated without any alteration of the ongoing formation of silica framework.

FTIR spectra show that no azidomethylpyrene is adsorbed on the material without being clicked since no azide peak (*ca* 2100 cm^{-1}) appears. Some of the peaks of the pyrene group are evident in the clicked material, especially those at 3049 (aromatic $\text{H-C}_{(\text{sp}^2)}$ stretching) and 2992 (insets). Other peaks could be seen in the region of aromatic $\text{C}=\text{C}$ stretching (1390, 1438 and 1599 cm^{-1}). Furthermore, the UV-vis spectrum (Figure 29) of dispersed **M5-op** in ethanol shows the same bands characteristic of substituted pyrene than in the molecular analogue, confirming the presence of the pyrene function within the material. **M6-op** presents a prominent band at 1735 cm^{-1} corresponding to the ester group (methyl pent-4-ynoate). The click reaction was characterized by the $\text{H-C}_{(\text{sp}^2)}$ stretching of the triazole ring at 3145 cm^{-1} (inset) in addition to the decrease of the intensity of the azide peak (N_3 , 2097 cm^{-1}). This latter is calculated to be 12% by using the ratio of intensities between the azide and siloxane bands before and after click reaction. Taking into account only 20% of added pent-4-ynoate and 12% of azide peak decrease, the extent of the click reaction is calculated to be around 60%.

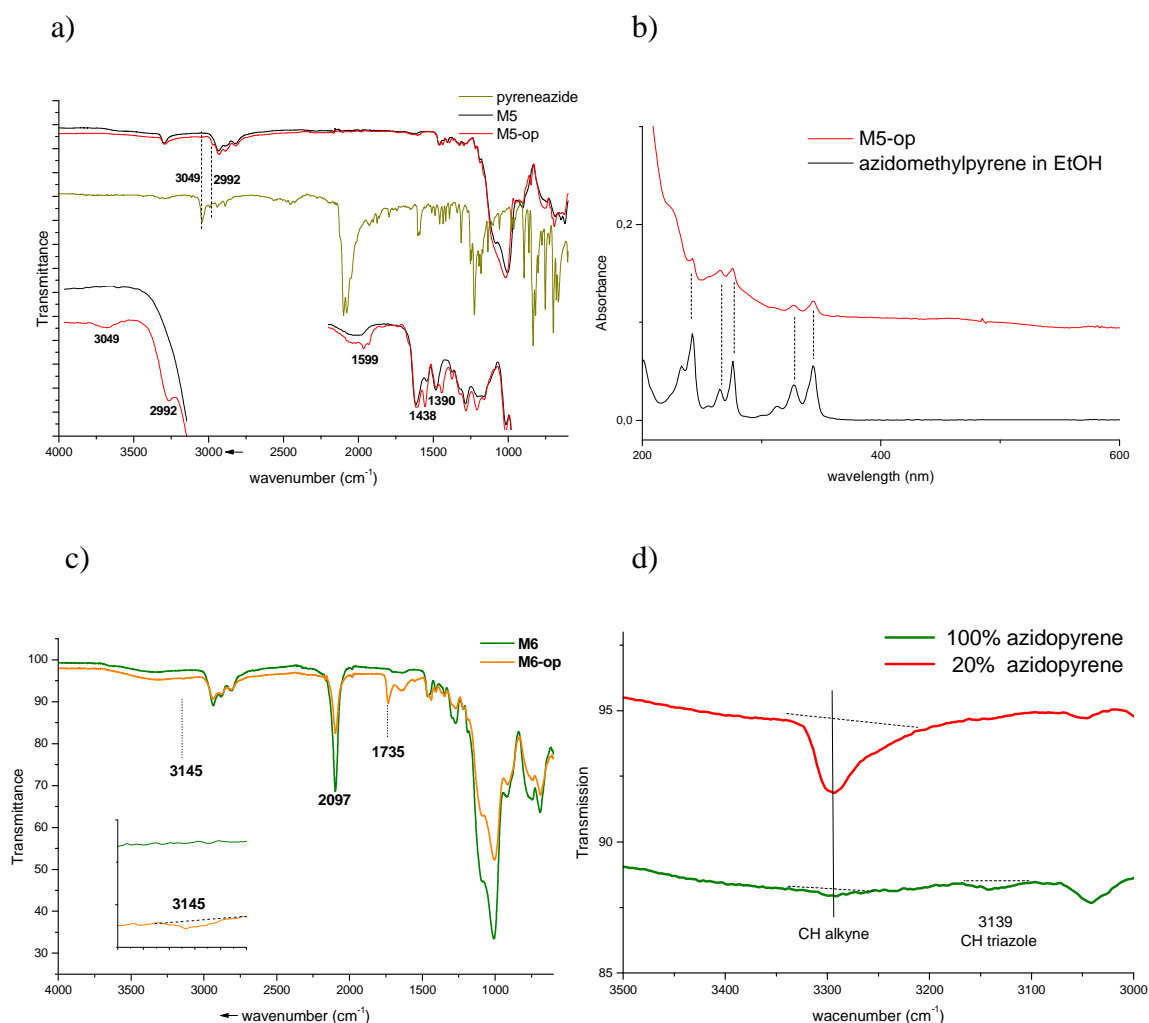


Figure 29: FTIR spectra (a) **M5** (black), **M5-op** (red) and the azidomethylpyrene (oil green), (b) UV-vis absorption spectra of **M5-op** (red) and azidomethylpyrene in ethanol (oil green), (c) **M6** (black), **M6-op** (orange) and (d) zoom on 3500-3000 cm⁻¹ for (green) 100% and (red) 20% clicked **M5-op**

Interestingly, a verification synthesis was made for **M5-op** by adding to **Prec-Alk** 100% molar equivalent of azidomethylpyrene (instead of 20%). FTIR (Figure 29 d) shows a vanishing of the C_{sp}H signal indicating that almost all the alkynes were reacted with the azidomethylpyrene. Thus, a quantitative reaction can be done using this “rapid” strategy.

Material **M5** SEM micrographs (Figure 30) exhibit blocks of aggregated nanoparticles with a size between 10 to 20 nm, its similar behavior to **M3** and **M4** in N₂-sorption suggest that **M5** presents close textural properties (Figure 31). A hysteresis loop (H4 type) with a plateau of saturation of mesoporosity is seen but since no surfactant is used here, the material is more compact than **M3** and **M4** and presents a 2 to 3 times lower accessible surface area (Table 3). For **M5-op**, irregular blocks are seen in the picture and no porosity could be detected by N₂-

sorption. **M5-op** is then an organic-based dense material which at (77 K, temperature of sorption experiments) becomes more rigid, explaining that no surface area could be detected.

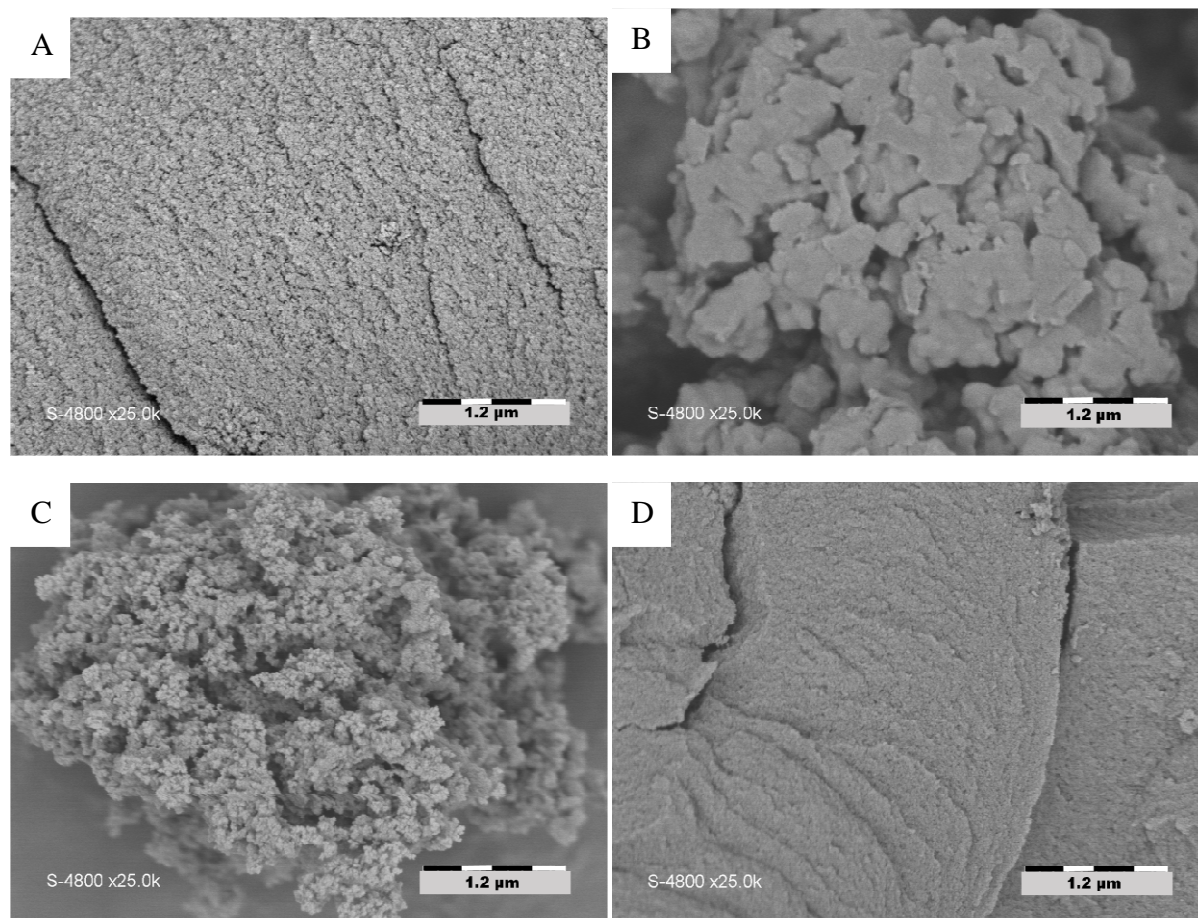


Figure 30: SEM micrographs of **M5** (A), **M5-op** (B), **M6** (C) and **M6-op** (D)

As for **M6**, this material is made of blocks of cross-linked particles with a close size (15-20 nm) but, which are expected to be non-regular. The nitrogen adsorption only takes place on the external surface of the particles assemblies which lead to a modest specific area. The H3-type hysteresis loop observed can be caused by the existence of some non-rigid aggregates of plate-like particles or assemblages of slit-shaped pores. SEM image indicates that the in situ click reaction led to a different structure of the material. No porosity could be evidenced by N₂-adsorption.

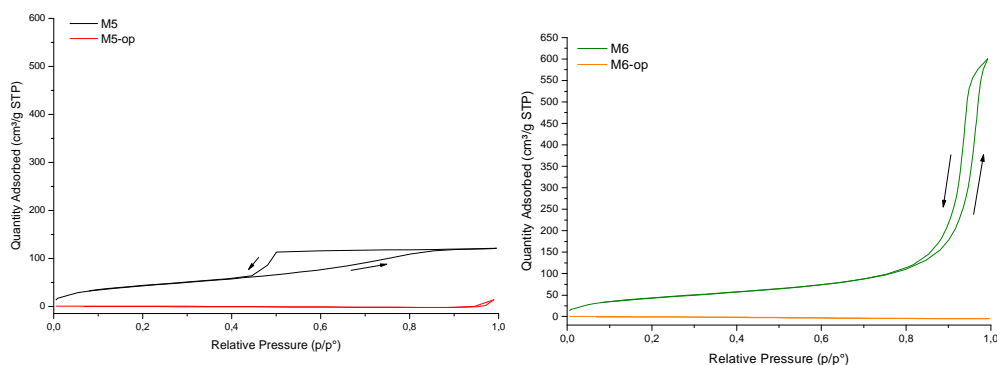


Figure 31: N₂ sorption isotherms of (left), **M5** (black) and **M5-op** (red) and (right) **M6** (green) and **M6-op** (orange)

	BET surface area (m ² /g)	Maximum uptake (cm ³ /g)
M5	161	121
M5-op	<10	<1
M6	164	125
M6-op	<10	<1

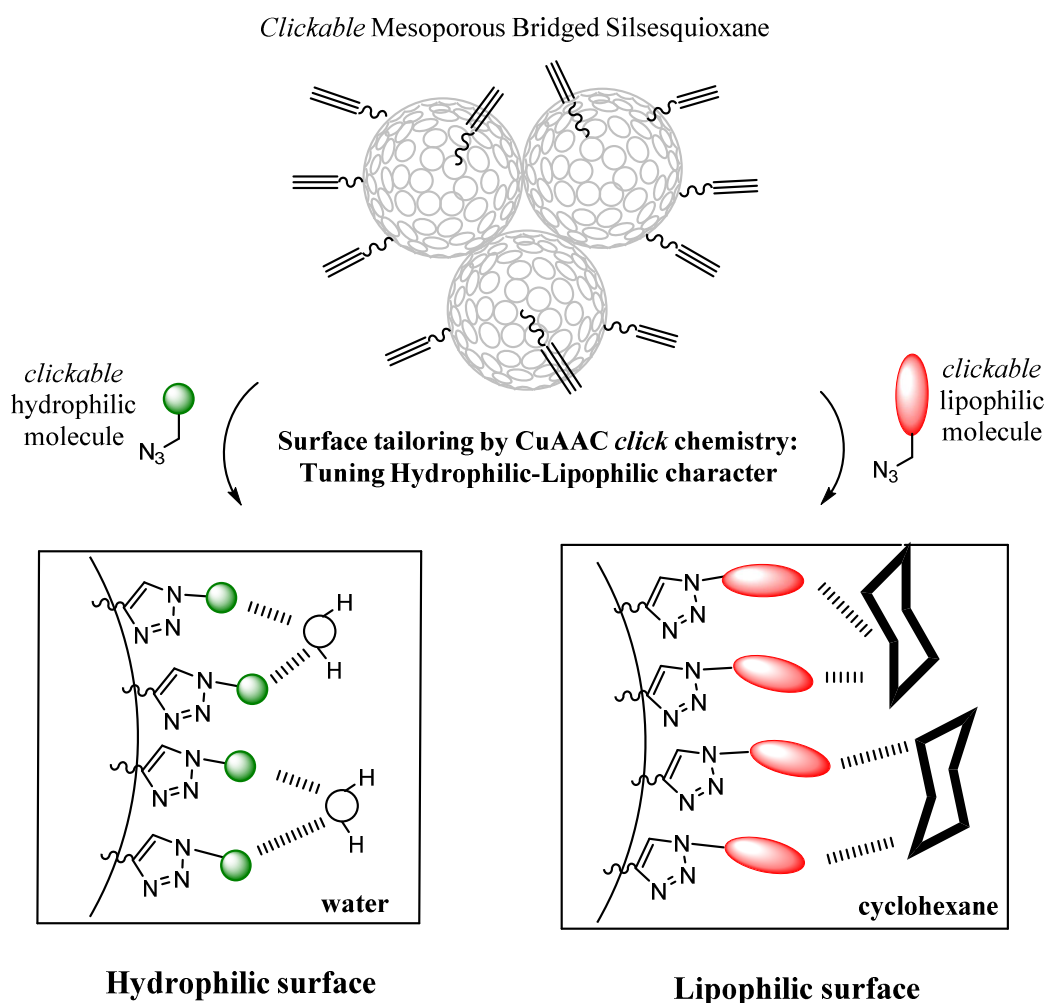
Table 3: BET surface area of made material using pathway 3

4.3. Conclusion

Taking benefit from the close kinetics of the CuAAC *click* reaction and the hydrolysis-condensation of the clickable precursor *via* sol-gel process we have proved that one-pot synthesis of a functional material can be done in one step without concerns about the size and the type of molecules. When no defined shape and structure are needed, this could combine two steps in only one, resulting in saving time and reactants.

In the previous part, we have developed new multifunctional organosilica using the CuAAC reaction by different strategies (post-functionalization of a pre-synthesized material, sol-gel reactions of a preformed functional precursor and one pot click and sol-gel process). The materials have shown good and in some cases quantitative conversions using model clickable molecule. Making use of this property, in the following part will show how CuAAC reaction can have drastic effect on the materials.

5. Tailoring the Hydrophilic/Lipophilic Balance of Clickable Mesoporous Organosilicas by CuAAC *Click*-Functionalization



Scheme 8: Surface tailoring by CuAAC reaction

5.1. Introduction

Organosilicas are attracting considerable attention owing to their wide range of application, which include catalysis^{131,132}, depollution^{93,109,133}, sensing, nanomedicine^{134,135}, electronics, optics or as anti-scratch coatings³³. For most applications, tailoring the surface properties is of primary importance¹³⁶. Indeed, the density of silanol groups at the surface of the final material as well as the presence of hydrophilic or hydrophobic organic groups can alter dramatically the properties for the desired application¹¹⁶. The introduction of a range of organic functionalities is being classically performed using a post-functionalization strategy, by reacting organo(alkoxy)silanes with the material¹³⁷. However, this approach is known to

result in a heterogeneous functionalization of the surface^{138,139}. Furthermore, it is limited to the availability of organo(alkoxy)silanes. In another approach, the sol-gel co-condensation of organo(alkoxy)silanes with an (organo)silica precursor can lead to homogeneous dispersions of the functional organic groups within the matrix, but the textural properties depend importantly on the functionality that is introduced¹⁴⁰. In order to circumvent these issues, several groups have used the CuAAC *click* post-functionalization approach^{90,92,93,95,96,109,141,142}, which is known to display a very wide functional group tolerance, to involve moisture-stable functional molecules, and to occur under mild conditions with very high conversions¹⁴³. By co-condensing silicon tetraalkoxides or bridged organosilanes with clickable organosilanes, new organosilica materials ready for post-functionalization can be produced. We recently introduced the preparation of **Prec-Alk** as a new precursor for clickable PMOs or mesoporous materials^{129,144,145}. These materials, which intrinsically exhibit the highest loading of clickable fragments for organosilicas can be derivatized with very high conversions (up to 90% \pm 10%) with simple clickable organic molecules without altering their morphology.²² These features make them ideal platforms for studying the impact of post-functionalization on the surface properties and on the hydrophilic/hydrophobic balance.

Sorption experiments represent the best strategy for determining the textural properties of porous or divided materials¹⁴⁶. Routinely, nitrogen is used as a probe in such experiments, the particular advantage of this sorbate being its low polarizability making it suitable for any kind of material as it does not favor any type of surface.¹⁴⁷ The main information gained when using N₂ is related to the textural properties of the material of interest whereas surface chemistry can be investigated by using the same technique but with specific sorption probes.¹⁴⁸ Indeed, sorbates with different affinities for hydrophilic or lipophilic surfaces may be used to characterize the hydrophilic or lipophilic character of the materials^{149–155}. More specifically, the affinity of a material for a sorbate can be characterized in the adsorption isotherm by the behavior at low p/p° values (0-0.01) which corresponds to the formation of the first monolayer on the surface. The comparison between sorbates such as low-polarizable N₂, polar water or an apolar alkane would thus enable a good understanding of the surface properties.

Despite the valuable information which can be drawn from these studies using a rather simple experimental setup, only few examples have been reported in literature to study the surface modification of silica materials^{149,154,156,157}. In order to draw a comparison between

different organically modified siliceous materials, a family of materials with similar morphologies but fully functionalized with variable organic fragments should be used. To this aim, we decided to make use of previously described mesoporous material-alkyne (**M3**, denoted M in this part) and to derivatize it with lipophilic, hydrophilic or fluorinated moieties taking advantage of the wide scope, high conversions and preservation of the morphology offered by the CuAAC functionalization reaction. We present here the structural characterizations and the comparative N₂, water and cyclohexane sorption studies of this family of materials.

Material **M** used in this section exhibits the same features as we have described in the first part of this chapter. Meanwhile, a more detailed description will be devoted to the physisorption analysis.

The nitrogen adsorption isotherm of the material before click reaction is shown in (Figure 32). It is a classical type IV adsorption isotherm, as defined by the IUPAC.¹⁵⁸ The main characteristics are the clear saturation plateau reached at $p/p^\circ = 0.85$ and a broad hysteresis loop. This H2 type hysteresis loop is usually obtained with materials aggregated as small particles, the voids between particles having a size in the same order of magnitude than the particles themselves. This interpretation is fully consistent with what was observed by TEM and SEM (Figure 32).

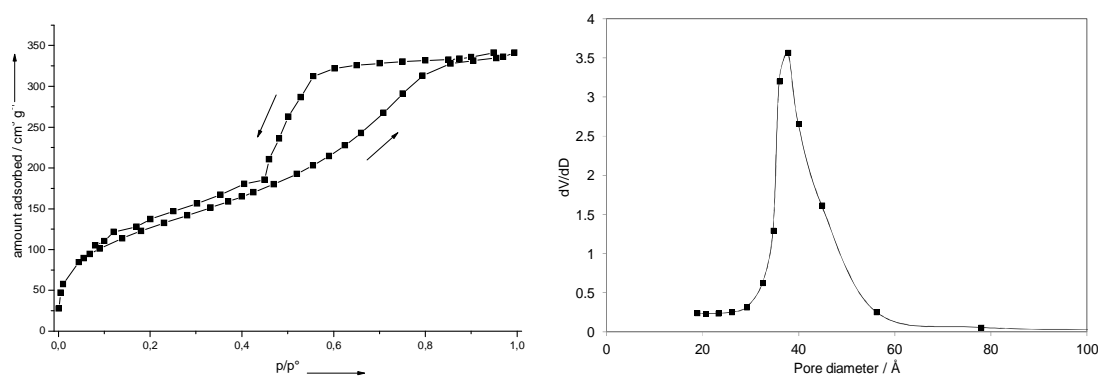


Figure 32: (left) N₂ sorption isotherm and (right) BJH plot after adsorption of nitrogen onto the parent material.

The pore size distribution (PSD) obtained for this material can be found in Figure 32. This PSD, obtained after BJH derivation of the desorption branch of the adsorption isotherm, shows a narrow pore size distribution centered around 4 nm. This result must be carefully considered. If this population of 4 nm pore diameter pores existed, it would be a striking feature, already apparent on the adsorption branch. In such a case, it would be possible to

observe a marked sorbate uptake in a very small relative pressure range, as it happens in the case of MCM-41 materials for instance. However, the adsorption branch only shows a gradual amount uptake in a wide range of relative pressure. In our case, this result is likely an artifact which can be classically attributed to the cavitation (also named as catastrophic desorption) of nitrogen from interconnected voids when the equilibrium pressure reaches 0.42 downwards¹⁵⁹. It is typically the case of aggregated mineral oxides such as ceria or zirconia¹⁶⁰. Additionally, after *t*-plot analysis, no microporosity was found in the parent material. Using small and wide angle X-ray scattering (SWAXS), it is possible to have complementary information about the structure of the material. For the parent material, the SAXS profile is compatible with an assembly of small dense nanospheres. The non-Porod regime ($I(q) \propto q^{-3}$) that is displayed at intermediate *q* values indicates that the nanospheres have rough surfaces (Figure 36). The weak pseudo-Bragg peak observed at $q \approx 0.55 \text{ \AA}^{-1}$ (corresponding distance 11.1 Å) might correspond to irregular repetitions of crater-like holes at the surface of the nanoparticles, which would confer nanoscale roughness to the material.

5.2. CuAAC Reaction

Mesoporous material **M** was then functionalized using different organic azides (Table 4), with functions that may confer it a hydrophilic, lipophilic or hydrophobic and lipophobic character.

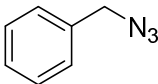
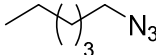
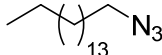
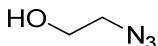
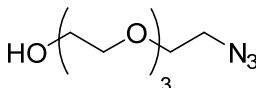
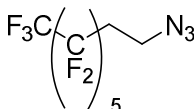
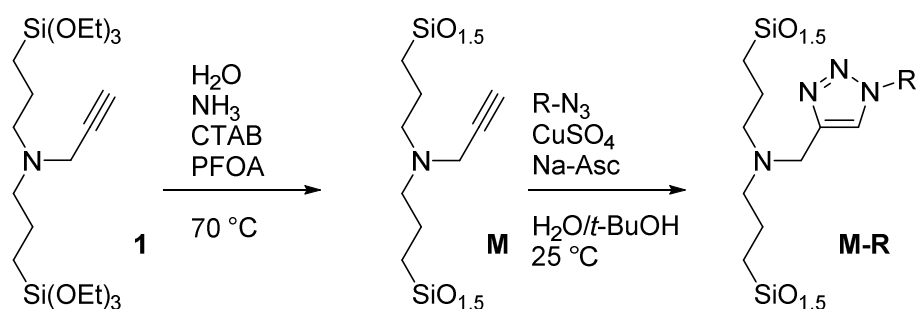
lipophilic		
		
Azidomethyl benzene (Ph)	6-azidohexane (C ₆)	16- azido hexadecane (C ₁₆)
hydrophilic		
		
2-azidoethanol (OH)	Tetraethyleneglycol azide (PEG)	
hydrophobic and lipophobic		
		
8-azido-1,1,1,2,2,3,3,4,4,5,5,6,6-tridecafluorooctane (F)		

Table 4: Organic azides that were clicked on the materials. The corresponding suffixes (R) are written in parenthesis.

The CuAAC *click* reactions were performed at room temperature in a mixture of water and tert-butanol, yielding materials denoted as M-R, the suffix R indicating the grafted organic

functions (Scheme 9).



Scheme 9: Formation of the parent material M and its functionalization by CuAAC.

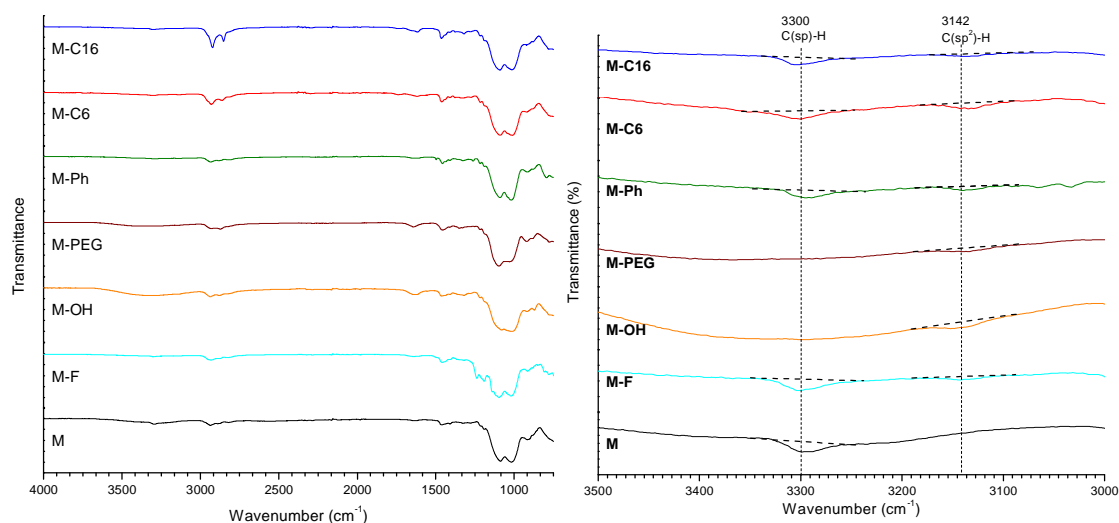
5.3. Characterization

The extent of click reaction was analyzed by FTIR (Figure 33-b). Indeed, during a CuAAC reaction, the $C_{(sp)}$ -H bond of the terminal alkyne is converted into a C_{sp2} -H bond in the triazole fragment, with a corresponding shift of the stretching vibration from $3300\text{ cm}^{-1}(\text{m})$ to $3142\text{ cm}^{-1}(\text{w})$. Whereas for all organic groups, the appearance of a weak C_{sp2} -H band is observed at 3142 cm^{-1} , the full vanishing of the $C_{(sp)}$ -H vibration at 3300 cm^{-1} is only visible in the case of the hydrophilic groups (PEG and OH). Therefore, despite precisely the same synthetic conditions used, the conversion of the alkynes into triazole does not proceed to the same extent, the highest conversions being observed with the hydrophilic azides, even with the long tetraethylene glycol group (12 C or O atoms). In addition, the decrease of the $C\equiv C$ stretching band in Raman (2105 cm^{-1}) compared to the $C_{(sp3)}$ -H band ($2800\text{--}3000\text{ cm}^{-1}$) (Figure 33) follows the same trend. The presence of the functional groups is mainly evidenced from the $C_{(sp3)}$ -H stretching region ($2840\text{--}2960\text{ cm}^{-1}$). Moreover, the successful removal of the excess azide reactants is proven by the absence of peaks at 2100 cm^{-1} , that would correspond to the strong vibration of the azide groups (Figure 33-a).

Solid-state ^{13}C CP-MAS NMR (Figure 34-a) confirms the information deduced from FTIR: the formation of the triazole linkers is evidenced by the appearance of signals at *ca* 125 and 145 ppm, while the intensity of the signals at 70-80 ppm, characteristic of the alkyne functions decreases. This decrease is more pronounced in the case of M-PEG and M-OH, though no quantitative information can be deduced from these spectra. The presence of the functional groups is evident for all materials except for M-F, with the appearance of intense

signals at 125 ppm in the case of M-Ph (aromatic carbons) at 58 ppm for M-PEG or 30 ppm for M-C6 or M-C16 (carbons from the alkylene chains). It is noteworthy that the ^{29}Si NMR spectra (Figure 34-b) remain unaltered during the CuAAC reaction: no Q signal (-90 to -130 ppm) is observed, that is indicative of Si-C bond cleavage, and the shape of the T band remains unaltered. Therefore, we can suggest that under the CuAAC reaction conditions, no rearrangement occurs in the siloxane framework despite the densification of the structure.

a)



b)

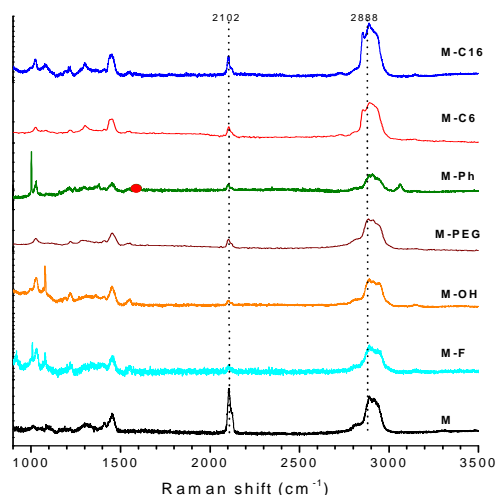


Figure 33: a) (left) Full and (right) zoom on 3000-3500 cm^{-1} region of the FTIR and b) Raman spectra of the parent (M) and of the functionalized materials (M-R)

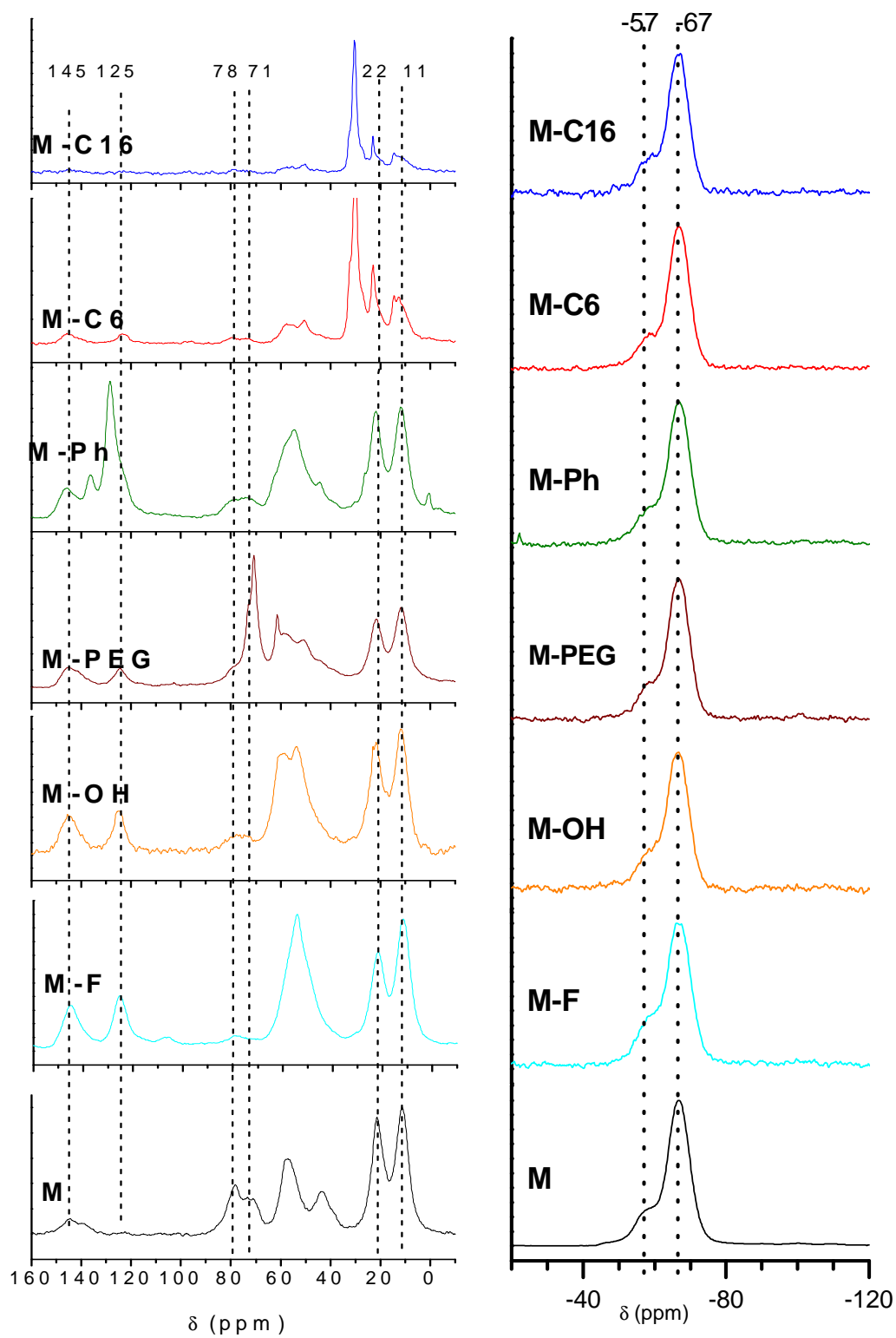


Figure 34 : (left) ^{13}C and (right) ^{29}Si solid-state CP-MAS NMR spectra of the parent (M) and the functionalized material (M-X)

On the structural point of view, SEM micrographs (Figure 35) show a preservation of the morphology of the material after the functionalization reaction.

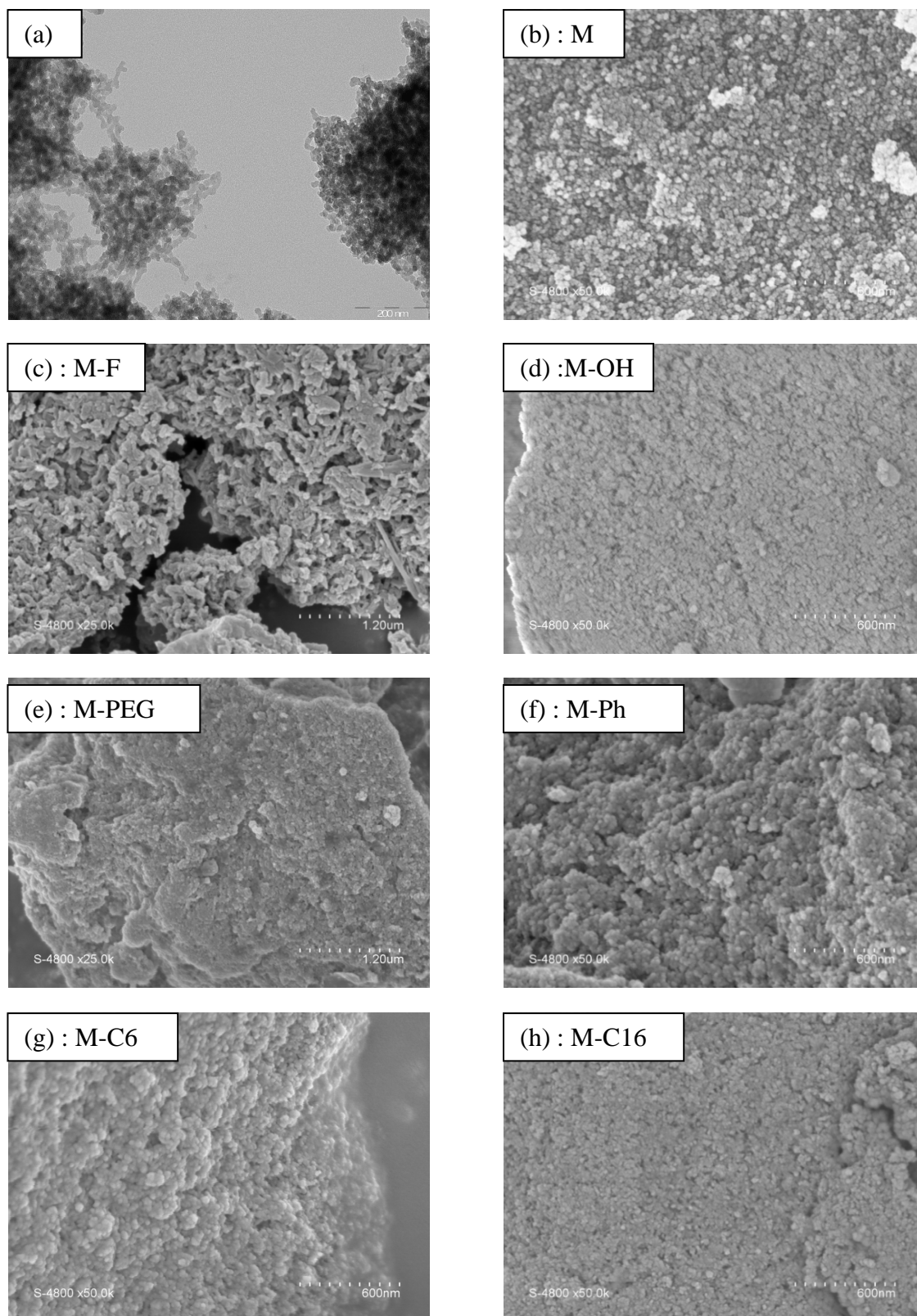


Figure 35:Transmission electron microscopy of the parent material (a), and SEM micrographs of raw and functionalized material M and M-R (b-h)

This is confirmed by SWAXS studies (Figure 36), with overall similar diffractogrammes, though for the functionalized materials, the medium angle region can be fitted as $I(q) \propto q^{-n}$ with $n=3.8$ except for the M-OH material with only $n=3.5$, compared to $n = 3.0$ in the case of M. This can be attributed to a reduced roughness after the grafting of the organic groups, the smallest $\text{CH}_2\text{-CH}_2\text{-OH}$ yielding a material with still a noticeable roughness.

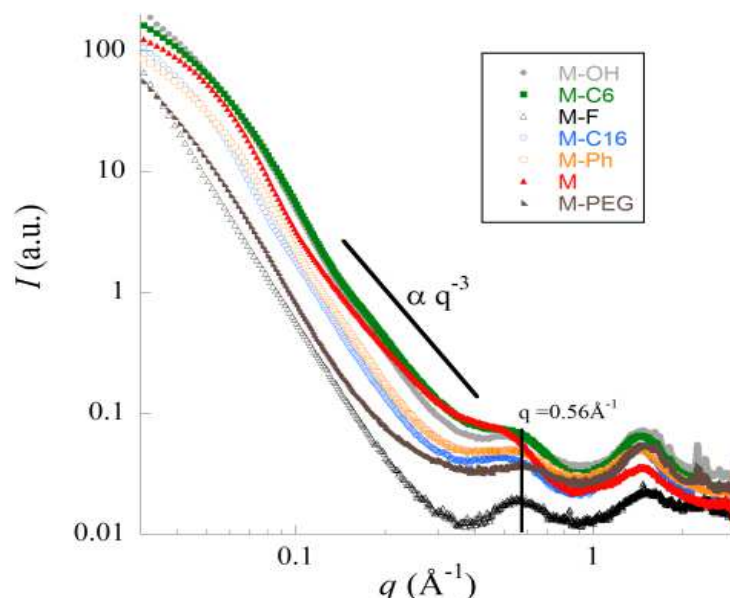


Figure 36: SWAXS on the parent and on the functionalized materials.

After click reaction, interesting results are found from the N_2 -sorption experiments (Figure 37). In the case of the materials M-C6, M-OH, M-C16 and M-Ph the same shape is obtained. It can be deduced that the textural properties of these clicked materials are similar to that of the parent material. However, there is a difference in the extent of adsorption at saturation which decreases by a factor 2 in the case of M-C6. This decrease is even more pronounced in the case of M-OH, M-Ph and M-C16. Different interpretations can account for this observation, (i) coalescence of particles after click reaction which decreases the number of accessible interparticular voids, (ii) void accesses blocked by the clicked molecules. It must be noted that the hysteresis loops are very similar, in terms of shape but also in terms of relative pressure at which hysteresis occurs. This suggests that the accessible pores of the related materials retain their original structure.

5.4. Gas-sorption study

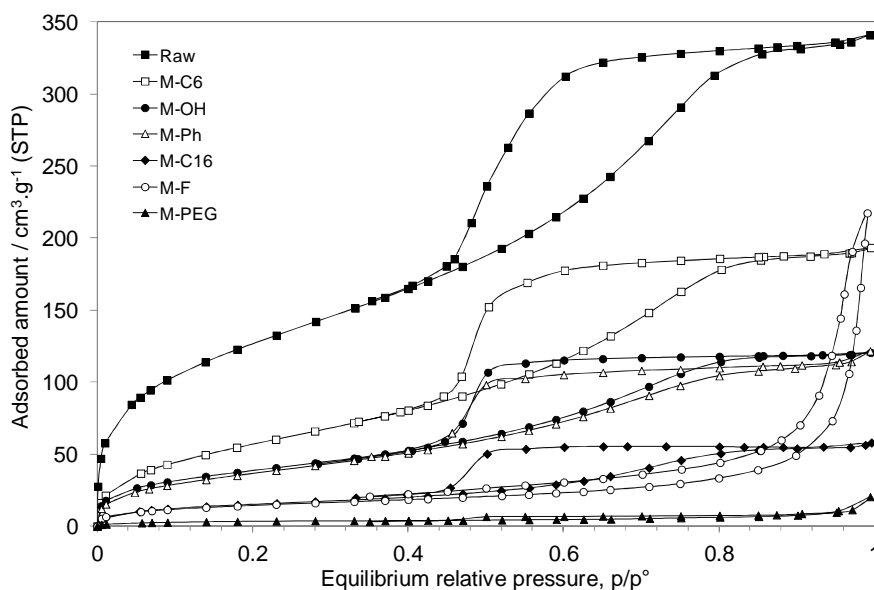


Figure 37: Nitrogen adsorption isotherms on parent and functionalized materials.

We mentioned that, as compared to the parent material, the hystereses of the clicked materials are less pronounced and the adsorbed amounts are lowered. This is especially the case for the materials M-F and M-PEG. In the latter case, adsorption is very limited and the hysteresis loop is absent. It can be deduced that the click reaction disables the interparticular voids. The nitrogen adsorption only takes place on the external surface of the particles assemblies which lead to a poor specific area. M-F leads to the same interpretations. The H3-type hysteresis loop observed can be caused by the existence of some non-rigid aggregates of plate-like particles or assemblages of slit-shaped pores¹⁴⁸.

The affinity between nitrogen through its quadrupolar moment and the different materials can be expressed in terms of Henry's constants derived from the slope of the adsorption isotherms at very low relative pressure. These have been implemented in Table 5 along with textural parameters.

	$S_{\text{BET}} / \text{m}^2 \cdot \text{g}^{-1}$	Uptake at saturation / $\text{cm}^3 \cdot \text{g}^{-1}$	Henry's constant / $\text{cm}^3 \cdot \text{g}^{-1}$
M	475	340	4872
M-F	52	60	581
M-OH	143	57	1570
M-PEG	12	20	111
M-Ph	139	121	1355
M-C6	221	190	1957
M-C16	166	58	528

Table 5: Textural properties of the different materials and Henry's constants of nitrogen determined at 77 K.

Clear differences can be seen between Henry's constants. Interestingly, a wide range of Henry's constants is found, the parent material leading to the highest constant whereas M-PEG leads to a poor Henry's constant. The interpretation of these differences is not straightforward since it can be assumed that all the different materials still have some surface silanols left. These adsorption sites interact with nitrogen as this happens in any mineral oxide. The material before click reaction, namely M, exhibits the higher Henry's constant which suggests a full accessibility to the most active surface sites, either on the silica surface or on the organic fragment. After click reaction, the Henry's constants are lowered, likely because the clicked molecule interacts at the expense of the hindered surface sites. The electric dipole polarizability of nitrogen is only 1.71 \AA^3 , which makes this probe ideal for physisorption on any type of surface^{146,161}. Indeed, this very low value will not really favor any surface site. However, finding such different Henry's constants values indicate that the nature of the surface of the clicked materials has been drastically modified. The prepared materials can be classified as hydrophilic (M-OH, M-PEG), hydrophobic (M-C6, M-C16, M-Ph) and strongly hydrophobic (M-F). The click reaction producing these materials can be validated by adsorbing specific probes, favoring hydrogen bonding or only dispersion forces. Specifically, cyclohexane and water were chosen as sorbates to evaluate the surface properties of the modified materials.

Before hand, it must be said that nitrogen adsorption onto these materials already showed important differences in terms of adsorbed amounts at saturation.

The adsorption isotherms of cyclohexane on the different materials are presented in Figure 38. Significant information can be deduced from two distinct regions: At high p/p° the uptake is

an indication of the accessible pore volume, whereas at low p/p° the slope of the curve (Henry's constant) outlines the sorbate-sorbent affinity. In fact, Henry's constants are derived not from the first adsorption site, but from adsorption taking place at relative pressure below $p/p^\circ = 0.01$.

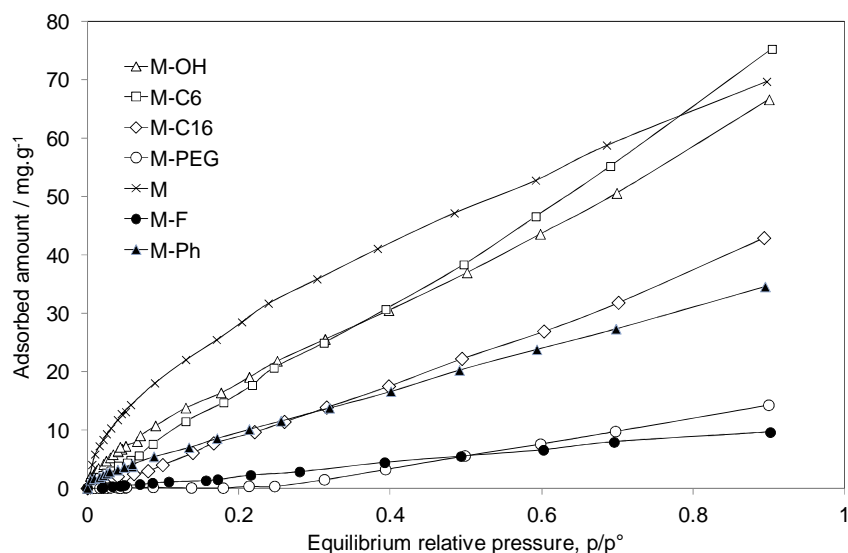


Figure 38: Adsorption isotherms of cyclohexane on the parent and the functionalized materials at 313 K.

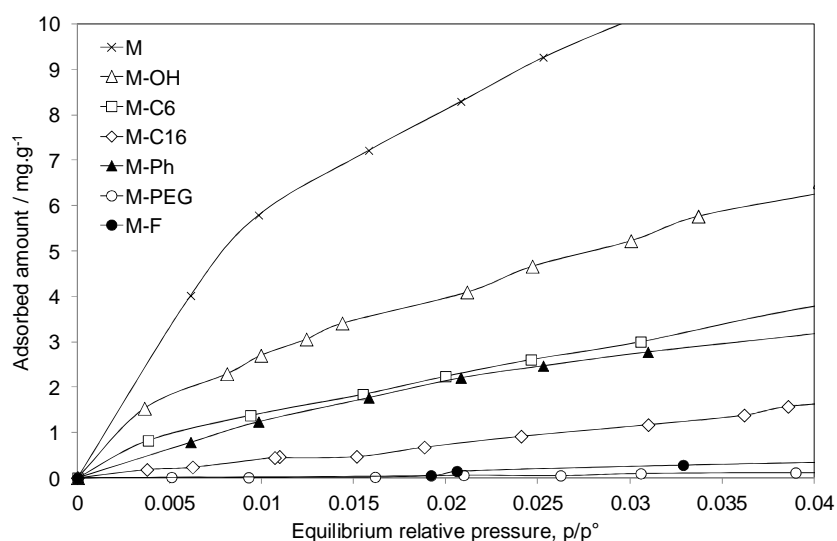


Figure 38-bis: Adsorption isotherms of cyclohexane on the parent and the functionalized materials at 313 K in the low relative pressure region.

The shape of the adsorption isotherms is rather similar, with significant maximum uptakes, and mainly differs in terms of affinity at low relative pressure. As already obtained with the adsorption of nitrogen, the highest interaction is obtained with the parent material. Having

consistent results is very interesting since cyclohexane only interacts through dispersive interaction. Furthermore, clicking organic functions such as C6 or C16 does not render the material more lipophilic than the parent material. This could be due to the fact that clicking the organic functions is at the expense of interaction sites. Considering the clicked materials, it is clear that cyclohexane preferentially interacts with lipophilic clicked species such as C6. One would have expected a similar result with C16. However, the size of C16 likely prevents the diffusion of cyclohexane into the material. If we go into more details, we can observe that the adsorption isotherms of M and M-OH exhibit a slight knee which is the indication of a specific interaction. On the other hand, M-C6 and M-C16 lead to straight line which is indicative of a true Henry's behavior. These two clicked materials act as a solvent for cyclohexane and the adsorbed amount is proportional to the relative pressure. Cyclohexane interacts very poorly with M-PEG likely because of the structuration of the material, as already discussed with the adsorption of nitrogen. Its specific surface area is very low and as a consequence the active sites of M-PEG are very scarce. A high relative pressure is required for cyclohexane to adsorb in M-PEG. From $p/p^\circ = 0.2$ upwards, M-PEG also acts as a solvent for cyclohexane. M-F exhibits a behavior very similar. However, the specific surface area of M-F is higher than that of M-PEG. It can be concluded that the fluorinated material results in a lipophobic material. The Henry's constants derived at low relative pressure confirms these findings (Table 6).

Adsorbate	M	M-F	M-OH	M-PEG	M-Ph	M-C6	M-C16
Cyclohexane	596	<5	245	<5	178	141	42
Water	26	34	113	62	38	54	17

Table 6. Henry's constants in mg.g^{-1} for the different systems at 313 K.

The original material, M, has a high specific surface area. This textural feature implies a large number of accessible surface sites and therefore a high Henry's constant. The click reaction with any organic molecule does not improve the affinity for cyclohexane. One reason is the specific surface areas of the clicked materials which are less than half of that of M. A second reason is the fact that M already has a large organic content. Since cyclohexane only interacts through dispersive interaction, it can be concluded that the behavior generally observed is closely related to that already discussed in the case of the adsorption of nitrogen. The Henry's constants are therefore sorted as in the case of those obtained with nitrogen. From this observation, it is interesting to focus on a polar sorbate such as water.

The adsorption isotherms of water on the different materials are presented in Figure 39. The shape of the adsorption isotherms is quite similar from one system to another. However, it can be already noted that water has less affinity for M than cyclohexane has. As mentioned above, the raw material M has already an organic content. Even if few residual silanols are present, this material is poorly hydrophilic. At low relative pressure, the adsorption isotherm is rather flat, which indicates a low affinity between water and M. This shape can be compared to those obtained with clicked materials. In the case of M-OH and M-PEG, slight knees can be observed which suggests a higher affinity. This is confirmed in Table 6 in which the Henry's constants are gathered. Despite a very low surface area, M-PEG leads to a high constant as well as M-OH (62 and 113 mg.g⁻¹ respectively). In the case of hydrophobic materials, unsurprisingly low Henry's constants are found. For instance, in the case of M-C6, the constant is 54 mg.g⁻¹ whereas it is 62 mg.g⁻¹ for M-PEG with a specific surface area 20 times lower. This comparison also holds true for the other hydrophobic clicked molecules M-Ph and M-C16.

These materials can be sorted according to a hydrophilic scale:

M-OH>M-PEG>M-C6>M-Ph>M-F>M-C16.

It can be anticipated that obtaining nanoparticles of M-PEG with accessible surface sites would make this material the most hydrophilic of this series.

By analyzing the wide angle zone of the SWAXS diffractogramme, (Figure 40), we observe the correlation peaks of water at q from 1 to 2 Å⁻¹ and we point out that the corresponding intensity due to the adsorbed water molecules from materials in normal condition might be correlated to the hydrophilic properties of material. Without any assumption on the specific surface or pore volume, a hydrophilic scale as following M-OH>M-C6>M-PEG>M-Ph>M-C16>M-F was deduced, which is close to the above Henry's constant order.

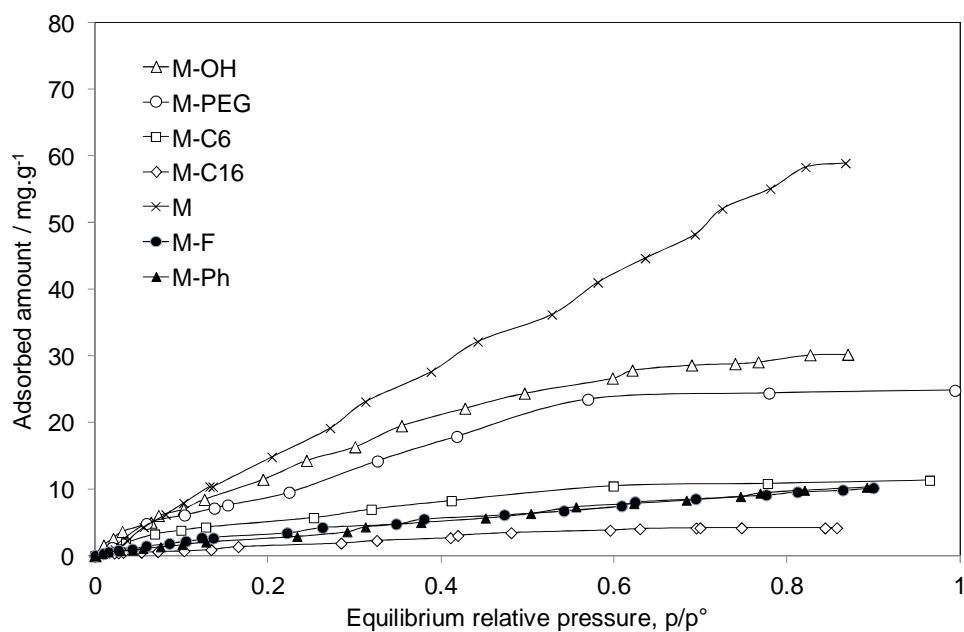


Figure 39: Adsorption isotherms of water on the parent and the functionalized materials at 313 K.

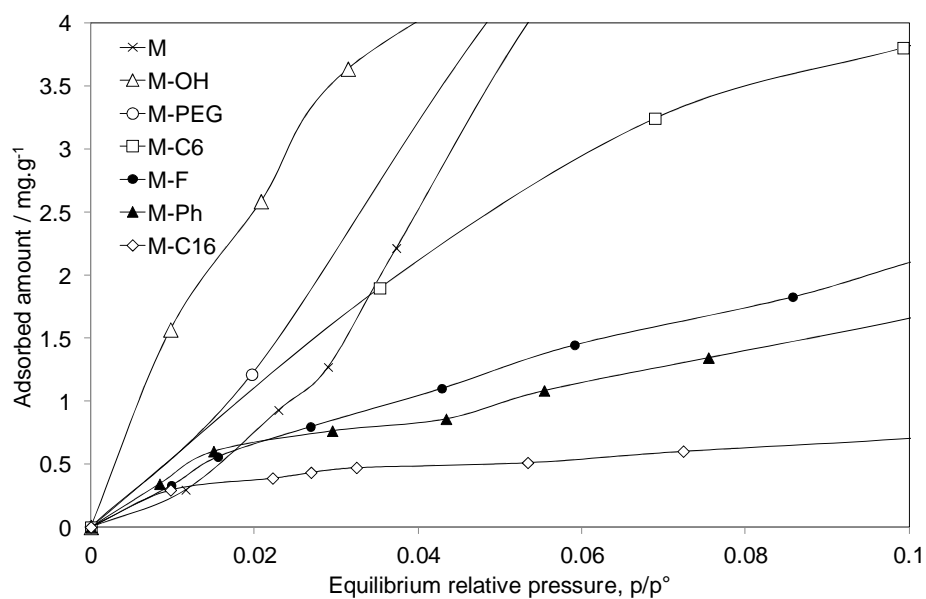


Figure 39-bis: Adsorption isotherms of water on the parent and functionalized materials at 313 K in the low relative pressure region.

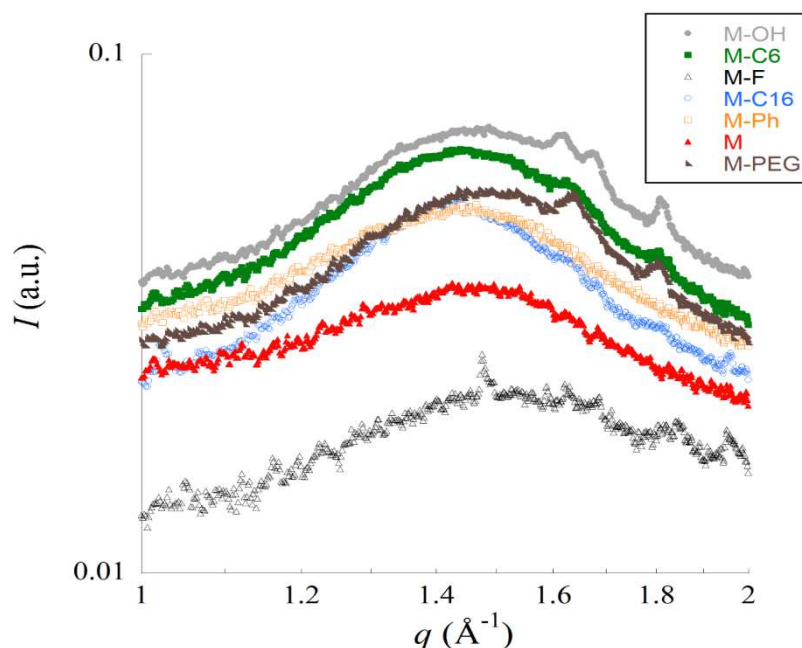


Figure 40: Zoom on the wide angle region of the SWAXS diffractogram for the parent and functionalized materials.

5.5. Conclusions

The goal of this study was to design and characterize materials having different surface chemistry, obtained from the same parent material. We demonstrated that the CuAAC *click* reaction could be used for this goal, thanks to its high conversions and excellent functional group tolerance. Indeed, we investigated the textural and adsorption properties of these materials with nitrogen, but also with water and cyclohexane. Nitrogen adsorption revealed that the different materials were made of aggregated nanoparticles, differing by the accessibility of their interparticular voids. This confirmed the microscopy and SWAXS results which already strongly suggested the occurrence of golf ball -like nanoparticles.

The parent material showed a good affinity for cyclohexane, higher than towards water. This was explained by the high organic loading and the very few surface silanol left in this material. The functionalized materials exhibited a preferential affinity for water or cyclohexane, depending on the grafted function. The quantification of the sorbate/sorbent affinity was obtained by means of Henry's constants. We obtained the following hydrophilic scale: **M-OH** > **M-PEG** > **M-C6** > **M-Ph** > **M-F** > **M-C16**. This scale was mostly confirmed by SWAXS measurements. We therefore clearly demonstrated that tailoring the hydrophilic/lipophilic balance of silica based materials could be possible by using the CuAAC *click* reaction.

6. General conclusion of chapter II

We made use of clickable bissilylated organosilanes, already described in our group, to successfully prepare, *via* the sol-gel process, clickable Periodic Mesoporous Organosilicas (PMOs) using anionic surfactant under acidic conditions by an interaction between the organic ammonium group with the surfactant, then clickable bridged silsesquioxanes as a Mesoporous Material using CTAB as surfactant in basic conditions based on the interaction between anionic silicates and cationic head of the surfactant. PMOs were carefully characterized using different analytical methods. Ordered periodic structures were characterized by electronic microscopy and X-ray scattering. However, the material was too fragile to be probed by N₂-sorption, although a very good reactivity towards complementary clickable molecules was observed. On the other hand, mesoporous materials exhibit high surface area and were used for further applications. Model molecules were clicked and the appropriate analytical methods evidenced a very good reactivity with high conversion for the CuAAC click reaction.

The bissilylated organosilanes were also used to provide new organosilanes bearing functional groups (*i.e.* thymine) *via* CuAAC reaction under anhydrous conditions then to afford the corresponding materials by the sol-gel process using nucleophilic catalysis with very high payloads of functional groups.

Moreover, a one-step approach for obtaining functional materials was established; CuAAC reaction and sol-gel polymerization were carried out simultaneously to make one pot functional material from the bissilylated organosilanes.

Finally, the scope of the CuAAC-grafting was used to induce radical changes to the surface properties of **M3**, by modifying the hydrophobic/hydrophilic balance after extensive click reaction with different molecules. Water and cyclohexane vapour adsorption studies demonstrated the drastic changes of the surface affinity of the CuAAC-modified materials depending on the clicked molecules. Hence, the character of the material was varied from hydrophilic (after modification with PEG or hydroxyethyl groups), to lipophilic (with grafted hexadecyl or hexyl chains) to hydrophobic and lipophobic (when fluorinated chains were clicked).

CHAPTER III

Multiclickable Mesoporous Silica Nanoparticles for Controlled Release of Cargo Molecules.

CHAPTER III: Multiclickable Mesoporous Silica Nanoparticles for controlled release of cargo molecules.

This chapter aims to demonstrate how mesoporous silica nanoparticles (MSNs) can be effectively functionalized by CuAAC click reaction by a diversity of molecules having very important properties. Based on collaboration with Jeffrey Zink's group in UCLA, we will focus specifically on functions enabling the controlled opening of the pores of MSN for cancer treatment purposes. We will try to demonstrate the juxtaposition of the functions to achieve a controlled release of cargo molecules.

1. From a normal cell to a cancer cell^{162–165}

Cells make up our human body; they are the “units” that form the tissues. These tissues have a normal regeneration process, called *mitosis*, which upon the organ needs splits a cell into two to replace a defective one or a cell coming to the end of its life span, thus making possible to preserve the integrity of tissues functions.

Cells program is ordered by the genes of the chromosomes inside the nucleus. When genes undergo a change, nucleus can send out abnormal messages making the whole cell go wrong. It multiplies uncontrollably and starts its own life cycle by multiplying cells containing the same defects, which proliferate forming the tumor around normal cells.

Tumors implement many blood vessels in order to survive by supplying them with oxygen and nutriment, this is *angiogenesis*. However, a tumor becomes really dangerous when cancer cells begin invading other tissues and spread through these blood vessels into surrounding organs contributing to produce new tumors: this spreading process is called *metastasis*.

There are many factors leading the cell to become a tumor, these factors can exist to different degrees such as hereditary genetic anomalies, exposure to some viruses (HIV, hepatitis B, C and D,...), exposure to toxic agents, chemical agents, radiation including sunlight, unhealthy behavior (Consumption of alcohol and tobacco, fatty diet). All these factors can be the origin of the above-mentioned gene mutations and thus induce a tumor.

Today, over 25 millions people live with a cancer and 7 millions die each year. However, means to fight cancer do exist. Mainly, three kinds of treatments are currently being in use:

- 1- Surgery which consists in removing the tumor in part or in its entirety.
- 2- Radiotherapy, using radioactive rays which prevent the diseased cells from multiplying and destroy them.
- 3- Chemotherapy: administering systematic active medicinal substances to the patient.

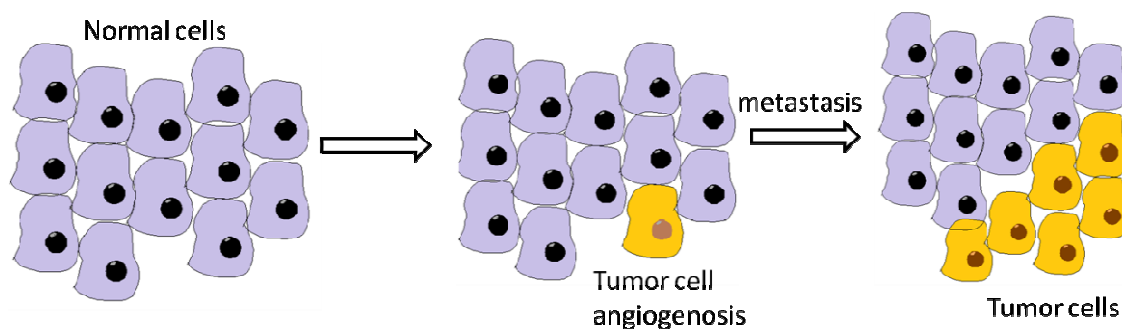


Figure 1: tumor cell expansion

Chemo- and radio-therapies act on cancer cells, but also on healthy cells, thus lack of specificity inducing severe side effects. Better knowledge of the characteristics of the cancer lead to developing therapies that target cancer cells more specifically. Current medicinal needs in cancer treatment focus on finding new approaches to route, in a protected way, the presently available medicinal substances directly to the tumor tissue¹⁶⁶. Ideally, this should consist in biocompatible, low toxic nanometer-scaled systems able to resist to physiological conditions, owning the capacity to bear functions that specifically target cancer cells, along with good concentrations of medicinal active molecules. Importantly, this drug must be protected from harsh conditions (enzymatic or chemical degradation) and only released on demand without any premature uncontrollable leaking.

2. Hybrid Mesoporous Silica Nanoparticles (MSNs)

Hybrid (inorganic/organic) Mesoporous Silica Nanoparticles (MSNs) have been extensively used as platform for different biomedical applications including diagnosis^{124,167}, biosensing¹⁶⁸ and drug delivery^{97,169–171}. MCM-41 were first reported as nanocarriers for the delivery of therapeutics in 2003¹⁷² using CdS nanoparticles to block the pore openings and controllably release the cargo upon specific stimulus. Since then, on the basis of the same concept, many efforts were devoted to design multifunctional MSNs as drug delivery nanocarriers owning

optimal characteristics for biocompatibility, high loading capacity of cargo molecules and tunable chemistry allowing the functionalization of the nanoparticles to fit different circumstances (spatiotemporal controlled release, luminescent properties for tracking, targeting agents for cell, and stability in physiological system).

2.1. Biocompatibility and morphology of MSNs

The features of any drug delivery nanocarrier must respect the cellular uptake mechanism. How does the cell internalize the MSN? What are MSNs features to reach an optimal uptake by the cell? These are critical questions to smartly design multifunctional MSN.

The most common pathway of MSNs internalization into the cell is *endocytosis*¹⁷⁰. This latter is a complex process in which the MSNs are encompassed by the membrane lipid bilayer forming the endosomes¹⁷³. The internal acidic pH leads to a degradation of the endosome liberating the MSN. Depending on the cell membrane properties, the morphology (size and shape) and the surface functionalization of MSNs are critical to optimize the endocytosis process.

In order to apply the MSN as drug delivery systems, their biocompatibility and cellular uptake have to be checked on a well-defined morphology of nanoparticles.

2.2. Morphology

Cellular uptake studies showed that particle sizes around 100 nm are the most effective for endocytic uptake¹⁷⁴. MSNs with larger size need more time to be internalized and this “wasted” time could be fatal since ambient conditions tend to degrade the silica matrix¹⁷⁵. Interestingly, rod-shaped nanoparticles display better uptake degree. Nanorods with aspect ratio from 2 to 4 exhibit better internalization than nanospheres or nanorods with smaller or larger aspect ratio^{176–179} in HeLa cells and A549 lung cancer cells.

2.3. Cytotoxicity

The main concern about silica cytotoxicity is related to silicosis.

Extensive investigations about the toxicity of silica nanoparticles were carried out because the recently-exploited high porosity (exposed surface) could lead to different types of interaction with the cell membrane and eventually create new ways of toxicity compared to the dense silica nanoparticles¹⁷⁹. There have been different reports about the toxicity of silica

nanoparticles depending on the synthesis conditions that affect the surface properties and then the interaction with the cells.

Zink, Nel and Brinker¹³⁰ have together studied the relation between cytotoxicity and structure for amorphous silica nanoparticles made either under soft conditions (colloidal route) or by a high temperature route by comparing the cytotoxicity to the silanols concentration, the aggregation state, the straining degree of siloxane bonds and the capability of producing hydroxyl radicals (Figure 1 bis). Interestingly, colloidal silica did not show any toxicity compared to fumed silica. The main conclusion of this study is that, structures with three-membered ring (3 Si-O elements) produced at high temperature, are responsible of producing oxygen radicals. Therefore, the framework, the surface chemistry and the fused chain like morphology resulted by high-temperature synthesis (>1300 °C) and rapid thermal quenching are the basic cause of high toxicity displayed for fumed silica.

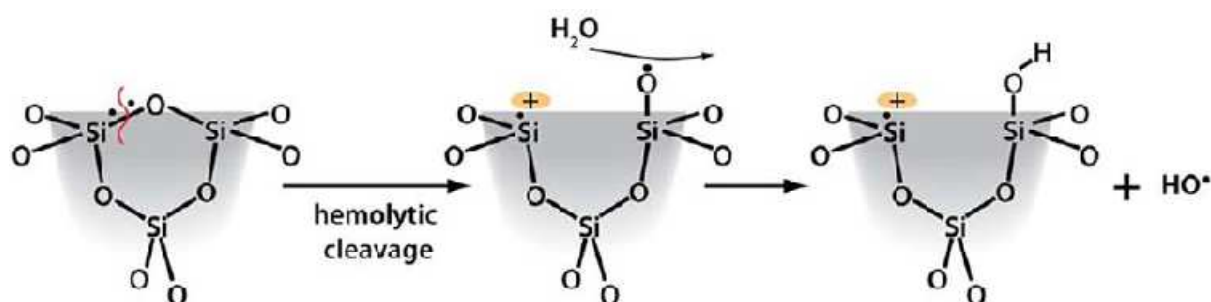


Figure 1 bis: strained three-membered ring role in the formation of oxygen radicals. Reproduced from ref¹³⁰

Wherefore, it has been admitted that the main cause of toxicity of silica nanoparticles is associated with the surface silanols¹⁸⁰ ($\equiv\text{Si-OH}$) that interact by hydrogen bonding to the cell membrane components¹⁸¹ or by electrostatic interaction with the phospholipids of the cell membrane¹⁸¹.

Consequently, mesoporous silica nanoparticles with high internal surface may decrease the extent of the silanols interacting with the cell membranes⁹⁸. For instance, non-modified 100 nm MSNs have shown no toxicity even when they are used with concentration above the dose needed for therapeutic treatments^{176,178}.

It was also shown that the toxicity of SiO₂ is cell-type dependent and that surface charge and pore size govern cellular toxicity¹⁷⁶.

In conclusion, silica nanoparticles were subject to many cytotoxicological investigations. Even though, the answer of the “absolute” biocompatibility of silica is far from being resolved

since silica nanoparticles are not made equally. In my opinion, studies are needed for punctual systems since MSN are used as multifunctional nanocarriers and the incorporated functions may drastically modify the toxicological behavior of the applied systems.

2.4. Targeting

In chemotherapy, the administering of cytotoxins with no specific target (and thus with high doses) will lead to strongly reduce their efficiency and cause many undesired effects by attacking healthy cells surrounding the tumor area.

Several studies have shown that optimally-shaped and sized nanoparticles with high physiological stability can passively accumulate in some cancer cells; this is based on the enhanced permeability and retention effect (EPR). This “natural” effect relies on the tendency of particles with small sizes of 100-200 nm (such as liposomes, nanoparticles) to take advantage of the leaky vasculature and poor lymphatic drainage of the tumor cells due to their rapid and active angiogenesis^{175,182,183}. However, EPR is not common for all types of tumors and presents a lack of specific targeting that may induce some resistance to administered drugs^{184,185} decreasing the therapeutic efficiency.

In this vision, the use of tumor cell specific targeting agents leads to more cellular uptake and less negative effect of the therapy. Tumor cells present molecular receptors in much higher concentration than the normal cells. Targeting relies on exploiting this overexpression to promote the MSN binding and recognition of tumor area. Among others, molecules or macromolecules such as Folic Acid (FA)^{186–196}, mannose¹⁹⁷, galactose¹⁹⁸, hyaluronic acid¹⁹⁹ were extensively investigated and proved to enhance significantly the uptake of MSNs due to the overexpression of the corresponding receptors on the cell membranes (10^4 - 10^5 receptor/cell) relative to normal cells.⁹⁸

2.5. Controlled release of cargo molecules

Mesoporous silica nanoparticles have the ability to hold appreciable amount of cargo molecules without altering the silica matrix due to their high surface area and pore volume. The loading extent of MSNs is higher than that of commonly used systems such as liposomes or polymer conjugates¹⁸³ since cargo molecules are retained inside the pores by non-covalent interactions (Van der Waals, H-bonding, electrostatic) allowing the loading capacity to be higher than the osmotic gradient loading⁹⁸.

Parent MSN have however very limited prospects if used as such. In fact, silica nanoparticles are not able to recognize the tumor cell without being modified by cell-recognition agents for targeting properties. On the other hand, even after incorporating targeting agents, the pores openings will lead to fast leakage of the payload (especially hydrophilic drugs¹³⁴) in the bloodstream. Consequently, the great advantage of payload protection offered by the nanocarrier is lost. Therefore, an optimized MSN must hold functions leading to a controllable release as well as targeting properties.

Controlling the delivery of cargo molecules from the pores of MSNs remains a primary goal in nanomedicine and a rally point of many scientists' efforts^{98,171,200–202}.

MSN are highly modular and can be chemically modified to respect many desired conditions. The functionalization of the MSNs by a variety of molecular or supramolecular moieties makes the delivery process highly controllable¹⁸³.

Controlled release systems are achieved by applying a mechanical control on the pore access^{169,203} to avoid any leakage of the cargo. This research area is very fruitful; tens of systems have been implemented by different groups (Jeffery Zink's, Victor Lin's, Thomas Bein's are the most active in the domain)^{89,97,166,168–170,175,180,204–210}. Three main strategies have been used to reach the controlled release: 1) Pore gating, 2) surface coating and 3) internal pore modification¹⁷⁵. Each strategy presents different systems that can be triggered by internal (lysosomal pH change, redox, enzymatic) or external stimuli (light^{208,211,212}, oscillating magnetic field²¹³, plasmonic heating²⁰²) (Figure 2).

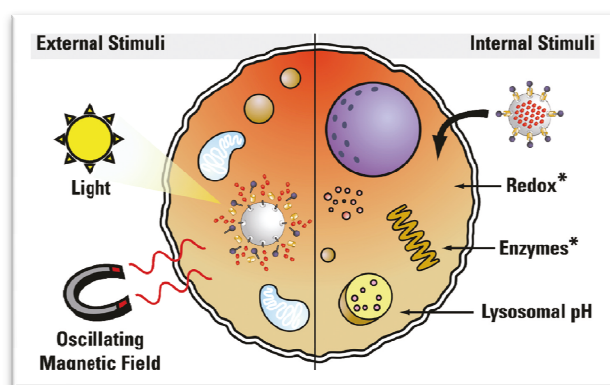


Figure 2: External and internal stimuli outlined for the activation of an internalized multifunctional MSN. Reproduced from ref¹⁶⁶

Pore gating consists of tethering a voluminous group to act as a gatekeeper without excitation. The voluminous group can be either a macromolecule (such as cyclodextrin^{214–218},

cucurbituril^{219–221}, rotaxane, pseudorotaxane^{222,223}, DNA linkers^{224–226},...) or metal nanoparticles (gold nanoparticles, iron oxide, cadmium sulfide²⁶,...). Upon specific stimulus, the gatekeeper is untethered allowing the cargo to exit.

Surface coating is a widely used strategy. It consists of blocking the pores accesses by coating the whole external surface of the nanoparticles with an organic phase (chitosan^{227–229}, polymers^{230–232}, supported lipid bilayer^{233–235}, ...) that is usually removed upon photolysis, phase transition, or enzymatic digestion in order to liberate the guest molecules.

The last main approach is the molecular modification of the inner pores by anchoring molecules owning coordinative bonds^{236,237}, electrostatic interactions²³⁸, disulfide linkage^{239,240}, that cleave upon pH variation or light excitation. An original work using the azobenzene as a nanoimpeller has been carried out by Zink's group consisting of the exploitation of the photoisomerization effect of azobenzene to retain in or expel out the cargo from the pores by a wagging motion made upon continuous light excitation^{208,211,212,241,242}. The afore-mentioned features transform the MSN into a “nanomachine” (Figure 3).

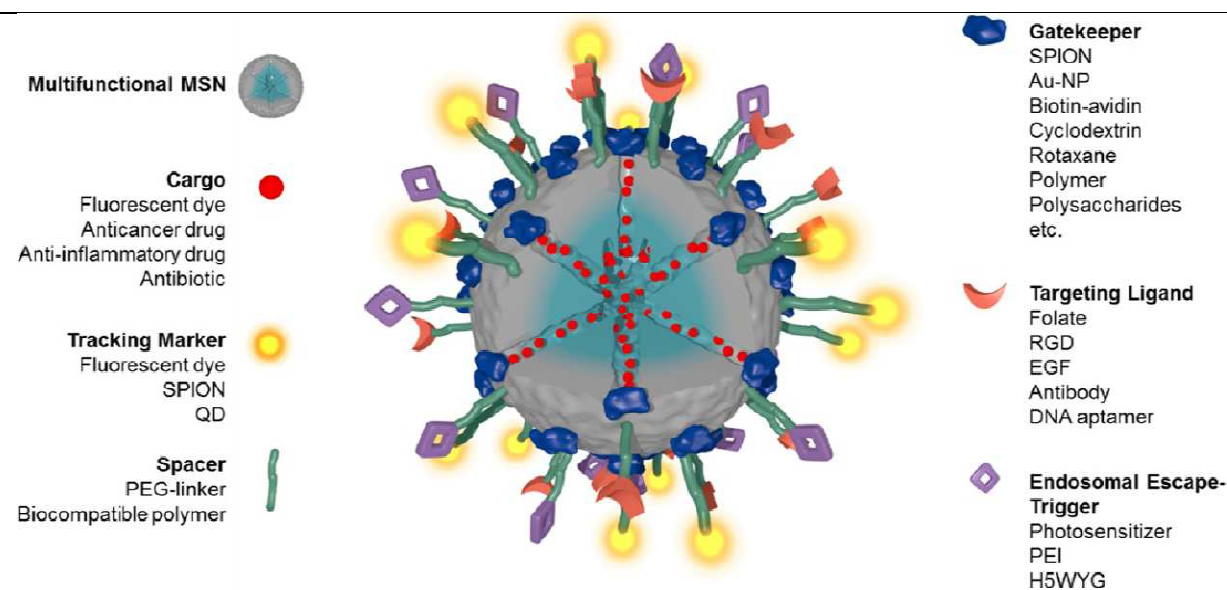


Figure 3: Schematic Illustration of a Multifunctional Mesoporous Silica Nanoparticle (MSN) Containing the Necessary Features for a Stimuli-Responsive Controlled Release. Reproduced from ref¹⁷⁵

The conception of the nanomachines requires a wise combination between the functional groups and the silica skeleton to generate the optimal morphology needed for the aimed study. Optimal nanomachines exhibit different features and thus contain several chemical functions. The incorporation of dense functional groups must be accompanied with a respect to the size,

the structuring and the shape which is a hard task due to the interference of the organic fragments with their ambient medium.

To date, the design of nanomachines is mainly based on the conventional functionalization methods, more precisely, the co-condensation of the functional moiety or the conventional grafting on the surface silanols. In this work, we will focus on the potential of the Click Chemistry, more specifically the CuAAC reaction in the conception of multiply-functionalized mesoporous silica nanoparticles as drug nanocarriers. The CuAAC reaction will offer a wide range of applications for the MSN since it allows incorporating homogeneously myriads of functions with less concern about their volume or their chemical nature. In this vision, a combination of functions can be easily integrated into the MSN according to the desired properties. For instance, clickable targeting agents, pore gates, tracking agents and inner pore modifiers, with different sizes can be incorporated to the MSN by CuAAC grafting.

Our work will highlight the conception of three light-triggered controlled release systems:

- MSNs based on a clicked azobenzene to prove the success of the click chemistry and to validate the impeller aspect.
- Nanomachines combining clicked azobenzene for controlled release and clicked folate for targeting.
- Nanomachines owning a clicked pH-sensitive pore gate sensitized by a clicked photoacid.

We will at first design “mono-clickable” MSN to highlight the ease of synthesis of impeller-based nanomachines; then “mutli-clickable” MSN will be conceived to make nanomachines based on the afore-mentioned bifunctional systems.

3. Monoclickable Mesoporous Silica Nanoparticles: Light-triggered clicked nanoimpeller for controlled release of cargo molecules

The main purpose of this part is to validate the CuAAC approach for the synthesis of nanomachines, using the well-studied nanoimpeller concept by introducing the azobenzene moieties by CuAAC on MSNs.

“Monoclickable” MSNs (bearing one type of clickable molecule) with different shapes and holding different concentrations of organic azide were synthesized. These nanoparticles were used as a platform for a light-induced nanomachine which showed good efficiency.

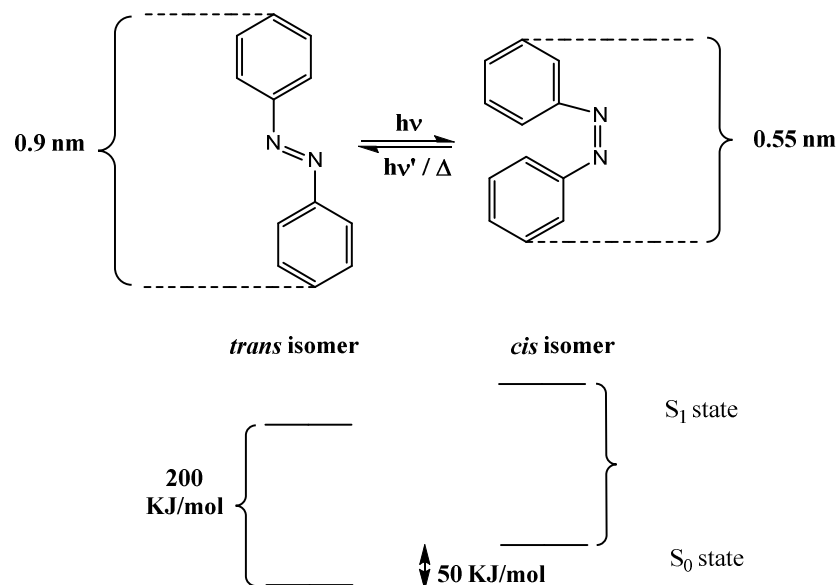
3.1. Concept of Nanoimpeller

This concept was introduced in 2006 by Zink’s group. Nanoimpeller system is a novel approach to remotely control the delivery of the molecules entrapped within the porous material. The up-to-date used nanoimpellers consist of azobenzene derivatives which properties inspired the concept of this system.

Azobenzene is a photo-responsive molecule that photoisomerizes (*cis* / *trans*) under light excitation at the appropriate wavelength. In the absence of light, azobenzene has naturally a dominant isomer (about 90% *trans*), thus presents a sufficient stereostability. These two key properties were used to give a controllable “impelling” behavior of the nanoparticles. After being covalently tethered to the silica matrix and without any excitation, the impellers block any access avoiding the unwanted exit of a payload. Under an appropriate stimuli (mainly, UV-visible light), they start a continuous dynamic wagging motion creating by their unbound terminus a disorder inside the pores assisting the release of the guest molecules.

3.2. Photochemical properties of azobenzene derivatives

The photoisomerization was first outlined by Hartley²⁴³. The *trans* to *cis* transition occurs by photochemical excitation and the reverse transition takes place either by spontaneous or also by photochemical pathway. Azobenzene’s *trans* conformer is thermodynamically more favored by a gap of about 50kJ/mol (Scheme 1).

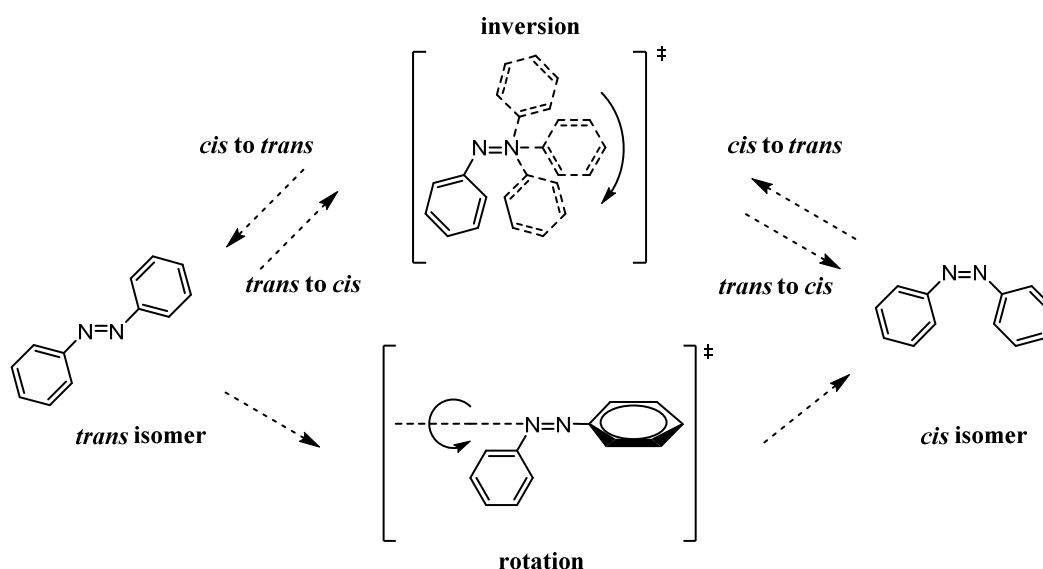


Scheme 1 : trans and cis isomers of azobenzene derivatives: size and difference of energy²⁴⁴.

3.3. Photoisomerization of Azobenzene

Azobenzene isomerization is a photochemical transformation presenting a HOMO-LUMO electronic transition from the fundamental state S_0 to either the first Singlet State S_1 ($n-\pi^*$) (when the electron transits from non-bonding orbital “n” to the first unoccupied orbital (π^*)) or the second excited Singlet state S_2 ($\pi-\pi^*$).

3.3.1. Mechanism



Scheme 2: photoisomerization mechanism of the azobenzene

The isomerization mechanism of the azobenzene was subject to many evolutions (Scheme 2). At first, it has been suggested that the *trans*-to-*cis* isomerization takes place by a rotation of an aromatic cycle around the N-N double bond plan²⁴⁵. Lately, it was found that an inversion of an aromatic cycle in the plan of the molecule also occurs²⁴⁵. Currently, the most plausible accepted mechanism passes through an inversion for the transition S_0 - S_1 and a rotation the transition S_0 - S_2 ²⁴⁶ and that the *cis*-to-*trans* return occurs only by inversion mechanism.²⁴⁷

Whatever the mechanism is, the motion that azobenzene is exhibiting upon light helped to design a very important strategy in controlled drug delivery.

3.3.2. Spectral properties of azobenzene

Figure 4 shows the UV-vis absorption spectra of the *trans* and *cis* isomers of one azobenzene derivative.

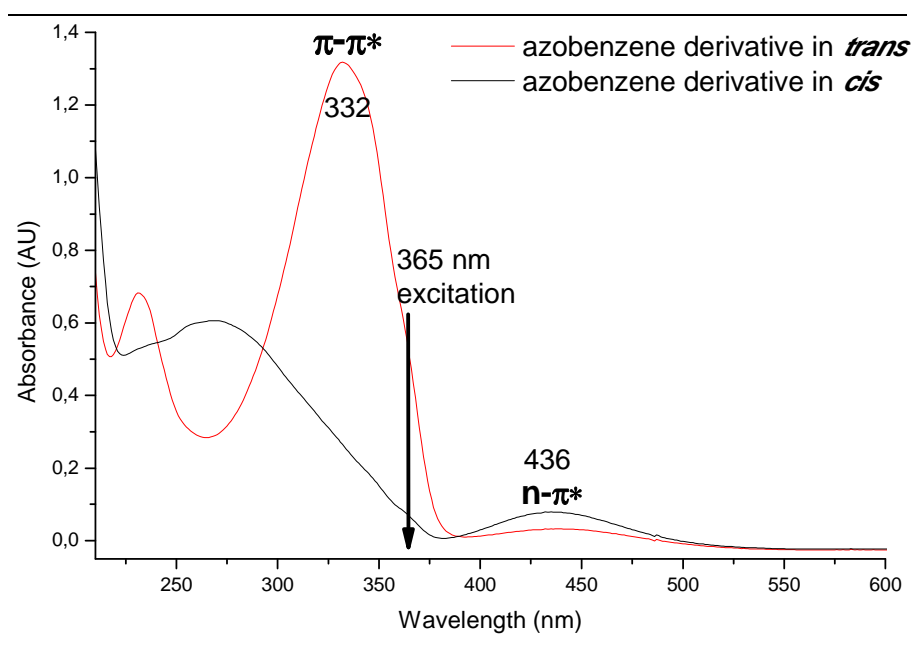


Figure 4: Extinction spectra of *trans* and *cis* isomers of azobenzene derivatives used in our system. The arrow denotes the excitation wavelength we have used for technical reasons.

The high absorbance at 332 nm corresponds to the strong π - π^* electronic transition while the absorbance at 436 nm is assigned to the weak n - π^* transition in addition to some azobenzene molecules in the *cis* form.²⁴⁸

Trans azobenzene isomerizes to *cis* when it is excited at a wavelength where the *trans* to *cis* transition is dominant over *cis* to *trans*. Thus, excitation in the π - π^* transition leads to an

overall *trans* to *cis* isomerization, while excitation in the $n-\pi^*$ transition leads to an overall *cis* to *trans* conversion. Both conversions depend on the absorption and the quantum yield at the corresponding excitation wavelength.²⁴⁹

UV-vis absorption spectrum of azobenzene shows a double absorption of both conformers (*trans* and *cis*) at a specific region of (about 390-400 nm). The excitation of the molecule at this wavelength makes its conformers permanently switch.

For technical reasons, we will use an excitation wavelength of 365 nm which is able to effectively photoisomerize azobenzene molecules.

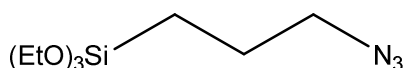
After having briefly presented the background that led the azobenzene to be used as a nanoimpeller, we switch to the practical work to validate the concept of the azobenzene *via* click chemistry (CuAAC) on silica platform.

3.4. Synthesis of Monoclickable Mesoporous Silica Nanoparticles

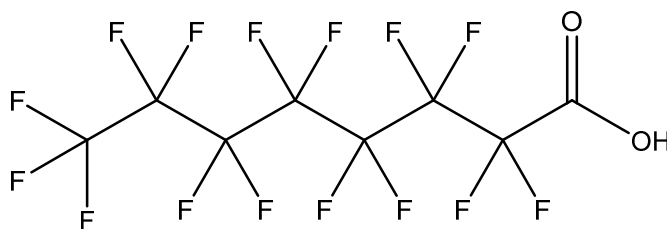
The synthesis of the nanoparticles was carried out as follows: In a typical synthesis, the silica source (TEOS), together with the clickable organosilane (AzPTES, 1%, 2% or 5% molar equivalent of total silica source) were added dropwise in a heated basic aqueous solution of the structure-directing agent CTAB (and eventually PFOA ($C_8HF_{15}O_2$) in the case of nanorods). After ageing, the resulted nanoparticles were repeatedly washed to remove the surfactant by ionic exchange ($H^+ \rightleftharpoons CTA^+$).

The nanoparticles will be denoted as (*x*% nanoshape with *x* is the concentration of organosilane and the shape is either spheres or rods *i.e.* 5% nanospheres, 5% nanorods).

The chemical composition was probed by vibrational spectroscopy (FTIR) and solid-state NMR. Electron microscopy, X-ray diffraction and N_2 -sorption were used to investigate the texture and morphology of the nanosized particles.



Azidopropyltriethoxysilane (AzPTES)



Perfluorooctanoic Acid (PFOA)

3.4.1. Characterization

FTIR spectra (Figure 5) show in all cases the typical profile of silica materials with the Si-O-Si (1050 cm^{-1}) and Si-OH (960 cm^{-1}) bands. In addition, the azide (N_3) band appear at 2105 cm^{-1} whose intensity increases with respect to the concentration of the co-condensed AzPTES (1%, 2% or 5%) (Figure 5, insets).

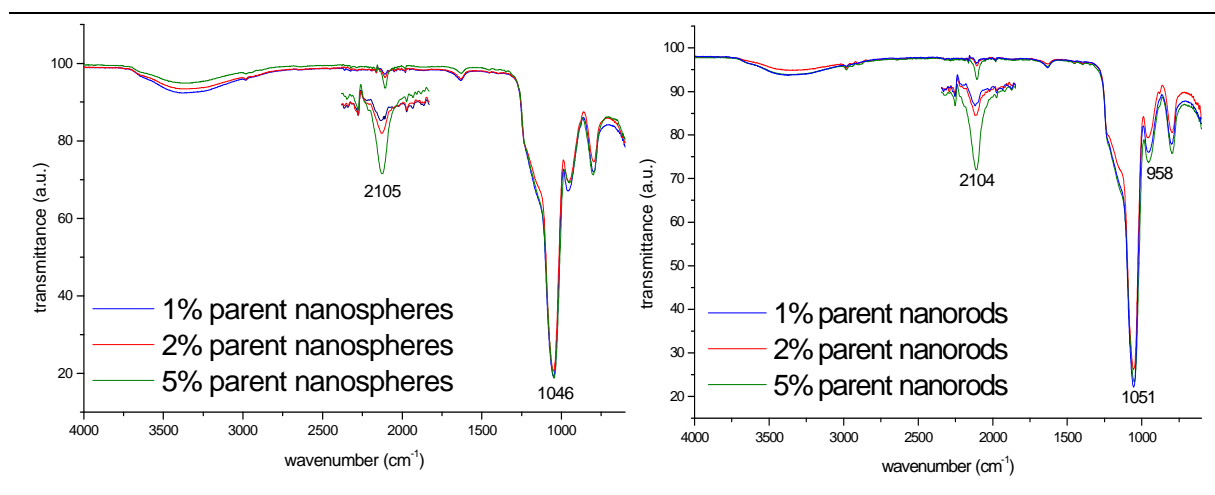


Figure 5: FTIR spectra of parent (left) nanospheres and (right) nanorods. Insets zoom on the zone $2050\text{--}2150\text{ cm}^{-1}$

Scanning electron micrographs show the primary textural properties of the obtained nanoparticles. Narrow sizes were obtained for the nanospheres ranging from 80 to 150 nm. (Figure 6 micrographs A1, B1, C1). As for the nanorods, SEM micrographs show for the three samples nanorods with close aspect ratio (3,5-4) with dimensions of *ca* $100 \times 400\text{ nm}$ (Figure 6 micrographs D1, E1, F1).

TEM micrographs (Figure 6 micrographs A2, B2, C2) show ordered pore channels for all the samples. The hexagonal structure of the nanospheres was seen by Fourier Transform of part of the image (Figure 6, insets). Micrographs D2, E2, F2 show nanorods with ordered pore channels with helical conformation as evidenced by alternate “fringes”. The fringes indicated by dark arrows correspond to (10) plane of the hexagonal structure, while the ones indicated by white arrows correspond to the (11) plane.

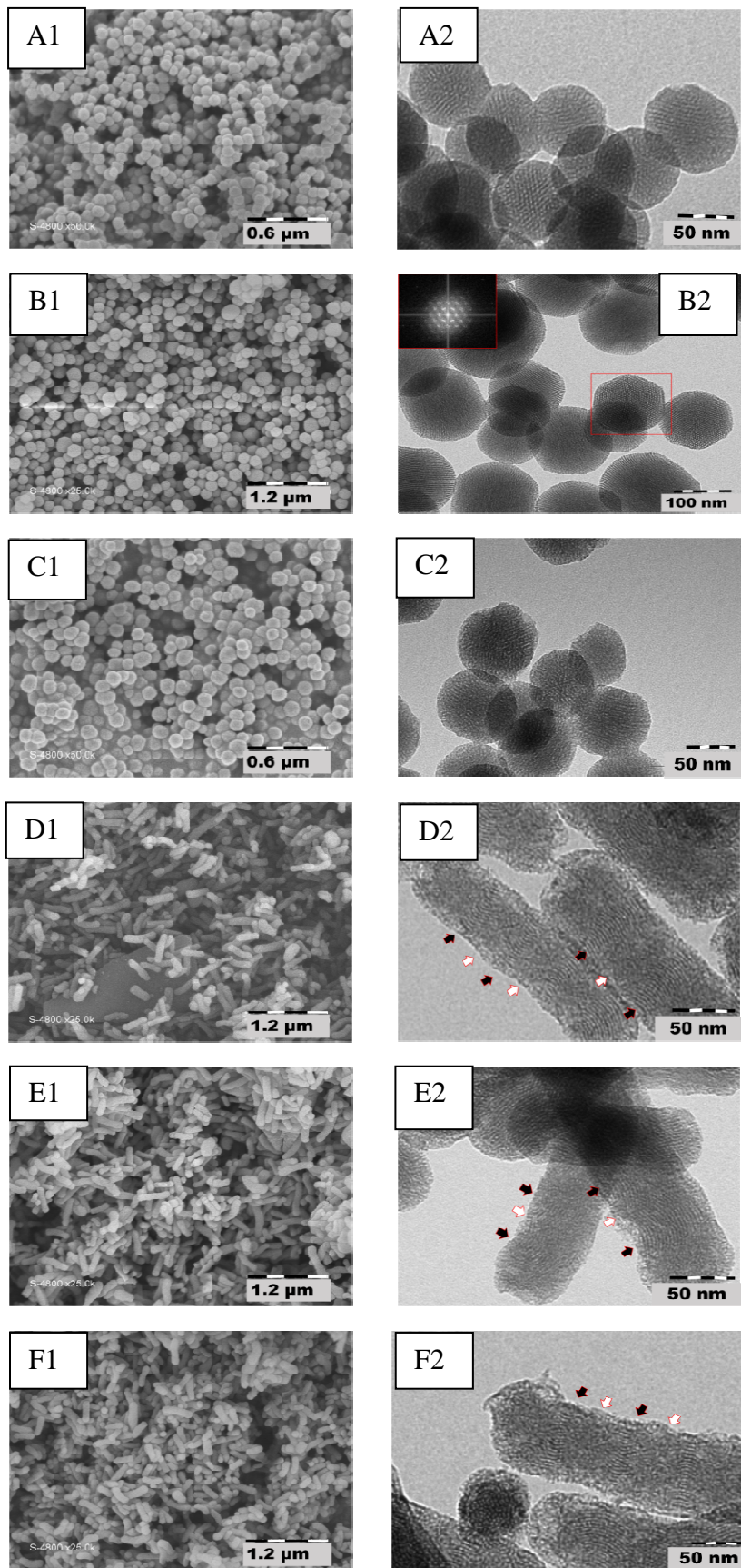


Figure 6: (Left) SEM and (right) TEM micrographs of the different nanoparticles: A1-A2, B1-B2, C1-C2 represent 1%, 2% and 5% nanospheres respectively. D1-D2, E1-E2, F1-F2 represent 1%, 2% and 5% nanorods respectively.

XRD patterns of each sample are shown in Figure 7 (A,B). The diffractograms are typical of the $P6mm$ group and show three resolved peaks corresponding to the planes that are indexed (10), (11) and (20) in the zone of $2\theta = 2$ to 5° . These peaks confirm the 2D-hexagonal structure of the nanoparticles suggested by TEM. Previous studies (helical rods) have shown that the use of a co-surfactant has no change on the structuring of non-functionalized nanoparticles, however, in our case the patterns of the nanospheres are sharper and better resolved than nanorods exhibiting the smallest d-spacing (3.82-3.87 nm).

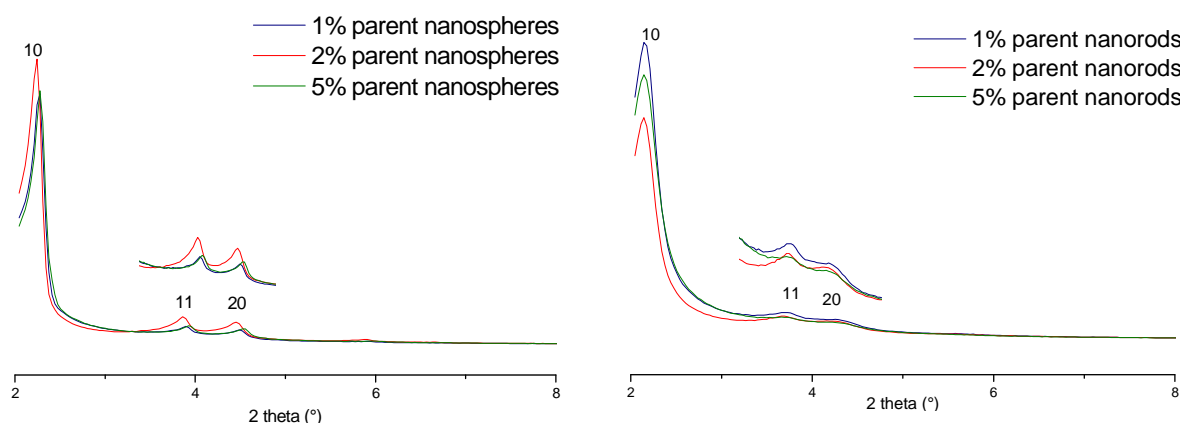


Figure 7: XRD-patterns of parent (left) nanospheres and (right) nanorods

N_2 physisorption for the parent nanoparticles indicate a type IV isotherm for the different nanoparticles (Figure 8). An inflexion typical for the monolayer-multilayer adsorption is seen at higher relative pressure ($P/P^\circ = 0.35$) for 1% and 2% nanoparticles than for 5% nanoparticles ($P/P^\circ = 0.28$) suggesting smaller pore sizes for the formers. The uptake at saturation which is the highest for 2% nanoparticles indicates the most important pore volume amongst the synthesized series (Table 1 bis).

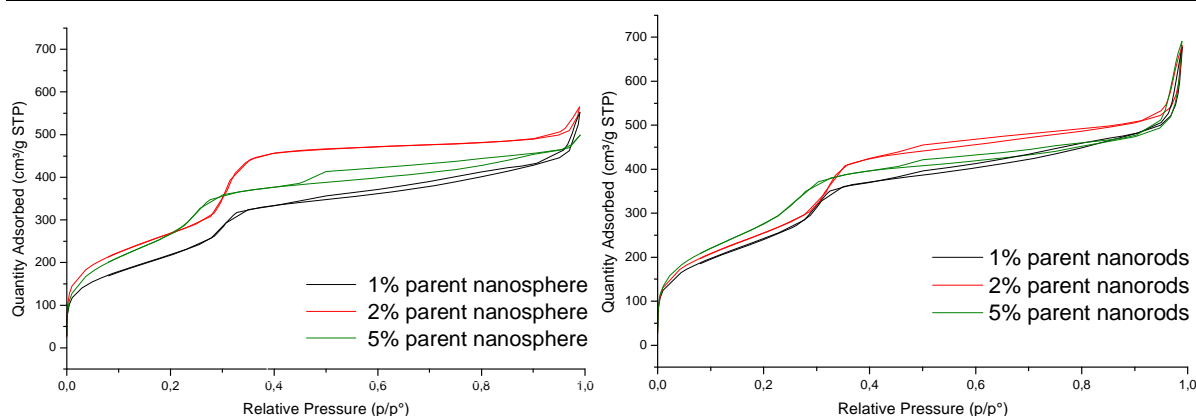


Figure 8: N_2 sorption isotherms for (left) parent nanospheres and (right) parent nanorods

The previous result concerning the most accessible surface area in the case of 2% clickable nanoparticles suggests also that, in this case, the functions are likely more localized at the external surface. Further investigations are needed to conclude.

The successfully characterized monoclickable mesoporous silica nanoparticles will be subjected to click reactions with azobenzene moieties in order to confer them the motion character.

3.5. CuAAC reaction on monoclickable nanoparticles

In order to mechanize the clickable MSNs, we decided to anchor azobenzene fragments by CuAAC reaction and test the functionalized nanoparticles as a controlled drug delivery system (Figure 9). CuAAC reaction was performed between azide-bearing MSNs and ethynylazobenzene using the conventional catalytic system (copper sulfate and sodium ascorbate in water and *t*-butanol).

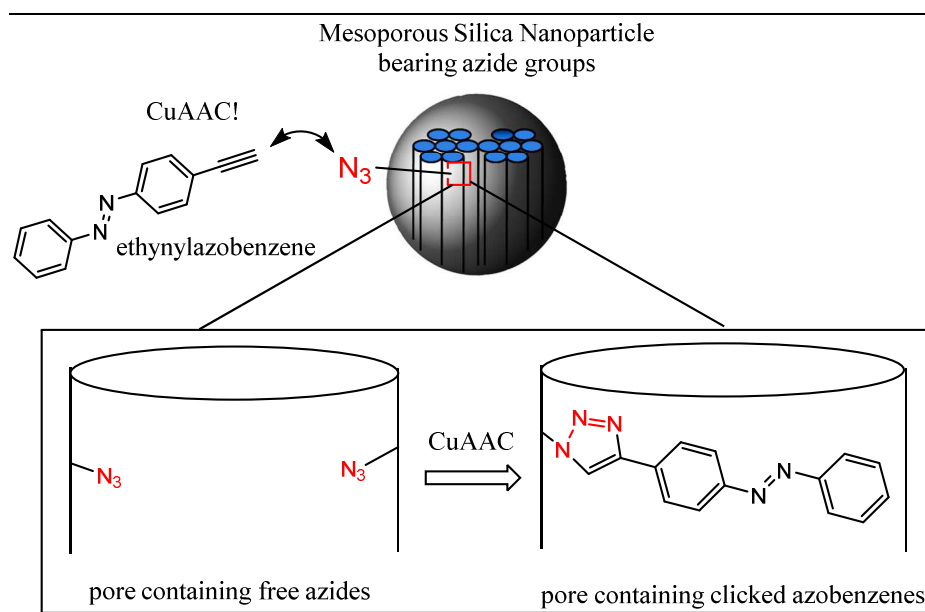


Figure 9: CuAAC reaction between ethynylazobenzene and azide pending groups on the MSNs

The success of the click reaction was monitored by vibrational and UV-vis spectroscopies (FTIR, UV-vis).

FTIR spectra (Figure 10, Figure S1) show in all cases an almost total vanishing of the band at 2105 cm^{-1} corresponding to the azide functions indicating the reactivity of (N_3) towards the ethynyl group of the azobenzene.

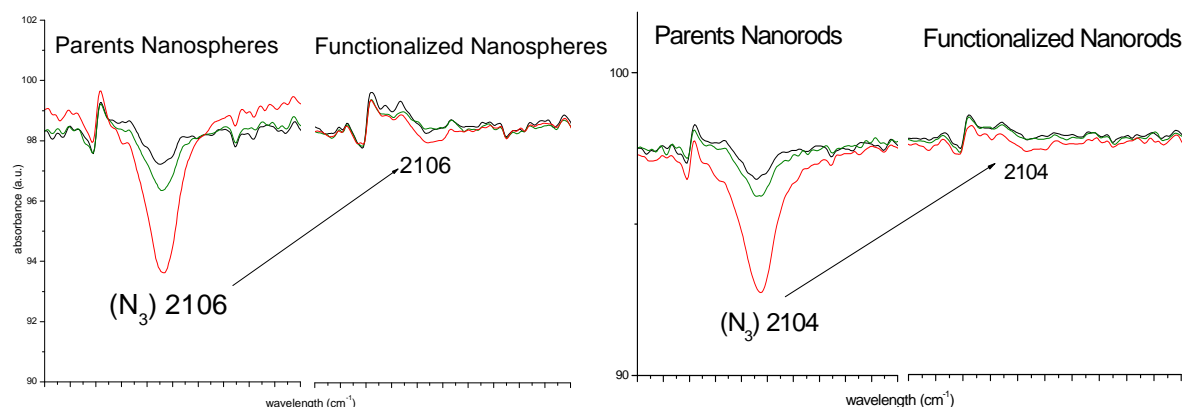


Figure 10: Zoom on FTIR spectra of (red) 5%, (green) 2% and (black) 1% - (left) nanospheres and (right) nanorods before and after CuAAC reaction with ethynylazobenzene.

The quantification of the amount of the clicked azobenzene was done from the UV-vis spectra. The concentration of the clicked azobenzene being dependant of the molar extinction coefficient (ϵ), it is practically difficult to measure the latter for an azobenzene clicked on a material. In addition, the ethynylazobenzene (used in the CuAAC on the nanoparticles) may have a different ϵ to the clicked molecule because of the different electronic properties of the ethynyl and the triazole groups (before and after click reaction). In this optic and in order to have the closest system to a clicked azobenzene, we have clicked in solution, the ethynylazobenzene with a non-conjugated alkyl chain (6-azidohexane) (Figure 11). This molecular clicked azobenzene (denoted hexane@azobenzene) should give a close molar extinction coefficient (ϵ) to the clicked azobenzene on a material. Calculations gave a molar extinction coefficient of about $22260 \text{ M}^{-1}\text{cm}^{-1}$ in ethanol with an absorption maximum at 351 nm. (figure S2)

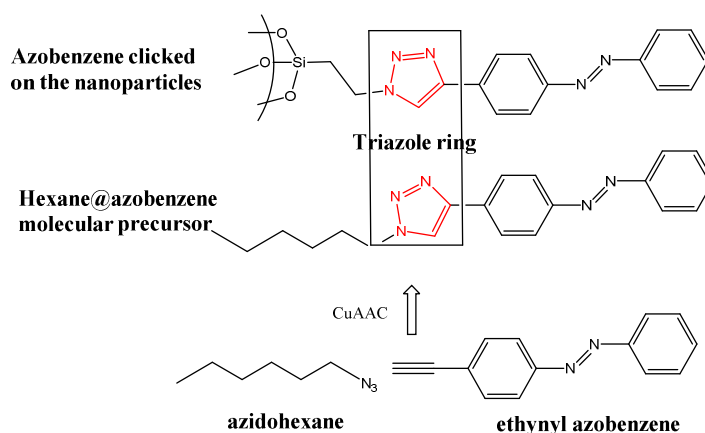


Figure 11: synthetic route hexane@azobenzene precursor.

At first, a control experiment was carried out by incubating the nanoparticles bearing azide functions in the same conditions of the CuAAC reaction but with azidoazobenzene instead of ethynylazobenzene to check if any molecule will be non-covalently adsorbed on the surface. After 24 h, only 3 washings by acetone were sufficient to observe a clear supernatant. After drying, a UV-vis spectrum was recorded (Figure S3), showing no absorption of azobenzene molecules thus indicating that the washings were complete. This result confirms that the upcoming absorption profiles after click reaction comes only from a covalently linked azobenzene.

UV-vis spectra (Figure 12) are measured for a suspension of the different nanoparticles with a concentration of 2.15 mM in ethanol. All the nanoparticles exhibit prominent absorption bands (λ 237, 350 and 460 nm) matching the molecular precursor and validating that azobenzene was successfully anchored on the nanoparticles by a CuAAC reaction (vanishing of azide peak in FTIR). Evidently, the absorbance of the clicked azobenzene increases with the concentration of clickable functions. This increase is more important respectful to the concentration increase in the nanospheres case especially for 5% nanoparticles where the concentration of azobenzene in the nanospheres is clearly higher than that for the nanorods.

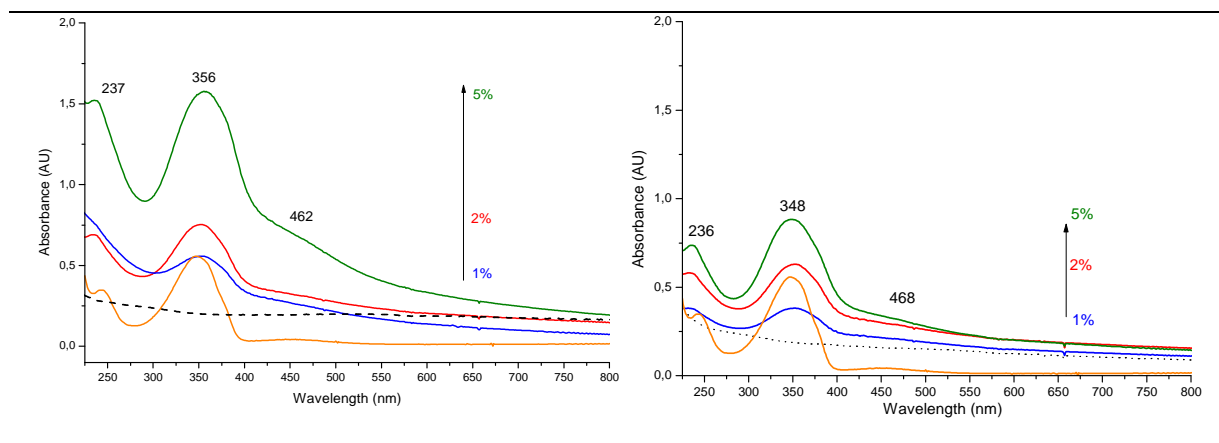


Figure 12: UV-vis spectra of the clicked (left) nanospheres and (right) nanorods. Black dashed lines denote the profile of corresponding parent nanoparticles; the orange spectrum corresponds to the hexane@azobenzene molecule.

The following table shows the functionalization rate on the different nanoparticles. This rate is calculated with the hypothesis that the organosilylated azide was completely co-condensed with the TEOS giving exactly 1, 2 and 5% of clickable functions over the nanoparticles.

[clickable functions] (%)	Functionalization (mmol/g) (conversion %)	
	Nanospheres	Nanorods
1%	0.08 (100%)	0.06 (78%)
2%	0.11 (78%)	0.09 (63%)
5%	0.23 (63%)	0.13(37%)

Table 1: Functionalization rate of monoclicked nanoparticles calculated according to Beer-Lambert relation from the UV-vis absorption spectra

The overall decrease of conversion while increasing the concentration of clickable functions is not surprising; the co-condensation of the clickable organosilane with the main silica source lead to a homogeneous distribution of the azides all over the particles. Some functions will not be accessible (oriented inside the walls) and this behavior increases with the concentration of function. On the other hand, the post-functionalization serves the most accessible functions: the external surface including the pores accesses are preferentially functionalized. Thus, the first grafted azobenzenes tend to block partially the access of the pores to the remaining molecules, which have less chance to enter deep inside and to be clicked.

The functionalization rate of the nanospheres is clearly more important than that of the nanorods. Presumably, the use of lipophobic PFOA as co-surfactant has induced more azidopropyl groups to be oriented into the walls making them inaccessible.

N₂ sorption studies: Isotherms of the clicked nanoparticles (Figure 13) exhibit the same profile as the parent nanoparticles (Figure 8) corresponding to a mesoporous material. Lower accessible surfaces and pore volumes are displayed; the hysteresis seen for 1% nanospheres is due to a larger distribution of the pores after the click reaction. This can presumably comes from eventual aggregation participating in the formation of interparticular pores.

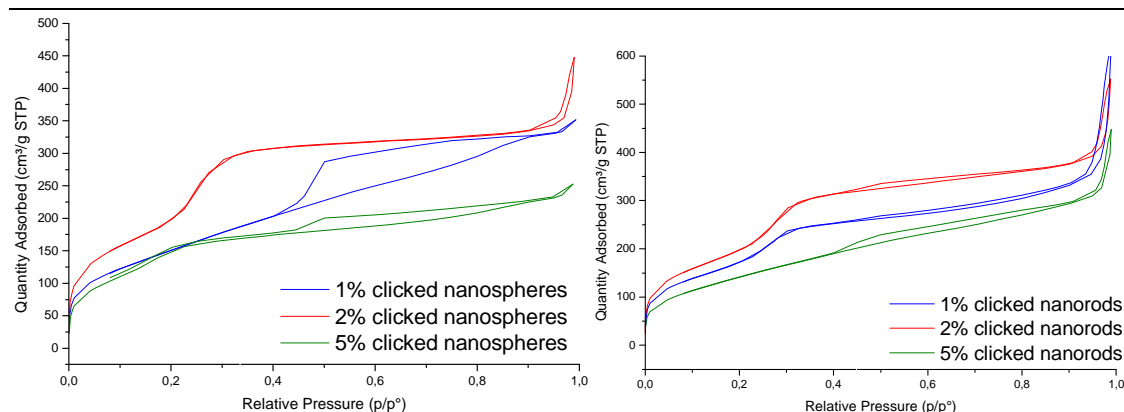


Figure 13: N₂ sorption isotherms of clicked (left) nanospheres and (right) nanorods

	Parent nanoparticles		Clicked Nanoparticles	
	BET Surface Area (m ² /g)	Pore Volume (cm ³ /g)	BET Surface Area (m ² /g)	Pore Volume at saturation (cm ³ /g)
nanospheres				
1%	998	0.51	565	0.54
2%	1144	0.87	903	0.52
5%	1162	0.77	558	0.39
nanorods				
1%	1012	1.04	730	0.52
2%	1035	1.05	897	0.58
5%	1154	1.07	530	0.46

Table 1 bis: textural data for the parent and clicked nanoparticles

XRD patterns (Figure 14) show a conservation of the 2D-hexagonal structure after the click reaction. However, a slight decrease in the lattice parameter occurs independently of the shape of the nanoparticles (Table 1 bis). After click reaction, both 2% nanoparticles in addition to 1% nanospheres conserve their three peaks indicating the preservation of a long-range structuring. In the other cases, only the Bragg peak was conserved after the same reaction conditions, which indicates a partial loss of the long-range order.

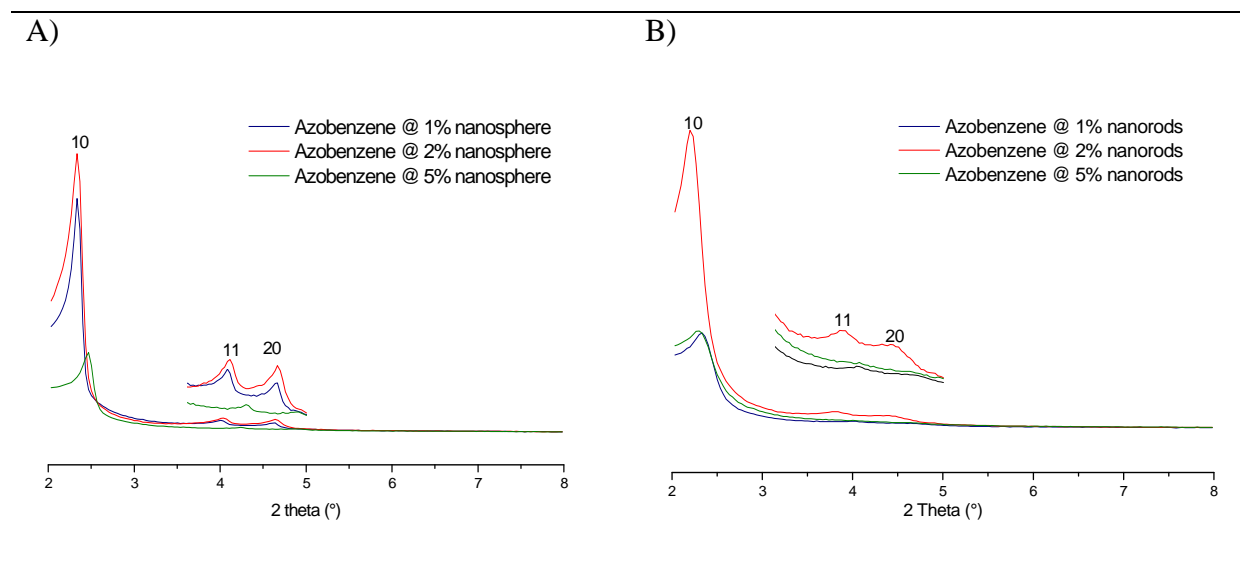


Figure 14: XRD-patterns of clicked (A) nanospheres and (B) nanorods

[clickable functions]	Parent nanoparticles		Clicked nanoparticles	
	d-spacing (d ₁₀₀)	Lattice parameter (nm)	d-spacing (d ₁₀₀)	Lattice parameter (nm)
nanospheres				
1%	3.82	4.42	3.72	4.38
2%	3.87	4.48	3.72	4.38
5%	3.82	4.42	3.52	4.15
Nanorods				
1%	4.04	4.66	3.71	4.36
2%	4.04	4.66	3.92	4.62
5%	4.06	4.68	3.79	4.46

Table 2: structural data (obtained by XRD) for the different parent and functionalized nanoparticles. Lattice parameter *a* is calculated for a 2D- hexagonal structure as $a = d_{100} (2/3)^{1/2}$

3.6. Cargo loading

A solution of rhodamine B in water (5 mM, 1 mL) was added to 3 mg of functionalized nanoparticles. The latter were sonicated for 10 minutes and stirred vigorously at room temperature for 24 hours in the dark. After successive washings with water (about 20 times centrifugation 22000 rpm, 5 mn) to eliminate the rhodamine B which is not retained in the pores, the particles were kept overnight for drying.

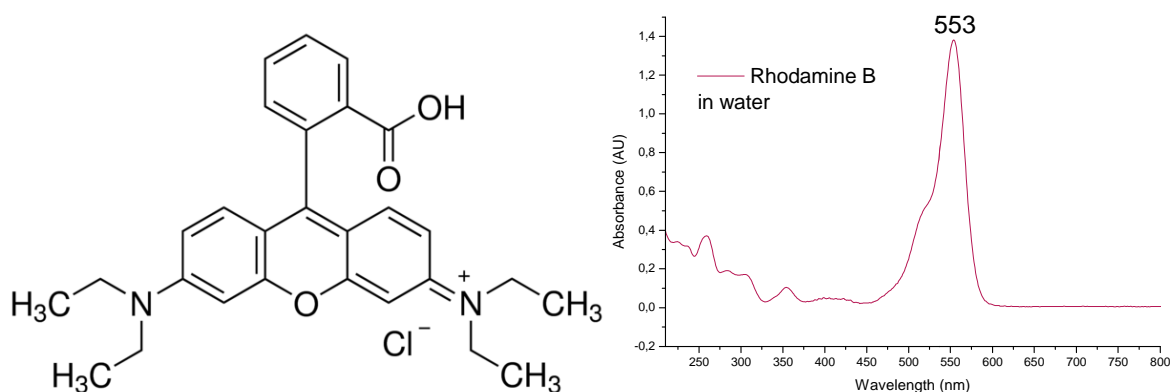


Figure 15: Rhodamine B (left) structure and (right) UV-vis absorption profile in water

3.7. Release Experiments

The nanoparticles were placed in a *cuvette* and slightly “ground” with the spatula to improve the diffusion of the dye. Distilled water was carefully added to ensure that no particles are floating into the aqueous phase (the analyzed zone, to not skew the results). The nanoparticles

were kept from one to two hours without any excitation and UV-vis spectra were recorded every 15 to 30 min to monitor any eventual leakage of the dye.

After ensuring that the cargo molecules are well retained within the pores, we placed the cuvette under 365 nm light excitation (Figure 16) and UV-vis spectra of the solution were recorded at different time intervals to track the released rhodamine B in solution. The absorbance of the rhodamine B was calculated as the difference between its maximum absorbance at 553 and a wavelength where it does not absorb (600 nm) (Figure 17).

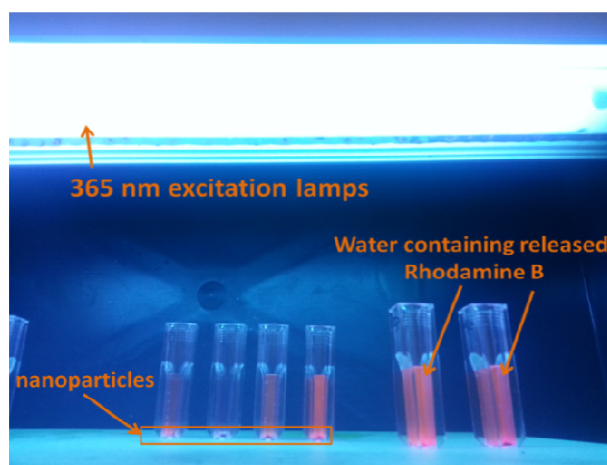


Figure 16: Release experiment under 365 nm excitation lamps. The cuvettes contain released rhodamine B in water after 3 h of excitation had started.

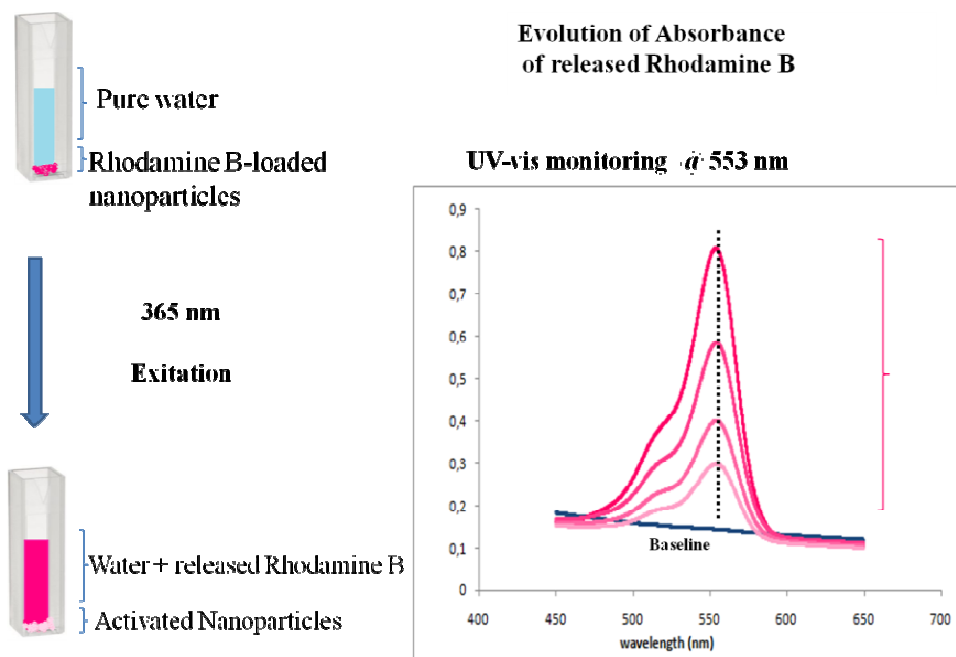


Figure 17: different steps of excitation and monitoring the release of Rhodamine B from the azobenzene-functionalized nanoparticles

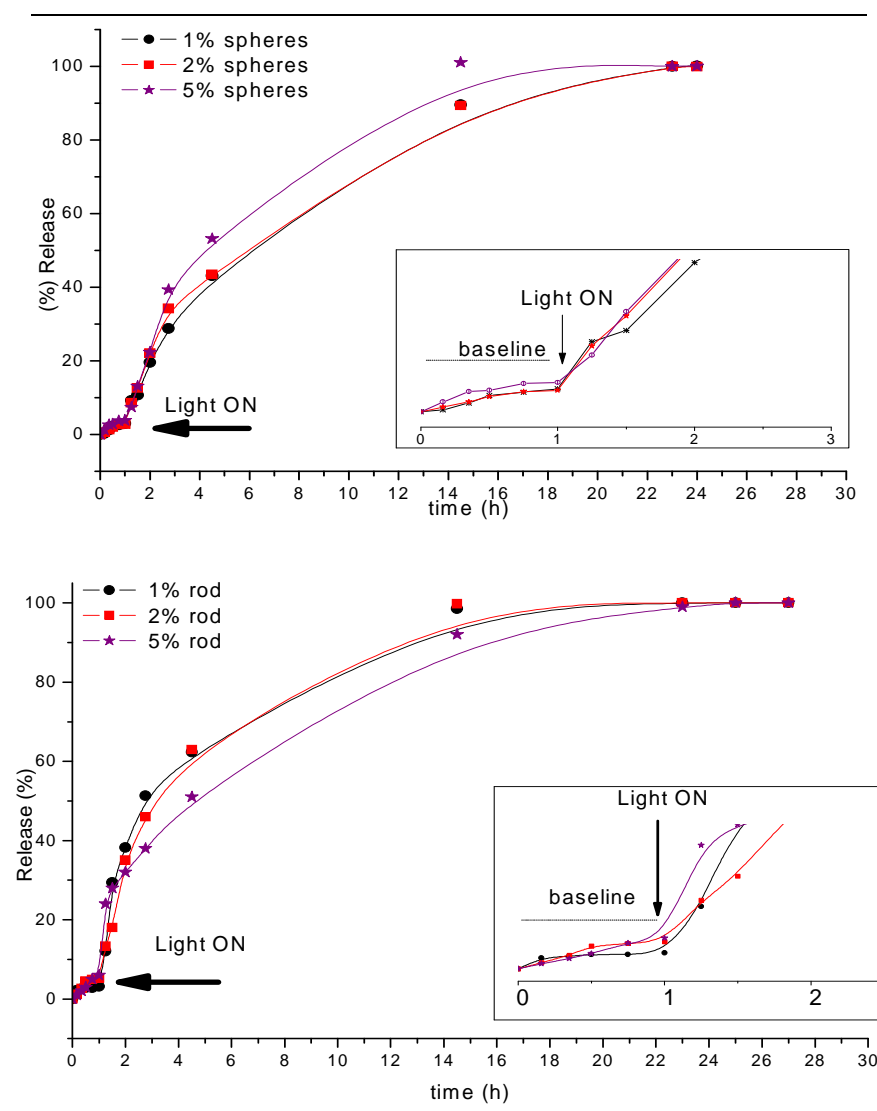


Figure 18: release profiles of rhodamine B from the azobenzene functionalized (up) nanospheres and (down) nanorods. Inset: zoom on the base line and the first hour of excitation

Nanospheres and nanorods show an exponential release profile (figure 18). Before light was turned ON they exhibit a flat baseline indicating that very little leakage occurs (maximum leakage 3%). Once the excitation started, a significant increase of the release was seen. The release pursued its progressive increase to reach, after 4 h of excitation, about 60% of released amount for 1% and 2% clicked and 50% for 5% clicked nanoparticles. Afterwards, the expelling percentage tends to decelerate to reach about 90% of the released amount after 14 hours of excitation. Beyond this, the maximum of release is attained after about 22 h.

The loading capacity of the nanoparticles is calculated as the weight of rhodamine (mg) retained by mg of nanoparticles. Figure 19 shows the release profile relative to the uptake amount for each sample. Both 2%-clicked nanorods and nanospheres exhibit the best loading

capacities with 4.5% and 4% respectively. The worst loading capacity goes to 5%-clicked nanoparticles with 1.5% and 1.6% for the nanospheres and the nanorods presumably due to hindered pores outlined by the lowest pore volume (Table 1 bis). 1%-clicked nanorods (3.2%) and nanospheres (2%) have medium values; this can be explained by the fact that less azobenzenes were incorporated inside the pores than 2%-clicked nanoparticles and thus, not reaching the optimal threshold to retain as much as 2%-nanoparticles. The balance of functionalization rate, the textural properties and the available space led to the best loading capacity in the 2% clicked nanoparticles. It is noteworthy that the evolution of the release percentage is in respect with the physisorption results (S_{BET} and pore volume) and that after more than 20 hours of irradiation some photobleaching of the dye may have occurred so the maximum loading capacity is in fact higher than the calculated one.

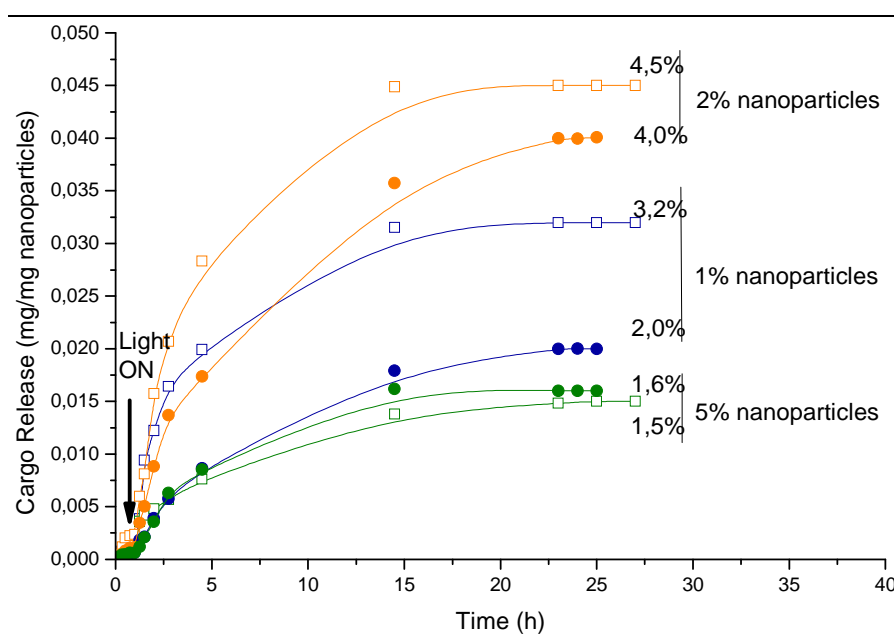


Figure 19: Release profile relative to the maximum uptake of rhodamine B for the clicked (spheres) nanorods and the (empty dots) nanospheres

3.8. Conclusion

In conclusion, the successful release of rhodamine B upon light excitation from mesoporous silica nanoparticles with clicked azobenzene has validated the CuAAC approach in making efficient nanomachines with impelling system. However, multifunctionalization of nanoparticles is needed in order to gain specificity to targeted cells or to tune the excitation properties (two-photon excitation) depending on the therapeutic needs. For instance, Croissant

*et al*²⁵⁰ have synthesized bifunctional nanoparticles by co-condensing an azobenzene derivative with a 2-photons sensitizer (antenna): A FRET phenomenon occurred between these two moieties inducing an impelling behavior of the azobenzene (Figure 20). This system showed very interesting results in *in vitro* assays.

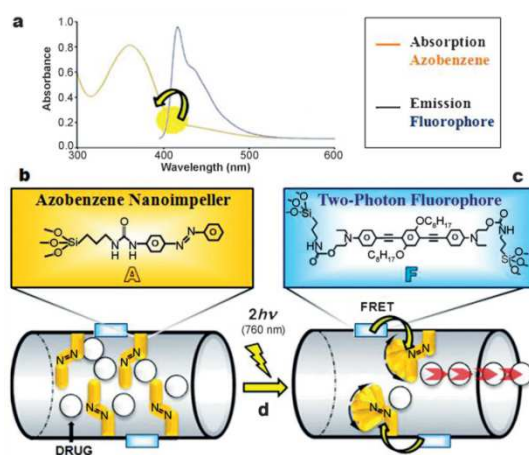


Figure 20: azobenzene photoisomerization by FRET from 2hv fluorophore on mesoporous silica nanoparticles. Adapted from ref ²⁵⁰

4. Bisclickable Mesoporous Silica Nanoparticles: A multifunctional platform for selected applications in cancer cell treatment

After validating the use of the CuAAC reaction on monoclickable MSN to form nanomachines based on the concept of clicked nanoimpeller, we will try to prepare multifunctional MSNs and use them as multi-clickable devices to anchor diverse molecules for selected properties.

4.1. Synthesis of the bisclickable nanoparticles

In a typical synthesis of monodisperse MCM-41 type nanoparticles, the silica source (TEOS), together with the clickable organosilanes bearing azide and alkyne (2% or 5% molar equivalent of total silica source, each) were added dropwise in a heated basic aqueous solution of the structure-directing agent CTAB (and eventually PFOA in the case of nanorods). After ageing and drying, the surfactant was extracted in acidic ethanol by ionic exchange ($H^+ \rightleftharpoons CTA^+$).

4.2. Characterization of the nanoparticles

FTIR spectra (Figure 21) exhibit a simple profile for the different parent bisclickable nanoparticles. All spectra showed mainly vibrations bands typical for Si-O-Si ($1000\text{--}1100\text{ cm}^{-1}$) and Si-OH (943 cm^{-1}). The azide (N_3) stretching peak is clearly shown at 2103 cm^{-1} corresponding to the anchored AzPTES group. Other weak peaks appear at ($1200\text{--}1450\text{ cm}^{-1}$) typical for C-C and C-N vibrations in addition to the CH_2 bands seen between 2800 and 3000 cm^{-1} .

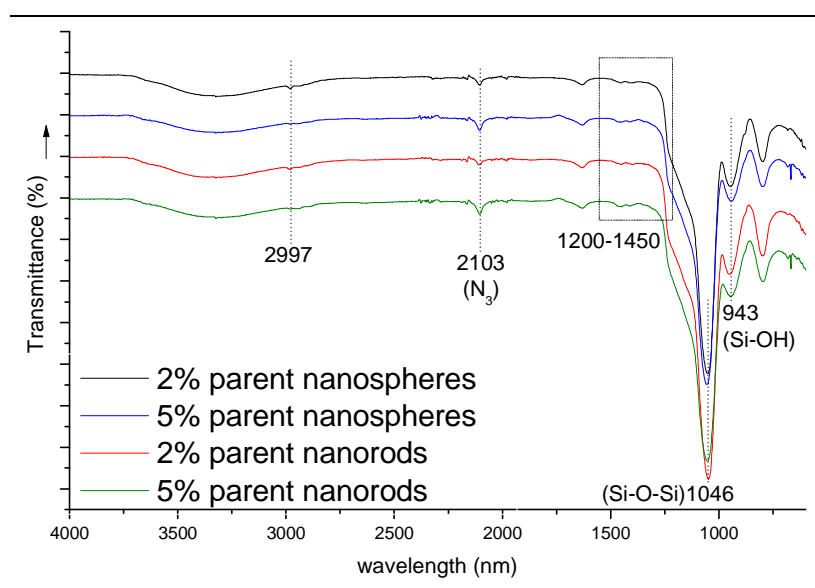


Figure 21: FTIR spectra of parent bisclickable nanoparticles

At low concentration, the H-C_{sp} stretching of the terminal alkyne ($\text{C}\equiv\text{C-H}$) could not be identified in FTIR. However, terminal (asymmetric) $\text{C}\equiv\text{C}$ vibration is seen by Raman spectroscopy (Figure 22). A prominent peak at 2130 cm^{-1} is seen for bis 5% parent nanospheres and nanorods confirming the anchoring of the **Prec-Alk** within the silica matrix.

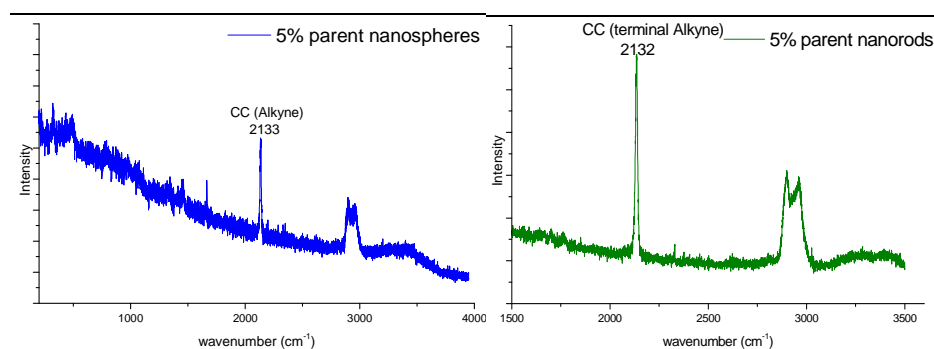


Figure 22: Raman spectra of parent (left) nanospheres and (right) nanorods bearing 5% clickable functions.

Textural analyses were carried out using scanning and transmission electron microscopy and X-ray diffraction techniques.

SEM micrographs (Figure 23) show nanospheres of 90 to 160 nm in diameter and aspect ratios ranging from 1 to 1.7 for 2% bisclickable nanospheres and diameters from 90 to 130 nm with aspect ratios ranging from 1 to 1.4 for 5% bisclickable nanospheres. As for the next two samples, nanorods with aspect ratio ranging from 3.0 (128×42 nm) to 4.5 (170×38 nm) for 2% bisclickable nanorods and from 3.5 (143×41 nm) to 4.5 (177×41 nm) for 5% bisclickable nanorods are seen. TEM micrographs show ordered pore channels for nanospheres and their hexagonal structure was deduced from Fourier Transform of part of the image (inset). Nanorods showed ordered pore channels with helical conformation evidenced by alternated “fringes”. The fringes indicated by dark arrows correspond to (10) plane of the hexagonal structure, while the ones indicated by white arrows correspond to (11) plane.

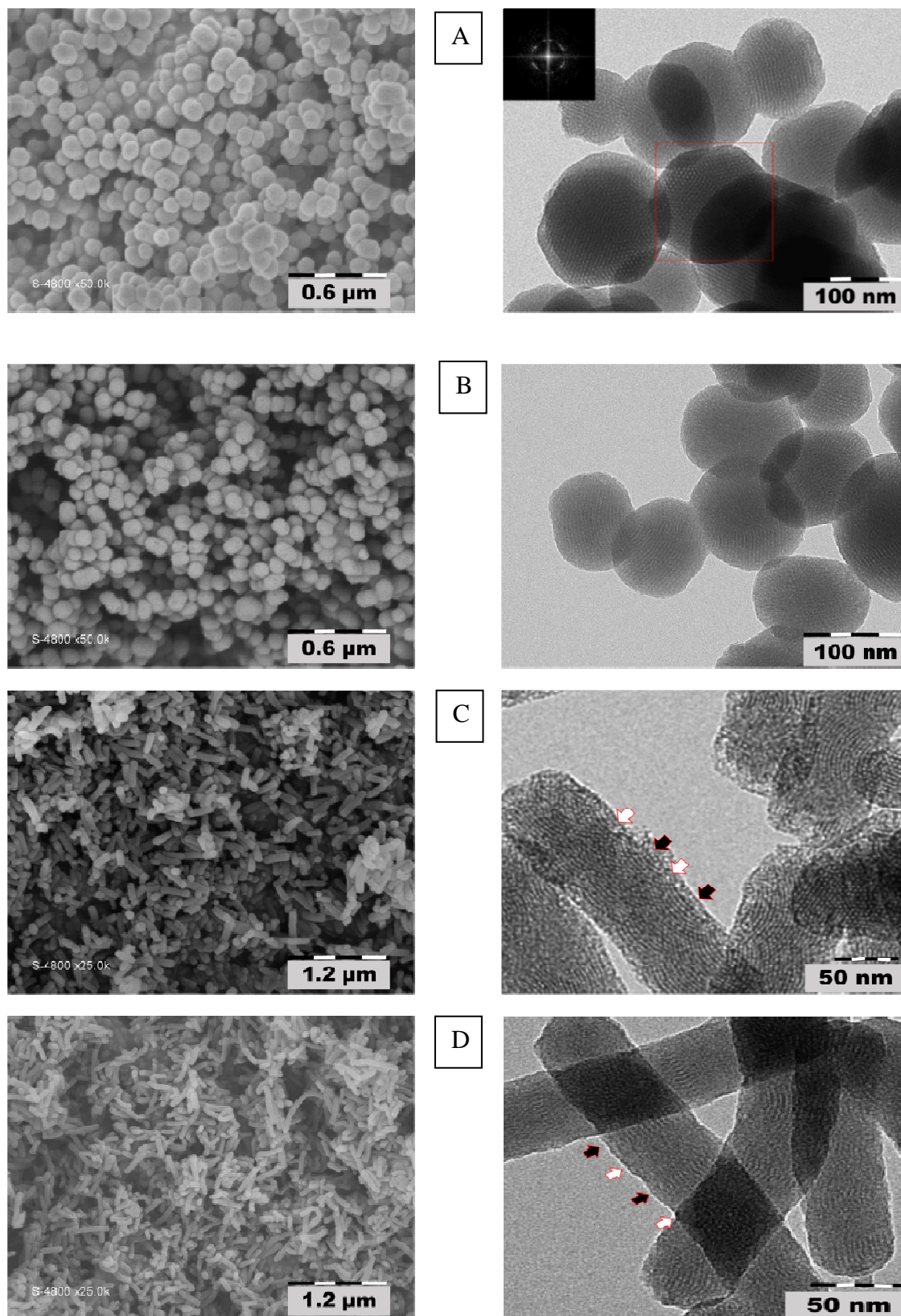


Figure 23: SEM (left) and TEM (right) micrographs of the parent bisclickable nanoparticles: nanospheres a) 2% b) 5% and nanorods c) 2% and d) 5%

X-ray diffraction confirms the 2D-hexagonal structure of the nanoparticles indicated by three main peaks corresponding to the (10), (11) and (20) plans (Figure 24). Nanospheres exhibit the same d-spacing while 2% nanorods present slightly higher distances compared with 5% nanorods. However, both nanorods show longer distances than nanospheres. Values of d-spacing and cell parameters are summarized in table 3.

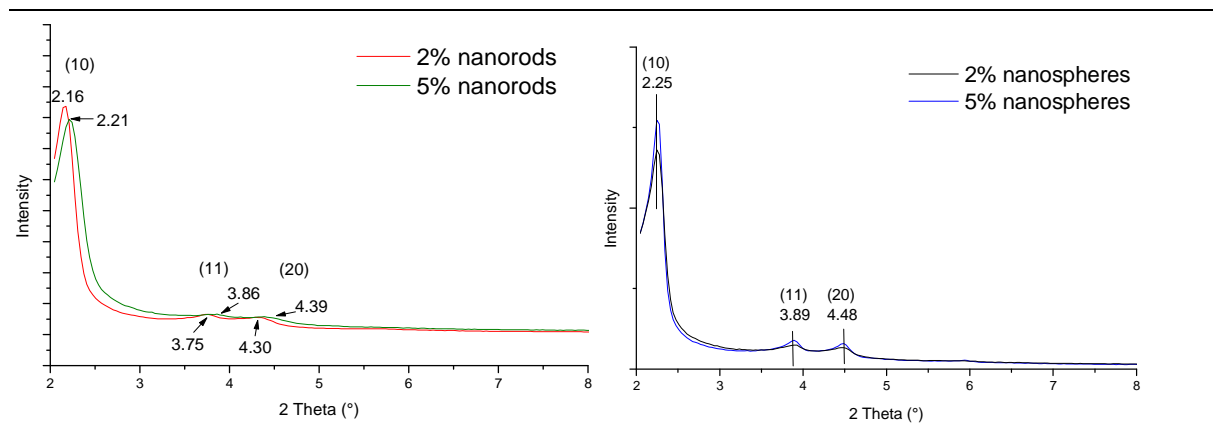


Figure 24: X-ray diffraction patterns for parent nanoparticles

	d_{10}	Cell parameter $a = (2d_{10}) 3^{-1/2}$	BET surface area (m^2/g)	Uptake at saturation (cm^3/g)	Total pore volume (cm^3/g)
2% nanospheres	3.86	4.46	1104	476	0.76
5% nanospheres	3.86	4.46	1087	375	0.67
2% nanorods	4.02	4.64	1198	500	0.79
5% nanorods	3.93	4.54	1164	422	0.69

Table 3: structural and textural data of the different parent nanoparticles.

N_2 physisorption isotherms of the four parent nanoparticles are shown in figure 25. The shape of the different isotherms is typical of a mesoporous material with a IUPAC's type IV adsorption branch. Indeed, the isotherms exhibit an inflexion of the N_2 adsorbed amount typical for monolayer-multilayer adsorption process which ends by a plateau indicating the saturation of the mesoporosity. The inflexion is seen at lower relative pressure values for bis 5% nanoparticles ($p/p^\circ = 0.18$) than those for bis 2% ($p/p^\circ = 0.27$) suggesting smaller pore sizes of the former. Moreover, the higher uptake at saturation for bis 2% nanoparticles (*ca* 475-500 cm^3/g) against (*ca* 370-420 cm^3/g) for bis 5% nanoparticles suggests wider pores for the nanoparticles holding lower organic functionality. This tendency is also seen at the pore

volume level (Table 3) where the maximum uptake for the four isotherms decreases from bis 2% nanoparticles to 5% nanoparticles.

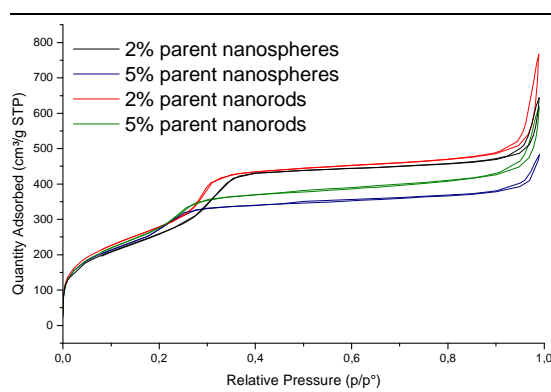


Figure 25: N₂ sorption isotherms and parent bisclickable nanoparticles

Multifunctional mesoporous silica nanoparticles were successfully synthesized and characterized to fulfill the criteria of a nanocarrier:

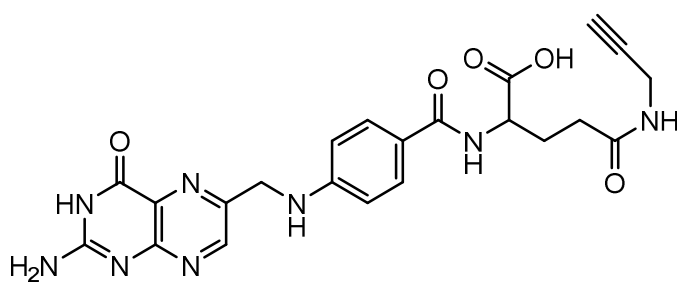
- Nanospheres and nanorods were prepared with aspect ratio ranging from 1 to 4 with a narrow size (90-150 nm) for a good cell endocytosis mechanism.
- High surface areas were achieved ($>1000 \text{ m}^2/\text{g}$) making possible the anchoring of appreciable amounts of functionalities and a high concentration of cargo.
- The carrier is bearing two clickable functions which enable incorporating different molecules combining several properties for an optimal effect of the nanomachine (Targeting agents, luminescent agent for tracking, impellers, pores gates).

After validating the success of the concept of the nanoimpeller on monoclickable MSN, we will move to make multifunctional nanoparticles and use them as multi-clickable devices to anchor diverse molecule with selected applications. Following the successful synthesis and characterization of the bisclickable nanoparticles, we will at first expand the usefulness of the impeller-clicked nanoparticles by incorporating targeting agents. Then we will try to probe the proximity of the clickable alkyne and azide contained in the silica framework by using the communication features between fluorophores (FRET). This feature is of critical importance since one of the application intended (pH-sensitive nanogate activated by a photoacid) relies on a proton spatial transfer and needs close spatial proximity between the active functions.

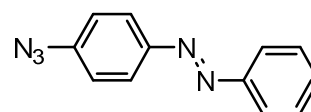
5. CuAAC on bisclickable nanoparticles: Light triggered controlled cargo release from a targeting nanocarrier

In this part, we will focus on the use of a double click reaction in order to make MSN containing the azobenzene as nanoimpeller for controlled release outlooks combined to a targeting agent in order to optimize the nanomachine's efficiency in cancer cell selectivity and on-demand offense.

Folate receptor is overexpressed on the surface of several cancer cell lines such as colorectal, endometrial, ovarian, lung, breast, and renal cells. Thus, folic acid has become an attractive function to selectively target tumor cells¹⁷⁵. In this context, folic acid was modified to bear a clickable alkyne group and clicked as well as the azobenzene on the bisclickable MSNs. The steps of synthesis, functionalization and activation of the nanomachine are gathered in Figure 26.



aminopropargyl-folic acid



Azidoazobenzene

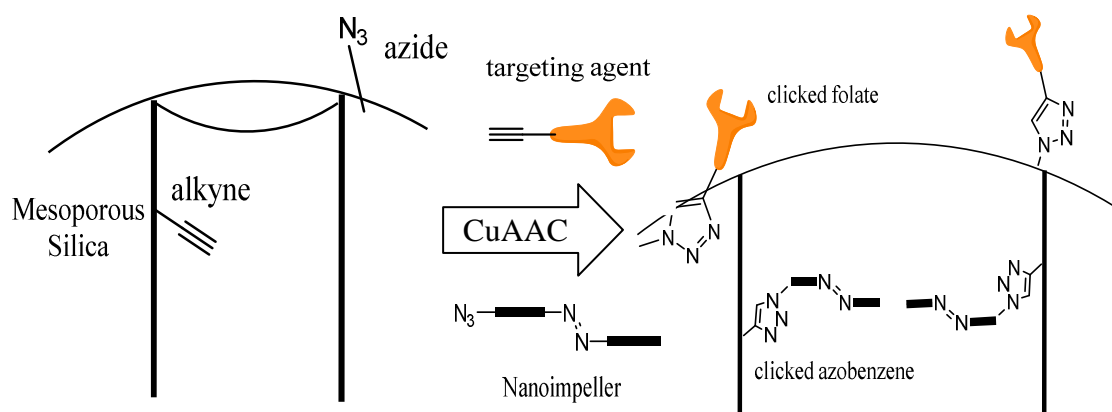
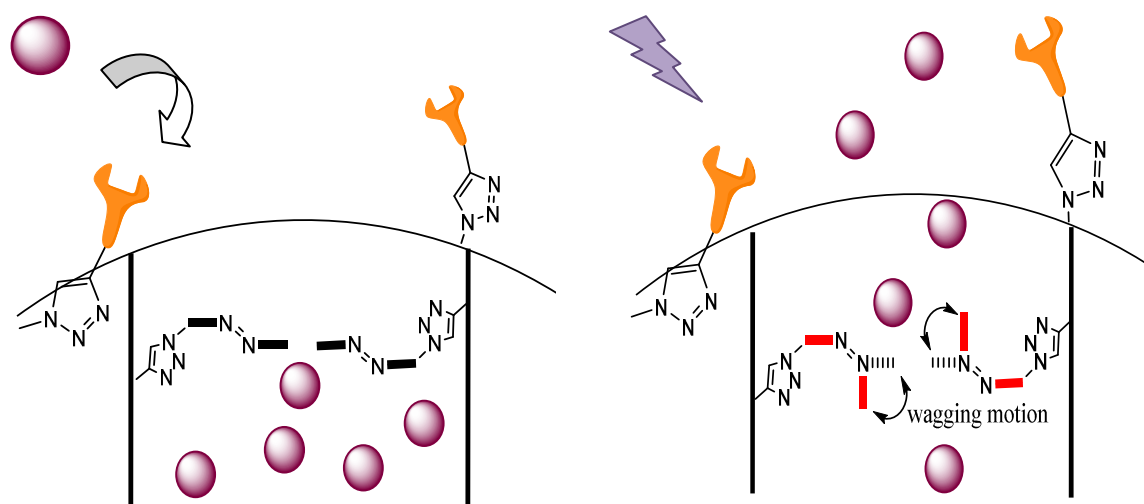
STEP-1- : Synthesis of bisclickable MSN**STEP-2- : double CuAAC reaction****STEP-3- Cargo loading****STEP-4- Light activation**

Figure 26: main steps of the design and activation of nanomachine bearing nanoimpeller and targeting agent.

5.1. Characterization of bisclicked nanoparticles

As usual, the chemical composition was checked using FTIR (Figure 27). The spectra show a significant decrease in the azide peak at 2104 cm^{-1} suggesting that a reaction was taking place with the propargyl group of folic acid. Other bands appearing between 1208 and 1700 cm^{-1} in addition to the bands around 2900 cm^{-1} corresponding the CH_2 and CH_3 vibrations confirm that organic moieties are incorporated into the nanoparticles.

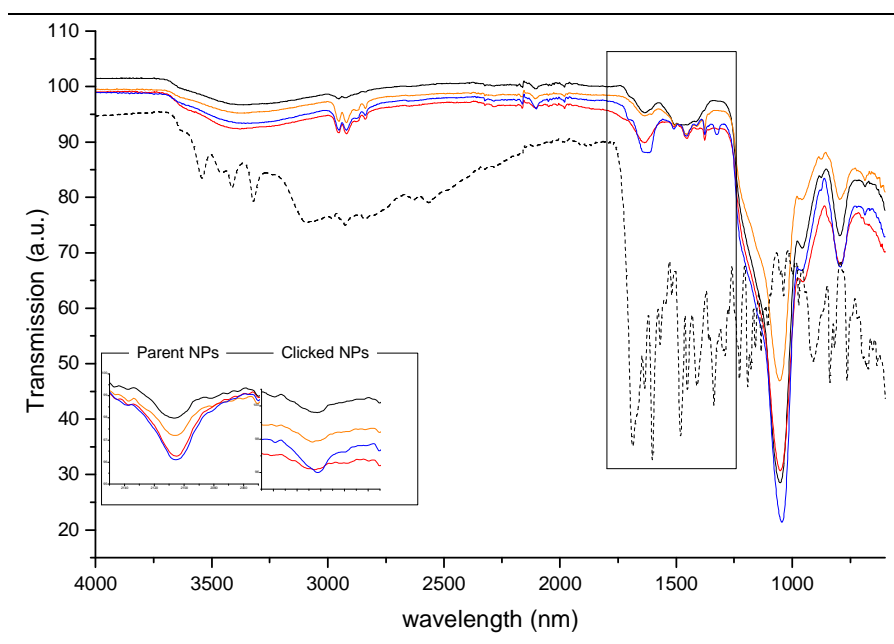


Figure 27: FTIR spectra of bisclicked nanoparticles: (black) 2% and (blue) 5% nanospheres, (red) 2% and (orange) 5% nanorods. Dashed line corresponds to the folate precursor. Inset: zoom on the zone 2200-2000 cm^{-1} before and after click reactions.

^{13}C CP-MAS NMR (Figure 28) shows signals typical of the triazole ring (δ 123 and 145 ppm) characteristic of the success of the CuAAC reaction. In addition, signals at 168 ppm and 174 ppm correspond to the amide ($\text{N}-\text{C}=\text{O}$) and the acid ($\text{OH}-\text{C}=\text{O}$) groups of folic acid. Triazole signature confirms the anchoring of folic acid via CuAAC reaction.

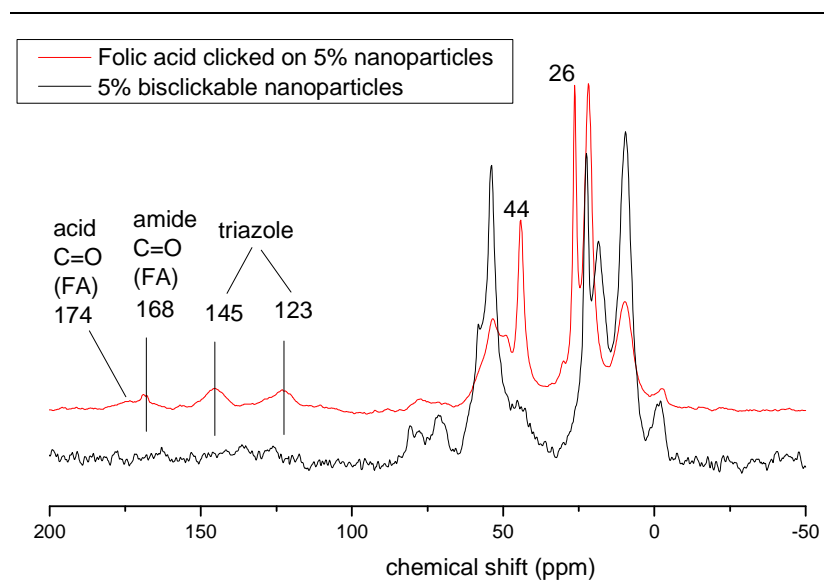


Figure 28: solid-state ^{13}C NMR of the (black) parent and (red) functionalized nanoparticles with folic acid

UV-Vis spectroscopy:

Clicked nanoparticles exhibit the same profile than the molecular precursors.

	Alk-Folate	Azobenzene
$\lambda_{(A \text{ max})} \text{ (nm)}$	288	334
$\epsilon \text{ (M cm)}^{-1}$	10280	31650

Table 4: spectral data of azobenzene and folate in DMSO

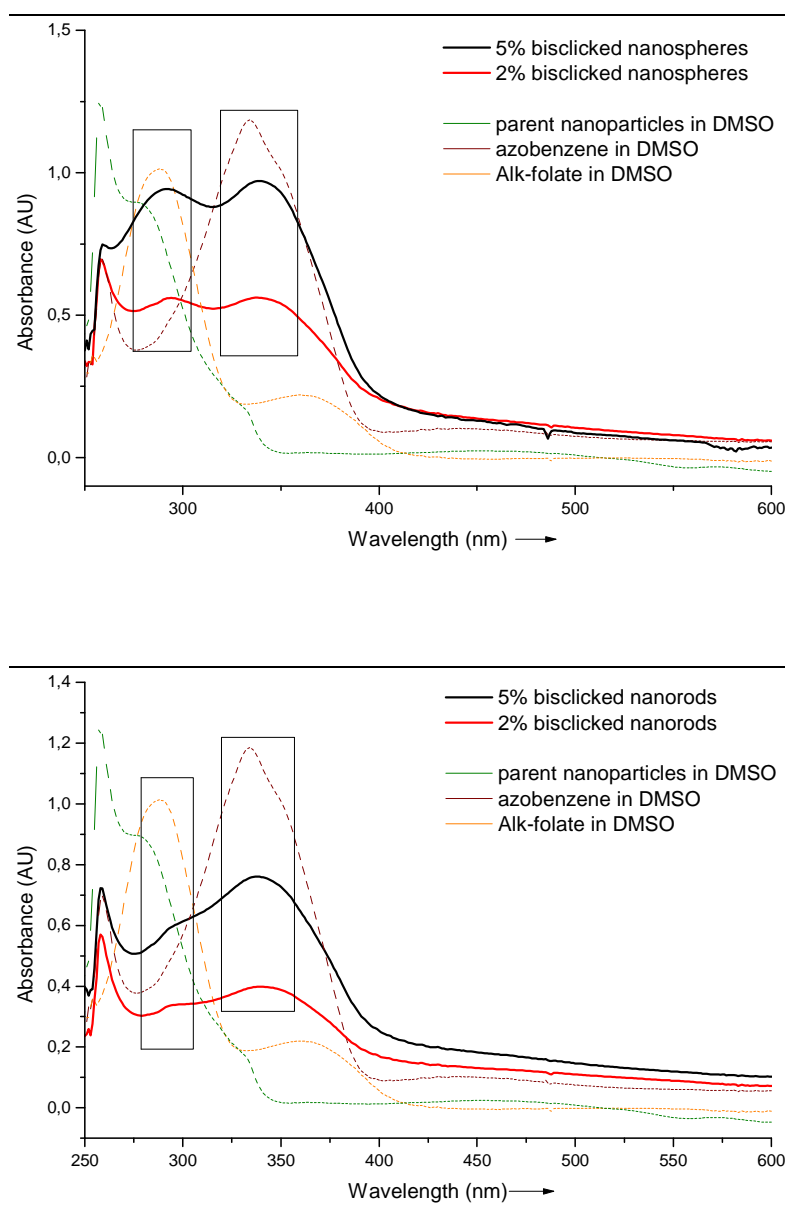


Figure 29: UV-vis spectra of bisclicked (up) nanospheres and (down) nanorods with (black) 5% and (red) 2% functions with (green dashes) parent nanoparticles in DMSO, (brown dashes) hexane@azobenzene and (orange dashes) alk-FA in DMSO.

[clickable functions]	Functionality (mmol/g) (conversion %)			
	Folic Acid (FA)		azobenzene	
	2%	5%	2%	5%
nanospheres	0.10 (71%)	0.18 (50%)	0.03 (25%)	0.06 (17%)
nanorods	0.06 (42%)	0.11 (31%)	0.02 (18%)	0.05 (15%)

Table 5: concentrations of the clicked molecules on the corresponding nanoparticles

N₂-sorption analyses show a decrease of the adsorbed amounts after CuAAC reactions with a decrease in BET surface area and the total pore volume (Table 6) compared with the parent nanoparticles (Figure 30, Figure S4). However, the surface area and the pore volume are still able to retain cargo molecules especially in the case of 2% clicked nanoparticles.

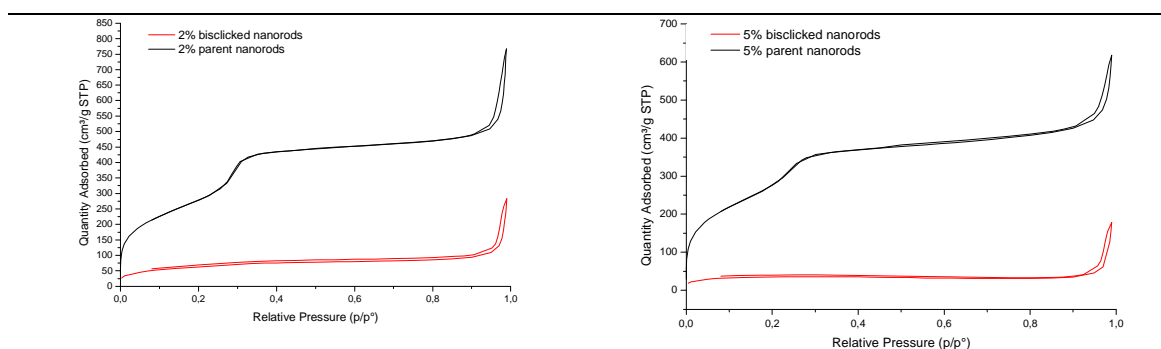


Figure 30: N₂ sorption isotherms of the (black) parent and (red) bisclicked nanorods (left) 2% and (right) 5% clickable functions

XRD patterns (Figure 31) show that nanoparticles maintained good structuring even after several treatment conditions. A diffraction peak corresponding to d₁₀ interreticular distance (Table 6) prominently appears. The vanishing of the harmonics is due to the double click reaction conditions and also the incorporating of voluminous organic molecules.

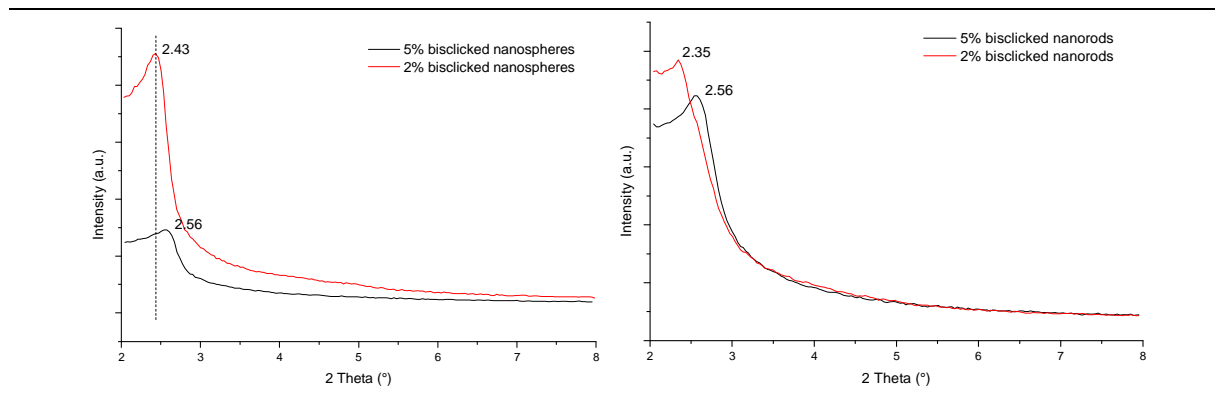


Figure 31: XRD patterns of the bisclicked (left) nanospheres and (right) nanorods with (red) bis 2% and (black) bis 5% clickable functions

	2% bisclicked nanospheres	5% bisclicked nanospheres	2% bisclicked nanorods	5% bisclicked nanorods
BET surface area (m ² /g)	297	109	225	112
Total pore volume at saturation (cm ³ /g)	0.19	0.09	0.16	0.05
d ₁₀ (nm)	3.57	3.39	3.69	3.39
Lattice parameter (nm)	4.13	3.92	4.27	3.92

Table 6: Textural data of the different clicked nanoparticles

5.2 Release profile

After loading the bisclicked MSNs with rhodamine B, release experiments were performed in solution using an excitation at 365 nm, as seen in the previous chapter.

The progressive increase of the released amount is typical of the nanoimpeller behavior. Nanospheres and nanorods exhibit an important release rate after light excitation start. The released amount reach 60% in only 3 hours with a same time-scale as for the monoclicked azobenzene which indicates that folic acid does not perturb the release process.

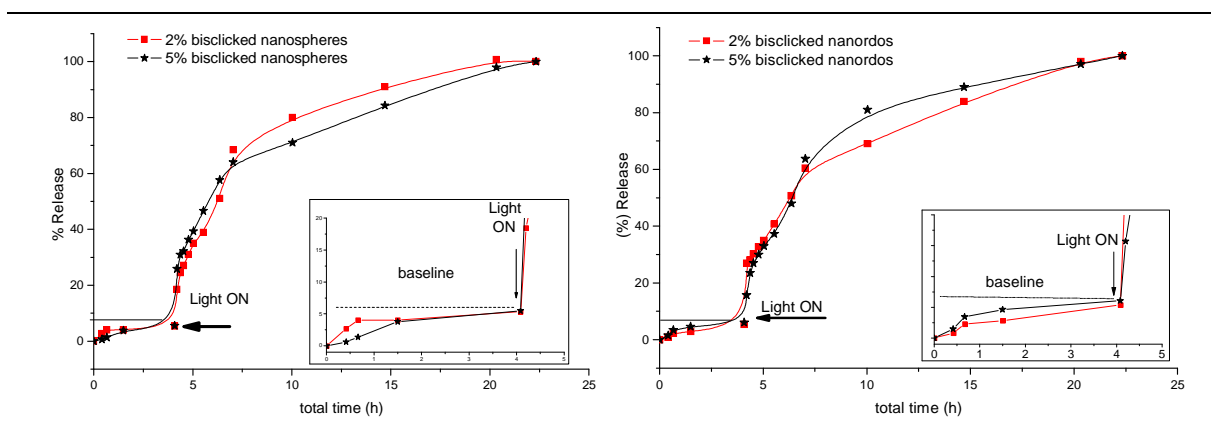


Figure 32: percentage of release profile of bisclicked (up) nanospheres and (down) nanorods with (red dots) bis 2% and (black stars) bis 5% clicked functions. Insets: zoom on the baseline before excitation starts.

The loading capacity of the nanoparticles exhibited again the highest amounts for 2% clicked nanoparticles which present 2 times more loading than 5% clicked nanoparticles (Figure 33).

Two control experiments were also carried out to confirm the on-demand activation and the light-controlled delivery. In the first case, the light was repetitively turned on and off (Figure 33). When the lamp is off, almost no release is noticed indicating that the azobenzene entities are not undergoing any wagging motion. Turning the light on, induce the photoisomerization of the azobenzene thus creating a disorder inside the pores and inducing the liberation of the dye. In order to validate the light activation phenomenon, another control experiment was carried out by increasing the temperature of the medium (until 50 °C). No release was noticed proving that the cargo liberation from the nanoparticles is induced solely by the activation of the azobenzene and not any local heating caused by the light (data not shown).

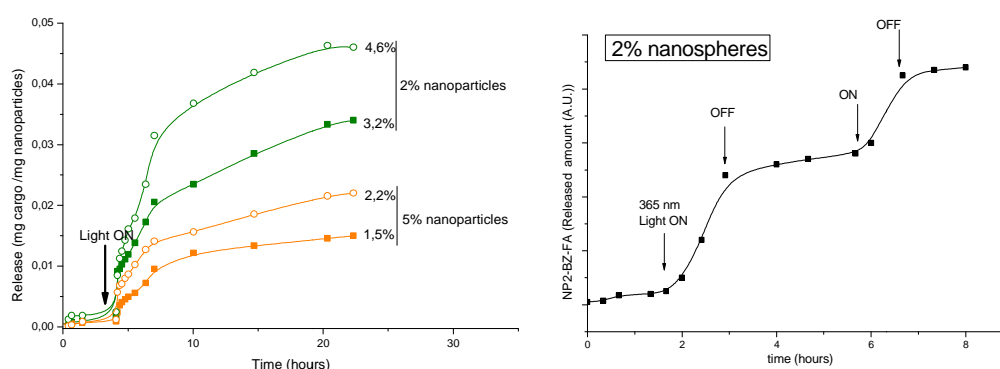


Figure 33: (left) Release profile relative to the maximum uptake of rhodamine B for the clicked (full dots) nanorods and the (empty spheres) nanospheres and (right) ON-OFF release profile of 2% nanospheres outlining the light-induced activation.

5.3. In vitro preliminary essays:

For biotests, all the experiments were carried out with 2% nanospheres since it is able to hold more important concentration of dye.

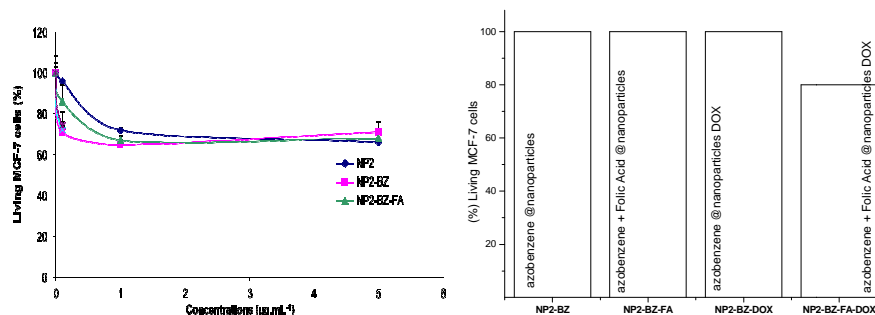


Figure 33 bis: (left) Cytotoxicity study on nanoparticles. Values are mean \pm SD of 3 independent experiments, (right) Cell viability assays using highlighting the crucial effect of the clicked folic acid on the cell targeting

Human breast cancer cells (MCF-7) were treated with a range of concentration (from 0.1 to 5 $\mu\text{g/ml}$) of different nanoparticles (Figure 33 bis). The quantification of cell death was realized after 72 h incubation and demonstrates the biocompatibility of the nanosystem without DOX. Clicked nanoparticles exhibit the same toxicity profile than parent nanoparticles and this confirms that no more cell toxic copper is remaining in the system after the washing steps. After a series of experiments, the concentration in nanoparticles was fixed at 2 $\mu\text{g/L}$ and was used along with a 6 hours time of incubation.

In order to probe the efficiency of the clicked folic acid, an irradiation with 400-440 nm light was carried out on 2% nanospheres clicked with clicked azobenzene solely and with both molecules clicked (bisclicked 2% nanospheres). These nanoparticles were loaded (or not) with doxorubicin to make control experiments. Results show that without any doxorubicin loaded, laser excitation does not induce cell death. The same result was obtained for azobenzene-monoclicked monosphere loaded by DOX although some cell death was expected. As for bisclicked nanosphere loaded by DOX, $17 \pm 4\%$ of cells have died. This result, compared with the previous, confirm that the clicked folic acid was essential for cell killing, and this can be explained by the fact of its targeting properties towards MCF-7 cells which likely helped the nanoparticles to be quickly internalized. In contrast, this was not found in azobenzene monoclicked nanosphere which could not be internalized by MCF-7 line (using the same timescale) and thus presented no effect on tested cells.

6. Double click reaction (CuAAC) on mesoporous silica nanoparticles: probing the proximity of functions by Förster Resonance Energy Transfer (FRET)

6.1. Introduction

Förster Resonance Energy Transfer (FRET) is a non-radiative transfer of an electronic excitation between distinct fluorophores; an excited “donor” and a neighboring “acceptor” in its ground state²⁵¹.

The FRET arises from a dipole-dipole interaction between the electronic states of the donor and the acceptor without emission or absorption of photon. FRET occurs by resonance between the donor excitation energy and an electronic gap of the acceptor²⁵². More precisely, the electron of the excited molecule induces an oscillating electric field that excites the acceptor electrons by perturbing the electron cloud without exchanging any electron. On the spectral level, this implies that the donor’s emission spectrum must overlap the absorption spectrum of the acceptor.

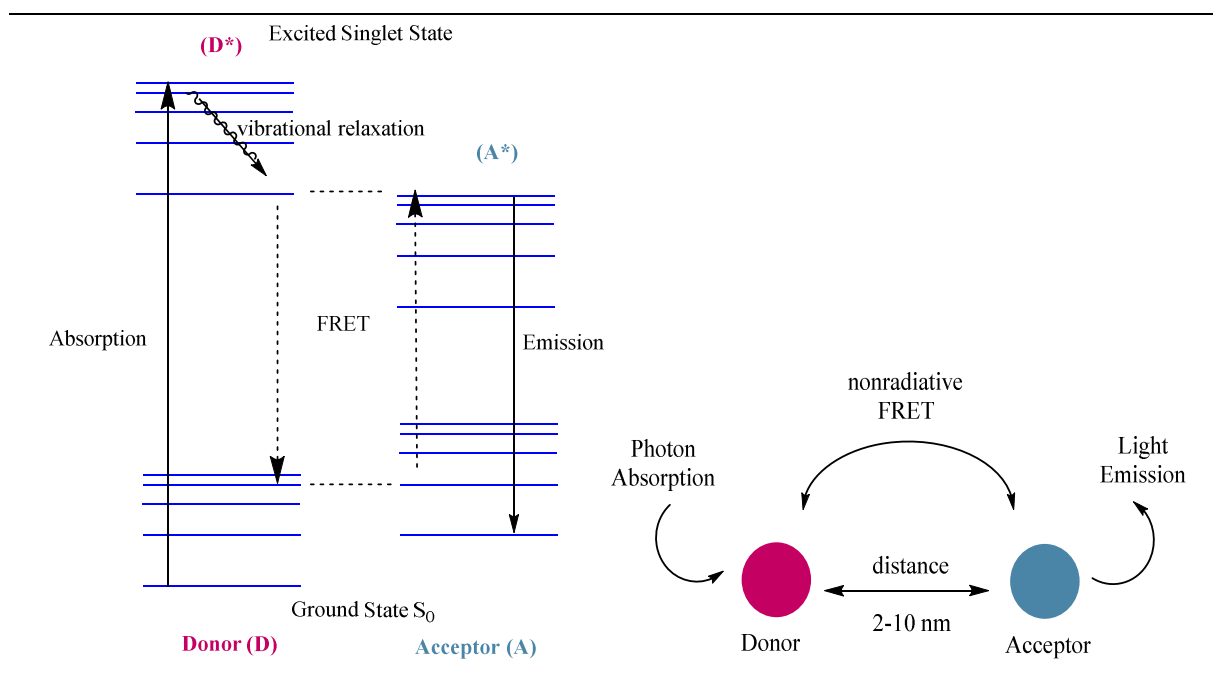


Figure 34: (left) Jablonski simplified diagram explaining the FRET and (right) schematic representation of the FRET dependence on the distance between the fluorophores

FRET between fluorophores is conditioned by several factors such as fluorescence quantum yield of donor, absorption coefficient of the acceptor, the relative orientation and the distance between the dipoles^{251,253}. Therefore, FRET strongly depends on the dipoles separation and

scales as $1/r^6$ with FRET efficiency $E = \frac{1}{1 + \left(\frac{r}{R_0}\right)^6}$.(equation 1.1)

Where r is the effective distance between fluorophores and R_0 is the Förster radius at which $E = 50\%$. In other terms, at Förster distance (R_0), the probability that a donor transfers its energy to the acceptor is 50% (in addition to 50% of spontaneous fluorescence). This probability increases as the distance between donor and acceptor decreases. Typically, the distance at which FRET occurs ranges from 2 to 10 nm; above this distance, only spontaneous deactivation of the donor takes place.

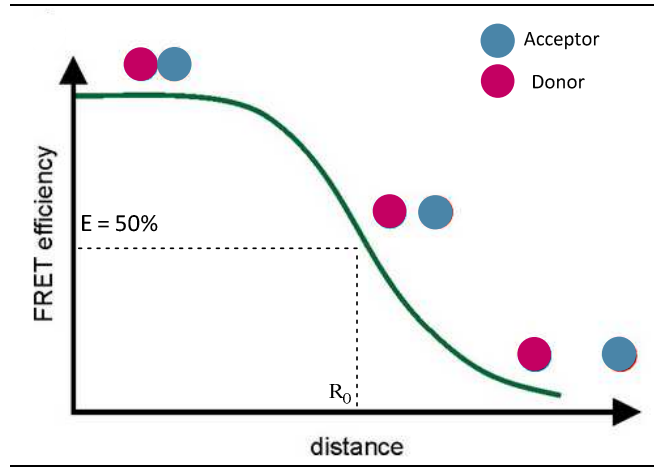


Figure 35: Decay of the FRET efficiency as distance between donor and acceptor decreases

The Förster Radius (R_0) is expressed as follows^{251–253}:

$$R_0^6 = 8.79 \cdot 10^{-5} \cdot n^{-4} \cdot \phi_D \langle \kappa^2 \rangle J \text{ (equation 2.1)}$$

Where J is the overlap integral between donor's emission and acceptor's absorption.

$$J = \left[\int_0^\infty \epsilon^A(\lambda) F^D(\lambda) \lambda^4 d\lambda / \int_0^\infty F^D(\lambda) d\lambda \right] \text{ in terms of wavelength (nm) (equation 2.2)}$$

Or,

$$R_0^6 = 9000 \ln(10) \cdot \phi_D \langle \kappa^2 \rangle J / (128 \pi^5 n^4 N_A) \text{ (equation 3.1)}$$

$$J = \left[\int_0^\infty \epsilon^A(\tilde{\nu}) F^D(\tilde{\nu}) \tilde{\nu}^4 d\tilde{\nu} / \int_0^\infty F^D(\tilde{\nu}) d\tilde{\nu} \right] \text{ in terms of wavenumber (cm}^{-1}\text{) (equation 3.2)}$$

λ (nm) is the wavelength.

$\tilde{\nu}$ (cm⁻¹) is the wavenumber calculated from λ as $\tilde{\nu}$ (cm⁻¹) = $10^7/\lambda$ (nm)

ϕ_D is the fluorescence quantum yield of the donor.

n is the refractive index of the ambient medium.

κ is the dipole orientational factor, given as an average $\langle \kappa^2 \rangle = 2/3$ for random and 0.475 for static orientational distribution of the dipole momentum.

ϵ^A is the molar extinction coefficient of the acceptor at each wavelength.

F^D is the fluorescence of the donor.

N_A is Avogadro's number = $6.023 \times 10^{23} \text{ mol}^{-1}$.

Fluorescence has high sensitivity to detect very low concentrations of fluorophores, thus FRET is employed for probing molecular interactions, spatial proximity and molecular distribution. Thus, it displays a broad range of applications and it is especially occupying a central stage in biology, biophysics and biotechnology such as monitoring protein-DNA or protein-protein interaction, protein conformational change²⁵².

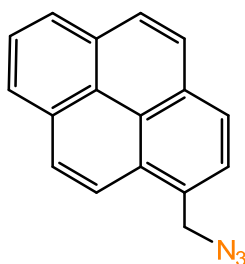
6.2. FRET on the mesoporous silica nanoparticles

At the scale of the mesoporous silica nanoparticles, FRET, which gives valuable information about the proximity and the interaction between two fluorophores, is undoubtedly a useful technique in order to probe the communication and estimate the distance between the functional groups clicked on the silica nanoparticles.

To this purpose, we made use of commercially available molecules that can be easily modified to bear clickable groups. Thus, we have clicked the azidomethylpyrene and the *N*-propargyl 4-aminonaphthalimide groups which display high spectral overlap between methylpyrene's fluorescence and 4-aminonaphthalimide's absorption (Figure 36).

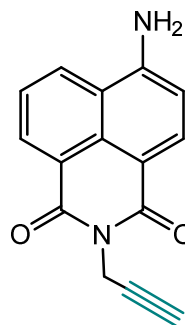
Donor:

Azidomethylpyrene



Acceptor:

N-propargyl 4-aminonaphthalimide



clickable donor and acceptor used in FRET.

Pyrene displays a strong absorption band at 340 nm, a wavelength where no (or negligible) absorption is shown for the naphthalimide. Exciting naphthalimide at this wavelength thus results in a weak emission. Furthermore, the absorption spectrum of the latter strongly overlaps with the emission of the pyrene. Hence, this overlap will be the most important factor to probe a FRET phenomenon between these two molecules after being clicked on the nanoparticles and thus estimate their coexistence at low distance. Therefore, after exciting the nanoparticles at 340 nm an energy transfer can occur between clicked pyrene and clicked naphthalimide that can be evidenced by a high emission of the acceptor and a decreased emission of the donor. (Overall phenomena: photon absorption by donor and photon emission by acceptor).

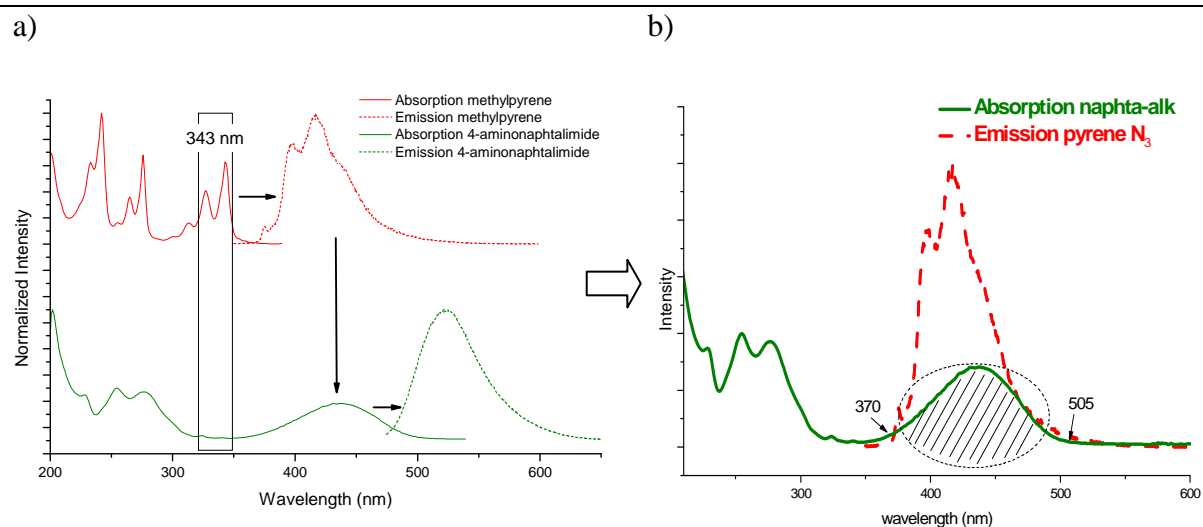


Figure 36: (a) Absorption and emission spectra of donor and acceptor and (b) overlap between donor's emission and acceptor's absorption

	azidomethylpyrene	<i>N</i> -propargyl 4-amino naphthalimide
$\lambda_{(\text{Absorption max})}$	242	260
$\varepsilon \text{ (M cm)}^{-1}$	69100	10400
$\lambda_{(\text{Emission max})}$	416	523

Table 7: spectral data of the used fluorophores

6.2.1. Ro Calculation

In order to estimate the distance separating the clicked fluorophores, we made use of the equations (3.1) and (3.2):

$$R_0^6 = 9000 \ln(10) \phi_D \langle \kappa^2 \rangle J / 128 \pi^5 n^4 N_A \text{ (eq 3.1)}$$

$$J = \left[\int_0^\infty \varepsilon^A(\tilde{\nu}) F^D(\tilde{\nu}) \tilde{\nu}^4 d\tilde{\nu} / \int_0^\infty F^D(\tilde{\nu}) d\tilde{\nu} \right] \text{ (eq 3.2)}$$

Considering the following values:

- The quantum yield of the donor is taken²⁵⁴ to be $\phi_D = 0.4$
- The dipole orientational coefficient is taken as $\langle \kappa^2 \rangle = 2/3$ since clicked fluorophores are believed to display random orientation.
- The refractive index of the medium is $n = 1.3$ (solvent = water)

According the (eq 3.1) R_0 is calculated to be 3.5 nm

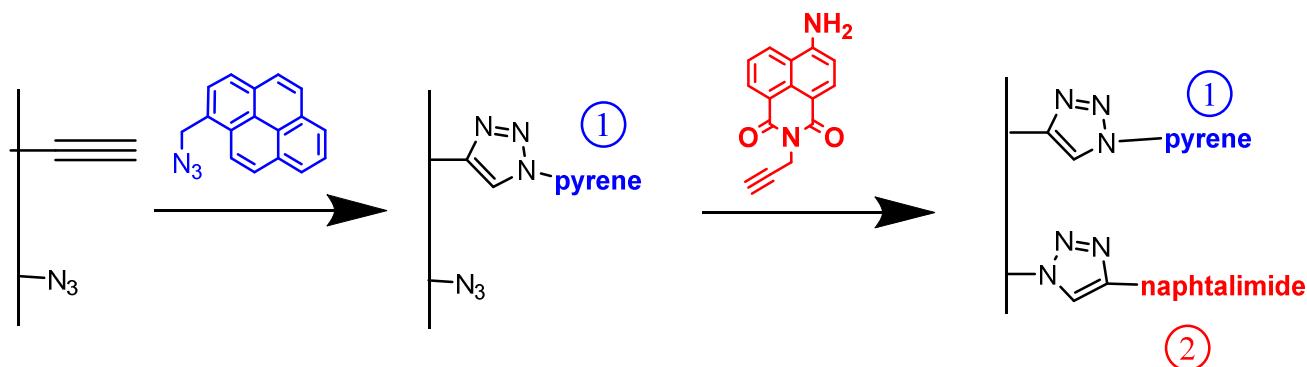
$R_0 = 3.5$ nm is the distance at which the fluorescence probability of pyrene is divided by 2.

6.2.3. CuAAC Click Reactions

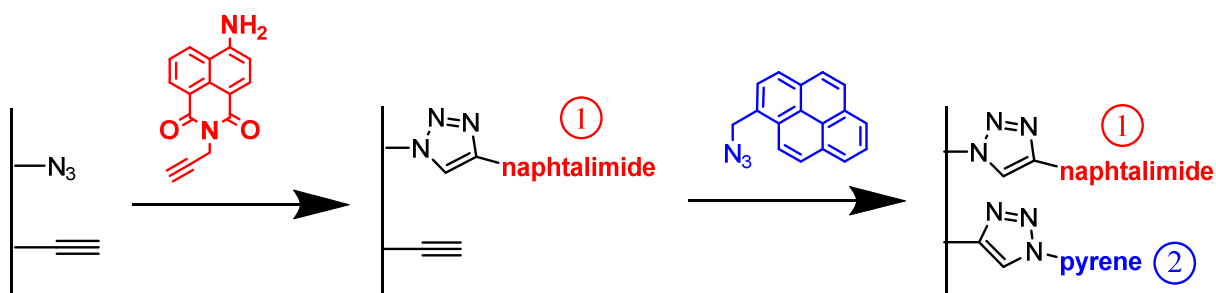
Two distinct fluorophores with appropriate spectral profiles (donor and acceptor) were clicked on the mesoporous silica nanoparticles (nanospheres) with 1%, 2% and 5% clickable functions via CuAAC reaction using Sharpless' conventional catalytic system. 1% bisclickable nanospheres were synthesized to this purpose (Figure S5). Bisclickable nanoparticles with 2% and 5% are the same that those made in Section 4.

Two pathways are possible for performing the CuAAC:

Click Path 1 (naphthalimide @ pyrene @ MSN): NPx-DA (Donor then Acceptor)



Click Path 2 (pyrene @ naphthalimide @ MSN): NPx-AD (Acceptor then Donor)



Scheme 1: Possible Paths of the double CuAAC.

6.2.4. Characterization of the CuAAC functionalization

i) Chemical Compositions

The composition of the clicked materials was at first probed by FTIR (Figure 38, Figure S6).

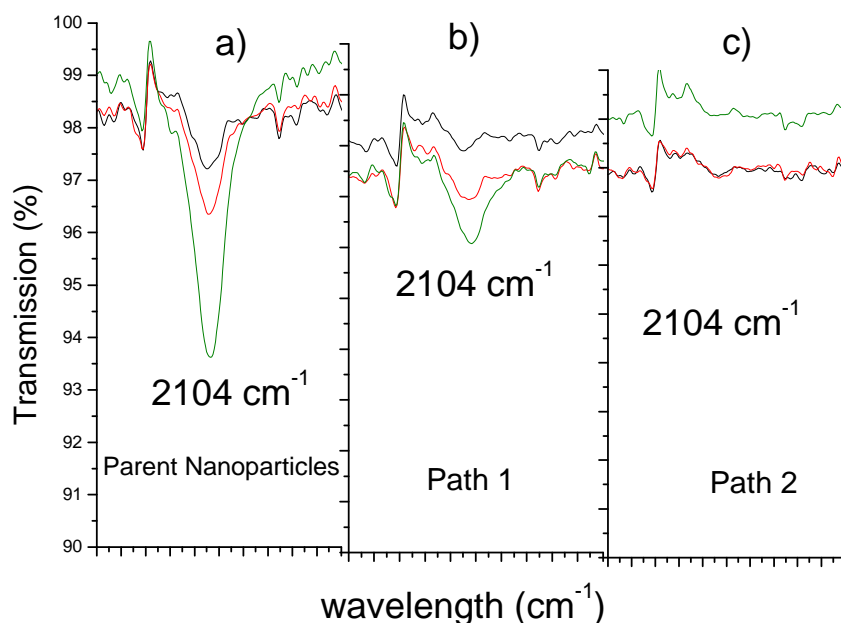


Figure 38: zoom on FTIR profile of (a) parent and (b,c) clicked nanoparticles *via* both paths

FTIR spectra show a strong decrease of the intensity of azide band (2104 cm^{-1}) from the parent nanoparticles to path 2 clicked nanoparticles and a total vanishing after click according to path 1. In Path 2, the naphthalimide was clicked at first and exhibits higher concentration thus more reactivity towards the azide.

UV-vis spectroscopy (Figure 39) confirms the successful incorporation of the fluorophores which absorption bands on the nanoparticles match with those of the free molecules in solution. Indeed, clicked methylpyrene absorption characteristic bands appear in the zone (λ 250-350 nm) whereas the absorption band at 450 nm corresponds to the clicked 4-aminonaphthalimide. UV-vis spectroscopy allows estimating the concentration of the fluorophores in the suspended nanoparticles.

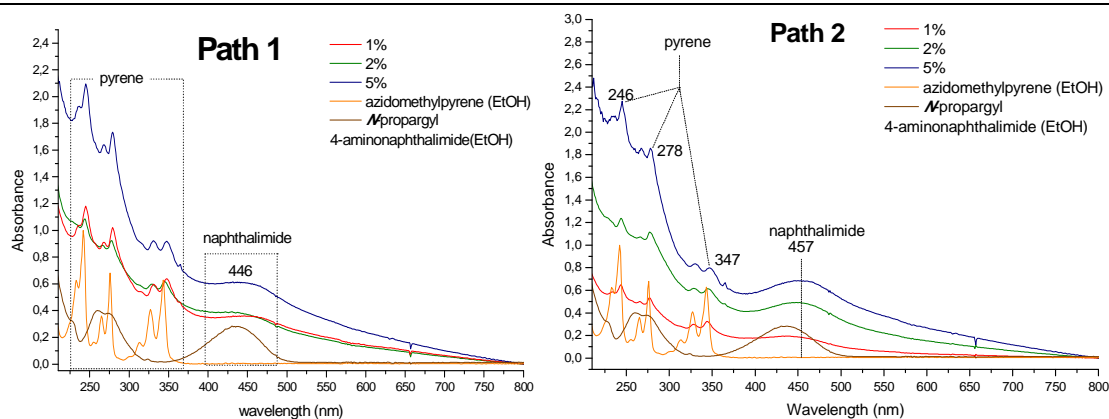


Figure 39: UV-vis absorption spectra of (red) 1%, (green) 2% and (blue) 5%- bisclicked nanoparticles via (left) path 1 and (right) path 2. Orange and brown spectra correspond to azidomethylpyrene and *N*-propargyl 4-aminonaphthalimide in ethanol respectively.

After baseline subtraction, the amounts of clicked fluorophores were quantified (Table 8).

	[Functionalization] (mmol/g) (conversion %)					
	Methylpyrene (donor)			4-aminonaphthalimide (acceptor)		
	1%	2%	5%	1%	2%	5%
x = [clickable functions]						
Path 1 (NPx-DA)	0,05 (63%)	0,05 (35%)	0,09 (25%)	0,08 (100%)	0,11 (78%)	0,18 (50%)
Path 2 (NPx-AD)	0,03 (38%)	0,05 (35%)	0,10 (28%)	0,06 (75%)	0,15 (95%)	0,20 (55%)

Table 8: Concentration of clicked fluorophores (donor and acceptor) on nanoparticles suspended in water

The results show that no major change in concentrations of clicked methypyrene occurs following the click order (except NP1-DA which presents higher concentration when pyrene was clicked at first). The same behavior for 4-aminonaphthalimide was shown as it displays little increase (for bis 2 and 5%) of clicked amount when it is reacted at first (path 2). NP1-AD shows higher amount when it is clicked secondly. The order of CuAAC reaction does not favor the concentration of one clicked molecule. However, both paths exhibit higher concentration for the acceptor than the donor, meaning that the acceptor is more efficiently clicked on the nanoparticles than the donor.

6.2.5. FRET effect by Fluorescence Spectroscopy: Proximity between the clicked functions.

After validating the composition of the bisclicked nanoparticles, the latter were analyzed by fluorescence spectroscopy to check if FRET is occurring and then to estimate the proximity between the clicked molecules.

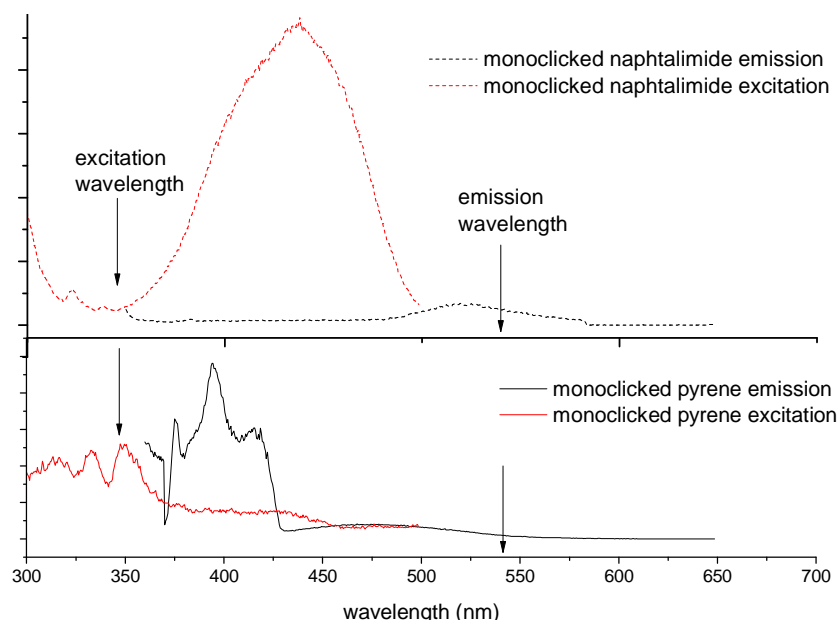


Figure 40: Emission (black) and Excitation (red) spectra of nanoparticles monoclicked by pyrene (complete line) or naphthalimide (dashed line). Recording wavelengths: Emission was at 343 nm and excitation at 540 nm.

At first, emission and excitation spectra were recorded on 5% nanoparticles clicked only by either donor or acceptor. Indeed, the emission spectrum ($\lambda_{exc} = 343$ nm) of nanoparticles clicked only by pyrene shows only bands corresponding to pyrene derivatives in its monomer form (λ 370-400 nm) and excimer (broad band, λ 430-550 nm) while nanoparticles only clicked by naphthalimide show evidently weak fluorescence since naphthalimide has low absorption at this excitation wavelength (Figure 40). When the bisclicked nanoparticles are excited at the same wavelength, a very strong band appears at 500-600 nm corresponding to the naphthalimide emission suggesting the occurrence of a FRET phenomenon from the pyrene (donor) to the naphthalimide (acceptor) (Figure 41, a,b).

This is confirmed by the excitation spectra ($\lambda_{em} = 540$ nm). Weak bands are displayed on pyrene-monoclicked nanoparticles while a prominent signal is seen on naphthalimide monoclicked samples (Figure 40). When the excitation spectra are recorded for bisclicked

nanoparticles (Figure 41, c, d), strong signals (λ 320–380 nm) for pyrene are shown out in addition to naphthalimide (λ 400–500 nm). This confirms that we have a strong interaction highlighted by a close proximity between the clicked fluorophores.

In spite of the clear emission band of naphthalimide evidencing the FRET, the considerable emission band of pyrene in both paths means that 1% bisclicked nanoparticles exhibit the highest segregation between FRET donor and acceptor where pyrene has clearly less neighboring acceptor molecules than in the case of 2% and 5% bisclicked nanoparticles. In these latter, very weak emission bands referring to pyrene are identified, which means that almost all the donor molecules are in close proximity with acceptor molecules with a high probability of FRET.

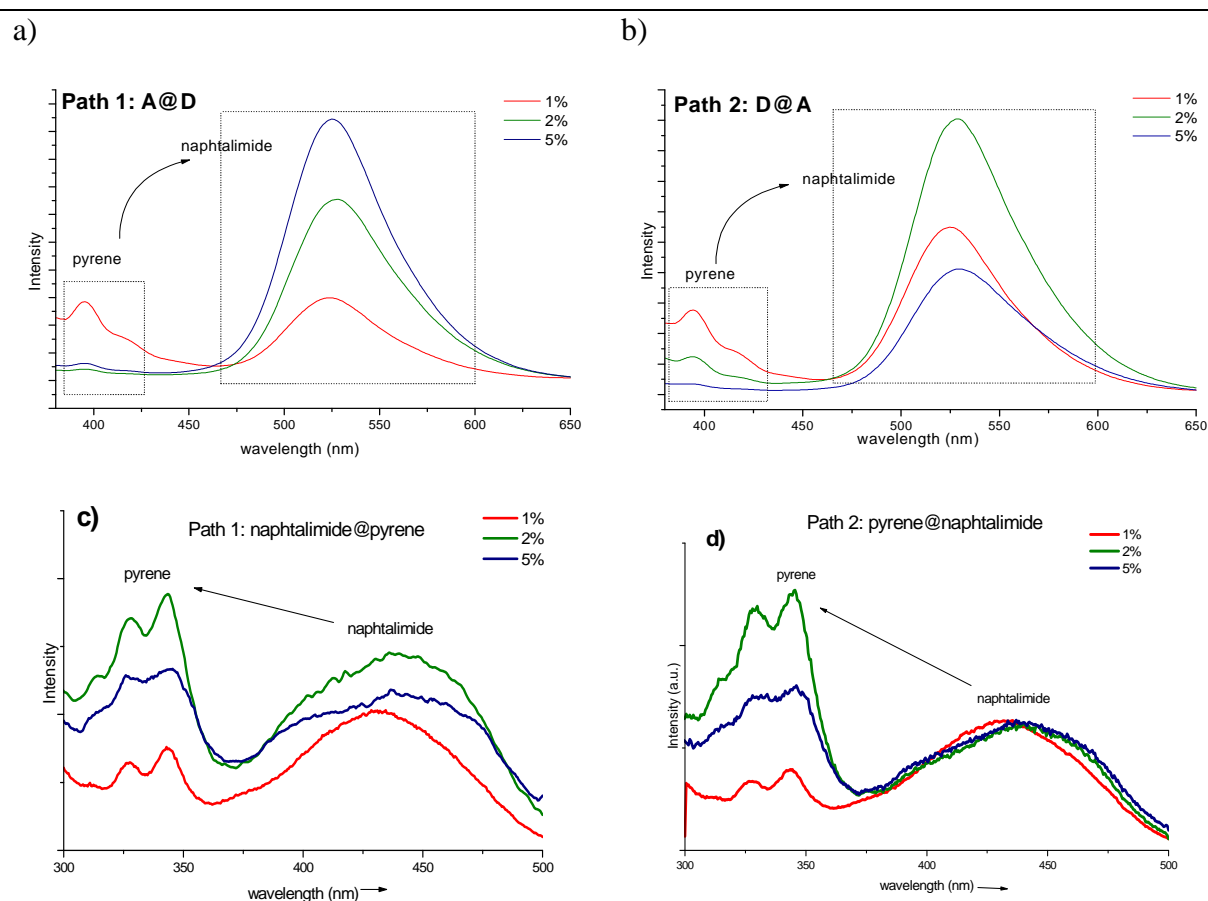


Figure 41: (up) Emission and (down) excitation spectra of (red) 1%, (green) 2% and (blue) 5% - bisclicked nanoparticles via (left: a and c) path 1 and (right: b and d) path 2

The energy transfer is more important as the acceptor and the donor are close and homogeneously distributed. This implies that the ratio of emission intensity of the acceptor (at

λ 540 nm) over the emission of the donor (which hasn't participated in FRET, at λ 340 nm) gives valuable information about FRET while correlated with excitation profile.

In principle, for the lower amount of “residual” pyrene appearing in the emission spectra, the highest pyrene absorption should be seen in the excitation spectra.

6.3. Conclusion

Two fluorophores (energy donor and acceptor) were successfully clicked on bifunctional MSN and characterized by vibrational and absorption spectroscopy. Emission and excitation fluorescence spectroscopy showed that an energy transfer phenomenon (FRET) is occurring between the functions. The success of the FRET shows that in average the distance between two functions lies below 3.5 nm whatever the concentration of the 2 functions in the range of [1% - 5%]. This R_0 distance is

comparable to the interpore distance in MCM-41 materials, which suggests that either in path 1 or path 2, the secondly clicked fluorophore can enter within the pores of the MSN. Owing to the possible communication between clicked entities in such MSN, we can design new nanomachines containing “antenna” which can transmit energy²⁵⁰, protons or electron to an active valve.

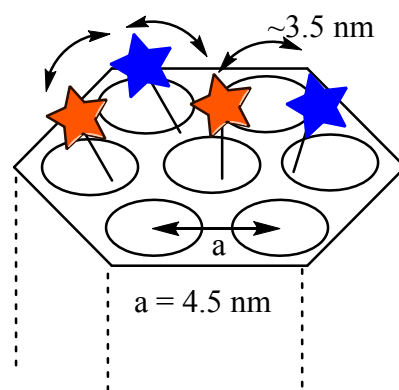


Figure 42 : fluorophores at comparable interpore distance

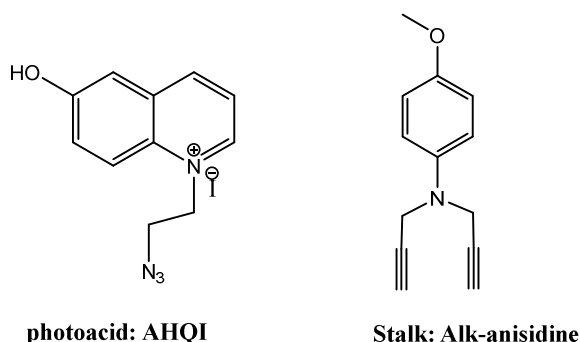
7. Activation of pH-Responsive Nanomachines through Photo-Responsive Proton Transfer

We have demonstrated by FRET that we are able to click two functions at low distance (between 1 and 10 nm). This feature will be used in order to make a novel controlled delivery system based on a proton transfer at low distance between two communicating clicked entities.

The controlled delivery system studied in this part consists of a clicked photoacid and a clicked pH-sensitive stalk bearing a supramolecule (Cyclodextrin) as a gatekeeper (Figure 43). Upon light excitation, the photoacid should liberate protons (H^+) that shall protonate the amine of the valve, thus destabilizing the supramolecular assembly formed with the gate keeper.

A Photoacid is a molecule that turns into a strong acid after a light excitation. Indeed, the excited state (singlet S_1) of a photoacid is more acidic than their ground state (S_0)^{255,256}.

In addition, some studies²⁵⁷ have shown a complexation phenomenon between the α -CD and some derivatives of the benzene molecule (aniline, toluene, ..). In particular, anisidine (*p*-methoxyaniline) is known to have a good affinity in water with the CD cavity due to their close hydrophobicity. The α -cyclodextrin will associate with the nanovalve capping the particles and preventing the cargo from escaping. Upon appropriate light excitation, the photoacid will protonate the stalk of the acid valve. After the amine in the acid valve has been protonated the α -cyclodextrin binding affinity decreases and it dethreads from the stalk. The dethreading unblocks the pore opening and allows the previously trapped cargo to escape into the solution.



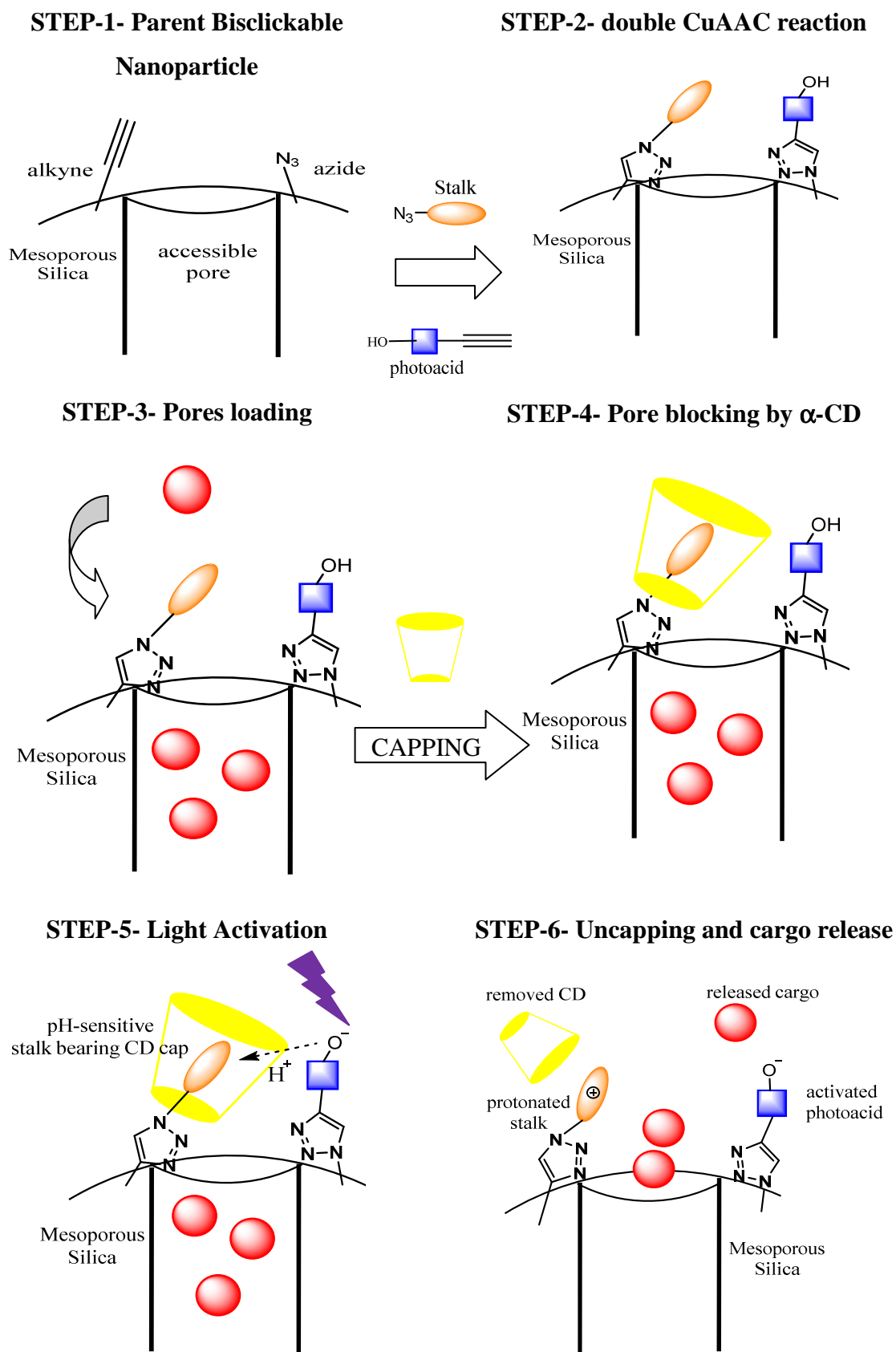


Figure 43: different steps in designing a nanomachine bearing pH-sensitive nanogate and a photoacid

7.1. Characterization of the nanoparticles

The bis-clickable nanoparticles were functionalized by CuAAC grafting with the stalk (alk-anisidine) then the photoacid (AHQI) and characterized by different techniques.

Vibrational spectroscopy (Figure 44, Figure S8):

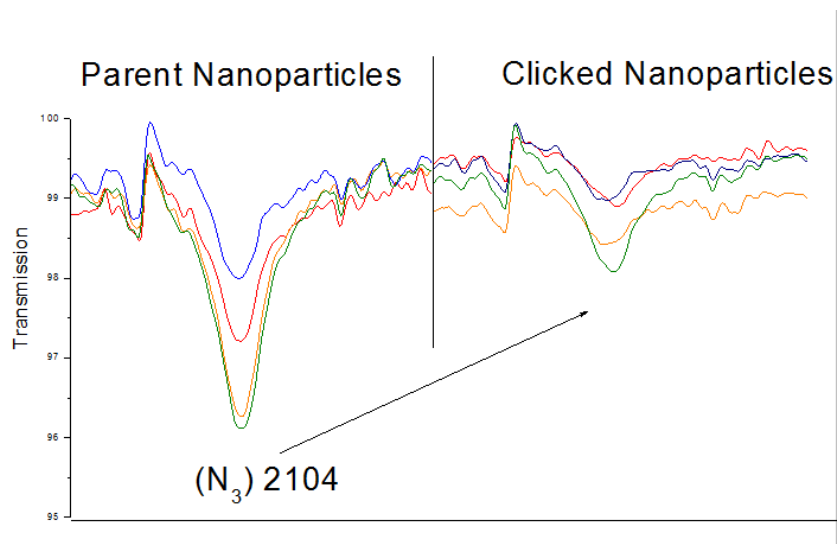


Figure 44: Zoom on FTIR spectra ($2200\text{--}2000\text{ cm}^{-1}$) of (left) parent and (right) bisclicked nanoparticles: (blue) 2% and (orange) 5% nanospheres with (red) 2% and (green) 5% nanorods.

The intensity decrease of the azide peak at 2104 cm^{-1} is a first indication that anisidine was successfully clicked. Several bands appear after click reaction at $1450\text{--}1510\text{ cm}^{-1}$ corresponding to the clicked molecules (Figure S8).

^{13}C CP-MAS NMR was carried out for bis 5% parent nanoparticles and clicked either by alk-anisidine or by AHQI (Figure 45).

The obtained spectra confirm the success of the click reaction of both molecules on the nanoparticles. Signals at $\delta 122\text{ ppm}$ and $\delta 144\text{ ppm}$ are typical for the triazole ring, characteristic of the CuAAC reaction, in addition to the signal at $\delta 30\text{ ppm}$ corresponding to the C in alpha position to the triazole. In the case of NP-AHQI-5 this is supported by a total vanishing of the alkyne signals at $\delta 71\text{--}77\text{ ppm}$ indicating their reactivity towards AHQI. Furthermore, the signals at $\delta 110\text{--}140\text{ ppm}$ correspond to the aromatic rings of clicked molecules. The slight increase of the alkyne signals could be due to one non-reacted of the two pending alkyne groups of the anisidine.

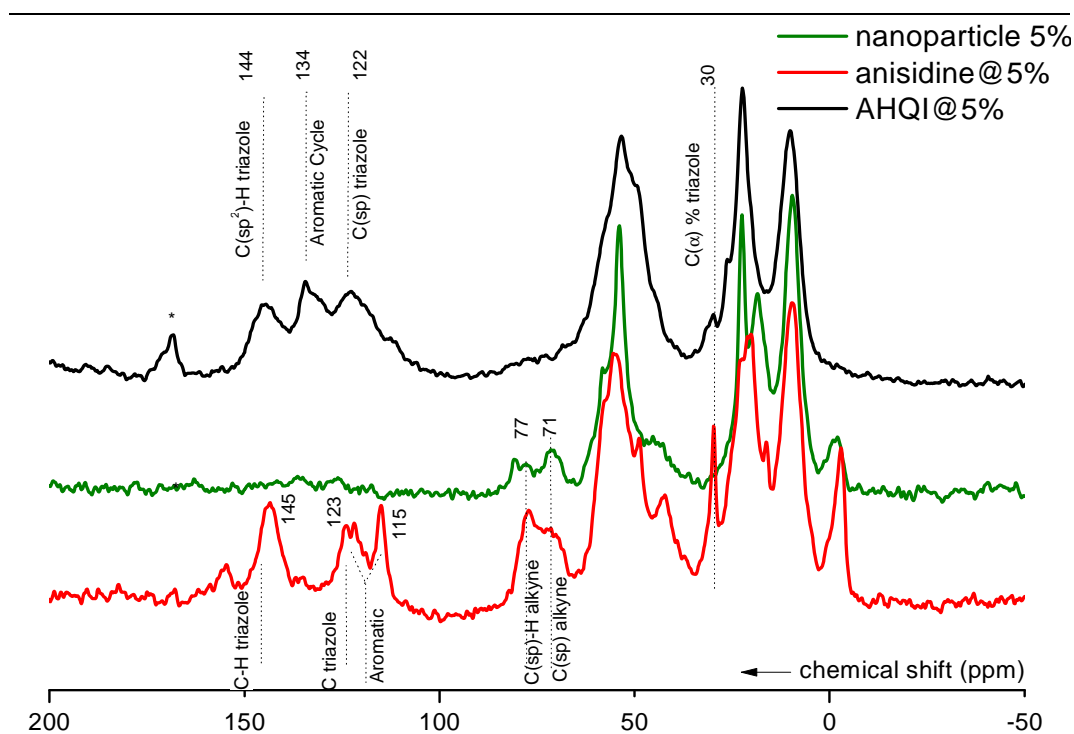


Figure 45: ^{13}C CP-MAS NMR spectra of (green) parent bisclickable nanoparticles and monoclicked (red) by Alk-anisidine and (black) by AHQI.

In order to quantify the click UV-vis absorption spectra were performed on the photoacid and the stalk:

Photoacid		pH-sensitive nanogate	
λ (A max)	ϵ (Mcm) $^{-1}$	λ (A max)	ϵ (Mcm) $^{-1}$
265	13200	261	4800

Table 9: spectral data of the photoacid and stalk molecules in ethanol

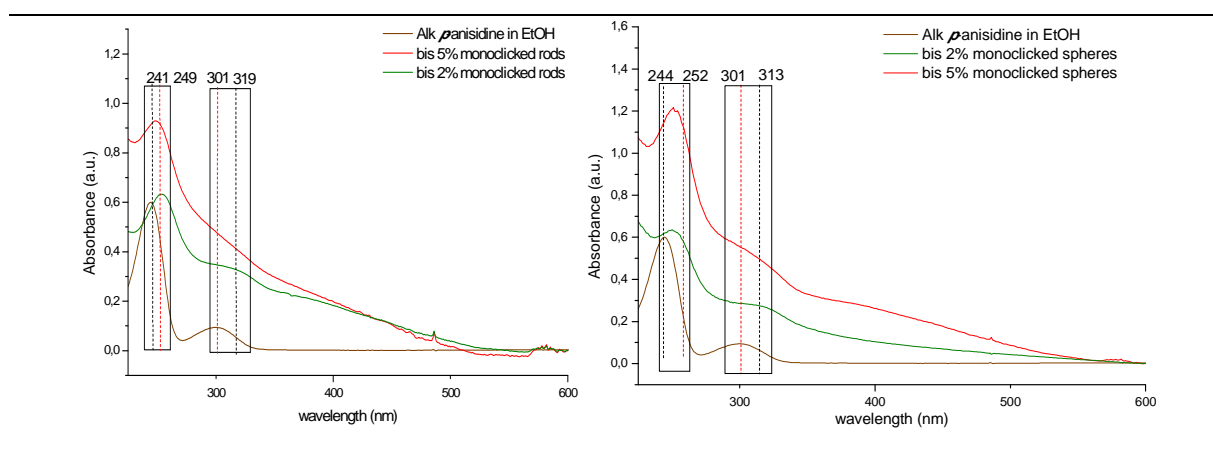


Figure 46: Absorption spectra of (green) 2% and (red) anisidine-monoclicked (left) nanorods and (right) nanospheres. Brown spectrum is the Alk-anisidine in EtOH.

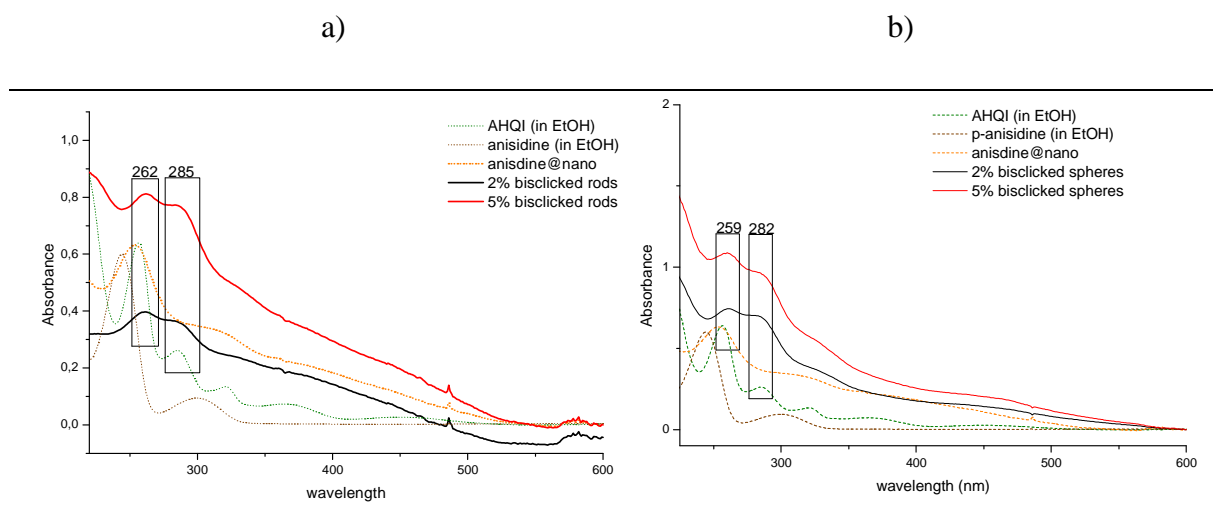


Figure 47: Absorption spectra of bisclicked (a) nanorods (a, red) bis 5% and (a, black) bis 2% and (b) nanospheres (b, red) bis 5% and (b, black) bis 2%. Dashed spectra are (orange) the corresponding anisidine monoclabeled nanoparticles (green) AHQI in ethanol and (brown) Alk-anisidine in ethanol.

UV-vis absorption spectra of the anisidine monoclabeled nanoparticles show an absorption profile (λ 249 and 319 nm) matching that of the alk-anisidine molecule in solution (λ 241 and 301 nm).

Absorption spectra of bisclicked nanoparticles are more complicated since the clicked molecules absorption highly overlaps. AHQI is displaying a higher molar extinction coefficient, however, it displays a clear modification relative to the monoclabeled absorption profile where a new strong absorption band appears at 285 nm mainly corresponding to the clicked AHQI. The functionalization rate is calculated for the first and the second click reaction. Evidently, the stalk which is clicked first provokes higher conversion than the photoacid. Nanospheres clearly showed a more important concentration of clicked molecules than the nanorods. In all the cases, the click conversions are higher in 2% bisclicked nanoparticles than their equivalents of 5%.

[Clickable functions]	Functionalization (mmol/g) (conversion%)			
	Stalk		Photoacid	
	2%	5%	2%	5%
Nanorods	0.16 (35%)	0.34 (29%)	0.05 (16%)	0.11 (13%)
Nanospheres	0.29 (65%)	0.41 (38%)	0.10 (30%)	0.14 (17%)

Table 10: functionalization rate of the clicked molecules on bisclickable nanoparticles

N₂-sorption analyses show a decrease of the adsorbed amounts after CuAAC reactions with a decrease in BET surface area and total pore volume (Table 11) compared with the parent nanoparticles (Figure 48, Figure S9). However, the surface area and the pore volume are still high enough to retain cargo molecules especially in the case of 2% clicked nanoparticles.

	nanospheres		Nanorods	
[functionality]	2%	5 %	2%	5 %
BET surface area (m ² /g)	432	107	297	100
Total pore volume (cm ³ /g)	0.23	0.09	0.19	0.05

Table 11: textural data of the bislicked nanoparticles

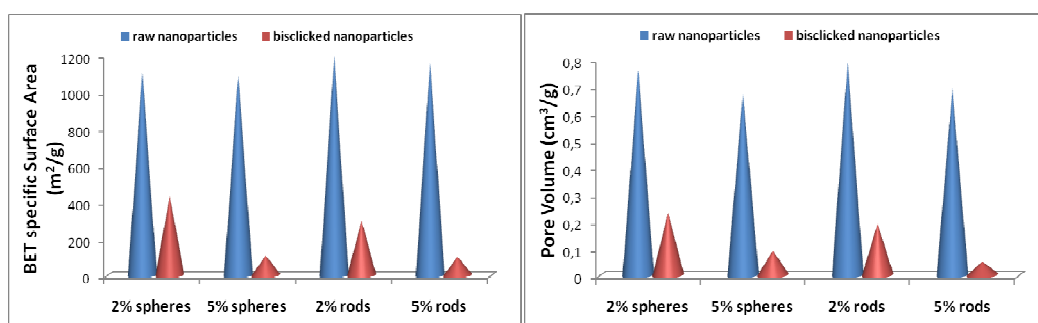


Figure 48: Evolution of the (left) specific surface area and (right) total pore volume in (blue cones) parent and (red cones) bislicked nanoparticles

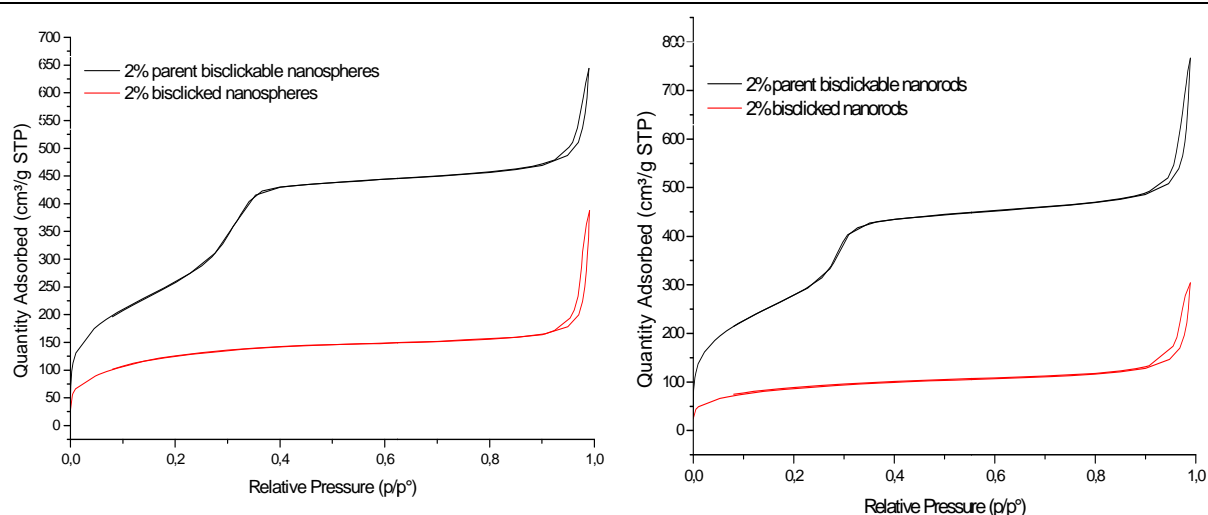


Figure 49: N₂ physisorption isotherms of (black) parent and (red) 2% bislicked (left) nanospheres and (right) nanorods.

7.2. Release Tests and photoacid effect control

The release of the rhodamine B dye was tested in water by irradiating with 365 nm UV-vis light a cuvette containing water and nanoparticles loaded with the dye and functionalized with the photoacid and the pH-sensitive nanogate.

Furthermore, in order to outline the effect of photoacid on the proton transfer, nanoparticles (5%) clicked only with the nanogate and capped by cyclodextrin were placed in the same conditions under light excitation. The green line (Figure 50) shows that no significant release occurred; only some leakage presumably due to either a residual absorption of the stalk at 365 nm or simply to a defective pore blocking is observed.

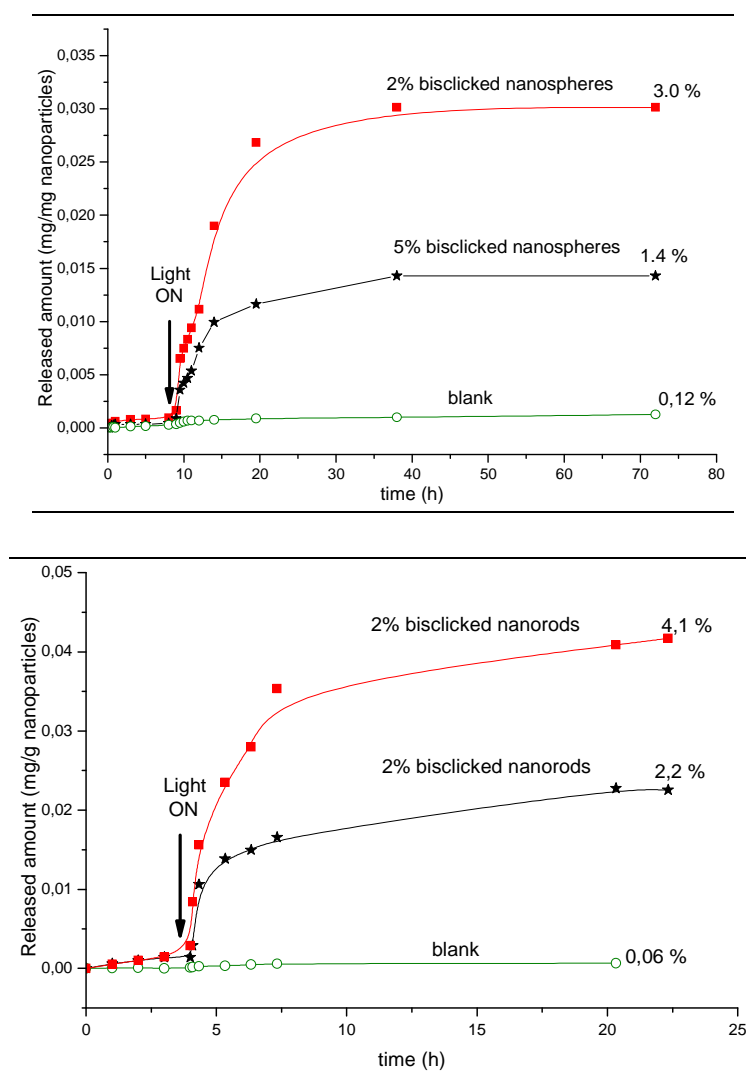


Figure 50: released amount (mg) profile of (up) nanospheres and (down) nanorods bisclicked with (red squares) bis 2% and (black stars) bis 5% clicked functions along with (green circles) the blank experiment with only stalk and cap.

Nanospheres and nanorods exhibit a close release profile (Figure S10). Before light excitation they exhibit a flat baseline indicating that minimum leakage occurs (5% in case of 2% nanorods maybe due to the low concentration of introduced functions). Once the excitation started, a drastic increase of the release was seen, after 1 to 2 h of excitation about 40% of the cargo amount was released. The nanorods display the higher release rate (80% released amount in 3 h against 7 h for the nanospheres). The maximum of release is attained after about 15 h for the nanorods and 30 h for nanospheres.

Again, both 2% nanorods and nanospheres exhibit the best loading capacity with 4.1% and 3% respectively. Only half of these amounts is retained in 5%-clicked nanoparticles with 2.2% and 1.4% for the nanorods and the nanospheres respectively.

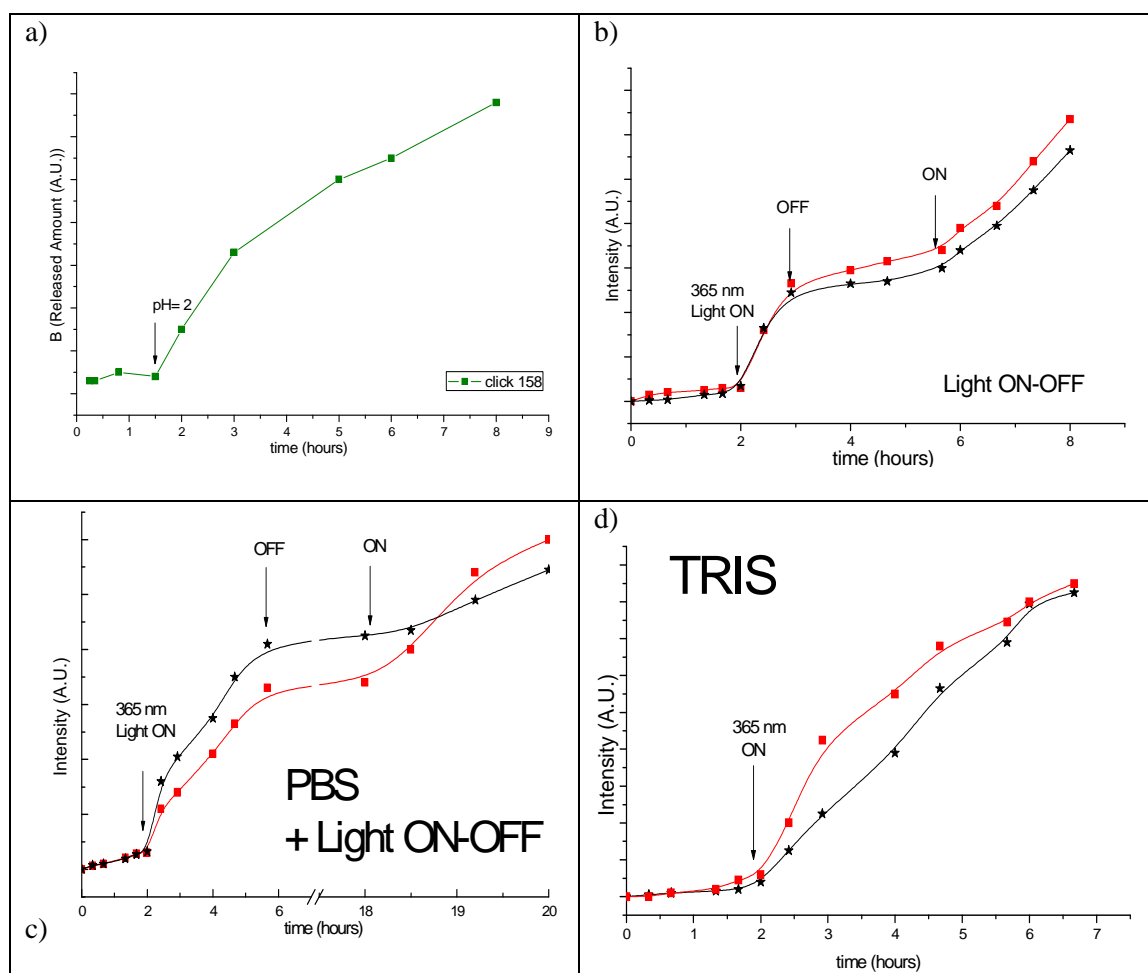


Figure 51: Monitoring of rhodamine B release profile after (a) bulk acidification of a stalk-monoclicked 2% nanorod, (b) sequential on and off cycles on a bislicked nanorods, (c) using PBS buffer while making sequential on and off cycles and (d) using TRIS buffer. Red and black traces are respectively 2% and 5% bislicked nanorods.

Following a bulk acidification of the medium to pH = 2 using 1 M HCl (Figure 51 a), a clear increase of the absorption is shown which is another proof of the effect of the H⁺ to destabilize the supramolecular valve and induce the dye escape.

7.2.1. On-command activation of the nanosystem

In order to prove the controlled activation of the nanomachine, the excitation light was repetitively turned on and off to track the variation of absorbance intensity in the medium (Figure 51 b). At first, the lamp was left off over 2 hours, no absorbance was detected. Once the 365 nm light was turned on, a clear increase of the absorbance of the liberated rhodamine was seen. One hour later the lamp was switched off and the absorbance increase becomes very limited which means that no more H⁺ is protonating the stalk hence no more dye is exiting. The light was turned on for a last time, the rate of release increases again confirming the controlled light-induced activation of the nanomachine. It is noteworthy that the on-command activation aspect was also proved in PBS buffer solution to ensure that the ambient medium has no effect on this studied character.

7.2.2. Release in PBS and TRIS buffer solutions

Testing the release feasibility in PBS buffer solution is of primary importance because of the close character to the physiologic media. The release experiments were also carried out in buffer solutions using PBS (pH =7.2) and TRIS (pH =8.4). Both experiments showed an important increase of absorbance intensity of the medium upon 365 nm light excitation (Figure 51 c). The successful release in buffered solutions means that the concentration of liberated protons is high enough to protonate the stalks. These results indicate that the cocondensation of clickable moieties followed by a CuAAC-functionalization can overcome the limitations encountered at this level by using the conventional grafting of functional groups on surface silanols.

7.3. Conclusion

Bisclickable MSNs were successfully clicked by both a molecular photoacid and a stalk on which a macromolecule (cyclodextrin) was non-covalently tethered, acting as a gatekeeper. The amounts of photoacid and stalk were deduced by analytical techniques (especially absorption spectroscopy). The presence of cyclodextrin was indirectly confirmed by the very low leaking before excitation.

Most importantly, the photoacid effect was also demonstrated by exciting gated nanoparticles with no photoacid clicked. Only very little cargo release was observed bringing into light the viability and the validity of the photoacid concept on this system.

8. General conclusion of chapter III

Mono and multi clickable mesoporous silica nanoparticles were successfully synthesized with an optimal size (close to 100 nm) with different shapes (spheres and rods with different aspect ratio) in respect to many cellular uptake studies results.

Monoclickable MSNs were demonstrated to constitute a very robust platform for controlled release of molecules. Azobenzene molecules were covalently tethered by CuAAC click reaction and fully characterized. The efficiency of the nanoimpelling system was outlined by *in vial* experiments.

Multiclickable MSNs were then conceived and successfully optimized. These nanoparticles hold two different clickable functions allowing them to combine different functionalities with selected properties and without real concerns about the type and the chemical nature of the molecule since CuAAC is carried out with mild conditions. Before transporting these nanoparticles into the universe of drug delivery, we had to investigate the possible interaction between the clickable functions in order to design novel systems in controlled drug release. Fluorophores have been clicked to prove by FRET the proximity and the available communication between functions. Therefore, we designed a light triggered system relying on a pore gate (cyclodextrin) that non-covalently binds a clicked stalk next to a photoacid that upon excitation transfers a proton to the stalk to decrease the affinity with the gate keeper, liberating then the entrapped cargo. Release experiments outlined the effect of the photoacid-to-stalk proton transfer and proved the on-command release of the cargo. Successful release was also achieved while using buffered solutions (PBS and TRIS) which can extend the application of this system to cell studies. Biotests will be carried out by our collaborators in IBMM-Montpellier.

The final approach also relies on the azobenzene impelling behavior but combined with a targeting agent (Folic Acid) that was successfully clicked. This system displays high importance since targeting agents are continuously required in cancer cell treatment to decrease side effects. *In vial* release tests demonstrated that the azobenzene efficiency is not altered by the presence of folic acid. The first *in vitro* studies show that the “raw” system has very little cytotoxicity and thus the CuAAC reaction is compatible with the bioapplications. A successful cell death was only seen in the case of the copresence of azobenzene and folic acid suggesting highlighting the crucial role of the folic acid in the cell targeting.

General conclusion of the thesis
&
Outlooks

General Conclusion of the thesis

In this work, we have first made use of clickable bissilylated precursors to synthesize clickable periodic mesoporous organosilica as microrods and mesoporous bridged silsesquioxanes bearing azide or alkyne groups as agglomerates of nanoparticles of 20-30 nm. These materials were subjected to extensive CuAAC click reactions using different model molecules having a signature by easily accessible analytical methods (vibrational spectroscopy, elemental analysis, solid-state NMR), in order to prove and quantify the conversion of the clickable fragments. High extents of functionalization (between 35 and 90% depending on the material and the clicked function) were characterized. Furthermore, we have demonstrated the feasibility of two more approaches to prepare functional silica by CuAAC and sol-gel, either by performing the hydrolysis-condensation of a sol-gel precursor bearing one functionality and obtained by the CuAAC reaction, or by carrying out the click reaction along with the sol-gel process taking benefit of their close kinetics.

The afore-mentioned clickable mesoporous bridged silsesquioxane has then undergone a significant surface modification *via* CuAAC in order to tune the hydrophilic/lipophilic balance. Water and cyclohexane vapor sorption experiments showed that the adsorption properties of the resulting materials were drastically modified with respect to the hydrophilic or lipophilic character of the adsorbate. This study highlights the potential of the CuAAC reaction to easily tailor the materials properties in view of the targeted applications.

Aiming at preparing complex controlled drug delivery systems in a reliable and controlled fashion, we then applied the CuAAC methodology to mesoporous silica nanoparticles (MSNs). This study was initiated by the need of multifunctional systems holding complex organic fragments (supramolecules, macrocycles, and metal nanoparticles) to produce new generations of nanomachines. The CuAAC-post-functionalization approach has allowed an easier design of nanoparticles bearing one or two types of functionalities. Indeed, we have conferred a dual functionality to MSNs by anchoring azobenzene groups as release controller and folic acid for specific targeting of cancer cells. The preliminary results of *in vitro* tests show an important effect for the combination of the clicked folic acid and the azobenzene in MCF-7 cell death.

We have then demonstrated by FRET that two distinct clicked fluorophores, for various loadings (1-5 mol %) can communicate owing to their close proximity (<3.5 nm). This feature

was exploited to design a novel type of light-triggered nanomachine for controlled drug delivery, based on a proton transfer between a clicked photoacid and a clicked pH-sensitive nanogate. The success and mechanism of this original approach was here also demonstrated *via* release experiments in solution (water) and even using buffer solutions making possible the extension of this system to bioapplications and highlighting the homogeneous concentration of the active moieties on the surface.

Outlooks

The CuAAC click reaction still has a fruitful future in several domains. Applying CuAAC to siliceous materials especially PMOs and BS may widely extend the scope of application to various research areas. In particular, it is fairly important to make clickable PMO nanoparticles for demanding applications especially in catalysis or nanomedicine.

Mesoporous silica nanoparticles were bi-functionalized via azide and alkyne groups. A third clickable group can be incorporated (such as protected alkyne-TIPS, hydroxyamine...) offering the possibility to prepare nanoparticles bearing more (bio)functionalities for increased performances in controlled drug release. Furthermore, the development of copper-free strain promoted azide-alkyne cycloaddition should allow circumventing the possible problems associated with remaining copper traces.

The *in vitro* tests of the nanomachines produced in Chapter II should be accomplished. To this aim, their colloidal stability should be investigated in conditions close to physiological medium by zeta potential measurements; the cellular uptake and toxicity should be investigated.

Experimental Section

Experimental Section

General

***Azide compounds are potentially explosive. Great care and protection are needed for heating of these compounds. ***

-All the syntheses of silylated molecules were carried out using Schlenk techniques under a dry atmosphere of nitrogen

- Microwave reactions were carried out in sealed tubes using a CEM Discover Microwave Reactor equipped with an infrared temperature sensor. All the clicked silylated molecules syntheses were made under strong stirring with irradiation at 100°C (P_{max}=200 W) for 5 min

- FTIR spectra were recorded using a Perkin100 spectrometer equipped with a mono internal reflexion ATR module (diamant).

- Raman spectra were recorded with a LabRAM ARAMIS (Horiba) spectrometer using a HeNe laser (633 nm)

-UV-Vis absorption spectra were obtained from dispersions of nanoparticles in ethanol or water using an Agilent 8453 UV-visible Spectroscopy System

-Fluorescence spectra were obtained using a Perkin-Elmer LS 55 fluorimeter.

-NMR spectra were recorded in CDCl₃ and DMSO-d₆ at 298 K. ¹H and ¹³C chemical shifts are reported in ppm relative to Me₄Si.

-Solid state ¹³C and ²⁹Si CP/MAS NMR experiments were recorded on a Varian VNMRS 300 MHz spectrometer using a two channel probe with 7.5 mm diameter-size ZrO₂ rotors and TMS as reference for the chemical shifts.

-Scanning electron microscopy (SEM): The SEM images were obtained with a Hitachi S-4800 apparatus after platinum metallisation.

-Transmission electron microscopy (TEM) micrographs were obtained using a JEOL 1200 EX2 apparatus equipped with a SIS Olympus Quemesa 11 Mpixel camera.

-The small and wide angle X-ray scattering (SWAXS) experiments were conducted using a Guinier-Mering setup with a 2D image plate detector. The X-ray source was a molybdenum anode, which delivered a high-energy monochromatic beam ($\lambda=0.71 \text{ \AA}$, E=17.4 keV), providing structural information over scattering vectors q ranging from 0.01 to 1.5 \AA^{-1} .

Helium flowed between the sample and the image plate to avoid air adsorption. The sample acquisition time was 3600s. The image azimuthal average was determined by the FIT2D software from ESRF (France). In order to normalize all spectra by the width of solid sample e_s , which depends on the material porosity, we determine it by using the experimental sample transmission T_s and the X-ray linear attenuation coefficient μ_s of the solid material from:

$$e_s = -\frac{\ln(T_s)}{\mu_s}$$

-The N₂-sorption measurements were performed on an ASAP 2020 (Micromeritics) at 77.4 K. The different samples were activated for 5 hours at 40 °C prior to the analysis. The BET specific surface areas were determined from the linear part of the BET transform of the adsorption isotherms. The Henry's constants were calculated by determining the slope of the adsorption isotherms below $p/p^\circ=0.01$. Prior to the vapour adsorption experiments cyclohexane (provided by Aldrich, purity >99.9%) was stored over an activated 3Å molecular sieve. The deionized water reservoir was outgassed for 10 minutes under reduced pressure. The sorption experiments were performed using a purpose-built adsorption apparatus already described.^{258,259} This set-up is based on gravimetric measurements, using a magnetic compensation balance provided by SETARAM, with a resolution better than 0.05µg. The pressure in the sample cell can be recorded by two capacitive pressure gauges (0-10 Torr and 0-1000 Torr). The materials were activated for 5 hours at 313 K before adsorption. Vapour adsorption was performed at 313 K with a thermal stability of the sample better than 0.1 K. For each point on the adsorption isotherm obtained, the system was considered to have reached a state of thermodynamic equilibrium when the mass did not vary over a period of at least 600 s. Allowing longer equilibration times gave the same sorption isotherms, thus validating the choice of 600 s as an equilibrium criterion. The exact time to reach equilibrium depended on the relative vapour pressure considered.

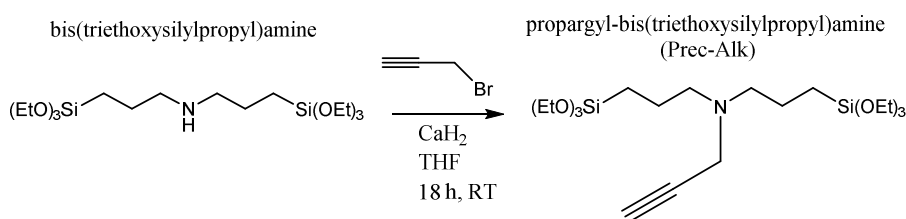
Syntheses

CHAPTER II

tris(triphenylphosphine)bromocopper: $\text{CuBr}(\text{PPh}_3)_3$ ²⁶⁰

MeOH is heated to boiling, and triphenylphosphine (4.7 g, 18 mmol) is slowly added. After complete dissolution, CuBr_2 (1.0 g, 4.5 mmol) is added in small portions. After completion of the addition, the contents are stirred for 30 minutes at reflux, and the flask is allowed to cool to room temperature. The precipitate is filtered off; and the white residue is washed with ethanol, then ethyl ether. The resultant solid is dried under vacuum, to yield $\text{CuBr}(\text{PPh}_3)_3$ as a white solid in quantitative yield.

Propargyl-bis(triethoxysilylpropyl)amine (Prec-Alk)



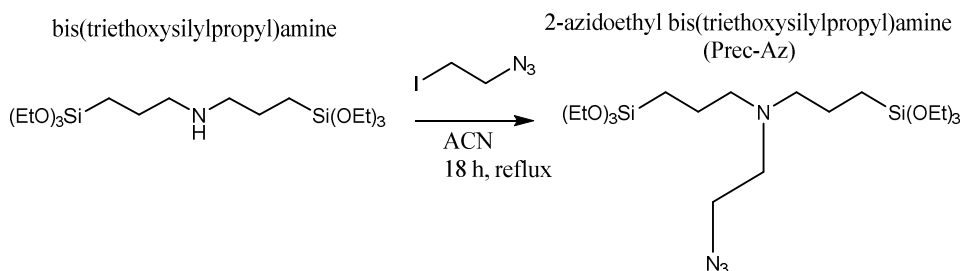
To a solution of bis(triethoxysilylpropyl)amine (25.5 g, 60.0 mmol) in moist THF containing 1000 ppm H_2O (250 mL), calcium hydride (6.2 g, 150 mmol) and propargyl bromide (80 wt% in toluene, 8.6 g, 72.0 mmol) were added successively. The reaction mixture was stirred overnight at room temperature under argon. After evaporation of the solvents, extraction of the reaction mixture with pentane and concentration, a yellowish viscous oil was obtained which was purified by distillation under reduced pressure ($130^\circ\text{C}/0.02\text{mbar}$) giving a colorless liquid (26.4 g, 56.8 mmol). Yield: 95 %.

^1H NMR (400 MHz, CDCl_3) δ = 3.81 (q, J = 7.0 Hz, 12H), 3.38 (d, J = 2.3 Hz, 2H), 2.56 – 2.34 (m, 4H), 2.13 (t, J = 2.3 Hz, 1H), 1.65 – 1.46 (m, 4H), 1.21 (t, J = 7.0 Hz, 18H), 0.66 – 0.56 (m, 4H).

^{13}C NMR (101 MHz, CDCl_3) δ = 79.0, 72.5, 58.4, 56.7, 41.83, 21.0, 18.4, 8.1.

HRMS (ESI⁺): calcd for $\text{C}_{21}\text{H}_{46}\text{NO}_6\text{Si}_2$, 464.2864; found, 464.2871.

(2-azidoethyl) bis(triethoxysilylpropyl)amine (Prec-Az)



A mixture of bis(triethoxysilylpropyl)amine (13.1 g, 30.5mmol), 1-azido-2-iodoethane (6.15 g, 30.5 mmol) and potassium carbonate (6.3 g, 60mmol) in dry acetonitrile (200 mL) was stirred overnight at 85°C in a sealed tube. The mixture was then concentrated, the product was extracted with pentane. The solution was filtered and the filtrate was concentrated giving a yellowish oil (14.5 g, 22.3mmol). Yield: 95 %.

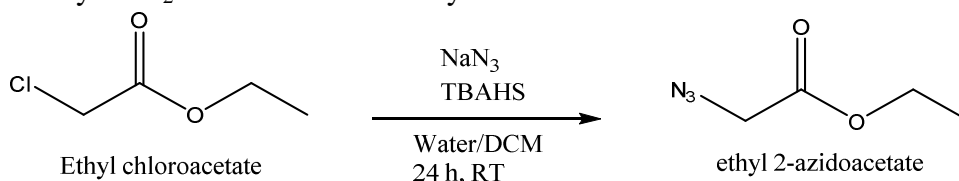
^1H NMR (400 MHz, CDCl_3) δ = 3.81 (q, J = 7.1 Hz, 12H), 3.25 (t, J = 6.4Hz, 2H), 2.65 (t, J = 6.4 Hz, 2H), 2.46 (t, J = 7.4 Hz, 4H), 1.54 (m, 4H), 1.22 (t, J = 7.1 Hz, 18H), 0.59 (m, 4H).

^{13}C NMR (101 MHz, CDCl_3) δ = 58.6, 57.6, 53.7, 49.8, 20.7, 18.6, 8.1.

HRMS (ESI⁺): calcd for $\text{C}_{20}\text{H}_{47}\text{N}_4\text{O}_6\text{Si}_2$, 495.3034; found, 495.3016.

Ethyl 2-azidoacetate²⁶¹:

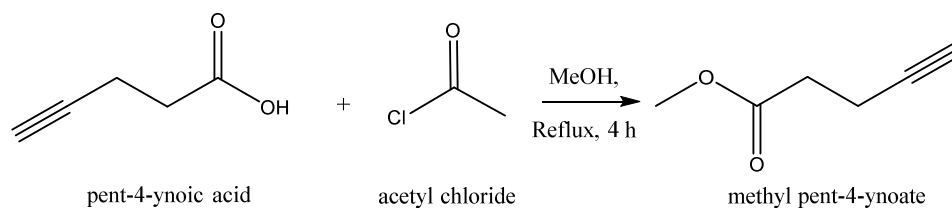
It is obtained by a $\text{S}_{\text{N}}2$ reaction between ethyl chloroacetate and sodium azide



Ethyl chloroacetate (12.2 g, 100 mmol) was dissolved in a (50mL / 50mL) water-dichloromethane mixture followed by the addition of NaN_3 (13 g, 200 mmol) and tetrabutylammonium hydrogenesulfate TBAHS (3.4 g, 10 mmol) and the mixture was stirred for 24 h at room temperature.

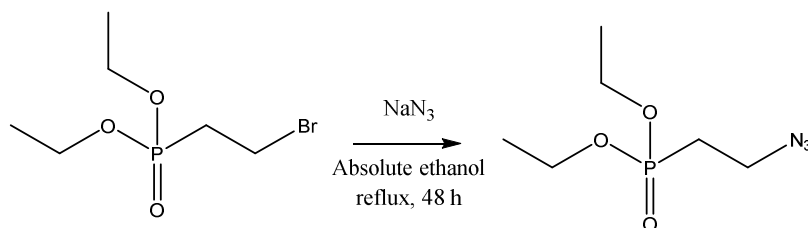
The aqueous phase was separated then extracted with 150 mL DCM and the combined organic layer was then dried over MgSO_4 , filtered and concentrated to afford ethyl azidoacetate as a clear liquid (12.7 g, 96 mmol) with 98% yield.

Methyl pent-4-ynoate:



Acetyl chloride (22.0 mL, 24.3 g, 0.31 mol) was added dropwise over 15 min. to a solution of 4-pentynoic acid (20 g, 204 mmol) in methanol (100 mL) and the mixture was heated under reflux for 4 h. The mixture was cooled, poured into aqueous sodium hydroxide (1M) and extracted with ether. The combined organic fractions were washed with aqueous sodium hydroxide (1M), dried (MgSO_4) and the solvent was evaporated under reduced pressure to give the title compound as pale yellow oil. Yield (22.5 g, 98%).

Diethyl 2-azido ethylphosphonate^{262,263}



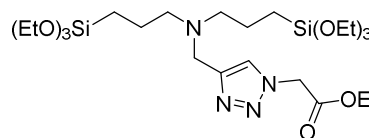
To a mixture of NaN_3 (1.3 g, 20 mmol) in 10 mL ethanol, diethyl 2-bromoethylphosphonate (1.0 g, 4.1 mmol) was added dropwise and the mixture was heated to reflux for 48 h. The solvent was then removed under reduced pressure and water was added to dissolve the salts. The product was extracted with DCM, washed with brine and dried over MgSO_4 . The combined organic phase was concentrated under reduced pressure to afford the 2-azido ethylphosphonate. Yield: 0.72 g, 86 %.

General procedure for the synthesis of functional precursors (A, B and C) by CuAAC reaction:

A microwave tube was filled under nitrogen with alkyne (2 mmol), azide (2 mmol / alkyne function), [CuBr(PPh₃)₃] (0.01 mmol / alkyne function), dry triethylamine (1 mL) and dry THF (2 mL) and then sealed. The mixture was irradiated by microwaves (P max = 200 W) under strong stirring at 100 °C for 5 minutes. The completion of the reaction was checked by FTIR or TLC. The reaction mixture was allowed to cool, and then the solvents were removed under vacuum. After addition of dry pentane, the mixture was extracted under reduced pressure, and the organic phase was concentrated to afford the title compound.

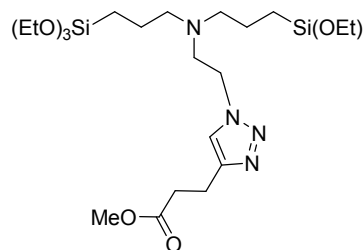
Precursor A

Yield: 92%. ¹H NMR (400 MHz, CDCl₃) δ = 7.56 (s, 1H), 5.11 (s, 2H), 4.23 (q, *J* = 7.2 Hz, 2H), 3.76 (s, 2H), 3.71 (q, *J* = 7.0 Hz, 12H), 2.41 (m, 4H), 1.56 (m, 4H), 1.27 (t, *J* = 7.2 Hz, 3H), 1.19 (t, *J* = 7.0 Hz, 18H), 0.57 – 0.34 (m, 4H). ¹³C NMR (101 MHz, CDCl₃) δ = 166.3, 146.2, 123.7, 62.3, 58.3, 56.6, 50.8, 48.8, 20.5, 18.3, 14.1, 7.9. HRMS (ESI⁺): calcd for C₂₅H₅₃N₄O₈Si₂, 593.3402; found, 593.3407.



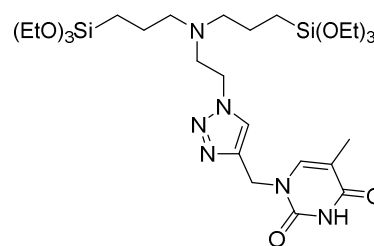
Precursor B

Yield: 98%. ¹H NMR (400 MHz, CDCl₃) δ = 7.44 (s, 1H), 4.33 (t, *J* = 6.5 Hz, 2H), 3.71 (q, *J* = 7.0 Hz, 12H), 3.67 (s, 3H), 3.02 (t, *J* = 7.5 Hz, 2H), 2.85 (t, *J* = 6.5 Hz, 2H), 2.73 (t, *J* = 7.5 Hz, 2H), 2.44 (m, 4H), 1.47 (m, 4H), 1.21 (t, *J* = 7.0 Hz, 18H), 0.57 – 0.34 (m, 4H). ¹³C NMR (101 MHz, CDCl₃) δ = 173.1, 145.8, 121.8, 58.2, 57.1, 54.2, 51.5, 48.7, 33.4, 20.9, 20.3, 18.2, 7.7. HRMS (ESI⁺): calcd for C₂₆H₅₅N₄O₈Si₂, 607.4069; found, 607.4048.



Precursor C

Yield: 98%. ^1H NMR (400MHz, CDCl_3), δ = 7.79 (s, 1H), 7.30 (s, 1H), 4.92 (s, 2H), 4.35 (t, J = 6.4 Hz, 2H), 3.80 (q, J = 7.1 Hz, 12H), 2.85 (t, J = 6.3Hz, 2H), 2.43 (m, 4H), 1.87 (s, 3H), 1.46 (m, 4H), 1.20 (t, J = 7.1 Hz, 18H), 0.51 (m, 4H). ^{13}C NMR (63 MHz, CDCl_3), δ = 164.3, 150.9, 142.1, 140.4, 124.5, 111.2, 58.6, 57.2, 54.3, 49.2, 43.2, 20.4, 18.5, 12.5, 8.05. HRMS (ESI+): calcd for $\text{C}_{28}\text{H}_{55}\text{N}_6\text{O}_8\text{Si}_2$, 659.3620; found, 659.3617.



Synthesis of periodic mesoporous organosilicas M1 and M2:

Precursor (**Alk** or **Az**) (2.0 mmol) was added to a mixture of sodium hexadecylsulphate SHS (containing 40% of sodium stearylsulphate, 531 mg, 1.5 mmol) in water (36 mL, 2.0 mol) and hydrochloric acid (1 M, 4 mL, 4 mmol) at 60°C. A white precipitate formed after 1 minute. The mixture was stirred for 30 min at 60 °C then filtered and washed with water and ethanol. The white solid was dried at 70 °C for 12 h. The surfactant was eliminated by washing the solid with a solution consisting of 200 mL of ethanol and 10 mL of NH_4NO_3 in ethanol (20 g/L) and the resulted material was dried at 50°C overnight. Yield **M1** m = 398 mg, **M2** m = 381 mg.

Synthesis of mesoporous materials M3 and M4:

Under vigorous stirring, **Prec-Alk** or **Prec-Az** (10mmol) was added to a mixture of CTAB (2.9 g, 8 mmol), PFOA (0.2 g, 6 %wt of CTAB, 0.48 mmol), distilled water (170 mL, 9.7 mol) and NH_4OH (25 %wt, 23 mL, 0.3 mol). The mixture was heated to 70°C and stirred for 24 hours.

The molar ratio of the starting compounds was **Prec-Alk** or **Prec-Az** /CTAB / PFOA/ $\text{NH}_3/\text{H}_2\text{O}$ = 1 : 0.79 : 0.048: 30 : 1500

The material was recovered by evaporating the water at atmospheric pressure. The surfactant was eliminated by repeated washings with a solution consisting of 100 mL ethanol and 5 mL of 37% HCl. Finally, the material was stirred overnight at RT in a solution of 100 mL ethanol and 3 mL NH_4OH 25% wt to afford the amine then dried at 50°C for 4 h. Yield **M3** 2.55 g, **M4** 1.95 g.

Synthesis of M-Thy:

Precursor **C** (0.46 g, 0.7 mmol) was dissolved in a solution of ethanol (1.4 mL, 42 mmol, [Si] = 1 M). Under vigorous stirring, distilled water (0.23 g, 4.2 mmol) was added together with NH₄F (1 M in water, 14 μ L, 14 μ mol). The mixture was stirred vigorously for two minutes then kept at room temperature. A gel was obtained after 12 h. After 48 h of aging, the temperature was raised to 70°C for 18 h. The resulting powder was washed with water, ethanol and acetone and finally dried at 60°C for 5 h. A light-green powder (365 mg) was obtained. The molar ratio of the starting compounds was

Prec C/ethanol/water/NH₄F 1: 60: 6: 0.02 .

Synthesis of M5 and M6

Clickable organosilylated precursor (**Prec Alk** or **Prec Az**) (1.7 mmol, 3.4 mmol Si) was dissolved in a solution of ethanol (3.4 mL, 102 mmol, [Si] = 1 M). Under vigorous stirring, distilled water (1.9 g, 10.6 mmol) was added together with NH₄F (1 M in water, 0.17 mL, 0.17 mmol, 5% eq Si). The mixture was stirred vigorously for two minutes then kept at room temperature. A gel was obtained 24 h later. After 48 h of aging, the temperature was raised to 70°C for 18 h. The resulting powder was washed with water, ethanol and acetone and finally dried at 60°C for 5 h. Materials afforded from Prec-Alk and Prec-Az are denoted respectively **M5** and **M6**. The molar ratio was: Si/ EtOH/ H₂O/F⁻ : 1/ 30 /3/0.05.

Synthesis of M5-op and M6-op

Clickable organosilylated precursor (**Prec Alk** or **Prec Az**) (1.7 mmol, 3.4 mmol Si) was dissolved along with the clickable partner (Azidomethylpyrene (80 mg, 0.4 mmol, 20% eq alkyne) or methyl pent-4-ynoate (40 mg, 20% eq azide)) and sodium ascorbate (12.6 mmol, 25 mg) in a solution of ethanol (3.4 mL, 102 mmol, [Si] = 1 M).

Under vigorous stirring, distilled water (1.9 g, 10.6 mmol) and THF (0.5g, 7 mmol) were added together with sol-gel hydrolysis catalyst NH₄F (1 M in water, 0.17 mL, 0.17 mmol, 5% eq Si) and CuAAC catalyst CuBr(PPh₃)₃ (60 mg, 64 μ mol). The mixture was stirred vigorously for two minutes then kept at room temperature. A gel was obtained 24 h later. After 48 h of aging, the temperature was raised to 60°C for 12 h. The resulting powder was copiously washed with water, ethanol and acetone and finally dried at 60°C for 5 h. The *in*

situ pyrene and pentynoate clicked materials are denoted respectively **M5-op** and **M6-op** (op: one pot).

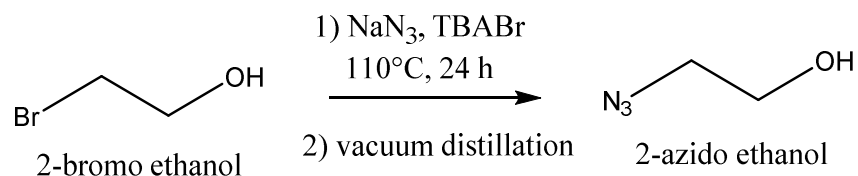
General procedure for the CuAAC reaction on the materials:

The clickable material (0.1 mmol) was incubated with the corresponding clickable partner (0.3 mmol) in the presence of copper sulphate CuSO₄ (0.1 mmol) and sodium ascorbate (0.4 mmol) in 3 mL of water/t-butanol mixture (v/v: 1). The mixture was stirred vigorously at room temperature for 48 h. The material was recovered by centrifugation (26000 rpm, 10 min) and washed with water, sodium *N,N*-diethyldithiocarbamate (0.1 M in methanol, 10 mL), methanol (10 mL) and acetone (10 mL). The last three washings were repeated 5 times. The resulting material was dried at 70 °C for 5 h.

B) Surface Tailoring

2-azido ethanol²⁶⁴:

This synthesis consists of a nucleophilic substitution (S_N2) reaction on 2-bromoethanol with sodium azide without any solvent.

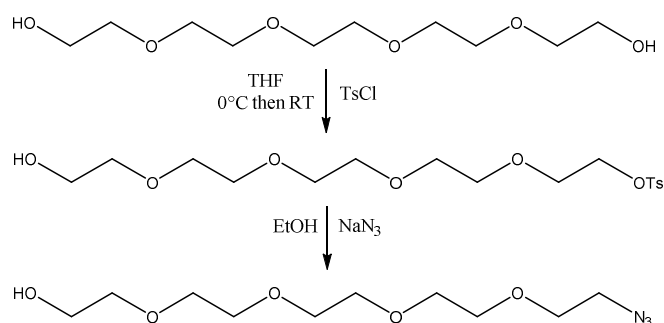


In three parallel experiments, 2-bromoethanol (15 g, 120mmol) was mixed with tetrabutylammonium bromide (1.0 g, 2.23 mmol) and sodium azide (10 g, 154 mmol) in a two-necked round bottom flask equipped with a condenser and heated to 110°C for 24 h.

! Danger: Protect the reaction flasks with a Plexiglas shield.

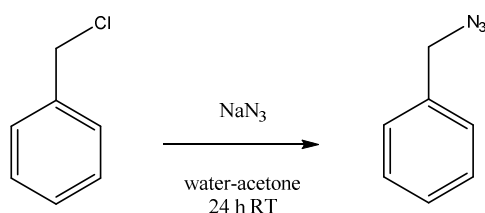
After cooling to room temperature, the content of the 3 flasks were mixed and filtered on celite while extracting with diethyl ether.

The filtrate was concentrated under reduced pressure to afford yellow oil. This latter was then distilled to give the ethanol azide as a clear liquid (m=27.5 g, yield = 90%).

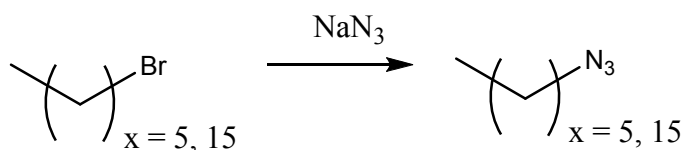
PEG-N₃²⁶⁵

A solution of tetra(ethylene glycol) (27.2 g, 140 mmol) and triethylamine (15 mL, 108 mmol) in dry THF (100 mL) was cooled to 0°C under nitrogen. To this was added *p*-toluenesulfonyl chloride solution (9.53 g, 50 mmol) in dry THF (10 mL) dropwise over 45 minutes.

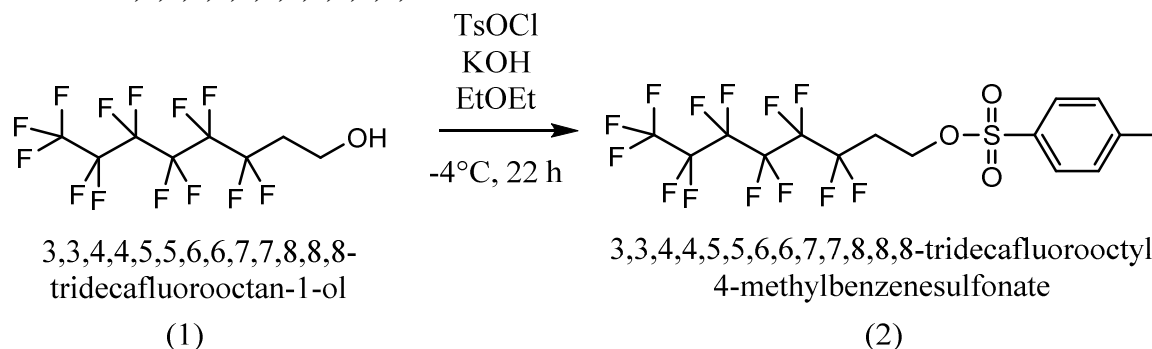
The reaction mixture was allowed to warm to RT and stirred for 16 h. The solvent was removed *in vacuo* and the yellow residue was dissolved in absolute ethanol (100 mL), then sodium azide (6.5 g, 100 mmol) was added as a solid and the mixture was refluxed for 22 h. The solvent was removed *in vacuo* and the residue diluted with Et₂O (250 mL) and washed with brine (50 mL). The organic layer was separated and the aqueous layer extracted with DCM (3 × 100 mL). The organic fractions were combined and dried over MgSO₄, filtered and the filtrate evaporated to yield crude, orange oil (~15 g). Purification by column chromatography (SiO₂, 1:1 cyclohexane/EtOAc to 100% EtOAc) yielded the product as a clear, colourless oil (5.5 g, 50%).

Benzyl azide²⁶⁶:

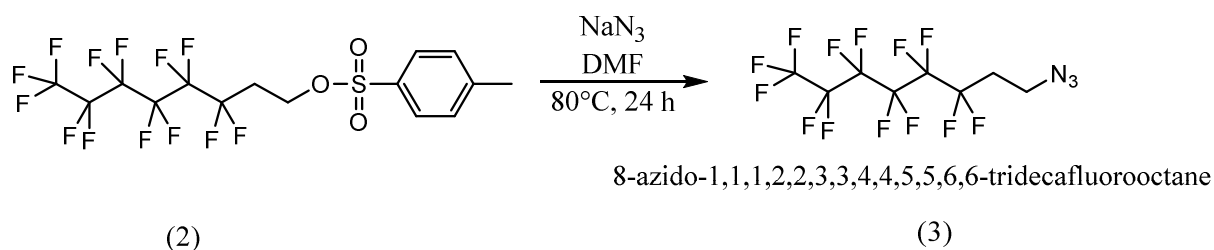
To a stirred solution of the corresponding bromide (1.0 eq) in a 50 mL water/acetone mixture (1:4) was added NaN₃ (1.5 eq). The resulting suspension was stirred at room temperature for 24 hours. DCM was added to the mixture and the organic layer was separated. The aqueous layer was extracted with 3 × 10 mL aliquots of fDCM and the combined organic layers were dried over MgSO₄. The solvent was removed under reduced pressure, and the azide was sufficiently pure to be used without further workup.

Hexylazide²⁶⁷, Hexadecylazide²⁶⁸:

Sodium azide (0.30 mol) was added to a solution of alkyl bromide (0.10 mol) in *N,N*-dimethylformamide (100 mL). The mixture was stirred for 24 h at room temperature. Afterwards, water (300 mL) and heptane were added. The phases were separated then the organic layer was washed with water. The resulting organic phase was concentrated under reduced pressure to afford the alkylazides as clear oils.

1-azido-3,3,4,4,5,5,6,6,7,7,8,8,8 tridecafluorooctane:²⁶⁹

To a solution of tosylchloride (2.1 g, 11.2 mmol) in diethylether (12 mL) at -4°C , tridecafluorooctanol (4.1 g, 11.2 mmol) was added followed by potassium hydroxide (1.58 g, 30 mmol) and the final mixture was stirred at -4°C for 24 h. After warming to room temperature, the mixture was poured into cold water and the organic phase was extracted with ethyl acetate, dried over MgSO_4 and concentrated under reduced pressure to afford compound (2) as a crystalline white powder. Yield 3.0 g, 100%.

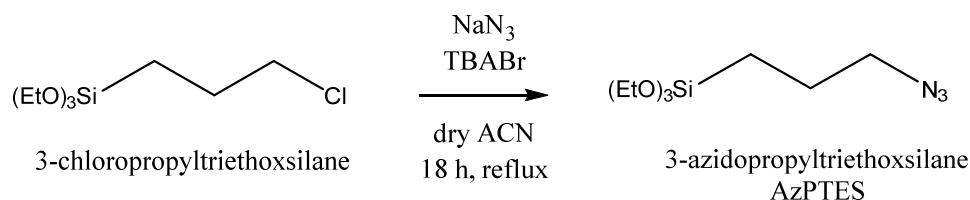


Compound 2 (4.0 g), and sodium azide (1.5 g) were added together to 50 mL DMF and stirred for 24 h at 80°C under argon atmosphere. The mixture was then poured into ice water

(400 mL) and the organic phase was extracted with diethyl ether, dried over MgSO_4 and concentrated to afford compound (3) as a yellowish oil.

CHAPTER III

3-Azidopropyltriethoxysilane : AzPTES⁹⁰.



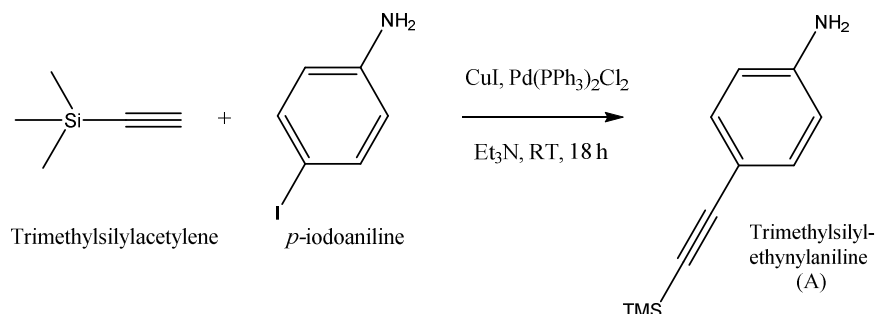
3-Chloropropyltriethoxysilane (20 g, 83 mmol) was added to a solution of sodium azide (10.8 g, 166 mmol) and tetrabutylammonium bromide (6.44 g, 20 mmol) in dry acetonitrile (500 mL), under argon atmosphere. The reaction mixture was stirred under reflux for 18 h. After completion of the reaction, the solvent was removed under reduced pressure. To the crude mixture was added n-pentane and the suspension was filtered over celite. The solvent was evaporated and the crude oil obtained was distilled under reduced pressure of 0.02 mbar at 50°C to give AzPTES as a colorless liquid. Yield: 19 g, 95%.

Monoclickable Mesoporous Silica Nanoparticles:

Synthesis of ethynyl azobenzene²⁷⁰ :

This synthesis is based on three reactions; it starts by a Sonogashira coupling to synthesize a protected ethynylaniline, which is reacted with nitrosobenzene to give the protected ethynylazobenzene. The last step is the removal of the protecting group in basic medium.

A) Sonogashira coupling²⁷¹.

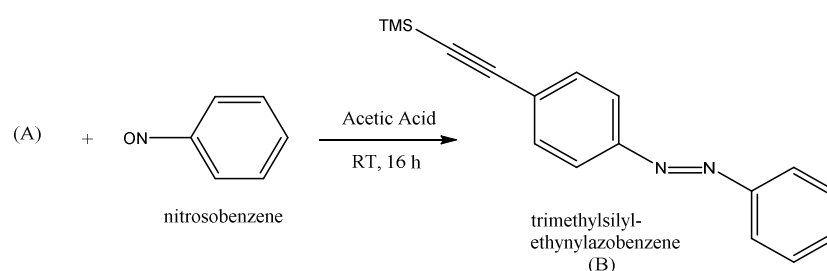


Iodoaniline was previously purified by sublimation under vacuum at 150°C for 4 h.

In a Schlenk round bottom flask, *p*-iodoaniline (3.45 g, 16 mmol), CuI (34 mg, 0.18 mmol), $\text{Pd}(\text{PPh}_3)_2\text{Cl}_2$ (0.1 g, 0.16 mmol) and dry Et_3N (30 mL, 225 mmol) were mixed under argon.

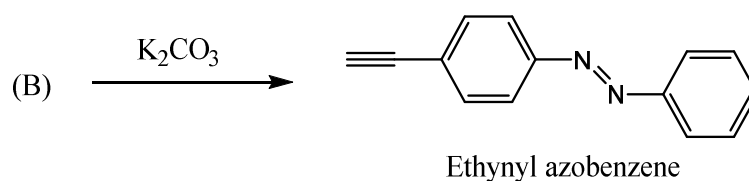
TMS-acetylene (2.5 mL, 17.6 mmol) was then added and the dark brown mixture was stirred at room temperature overnight (18 h). The reaction mixture was then poured into 130 mL of 1 M hydrochloric acid and extracted with diethyl ether. The combined organic layers were washed with concentrated aqueous NaHCO_3 solution and water. The organic phase was finally dried on MgSO_4 , filtered and concentrated under reduced pressure to give a dark brown residue. The latter was purified by chromatography (silica gel 60, particle size 0.040-0.063 mm, the eluent was cyclohexane/ethyl acetate 4:1).

The second step is the reaction of the obtained product (A) with nitrosobenzene as follows:



In a 100 mL bottom rounded flask, (trimethylsilylethynyl) aniline (A) (1.1 g, 5.8 mmol) was dissolved in 30 mL of acetic acid. After the addition of nitrosobenzene (0.58 g, 5.4 mmol, 1 eq), the reaction was stirred at room temperature overnight (18 h). The solvent was then evaporated and the obtained dark orange powder was recrystallized with absolute ethanol to yield the trimethylsilylethynylazobenzene (B).

Finally, the deprotection of (B) occurs as follows:

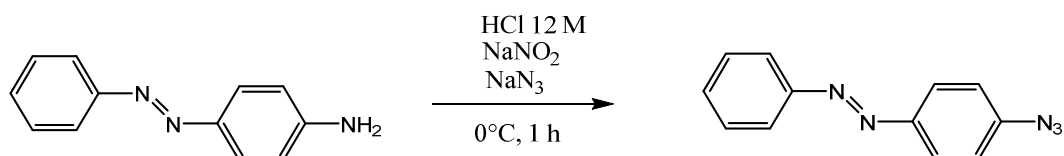


(B) (3.2 g) was dissolved in 25 mL methanol before the addition of K_2CO_3 (3.5 g). The mixture was stirred for 4 h at room temperature. The reaction was monitored by TLC (Eluant: ethylacetate/cyclohexane 1:4). The reaction mixture was then diluted with brine (50 mL) and the organic phase was extracted with diethyl ether, dried over MgSO_4 , filtered and concentrated under reduced pressure to afford the ethynylazobenzene as an orange powder (2.4 g, 75% overall yield).

Bisclickable Mesoporous Silica Nanoparticles:

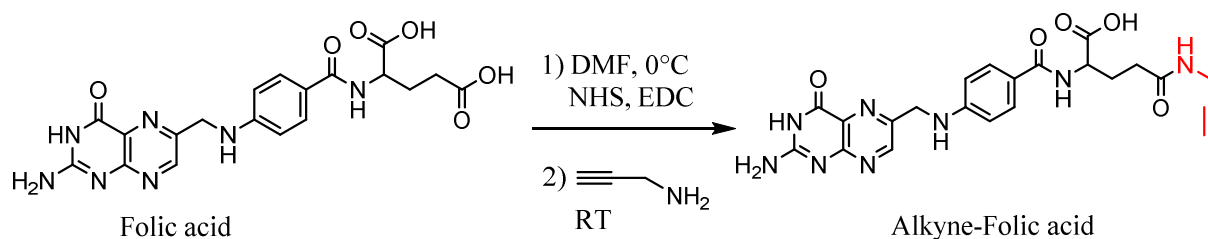
Light-triggered controlled cargo release from a targeting nanocarrier

Azidoazobenzene:



4-aminoazobenzene was stirred with 50 mL water at 0°C. Concentrated HCl (4.1 mL) was added resulting in the solubilisation of the reactant. After 20 min, NaNO₂ (1.6 g, 24 mmol) in water (14 mL) was added over 10 min using an addition funnel. After one hour, NaN₃ (1.44 g, 221 mmol) in water (10 mL) was added slowly while controlling frothing due to evolution of nitrogen. The mixture was then filtered and the obtained red-orange powder was recrystallized in toluene to afford the 4-azidoazobenzene (3.8 g, 85% yield).

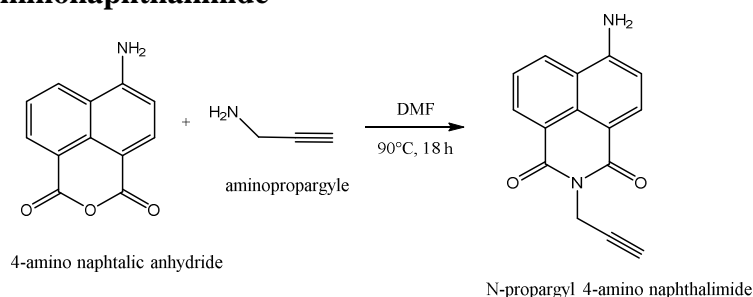
Propargyl derivative of Folic acid ²⁷²



Folic acid (1.0g, 2.26 mmol) was mixed with 20 mL DMF and cooled to 0°C in a water-ice bath. N-hydroxysuccinimide (NHS) (260 mg, 1.1 eq) was then added followed by 1.1 eq of 1-Ethyl-3-(3-dimethylaminopropyl)carbodiimide hydrochloride (EDC). After 10 min, propargylamine (0.13 g, 1 eq) was carefully added. The reaction mixture was warmed to room temperature and stirred overnight. The mixture was then poured into water (150 mL) and stirred for one hour to form a white precipitate. This latter was filtered, washed with acetone and dried under reduced pressure to afford the alkyne-folic acid as an orange powder with 95% yield.

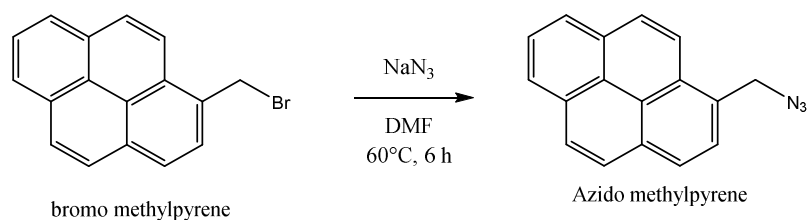
Probing the proximity of functions by Förster Resonance Energy Transfer (FRET)

N-propargyl 4-aminonaphthalimide²⁷³



A mixture of 4-aminonaphthalic anhydride (0.3 g, 1.4 mmol) and propargylamine (0.16 g, 2.8 mmol) in DMF (10 mL) was heated to 90°C for 48 h under inert atmosphere. The mixture was then poured into ice-water and a brown precipitate appeared instantaneously. The solid was recovered by filtration, washed with water and dried at 70°C overnight.

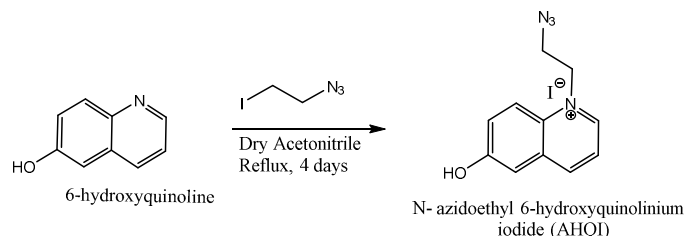
Azidomethylpyrene²⁷⁴:



Sodium azide (164 mg, 2.54 mmol) was added to a solution of bromomethylpyrene (500 mg, 1.69 mmol) in 3 mL of anhydrous DMF and the suspension was heated at 60 °C for 6 h. The mixture was then cooled and diluted with water. The aqueous phase was extracted with Et₂O, the combined organic phase was dried (MgSO₄), and the solvent was evaporated to yield the azide as a yellow waxy solid (395 mg, 91%). Mp 59-61°C.

Activation of pH-Responsive Nanomachines through Photo-Responsive Proton Transfer

Photoacid AHQI:



In a two-necked round bottom flask with a condenser, 6-hydroxyquinoline (1.0 g, 6.9 mmol) was suspended in 10 mL acetonitrile. 1-azido 2-iodoethane (3.0 g, 15 mmol) was then added; the mixture was then stirred at 80°C for 4 days (The reaction progress was monitored by ^1H NMR).

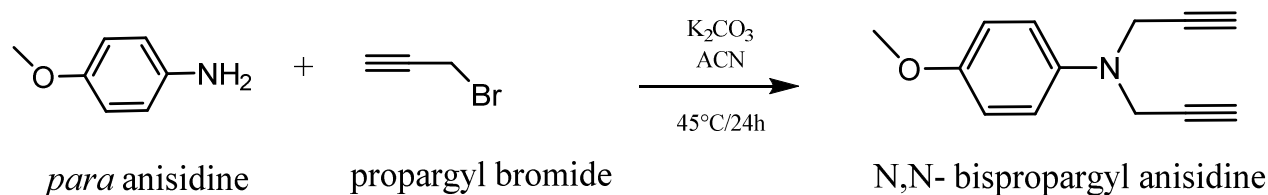
The acetonitrile was removed under reduced pressure and the product was precipitated with diethyl ether. After filtration, AHQI was afforded as a dark green solid with a 85 % yield.

^1H NMR (400 MHz, DMSO- d_6) δ = 11.2 (s, 1H, OH), 9.25 (d, 5.4 Hz, 1H), 9.11 (d, 8.5 Hz, 1H), 8.53 (d, 8.5 Hz, 1H), 8.08 (m, 1H), 7.75 (dd, 8.5 Hz and 1.5 Hz; 1H), 7.63 (d, 1.5 Hz, 1H), 5.20 (br, 2H), 4.06 (br, 2H)

^{13}C NMR (101 MHz, DMSO- d_6) δ = 158.0, 146.7, 145.7, 132.2, 131.9, 127.6, 121.8, 120.9, 110.7, 56.0, 49.4.

HRMS: calculated for $\text{C}_{11}\text{H}_4\text{N}_4\text{O}^+$: 215.0933 found 215.0935

Synthesis of the stalk: Alk-anisidine²⁷⁵



Para-anisidine (10 g, 80 mmol, 1 eq) was dissolved in acetonitrile (200 mL). Potassium carbonate (16 g, 116 mmol) was then added, followed by propargyl bromide (18 mL, 160 mmol, 2 eq) and the mixture was stirred for 24 h at 45°C. The reaction progress was monitored by TLC. Water was added to the final mixture to dissolve the excess of K_2CO_3 and the organic phase was extracted with diethylether. The combined organic phase was dried over

MgSO₄ and concentrated under reduced pressure to give a brown crystalline powder. Yield 15.9 g, 98%

Synthesis of monoclickable mesoporous silica nanoparticles:

Nanospheres:

To a solution of sodium hydroxide NaOH 2 M (1 mL, 2 mmol) in distilled water (80 mL, 4.4 mol), cetyltrimethylammonium bromide (CTAB) (0.3 g, 0.8 mmol) was added. The mixture was heated to 80°C and stirred vigorously until the total dissolution of the surfactant. The silica source was then added: tetraethylorthosilicate (TEOS) (9-x mmol), AzPTES (x mmol) (x =1,2 or 5% mol of the total silica source) were added dropwise. A white precipitate appeared after one minute and the reaction mixture was stirred at 80°C for two more hours. The white precipitate was then filtered, washed copiously with water and methanol and dried at RT. The surfactant extraction was achieved by continuous extraction (24 h) of the material in a solution of 200 mL ethanol and 10 mL HCl 12 M.

Nanorods: the same procedure was used, PFOA (6% *wt* relative to CTAB) being added along with CTAB.

Synthesis of bisclickable mesoporous silica nanoparticles:

The same procedure was used, the silica source being tetraethylorthosilicate (TEOS) (9-2x mmol), AzPTES (x mmol) and propargylbis(propyltriethoxysilyl)amine (x mmol) (x =1,2 or 5% mol of the total silica source). The use of PFOA (6% *wt* relative to CTAB) during the addition of CTAB affords nanorods.

General procedure for the CuAAC reactions:

CLICK -1-: Mono- or bis-clickable nanoparticles (90 mg, with x% mol of azide= 1 eq) were incubated with 3 eq of the corresponding alkyne in the presence of copper sulfate CuSO₄·2H₂O (0.2 eq) and sodium ascorbate (0.4 eq) in 4 mL water/t-butanol mixture (v/v :1/1). The mixture was stirred vigorously at RT for 48 h. The nanoparticles were recovered by centrifugation (8000 rpm, 10 min) and washed with water, sodium *N,N*-diethyldithiocarbamate (0.1 M in methanol, 10 mL), methanol (10 mL) and acetone (10 mL). The last three washings were repeated 5 times. The resulting material was dried at 70°C for 6 h.

CLICK -2-: For the bis-clickable nanoparticles, the resulting “first-clicked” material was incubated with 3 eq of the corresponding azide under the same conditions as for the first CuAAC reaction.

SUPPORTING INFORMATION

Supporting Information

CHAPTER III

3. Monoclickable Mesoporous Silica Nanoparticles: Light-triggered clicked nanoimpeller for controlled release of cargo molecules

3.5. CuAAC reaction on monoclickable nanoparticles

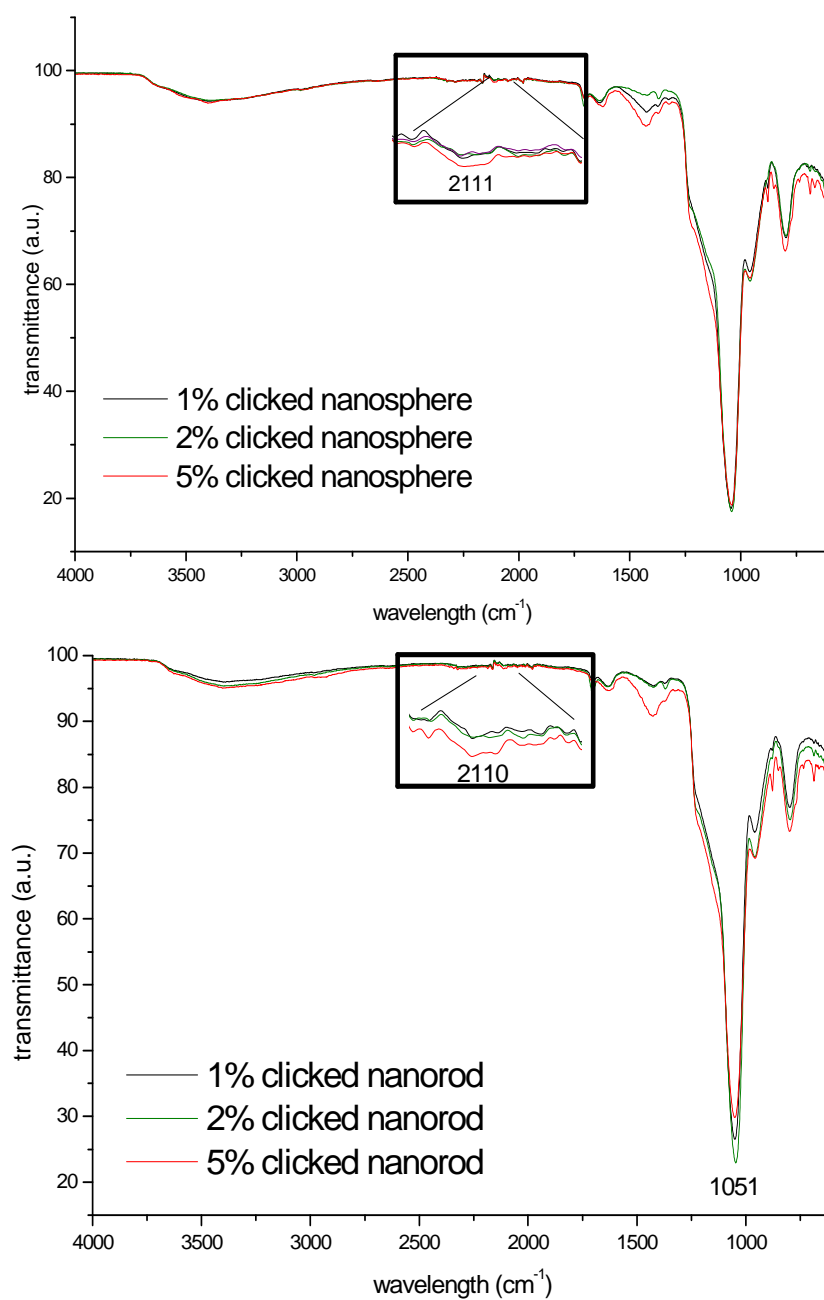


Figure S1: FTIR spectra of (up) nanospheres and (down) nanorods after CuAAC reaction with ethynylazobenzene. Inset: zoom on (2200-2000 cm^{-1}) region

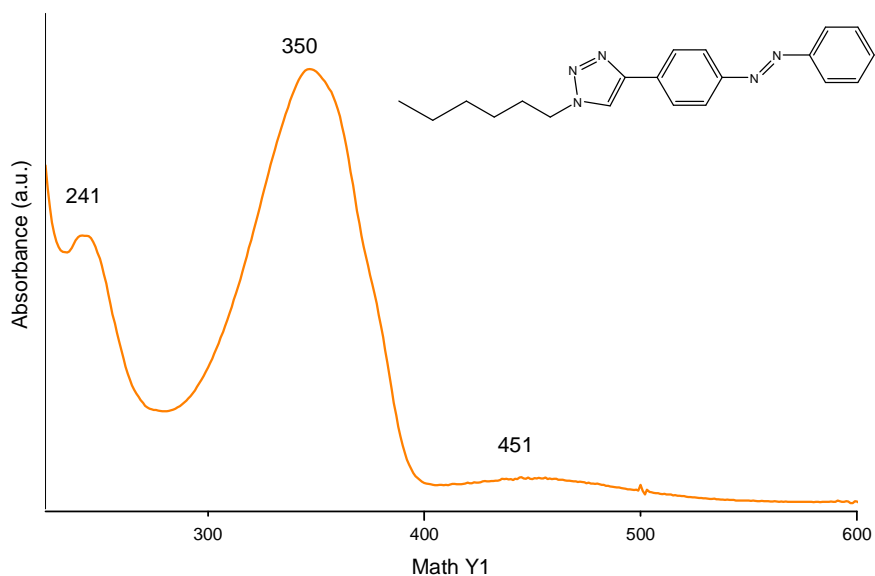


Figure S2: UV absorption spectrum of (hexane@azobenzene)

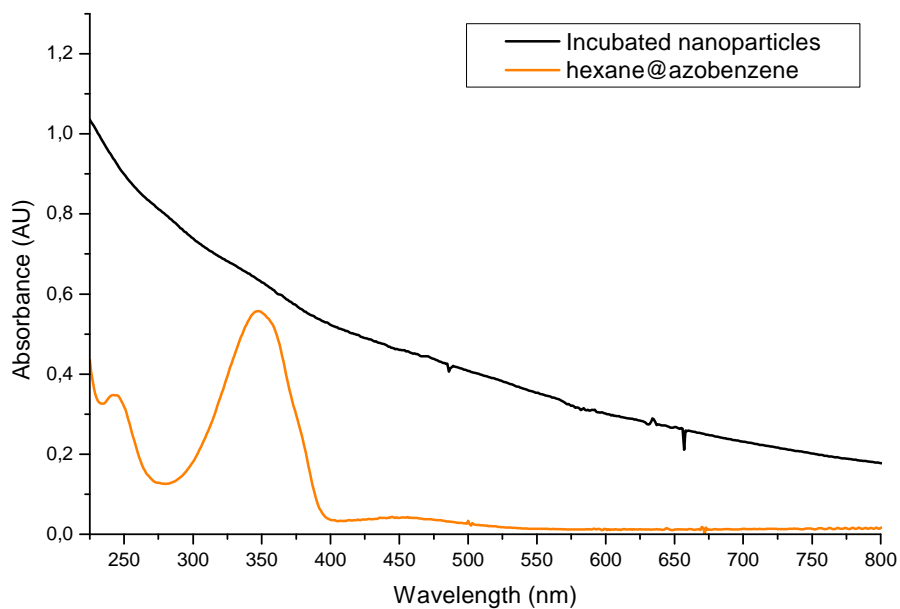


Figure S3: UV-vis spectra of nanoparticles incubated with azobenzene without click reaction.

5. Light triggered controlled cargo release from a targeting nanocarrier

5.1. Characterization of bisclicked Nanoparticles

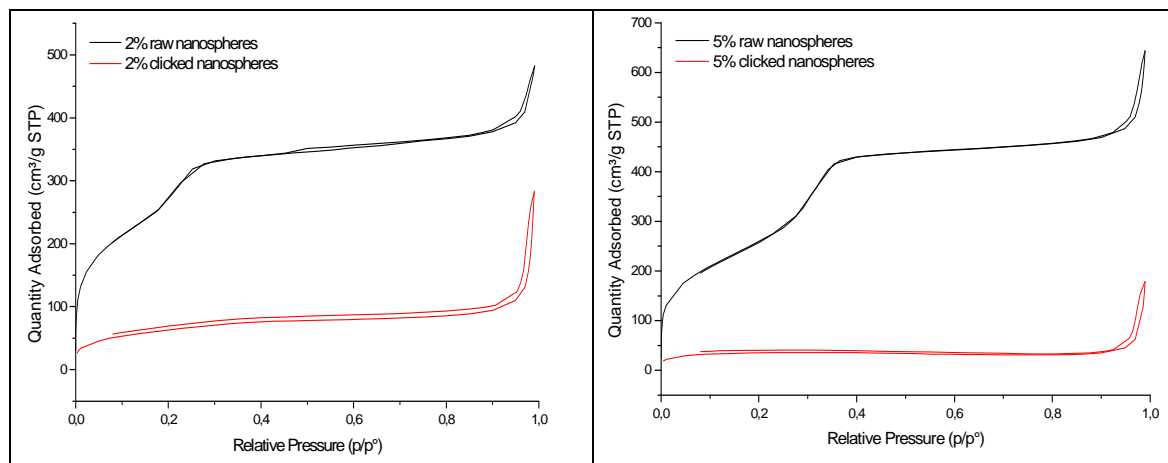


Figure S4: N_2 sorption isotherms of the (black) raw and (red) bisclicked nanospheres with (left) 2% (right) 5% clickable functions

6. Double click reaction (CuAAC) on mesoporous silica nanoparticles: probing the proximity of functions by Förster Resonance Energy Transfer (FRET)

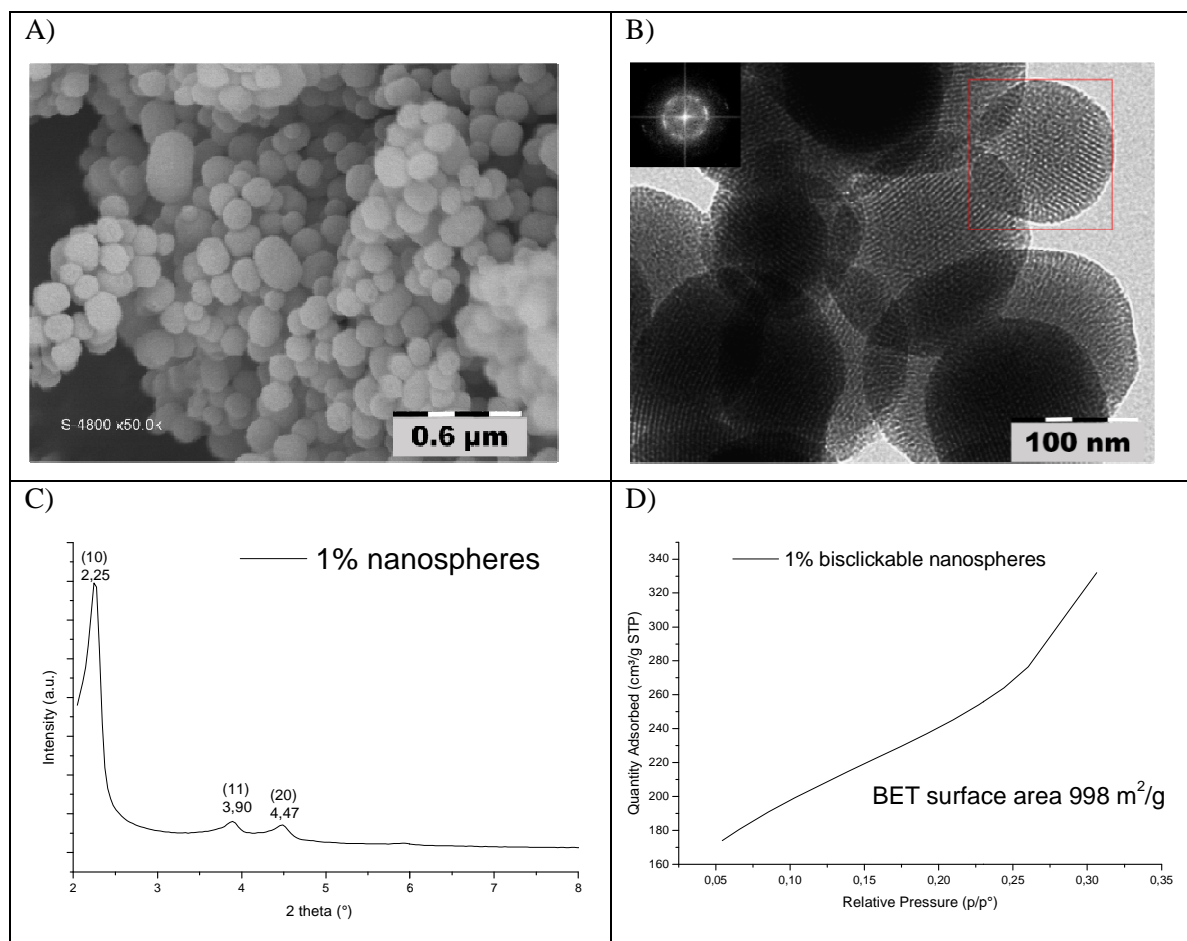


Figure S5: Textural analyses of 1% bisclickable nanoparticles. (A) SEM, (B) TEM micrographs, (C) XRD patterns and (D) BET adsorption isotherm

6.2.4. Characterization of the CuAAC functionalization:

FTIR:

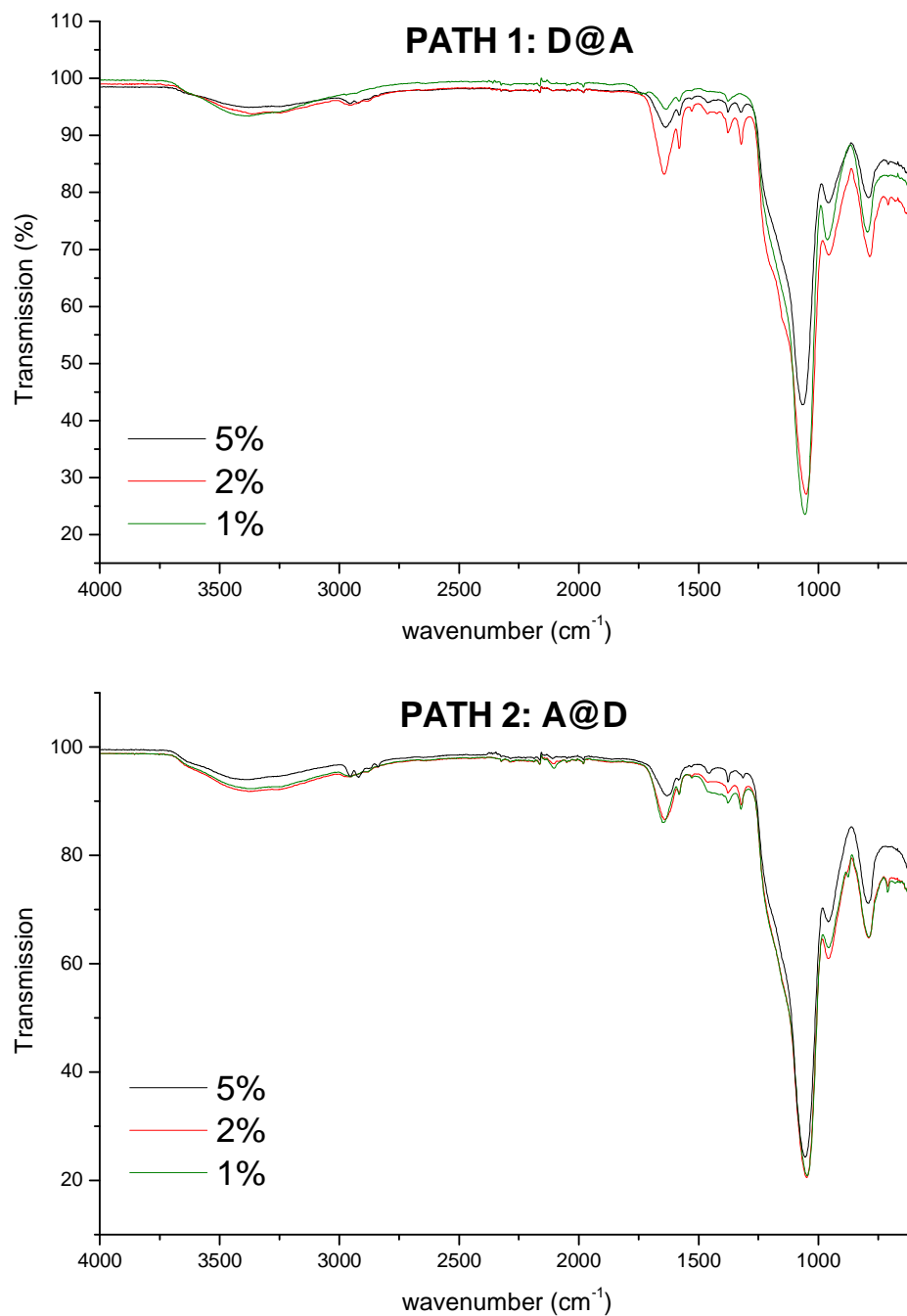


Figure S6: complete FTIR profile of clicked nanoparticles *via* (up) path 1 and (down) Path 2

Effect of concentration of the suspended nanoparticles in the analyzed medium:

In order to confirm that the energy transfer is intraparticular (interaction of donor and acceptor with the same nanoparticles) instead of different particles interaction at high concentration, one of the samples (NP1-DA) naphta@py 1% was diluted from 10 to 50 times (from 300 to 30, 15, 10 and 6 mg/L) and the emission spectra were recorded for the samples. The ratio of emission intensities between naphthalimide (525 nm) and pyrene (395 nm) remains very close and does not decrease with of concentration confirming that an intraparticular FRET is occurring.

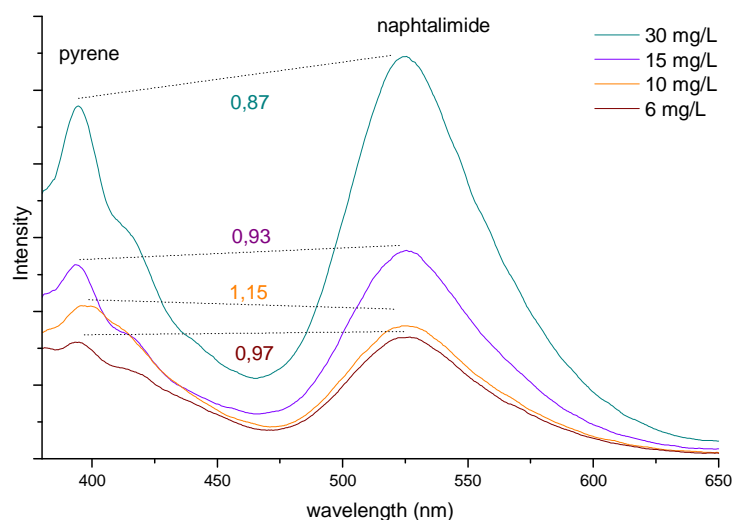


Figure S7: Emission spectra of NP1-DA with different concentrations.

7. Activation of pH-Responsive Nanomachines through Photo-Responsive Proton Transfer

7.1. Characterization of the nanoparticles

FTIR:

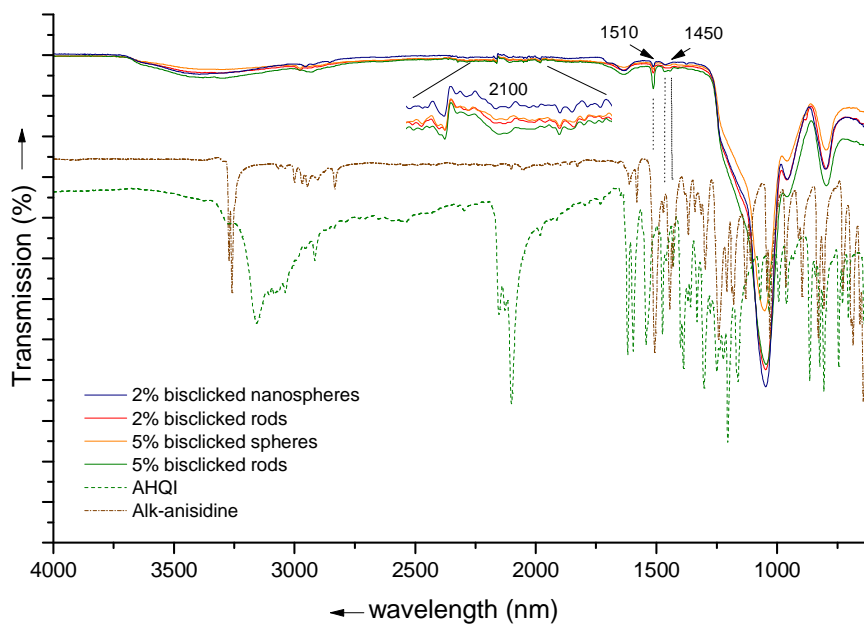


Figure S8: FTIR spectra of bisclicked nanoparticles: (blue) 2% and (orange) 5% nanospheres with (red) 2% and (green) 5% nanorods. Dashed lines correspond to the (green) AHQI and (brown) Alk-anisidine precursors. Inset: zoom on N₃ peak in the zone 2050-2150 cm⁻¹

N₂ sorption

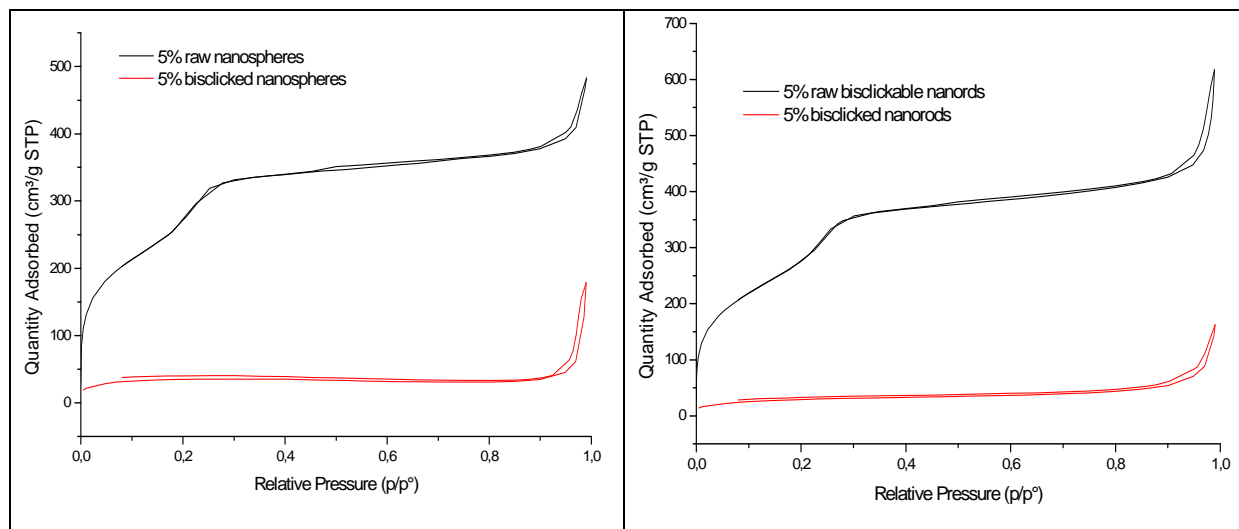


Figure S9: N₂ sorption isotherms of the (black) raw and (red) 5% bisclicked (left) nanospheres (right) nanorods

Release experiments

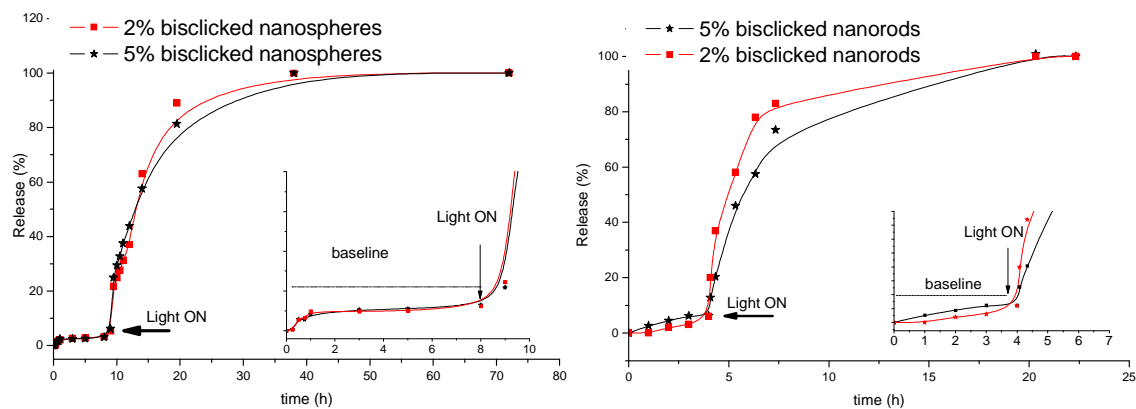
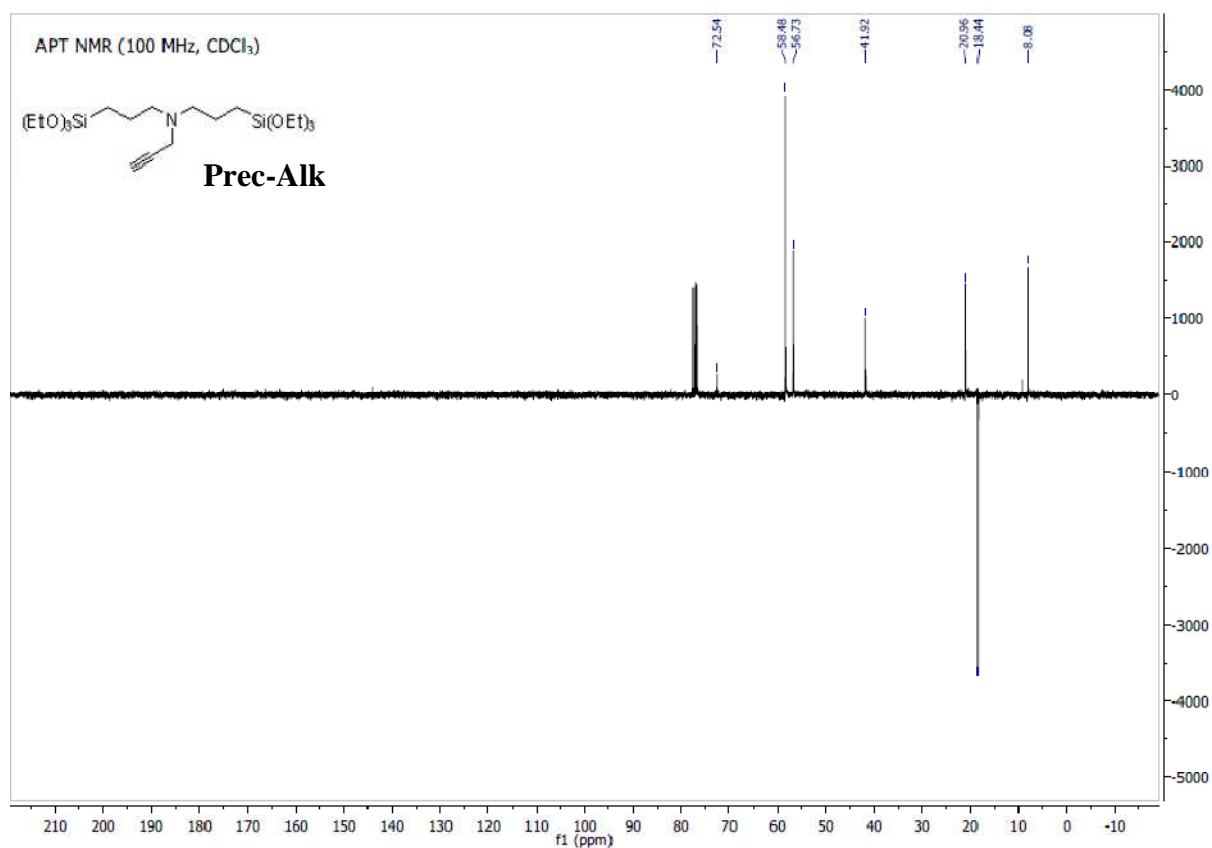
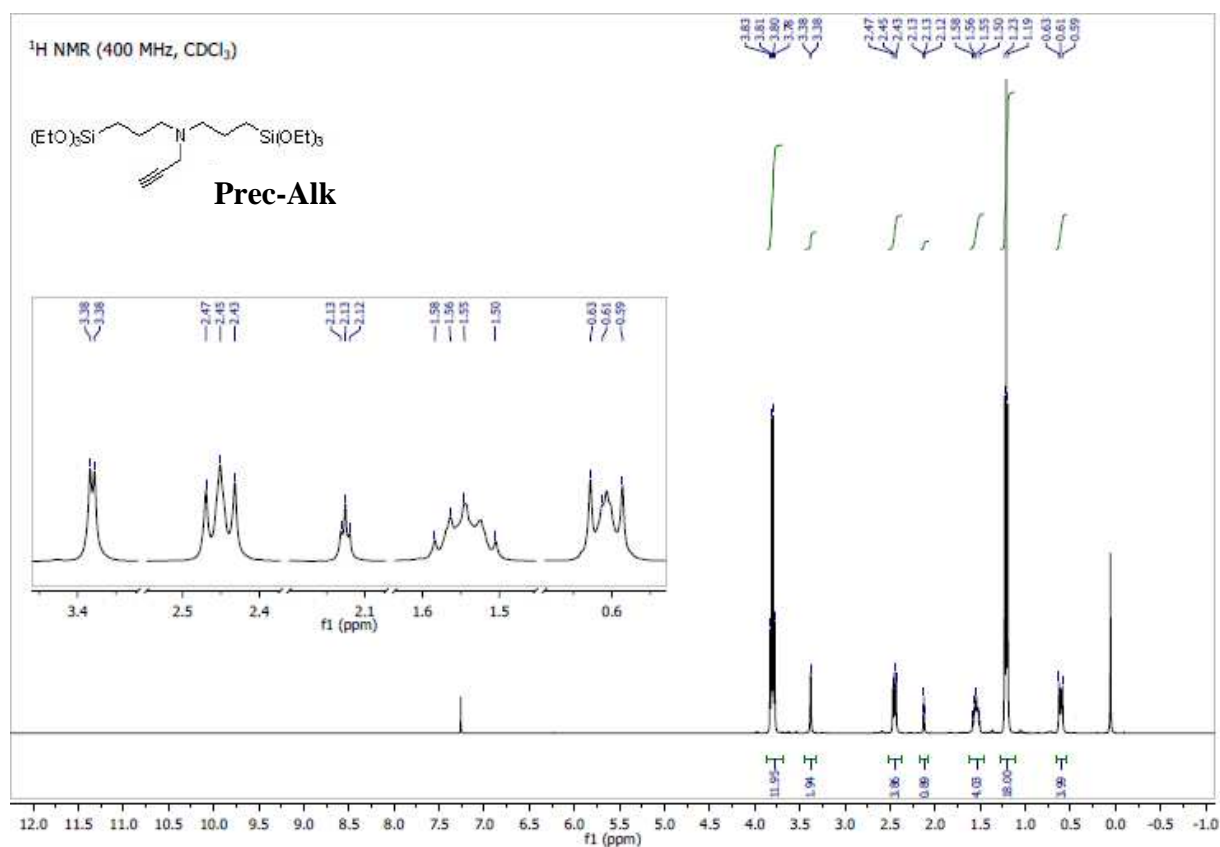
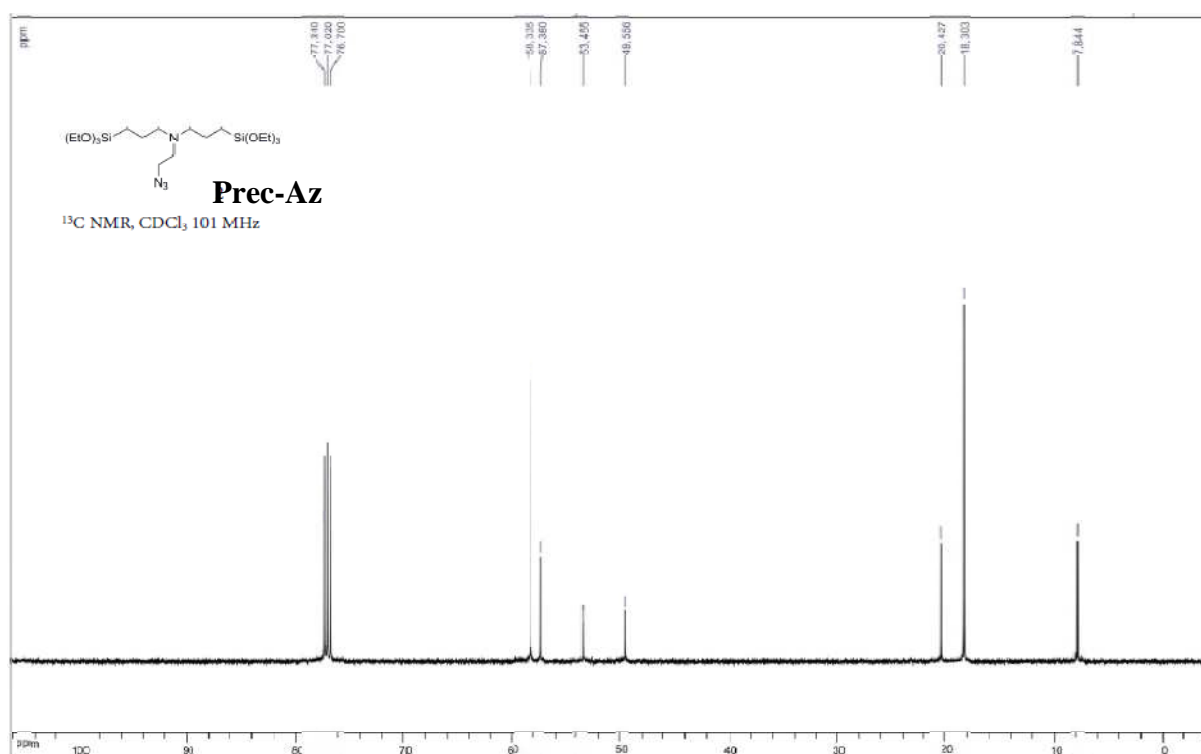
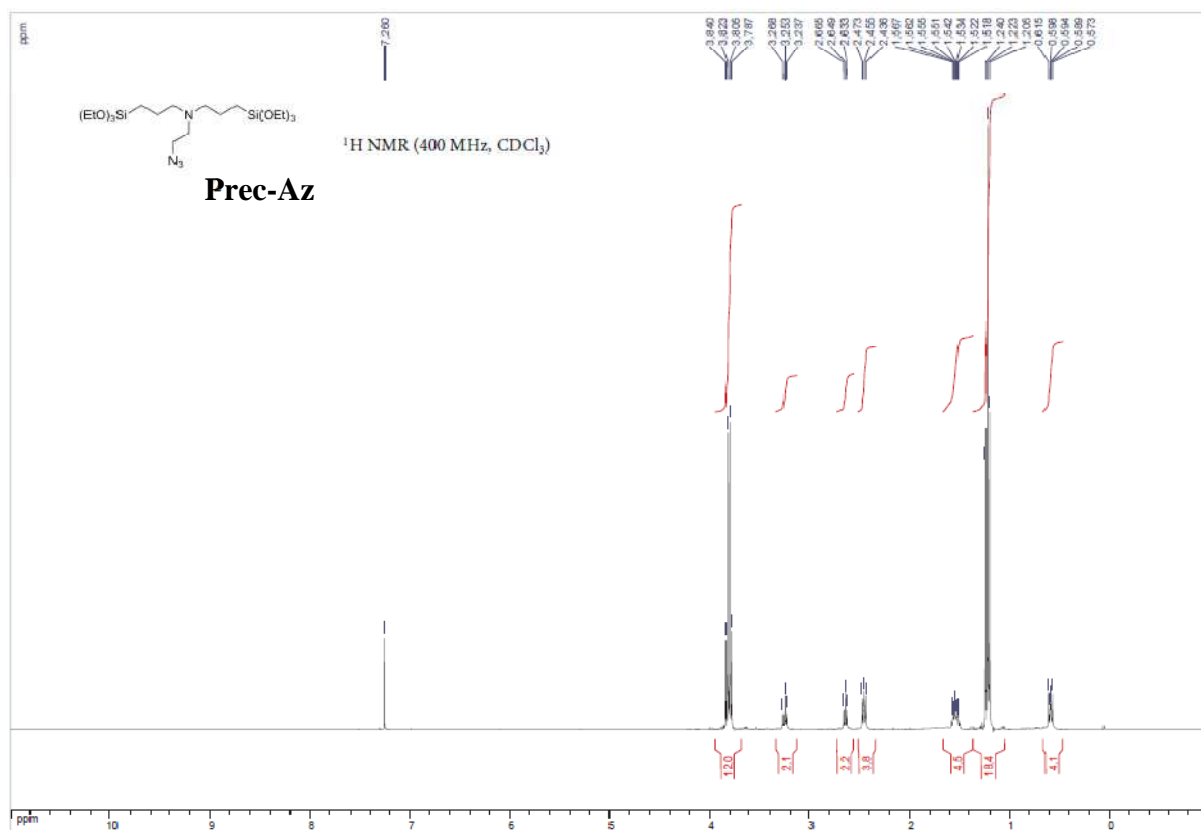
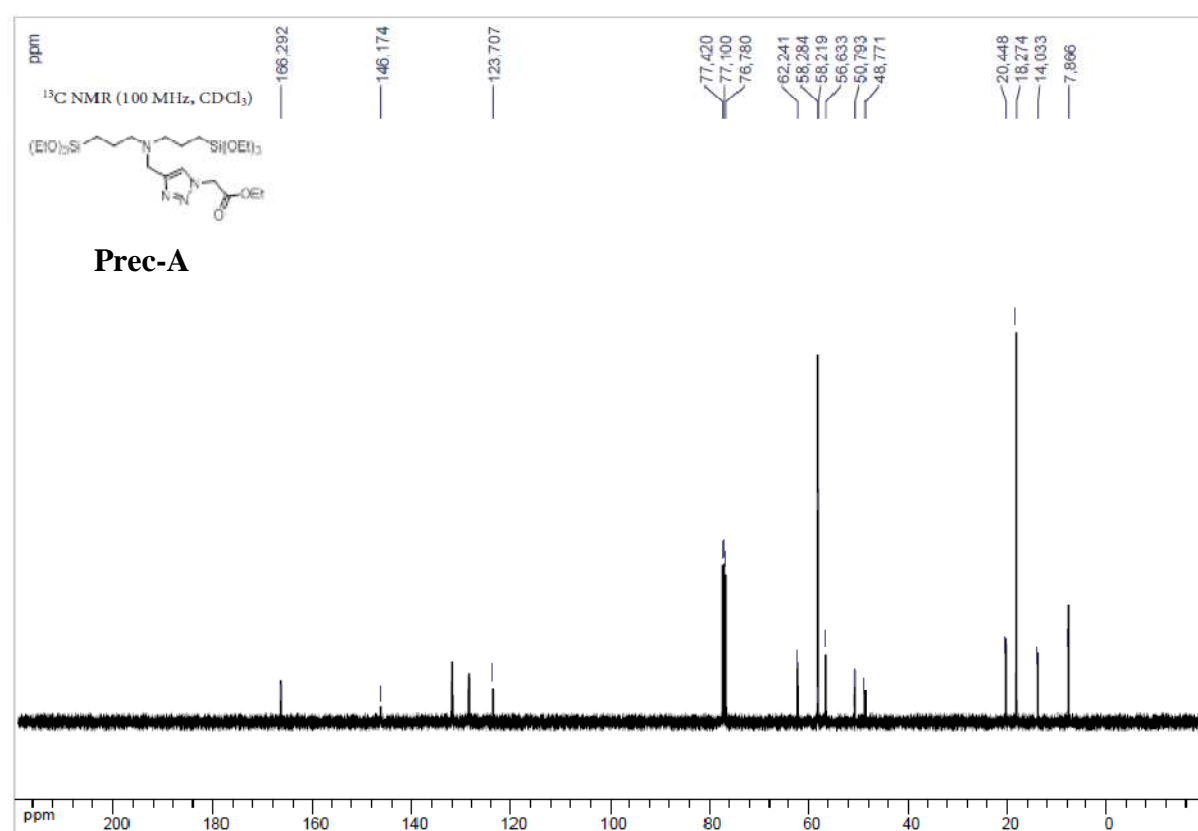
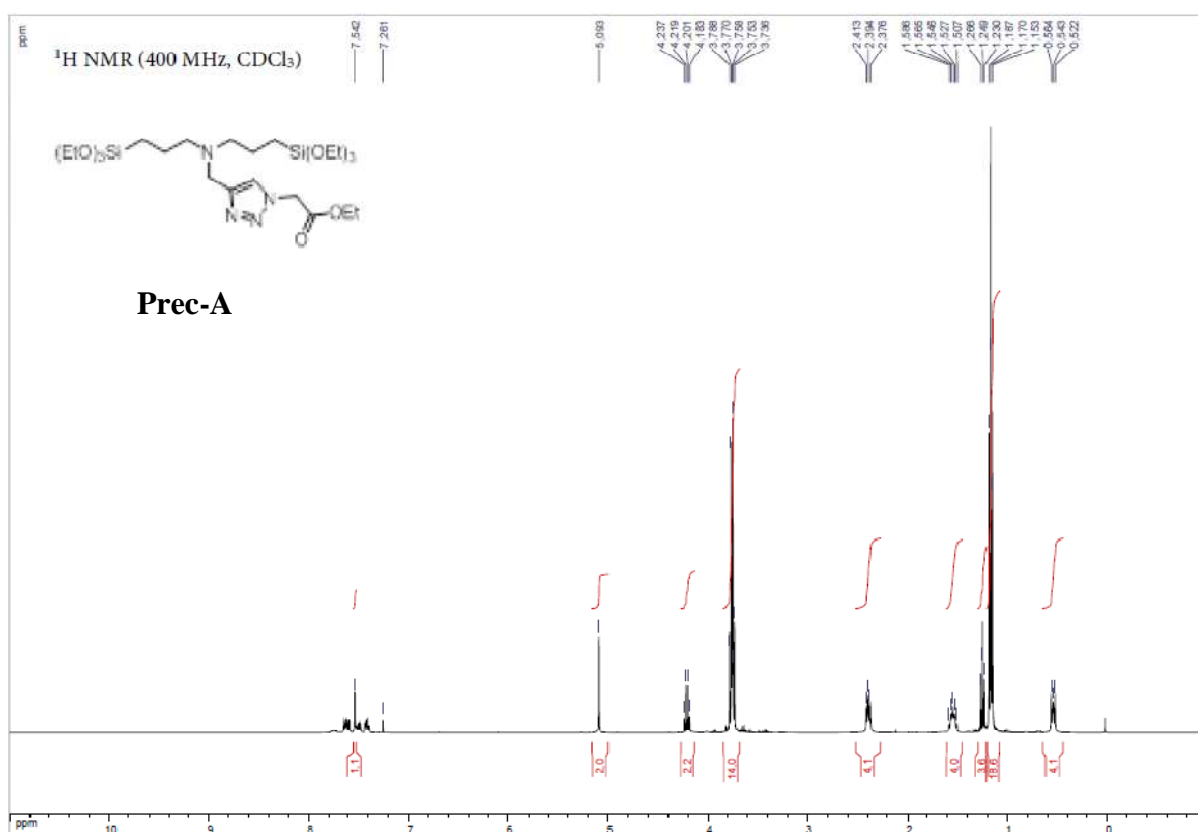


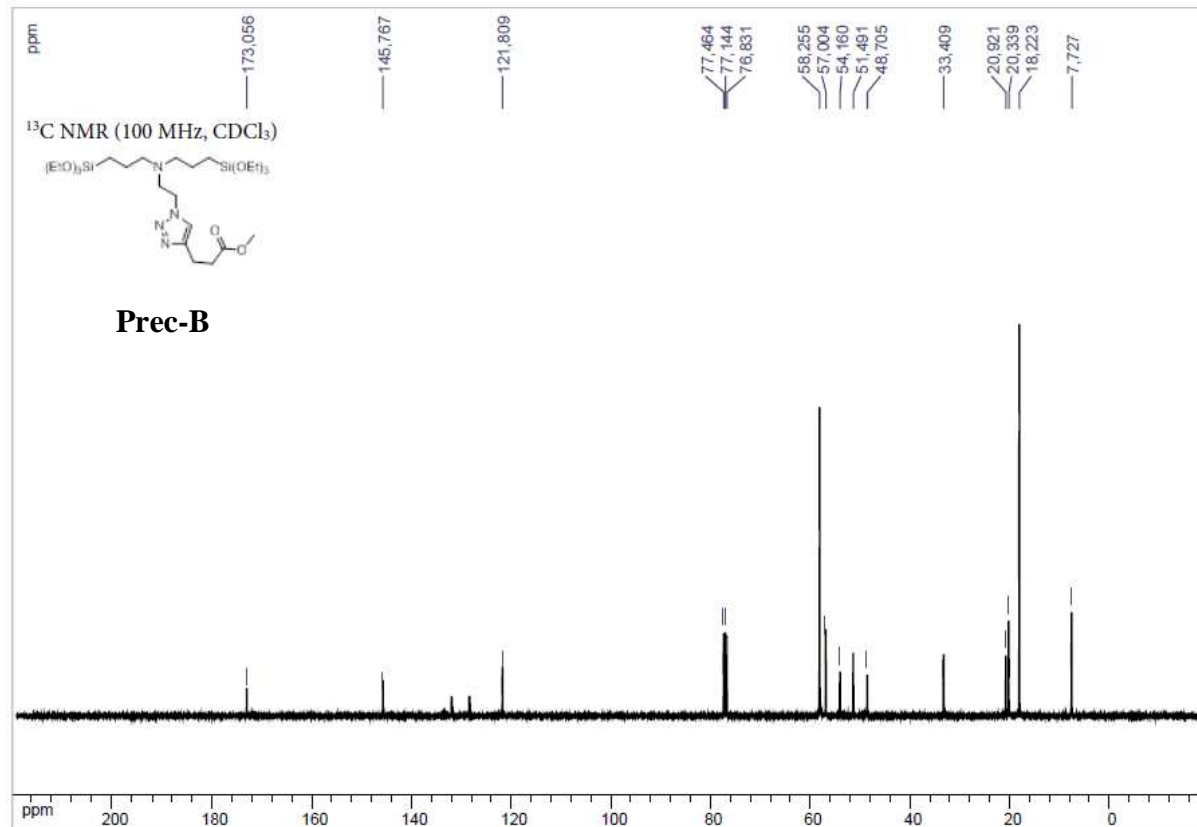
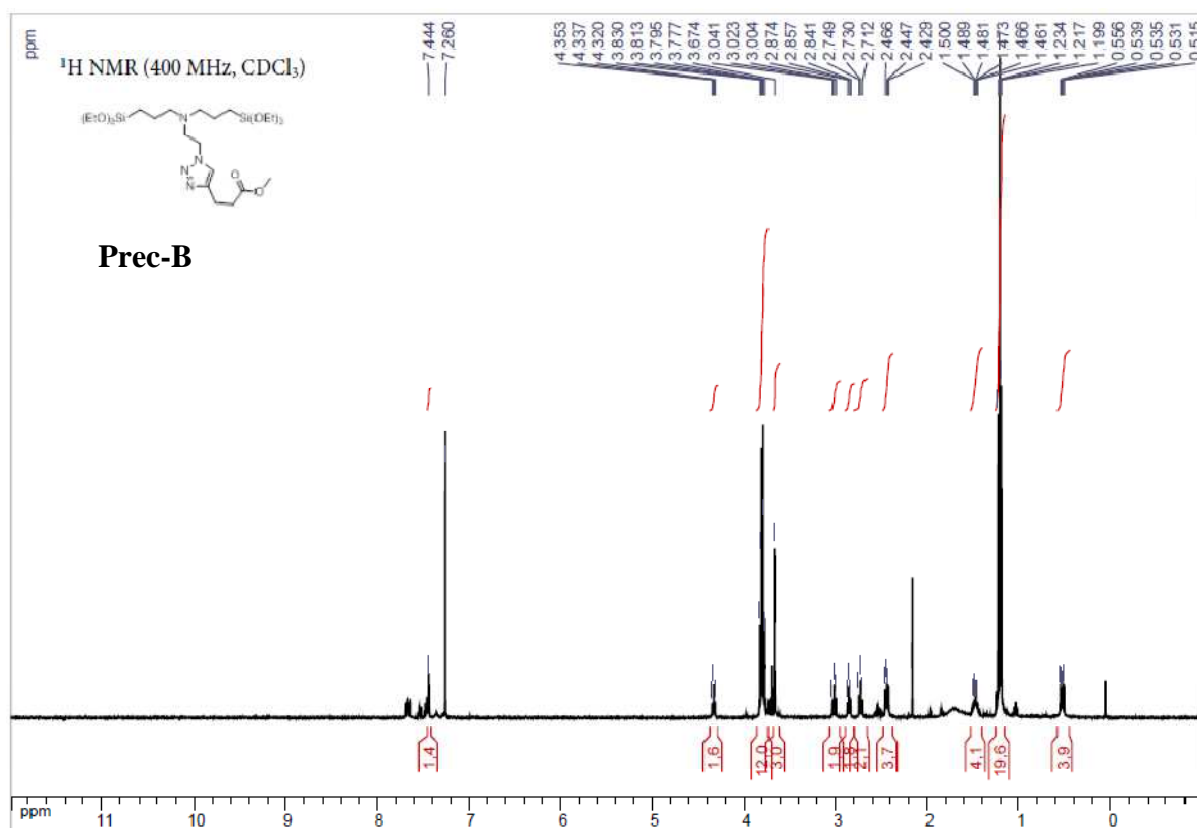
Figure S10: percentage of release profile of bisclicked (left) nanospheres and (right) nanorods with (red squares) bis 2% and (black stars) bis 5% clicked functions . Insets: zoom on the baseline before excitation starts.

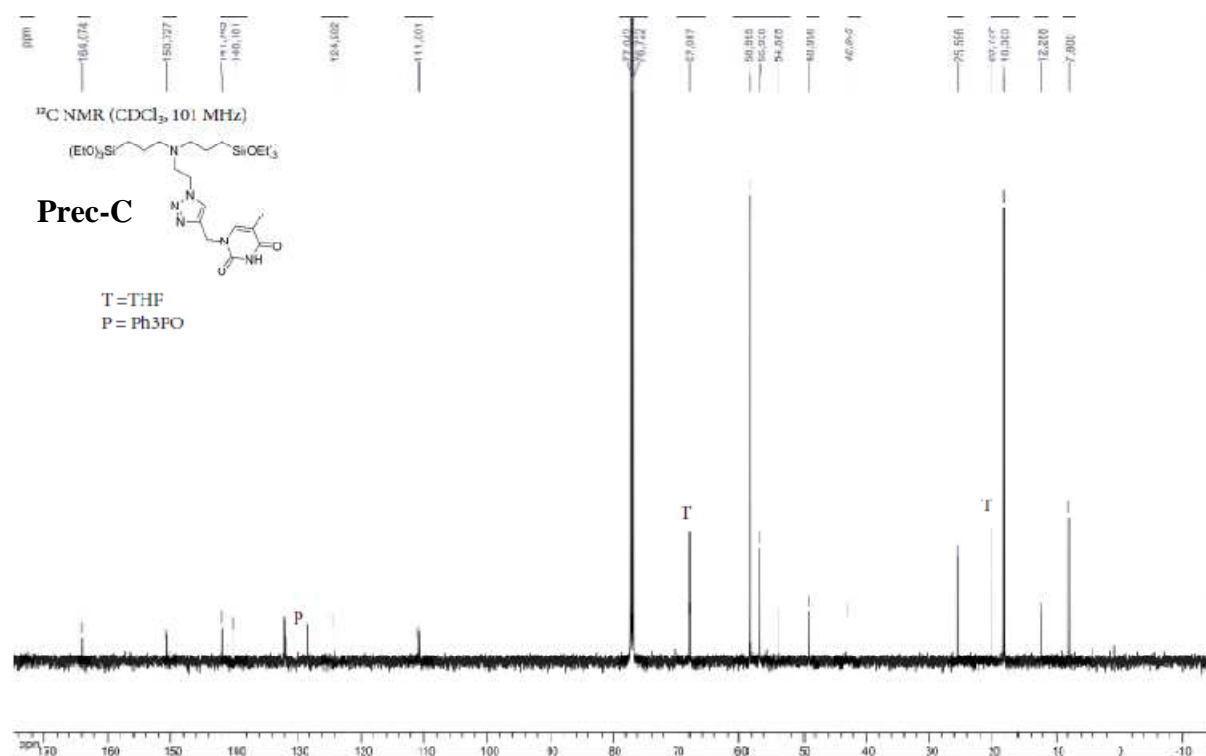
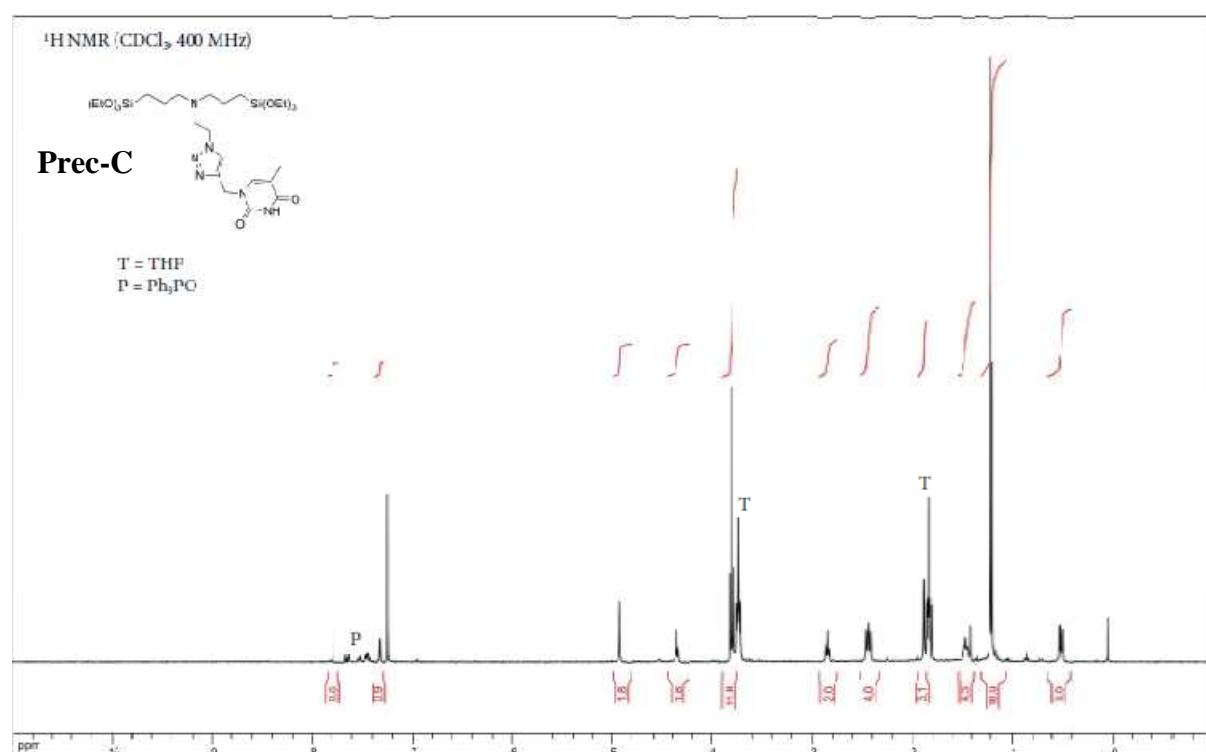
^1H and ^{13}C NMR spectra of: Prec-Alk, Prec-Az, Prec, Prec B and Prec C:











RESUME EN FRANCAIS

Résumé en français

Introduction :

Le procédé sol-gel est une méthode de préparation de matériaux solides de type oxydes métalliques obtenus à partir de précurseurs moléculaires par des réactions successives d'hydrolyse-condensation menant à la formation d'une structure tridimensionnelle. Plusieurs éléments métalliques peuvent être utilisés dans ce procédé mais le silicium reste le plus largement utilisé. Les conditions douces employées permettent d'introduire des fonctions organiques pour conférer aux matériaux (dits alors hybrides) des propriétés modulables pour un large éventail d'applications dans plusieurs domaines (nanomédecine, catalyse, revêtements, dépollution, électronique...).

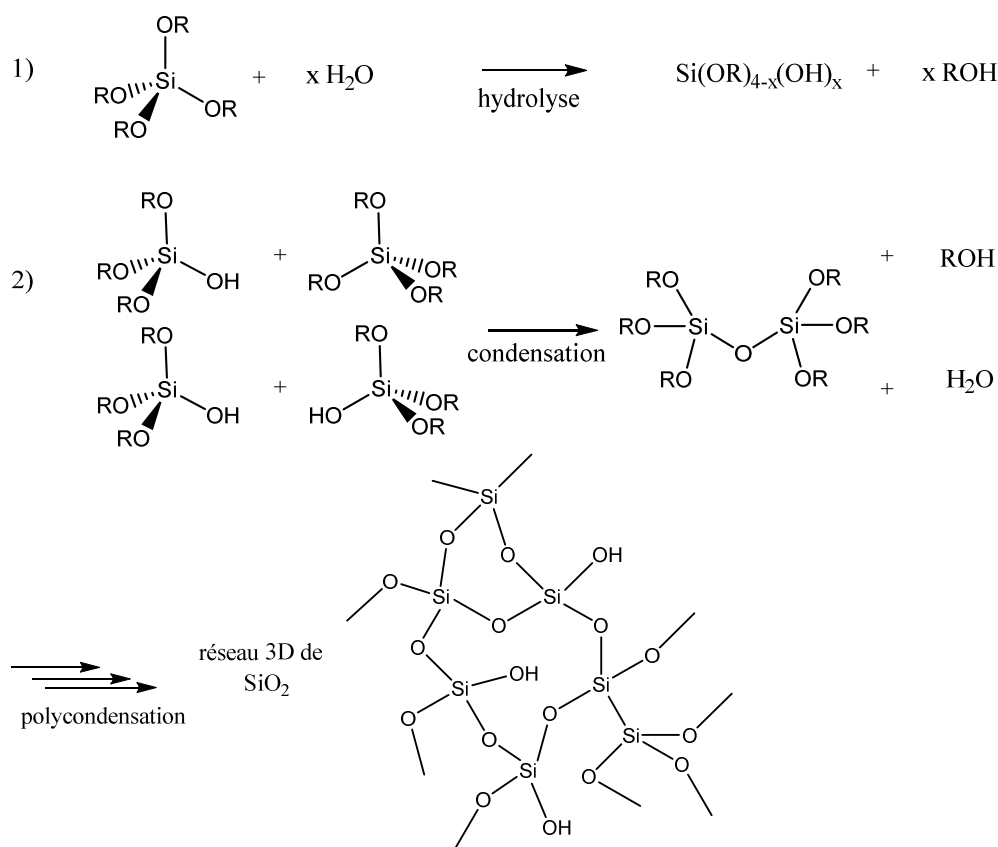


Figure R1: Réactions d'hydrolyse et de condensation se produisant durant le procédé de sol-gel pour la formation de silice

Les matériaux à base de silice hybride constituent une famille de matériaux dans laquelle une fraction organique est intimement liée à la matrice silicique à l'échelle nanométrique. Selon le

lien entre la fonctionnalité organique et la matrice, les matériaux hybrides fonctionnels sont divisés en deux classes (Figure R2):

Classe I : Le lien entre les deux fragments se fait par une interaction faible (Van der Waals, électrostatique, liaison hydrogène)

Classe II : Introduction de la partie organique par des liaisons covalentes fortes

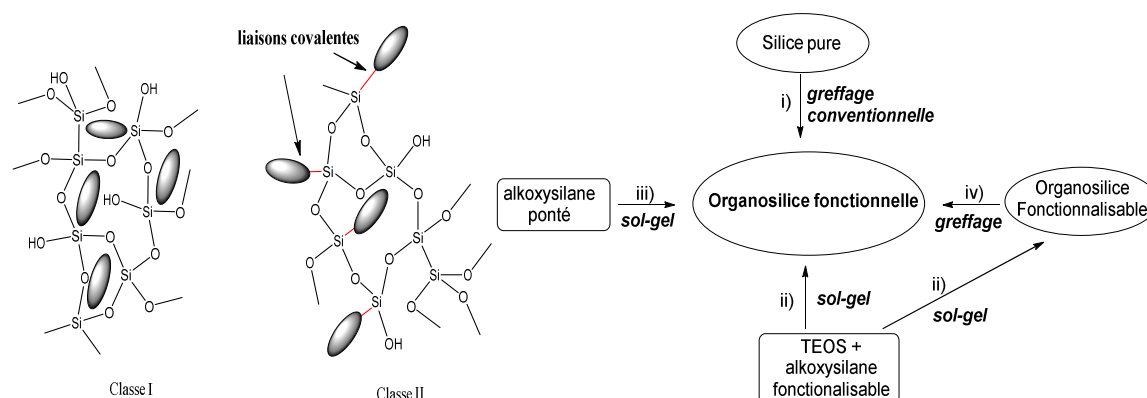


Figure R2: (gauche) les deux classes de matériaux hybrides fonctionnels et (droite) les différentes routes possibles pour la conception d'un matériau fonctionnel de classe II

Les matériaux appartenant à la classe II sont largement plus utilisés que ceux de la classe I en raison de leur stabilité supérieure vis-à-vis des conditions extérieures surtout au niveau de perte de la charge.

La préparation des matériaux de silice hybride de classe II se fait conventionnellement soit par greffage d'une molécule organosilylée sur les silanols de surface (Figure R2, i) soit par co-condensation avec la source de silice (typiquement TMOS, TEOS) (Figure R2, ii). Ces méthodes sont contraintes par la quantité introduite de fonctions qui reste limitée.

La préparation de matériaux hybrides à base d'organosilane pure (silsesquioxanes pontés BS ou organosilice à mésoporosité périodique PMOs) s'avère très prometteuse et commence à prendre de l'ampleur dans plusieurs domaines en raison de la charge très élevée de fonctions organiques que le matériau présente. Toutefois, la formation des PMOs est très dépendante de la structure du précurseur de départ et seuls les PMOs à base de molécules polysilylées portant de petits groupements organiques (éthylène, éthylenylène, phénylène) ont été préparés avec succès.

Dans le but de s'affranchir de ces limitations, la post-fonctionnalisation des organosilices (BS et PMOs) formées à partir de petites molécules fonctionnalisables s'avèrent une stratégie très

prometteuse. Les réactions les plus efficaces pour accomplir cette tâche avec de très bonnes conversions pour une gamme très large de fonctions organiques sont classées comme des réactions dites *click*.

La chimie click est une stratégie de synthèse comprenant plusieurs types de transformations chimiques simples, modulables et ayant un rendement élevé telles que les cycloadditions dipolaire, les réactions thiol-ène, les réactions de Diels-Alder, la formation d'oximes ou d'hydrazones). De plus, la cycloaddition azoture-alcyne catalysée par le cuivre (CuAAC) reste de loin la réaction la plus utilisée en raison de sa tolérance exceptionnelle aux fonctions organiques, sa cinétique rapide, ses chimio et régio-sélectivités.

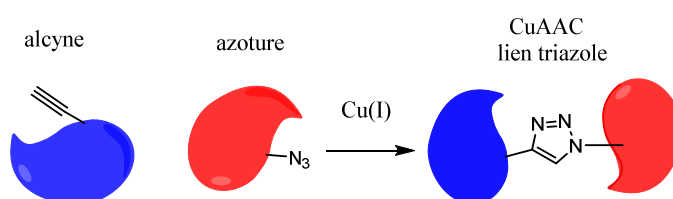


Figure R3: Réaction CuAAC pour la construction de nouvelles entités

Travaux antérieurs :

Les travaux pionniers concernant l'utilisation de la réaction click de CuAAC sur les matériaux sol-gel ont vu le jour indépendamment dans les groupes de Zink, Bein et Stack en 2008. Plusieurs fonctions biochimiques (trypsine, TPA), normalement difficiles à immobiliser de façon covalente sur un support solide ont été incorporées avec succès par la chimie click sur un matériau SBA-15. Ce travail a été considéré comme une percée dans ce domaine en raison de la grande difficulté d'insérer d'une façon homogène des fonctions volumineuses dans le matériau.

Notre groupe s'est intéressé à cette stratégie et plusieurs travaux ont été menés afin de mettre en place une méthodologie solide de fonctionnalisation des matériaux obtenus par voie sol-gel par CuAAC. Dans ce cadre, des précurseurs fonctionnels ou fonctionnalisables par réaction de CuAAC ont été synthétisés et ont servi à la synthèse de nanoparticules de silice mésoporeuse et de microplots mésoporeux clickables.

Objectif :

Cette thèse porte sur une étude méthodologique pour consolider la stratégie de fonctionnalisation click par CuAAC des matériaux à base de silice hybrides obtenus par le procédé sol-gel.

Deux axes seront principalement développés, dans le but de préparer de nouveaux types de matériaux fonctionnels par CuAAC (organosilice à mésoporosité périodique PMO et silsesquioxanes pontés BS, nanoparticules de silice mésoporeuse bifonctionnelles) et de montrer leur efficacité en vue d'une application en nanomédecine en collaboration avec Prof JI Zink (UCLA).

Dans une première approche, nous allons synthétiser des BS mésoporeux et des PMOs entièrement clickables à partir des précurseurs organosilanes correspondants. Ensuite, plusieurs molécules types seront greffées *via* CuAAC pour mettre en lumière la conversion importante et l'excellente tolérance fonctionnelle offertes par la réaction de CuAAC. En se basant sur cette propriété nous allons procéder à une modification extensive de la surface d'un silsesquioxane ponté mésoporeux clickable pour moduler de façon importante la balance hydrophile/lipophile par greffage CuAAC de molécules présentant des caractères hydro/lipophile différents.

Dans la deuxième partie, nous nous intéresserons aux nanoparticules de silice mésoporeuse multifonctionnelles par greffage CuAAC dans le but de les transformer en nanotransporteurs pour la délivrance contrôlée de principes actifs. Dans cette optique, la réaction de CuAAC va conférer aux nanoparticules des propriétés importantes telles que le ciblage des cellules cancéreuses, la fermeture ou l'ouverture des accès des pores sous l'action d'un stimulus. Grâce à ces développements méthodologiques, des nanomachines fonctionnant avec un mécanisme innovant basé sur la stimulation d'un photoacide et l'ouverture d'une valve sous l'effet de la protonation seront développées pour libérer à la demande un principe actif.

Résultats :

Organosilices à Mésoporosité Périodique (PMO) et Silsesquioxanes Pontés (BS) Fonctionnalisés par Chimie Click (CuAAC)

Dans cette partie, nous nous servons de deux organosilanes clickables pour concevoir les matériaux à base d'organosilice pure (BS et PMOs).

Synthèse de PMO clickables : La synthèse des PMOs se fait à partir des précurseurs clickables bisilylés en milieu acide en utilisant un surfactant anionique pour la structuration du matériau du fait de l'interaction électrostatique qui peut avoir lieu entre la tête hydrophile chargée négativement et les ions ammonium.

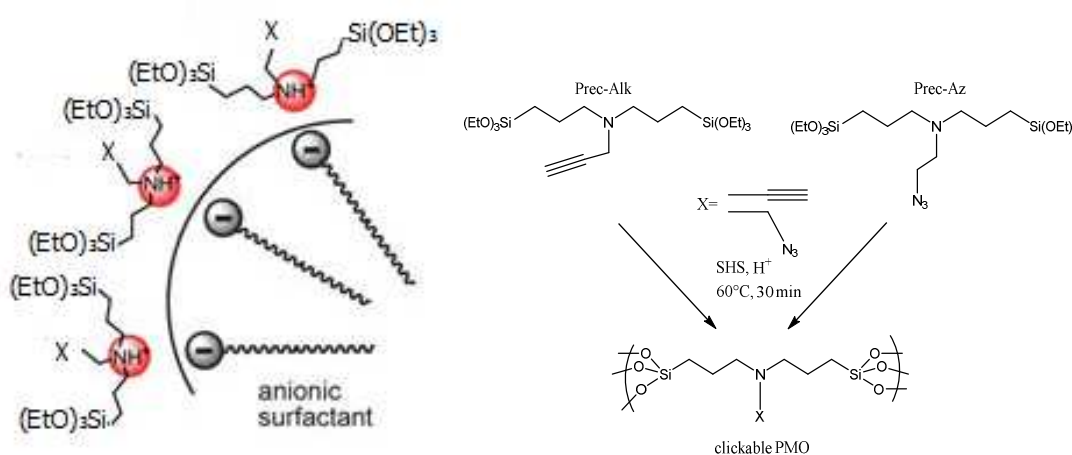


Figure R4 : Formation du PMO clickable à partir de précurseurs azoture et alcyne en milieu acide avec surfactant anionique

Les matériaux en question ont été caractérisés dans un premier temps par spectroscopie vibrationnelle, RMN du solide et analyse thermique afin de valider leur composition chimique. Des analyses structurales ont été aussi réalisées, telles que la microscopie électronique à balayage et en transmission en plus de la diffraction des rayons X pour sonder la structure et la morphologie des matériaux. Toutes les analyses sont en accord avec les résultats prévus (structure hexagonale 2D, porosité régulière, perte de masse concordant avec la charge en partie organique). La porosité des matériaux n'a pas pu être analysée, très probablement à cause de l'effondrement de la structure suite aux conditions de dégazage (révélé par des analyses SAXS) ce qui bloque toute surface accessible aux molécules d'azote.

Malgré ce résultat la réaction click a été réalisée avec succès. En utilisant des fonctions organiques sondables par des techniques analytiques simples (esters), nous avons obtenu un

taux de fonctionnalisation très élevé (environ 60% dans le cas du PMO-azoture). La réaction click a été aussi mise en évidence par RMN du solide ^{13}C où les signaux typiques du cycle triazole apparaissent, avec une disparition du signal correspondant à l'alcyne terminal. La réaction click n'a pas d'effet sur la morphologie des matériaux mais elle résulte en une perte partielle de l'organisation à longue distance des pores des matériaux.

Dans le but de mettre en œuvre des matériaux plus stable, les précurseurs bisilylés ont été mis en réaction en milieu basique en présence du CTAB comme surfactant et de l'acide perfluorooctanoïque comme co-surfactant pour former un gel qui après séchage a donné lieu à un matériau. La caractérisation structurale de ce matériau a montré qu'il est constitué d'agrégats de nanoparticules de taille moyenne 20-30 nm avec une surface extérieure rugueuse et une surface spécifique élevée (*ca* 450 m²/g pour le matériau alcyne et environ 325 m²/g pour le matériau azoture). La réaction click sur ces matériaux a été validée par RMN du solide mais aussi quantifiée par FTIR et analyse élémentaire. De très bonnes conversions ont été obtenues (*ca* 40% avec le 2-azidoéthylphosphonate de diéthyle pour le matériau alcyne et jusqu'à 80-90% avec le matériau azoture en utilisant le pentynoate de méthyle respectivement). La réaction click n'a pas changé la morphologie des matériaux mais a juste diminué la rugosité de la surface (SAXS).

Ces excellentes conversions sont d'une importance cruciale puisqu'elles confèrent aux matériaux des propriétés modulables selon la nature de la molécule clickée. C'est exactement dans cette optique que nous avons procédé à une modification drastique des propriétés de surface du matériau mésoporeux-alcyne en cliquant différentes molécules à caractère hydrophile ou lipophile (azido-éthanol, azido-tetraéthylène glycol, azido-hexane, azido-hexadecane, azoture de benzyle et azidooctane tridécafluoré). Les études d'adsorption d'eau et de cyclohexane couplées à des analyses SAXS ont montré que la réaction click a changé d'une manière très efficace la balance hydrophile/lipophile du matériau selon la molécule clickée.

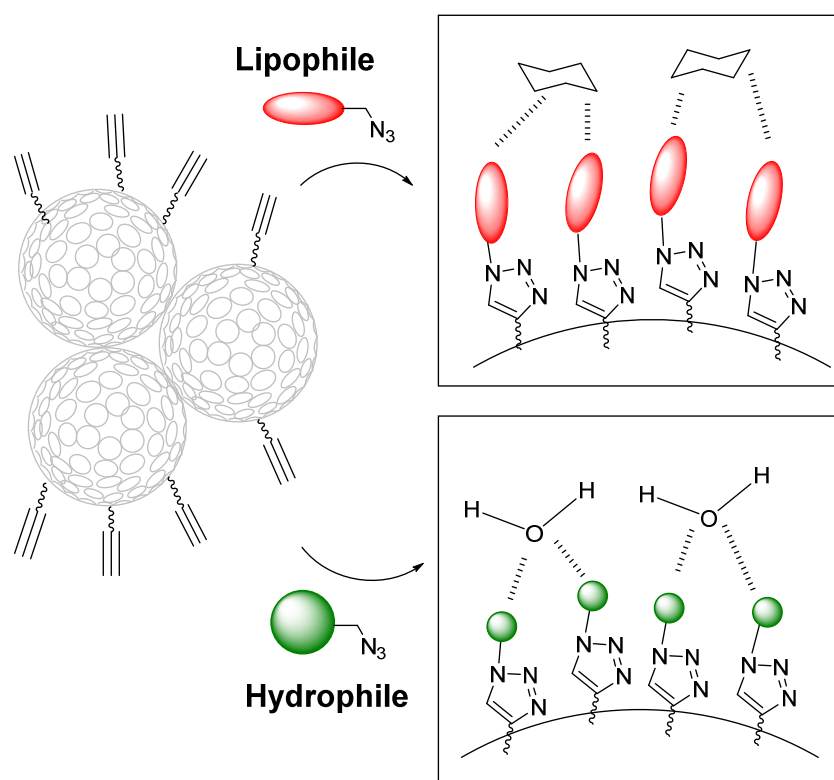


Figure R5 : modification de la surface du matériau mésoporeux-alcyne par des molécules hydro/lipophiles à l'aide du greffage CuAAC.

Adsorbat	M	M-OH	M-PEG	M-C6	M-Ph	M-F	M-C16
Cyclohexane	596	245	<5	141	178	<5	42
Eau	26	113	62	54	38	34	17

Table R1: Constantes de Henry en mg.g^{-1} pour les différents systèmes conçus (à 313 K).

Les constantes de Henry traduisent l'affinité d'un matériau vis-à-vis des molécules sondes et nous informent donc de son état de surface et sa modification selon la molécule clickée. Cette étude a permis de classer les matériaux par ordre d'hydrophilie : **M-OH>M-PEG>M-C6>M-Ph>M-F>M-C16**, ce qui a été confirmé par SWAXS.

La fonctionnalisation des matériaux par chimie click (CuAAC) s'avère donc une stratégie très fructueuse pour orienter un même matériau (parent) vers plusieurs applications en modifiant ses propriétés d'une façon extensive.

Nanoparticules Multiclickables de Silice Mésoporeuse (MSNs) pour la Délivrance Contrôlée de Principes Actifs

Les MSNs s'avèrent être des systèmes très prometteurs dans le domaine biomédical (détection, diagnostic, délivrance des substances médicamenteuse) grâce à leurs propriétés très intéressantes de biocompatibilité. Dans cette partie, nous avons cherché à mettre en œuvre des méthodes de fonctionnalisation multiple de MSNs par la chimie click afin de les utiliser comme plateformes pour le traitement des cellules cancéreuses.

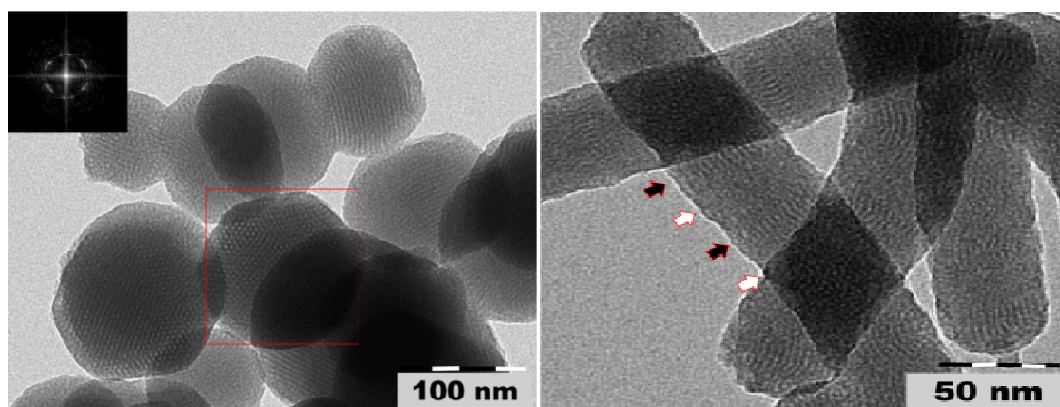


Figure R6 : Les nanosphères et nanobâtonnets bifonctionnels utilisés dans notre travail

Dans un premier temps, nous avons conçu des nanoparticules bifonctionnelles de silice mésoporeuse de formes sphérique ou allongées puisque le facteur de forme entraîne en général un comportement différent quant à l'internalisation dans les cellules.

En premier lieu, le système bifonctionnel a été clické par un dérivé d'acide folique pour un ciblage des cellules cancéreuses et aussi par un dérivé azobenzène qui va avoir le rôle clé dans la protection de la charge en tant que nano-propulseur (*nanoimpeller*). L'azobenzène est une molécule photosensible qui, suite à une excitation lumineuse, se photoisomérisse ce qui créera un désordre local et induira l'expulsion des molécules incluses dans les pores. Le succès de ce système quant au relargage contrôlé a été confirmé par un suivi en spectroscopie UV d'un colorant (Rhodamine B) chargé dans les pores avant et après excitation lumineuse (Figure R7). L'effet de l'acide folique ne pourra être testé qu'au cours d'études *in vitro*. Ces études sont en cours avec nos partenaires à l'IBMM. Les résultats préliminaires montrent qu'aucune mort cellulaire (MCF-7) ne peut être détectée sans la présence de l'acide folique en plus de l'azobenzène. Ceci montre que le système bifonctionnel (nanopropulseur + agent de ciblage) s'avère assez solide pour favoriser le ciblage des cellules cancéreuses.

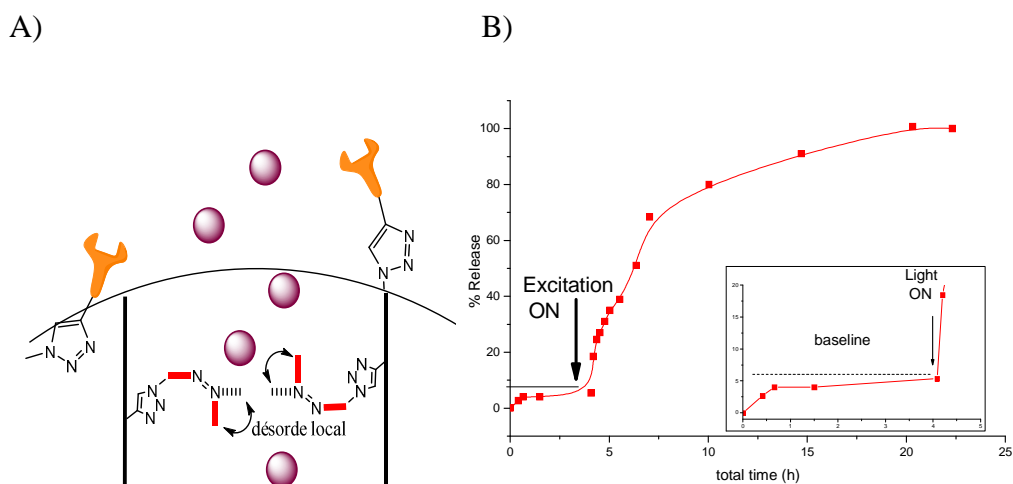


Figure R7 : (A) schématisation du système à délivrance contrôlée impeller+ agent de ciblage avec (B) le profile de relargage de la charge suite à l'excitation lumineuse

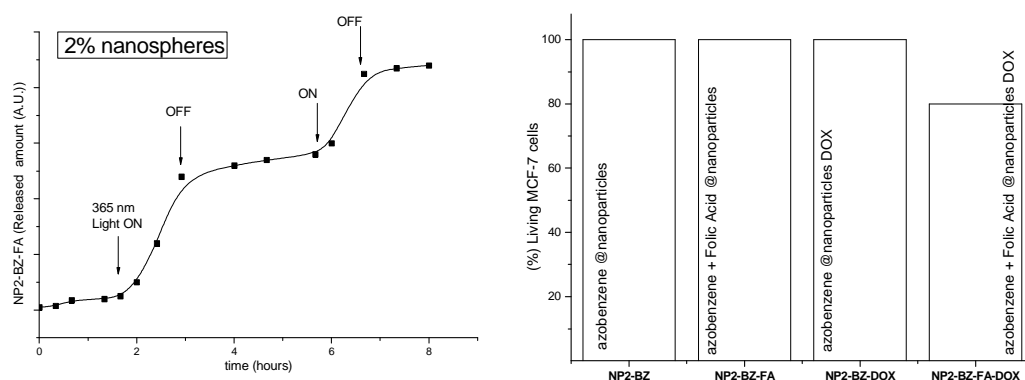


Figure R7 bis : (gauche) suivi UV-vis du relargage de rhodamine B suite à des séquences d'excitation ON-OFF, (droite) mort cellulaire induit par les différents systèmes utilisés mettant en évidence le rôle de l'acide folique

Ensuite, nous avons étudié la communication entre les entités clickées en fonctionnalisant les nanoparticules par des fluorophores distincts (fonctions méthylpyrène et 4-aminonaphthalimide) avec plusieurs concentrations [1-5%] afin de sonder par FRET la proximité des fonctions.

Le rayon de Forster (R_0) représente la distance à laquelle la probabilité de transfert d'énergie par FRET est égale à 0.5. Le phénomène de FRET peut être utilisé pour sonder la distance entre fluorophores dans un milieu donné.

Ro est calculé par la formule :

$R_0^6 = 8.79 \cdot 10^{-5} \cdot n^4 \cdot \Phi_D \cdot \langle \kappa^2 \rangle \left[\int_0^\infty \epsilon^A(\lambda) F^D(\lambda) \lambda^4 d\lambda / \int_0^\infty F^D(\lambda) d\lambda \right]$ d'où $R_0 = 3.5 \text{ nm}$ dans le cas du méthylpyrène et de l'aminonaphthalimide.

Les profils d'émission et d'excitation (Figure R8) ont validé l'existence d'un phénomène de FRET entre les fluorophores clickés, et ont donc montré que les deux fonctions ont une distance moyenne inférieure à 3.5 nm environ, quelle que soit la charge en fonctions clickables dans le matériau initial (entre 1 et 5% en mol).

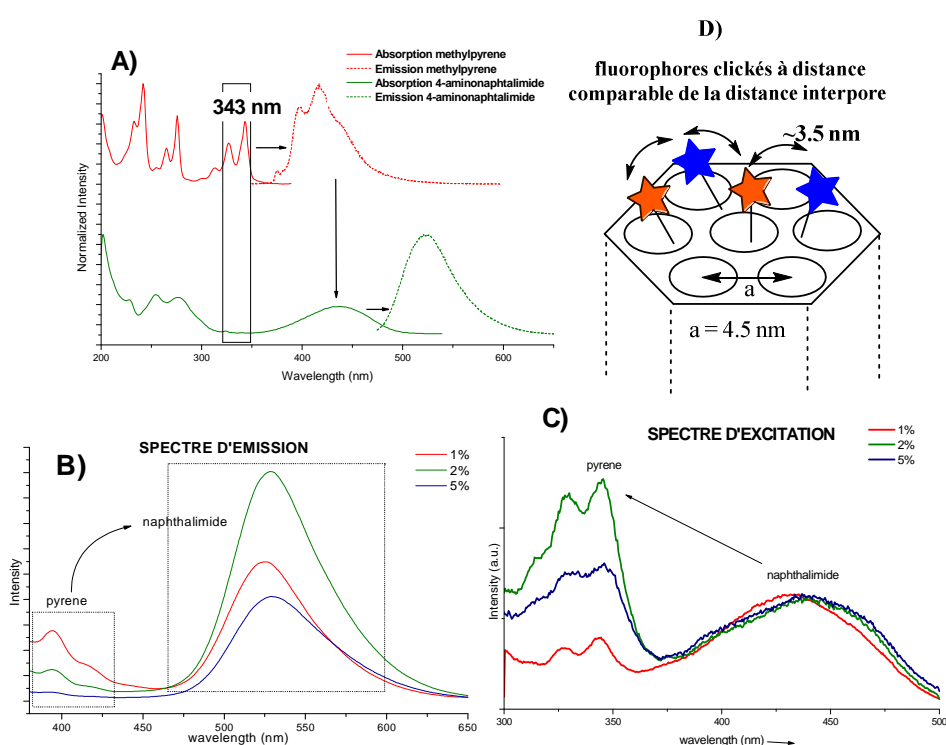


Figure R8 : (a) profils d'absorption et d'émission des fluorophores utilisés (b) les spectres d'émission (λ_{ex} 342 nm) et (c) d'excitation (λ_{em} = 540 nm) du système nanoparticules clickées. (d) une schématisation de la distance des fluorophores sur une nanoparticule à mésoporosité hexagonale

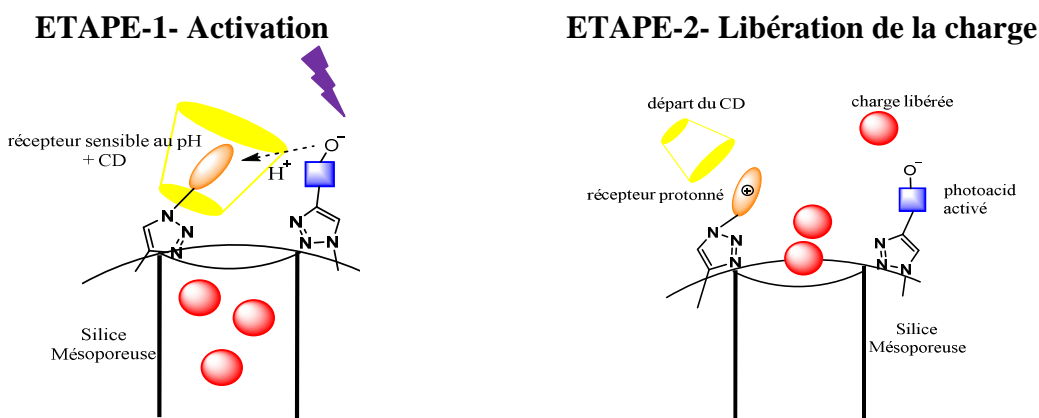
Après avoir validé qu'un transfert d'énergie se produit sur les nanoparticules, nous avons procédé à la conception d'un nouveau système de délivrance contrôlée basée sur un transfert de protons entre entités clickés en communication.

Il s'agit de cliquer un photoacide « émetteur » et un « récepteur » qui a une affinité avec la cyclodextrine qui vient s'y associer pour bloquer l'accès des pores. Après excitation

lumineuse, le photoacide transfère un proton qui vient protonner l'amine du récepteur, diminuant ainsi l'affinité avec la cyclodextrine, induisant son départ et ainsi la fuite de la charge.

Le suivi en spectroscopie UV de la concentration de rhodamine B dans le milieu montre que le système est bien stable (pas de fuite) dans le noir, et qu'après excitation lumineuse à une longueur d'onde appropriée, la molécule fluorescente a été libérée dans le milieu indiquant ainsi l'ouverture des pores. L'effet du photoacide a été validé par une expérience de contrôle où seul le récepteur avec la cyclodextrine a été clické. Suite à l'excitation à la même longueur d'onde, aucune absorbance de rhodamine n'a pu être détectée en dehors des nanoparticules. Ensuite l'activation sur commande a été aussi validée par des cycles ON-OFF de la source excitatrice. En dehors d'excitation, il n'y a pas de relargage de rhodamine mais suite à l'exposition lumineuse l'absorbance du milieu augmente mettant en évidence un système à activation photo-induite. Cette activation s'avère aussi possible dans des solutions tampons (PBS et TRIS) mettant l'accent sur une concentration assez importante de protons susceptibles d'ouvrir les pores en déstabilisant le complexe supramoléculaire. Le succès de relargage dans les milieux tampons ouvre les perspectives de ce système sur les bioapplications.

A)



B)

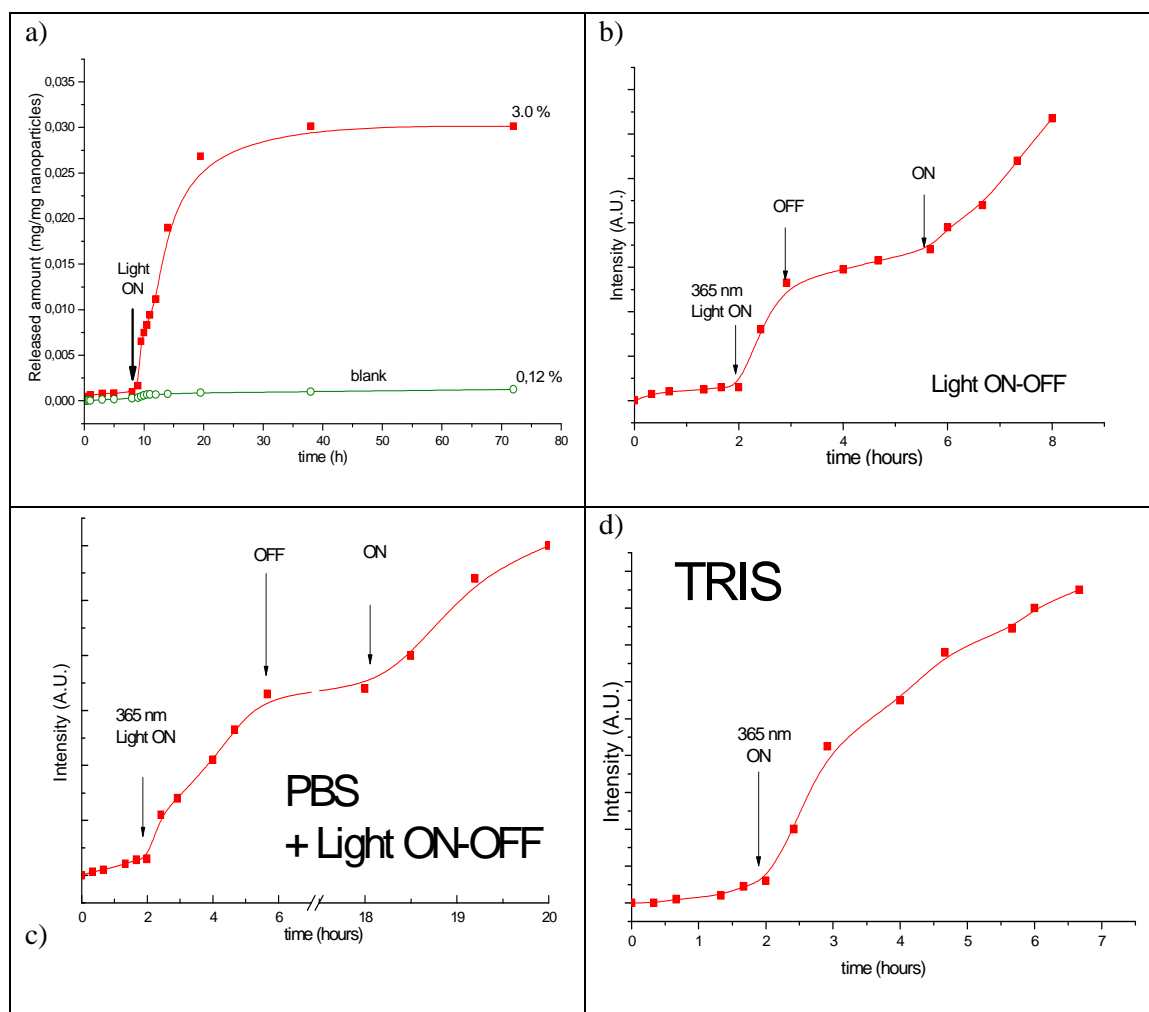


Figure R9 :(A) schématisation du système photoacide + récepteur + cyclodextrine et (B) le profil de délivrance de Rhodamine B suite à (a) l'excitation lumineuse continue, (b) séquences on-off sur nanobâtonnets, (c) dans une solution tampon PBS avec des séquences on-off et (d) en utilisant le tampon TRIS.

Conclusion :

Nous avons développé dans cette thèse une méthodologie de fonctionnalisation par la réaction de CuAAC des matériaux siliciques faits par voie sol-gel. Nous avons conçu de nouveaux matériaux à base d'organosilice pure et les avons fonctionnalisés par réaction CuAAC par une multitude de fonctions montrant ainsi l'apport de cette chimie quant à la possibilité de conférer de nouvelles propriétés aux matériaux. De nouvelles nanoparticules de silice

mésoporeuse et multifonctionnalisables par CuAAC ont été préparées. Ce système clickable a été fonctionnalisé de façon multiple par des molécules lui conférant des propriétés importantes en nanomédecine telles que le ciblage des cellules cancéreuses et la délivrance sur demande de principes actifs.

References

References

- (1) Livage, J.; Barboux, P.; Navabi, M.; Judeinstein, P. *Solid State Ionics* **1989**, *135*, 131.
- (2) Brinker, C. J.; Sherrer, G. W. *Sol-Gel Science, the Physic and Chemistry Sol-Gel Processing.*; Academic Press: San Diego, 1989.
- (3) Livage, J.; Henry, M.; Sanchez, C. *Solid State Chem.* **1988**, *18*, 259–342.
- (4) Ring, T. A.; Gallagher, D. *Sol-gel proccessing Ceram. Film. Chim.* **1989**, *43*, 298–304.
- (5) Kagaruma, Y. *Phys. Rev. B* **1988**, *14*, 9797.
- (6) Xu, L.; Chen, K.; Zhu, J.; Chen, H.; Huang, H.; Xu, J.; Huang, X. *Superlattices Microstruct.* **2001**, *29*, 67.
- (7) Wind, O.; Gingele, F.; Woggon, U. *J. Lumin.* **1997**, *72*, 300.
- (8) Zhang, Q.; Lü, F.; Li, C.; Wang, Y.; Wan, H. *Chem. Lett.* **2006**, *35*, 190–191.
- (9) Taguchi, A.; Schüth, F. *Microporous Mesoporous Mater.* **2005**, *77*, 1–45.
- (10) Yanagisawa, T.; Shimizu, T.; Kuroda, K.; Kato, C. *Bull. Chem. Soc. Jpn.* **1990**, *63*, 988–992.
- (11) Beck, J. S.; Vartuli, J. C.; Roth, W. J.; Leonowicz, M. E.; C.T.; Kresge; Schmitt, K. D.; Chu, C. T. W.; Olson, D. H.; Sheppard, E. W.; McCullen, S. B.; Higgins, J. B.; Schlenker, J. L. *J. Am. Chem. Soc.* **1992**, *114*, 10384.
- (12) Kresge, C. T.; M.E. Leonowicz; Roth, W. J.; Vartuli, J. C.; Beck, J. S. *Nature* **1992**, *359*, 710.
- (13) Attard, G. S.; Glyde, J. C.; Göltner, C. G. *Nature* **1995**, *378*, 366.
- (14) El Haskouri, J.; Guillem, C.; Latorre, J.; Beltra, D.; Marcos, M. D. *Solid State Sci.* **2000**, *2*, 405–420.
- (15) Huo, Q.; Margolese, D. I.; Stucky, G. D. *Chem. Mater.* **1996**, *8*, 1147.
- (16) Firouzi, A.; Kumar, D.; Bull, L. M.; Besier, T.; Sieger, P.; Huo, Q.; Walker, S. A.; Zasadzinski, J. A.; Glinka, C.; Nicol, J.; Margolese, D. I.; Stucky, G. D.; Chmelka, B. *F. Science (80-.).* **1995**, *267*, 1138.

- (17) Huo, Q.; Leon, R.; Petroff, P. M.; Stucky, G. D. *Science* (80-.). **1995**, 268, 1324.
- (18) Papirer, E. *Adsorption on Silica Surface.*; dekker: New York, 2000.
- (19) Soler-Illia, G. J. D. A. A.; Sanchez, C.; Lebeau, B.; Patarin, J. *Chem. Rev.* **2002**, 102, 4093–4138.
- (20) Kobler, J.; Möller, K.; Bein, T. *ACS Nano* **2008**, 2, 791–799.
- (21) Lu, J.; Liong, M.; Zink, J. I.; Tammanoi, F. *small* **2007**, 3, 1341–1346.
- (22) Lu, Y. F.; Fan, H. Y.; Stump, A.; Ward, T. L.; Rieker, T.; Brinker, C. J. *Nature* **1999**, 398, 223–226.
- (23) Suzuki, K.; Ikari, K.; Imai, H. *J. Am. Chem. Soc* **2004**, 126, 462–463.
- (24) El Haskouri, J.; Ortiz de Zarate, D.; Guillem, C.; Beltran-Porter, A.; Caldes, M.; Marcos, M. D.; Beltran-Porter, D.; Latorre, J.; Amoros, P. *Chem. Mater.* **2002**, 14, 4502–4504.
- (25) Fowler, C. E.; Khushalani, D.; Lebeau, B.; Mann, S. *Adv. Mater.* **2001**, 13, 649–652.
- (26) Lai, C.-Y.; Trewyn, B. G.; Jeftinija, D. M.; Jeftinija, K.; Xu, S.; Jeftinija, S.; Lin, V. S.-Y. *J. Am. Chem. Soc.* **2003**, 125, 4451–4459.
- (27) Anwender, R. *Chem. Mater.* **2001**, 13, 4419–4438.
- (28) Meynen, V.; Cool, P.; Vansant, E. F. *Microporous Mesoporous Mater.* **2009**, 125, 170–223.
- (29) Perego, C.; Millini, R. *Chem. Soc. Rev.* **2013**, 42, 3956–3976.
- (30) Corma, A. *Chem. Rev.* **1997**, 97, 2373–2420.
- (31) Zhao, D. Y.; Huo, Q. S.; Feng, J. L.; Chmelka, B. F.; Stucky, G. D. *J. Am. Chem. Soc.* **1998**, 120, 6024–6036.
- (32) Judeinstein, P.; Sanchez, C. *J. Mater. Chem.* **1996**, 6, 511–525.
- (33) Sanchez, C.; Boissiere, C.; Cassaignon, S.; Chaneac, C.; Durupthy, O.; Faustini, M.; Grosso, D.; Laberty-Robert, C.; Nicole, L.; Portehault, D.; Ribot, F.; Rozes, L.; Sasse, C. *Chem. Mater.* **2014**, 26, 221–238.
- (34) Sanchez, C.; Ribot, F. *New J. Chem.* **1994**, 18, 1007–1047.
- (35) Sanchez, C.; Shea, K. J.; Kitagawa, S. *chem.Soc.Rev.* **2011**, 40, 453–1152.
- (36) Hartmann, M. *Chem. Mater.* **2005**, 17, 4577–4593.
- (37) Cauvel, A.; Renard, G.; Brunel, D. *J. Org. Chem* **1997**, 62, 749–751.

- (38) Zhao, X. S.; Lu, G. Q. *J. Phys. Chem. B* **1998**, *102*, 1556–1561.
- (39) Burkett, S. L.; Sims, S. D.; Mann, S. *Chem. Commun.* **1996**, 1367–1368.
- (40) Burleigh, M. C.; Markowitz, M. A.; Spector, M. S.; Gaber, B. P. *J. Phys. Chem. B* **2001**, *105*, 9935–9942.
- (41) Huh, S.; Wiench, J. W.; Yoo, J.-C.; Pruski, M.; Lin, V. S.-Y. *Chem. Mater.* **2003**, *15*, 4247–4256.
- (42) Diaz, I.; Mohino, F.; Perez-Pariente, J.; Sastre, E. *Thermochim. Acta* **2004**, *413*, 201–207.
- (43) Esquivel, D.; Voort, P. Van Der; Romero-salguero, F. J. *AIMS Mater. Sci.* **2014**, *1*, 70–86.
- (44) Park, S. S.; Santha Moorthy, M.; Ha, C.-S. *NPG Asia Mater.* **2014**, *6*, 96.
- (45) Mizoshita, N.; Tani, T.; Inagaki, S. *Chem. soc. rev.* **2011**, *40*, 789–800.
- (46) Corriu, R.; Moreau, J.; Thepot, P.; Wong Chi Man, M. *Chem. Mater.* **1992**, *4*, 1217–1224.
- (47) Loy, D. A.; Shea, K. J. *Chem. Rev.* **1995**, *95*, 1431–1442.
- (48) Shea, K. J.; Loy, D. A.; Webster, O. W. *Chem. Mater.* **1989**, *1*, 572–574.
- (49) Nguyen, T. P.; Hesemann, P.; Gaveau, P.; Moreau, J. J. E. *J. Mater. Chem.* **2009**, *19*, 4164–4171.
- (50) Nguyen, T. P.; Hesemann, P.; Moreau, J. J. E. *Microporous Mesoporous Mater.* **2011**, *142*, 292–300.
- (51) El Hankari, S.; Motos-Pérez, B.; Hesemann, P.; Bouhaouss, A.; Moreau, J. J. E. *Chem. Commun.* **2011**, *47*, 6704–6706.
- (52) Mizoshita, N.; Tani, T.; Shinokubo, H.; Inagaki, S. *Angew. Chemie* **2012**, *51*, 1156–1160.
- (53) Kolb, H. C.; Finn, M. .; Sharpless, K. B. *Angew. Chem. Int. Ed.* **2001**, *40*, 2004–2021.
- (54) Lahann, J. *Click Chemistry for Biotechnology and Materials Science.*; John Wiley & Sons Ltd, 2009.
- (55) Bock, V. D.; Hiemstra, H.; van Maarseveen, J. H. *Eur. J. Org. Chem* **2006**, *2006*, 51–68.
- (56) Lemieux, G. A.; Bertozzi, C. R. *Trends Biotechnol.* **1998**, *16*, 506–513.

- (57) Kochendoerfer, G. G.; Chen, S. Y.; Mao, F.; Cressman, S.; Traviglia, S.; Shao, H.; Hunter, C. L.; Low, D. W.; Cagle, E. N.; Carnevali, M.; Gueriguian, V.; Keogh, P. J.; Porter, H.; Stratton, S. M.; Wiedeke, M. C.; Wilken, J.; Tang, J.; Levy, J. J.; Miranda, L. P.; Crnogorac, M. M.; Kalbag, S.; Botti, P.; Schindler-Horvat, J.; Savatski, L.; Adamson, J. W.; Kung, A.; Kent, S. B.; Bradburne, J. A. *Science* (80-.). **2003**, 299, 884–887.
- (58) Shao, H.; Crnogorac, M. M.; Kong, T.; Chen, S. Y.; Williams, J. M.; Tack, J. M.; Gueriguian, V.; Cagle, E. N.; Carnevali, M.; Tumelty, D.; Paliard, X.; Miranda, L. P.; Bradburne, J. A.; Kochendoerfer, G. G. *J. Am. Chem. Soc.* **2005**, 127, 1350–1351.
- (59) Schlick, T. L.; Ding, Z. B.; Kovacs, E. W.; Francis, M. . *J. Am. Chem. Soc.* **2005**, 127, 3718–3723.
- (60) Ranjan, R.; Brittain, W. J. *Macromol. Rapid Commun* **2008**, 29, 1104–1110.
- (61) Ranjan, R.; Brittain, W. J. *Macromolecules* **2007**, 40, 6217–6223.
- (62) Binder, W. H.; Petraru, L.; Sachsenhofer, R.; Zirbs, R. *Monatsh. Chem* **2006**, 137, 835–841.
- (63) Binder, W. H.; Sachsenhofer, R.; Straif, C. J.; Zirbs, R. *J. Mater. Chem* **2007**, 17, 2125–2132.
- (64) White, M. A.; Johnson, J. A.; Koberstein, J. T.; Turro, N. J. *J. Am. Chem. Soc.* **2006**, 128, 11356–11357.
- (65) Fleming, D. A.; Thode, C. I.; Williams, M. E. *Chem. Mater* **2006**, 23, 11991–11995.
- (66) Thode, C. J.; Williams, M. E. *J. Colloid Interface Sci* **2008**, 320, 346–352.
- (67) Hirsch, A.; Brettreich, M. *Fullerenes- chemistry and reactions.*; Gmbh, C. W. V., Ed.; 2005.
- (68) Guo, Z.; Liang, L.; Liang, J.-J.; Ma, Y.-F.; Yang, X.-Y.; Ren, D.-M.; Chen, Y.-S.; Zheng, J.-Y. *J. Nanopart. Res* **2008**, 10, 1077–1083.
- (69) Campidelli, S.; Ballesteros, B.; Filoramo, A.; Díaz, D. .; de la Torre, G.; Torres, T.; Rahman, G. .; Ehli, C.; Kiessling, D.; Werner, F.; Sgobba, V.; Guldi, D. M.; Cioffi, C.; Prato, M.; Bourgoïn, J. P. *J. Am. Chem. Soc* **2008**, 130, 11503–11509.
- (70) Tornøe, C. W.; Christensen, C.; Meldal, M. *J. Org. Chem.* **2002**, 67, 3057–3064.
- (71) Meldal, M.; Tornøe, C. W. *Chem. Rev.* **2008**, 108, 2952–3015.
- (72) Rostovtsev, V. V.; Green, L. G.; Fokin, V. V.; Sharpless, B. K. *Angew. Chem., Int. Ed* **2002**, 41, 2596.
- (73) Straub, B. F. *Chem. Commun.* **2007**, 3868–3870.

- (74) Rodionov, V. O.; Fokin, V. V.; Finn, M. G. *Angew. Chemie* **2005**, *44*, 2210–2215.
- (75) Jones, G. O.; Ess, D. H.; Houk, K. N. *Helv. Chim. Acta* **2005**, *88*, 1702.
- (76) Pérez, P.; Domingo, L. R.; Aurell, M. J.; Contreras, R. *Tetrahedron* **2003**, *59*, 3117–3125.
- (77) Worrell, B. T.; Malik, J. a; Fokin, V. V. *Science (80-.)*. **2013**, *340*, 457–460.
- (78) Adam, G. C.; Vanderwal, C. D.; Sorensen, E. J.; Cravatt, B. F. *Angew. Chem., Int. Ed* **2003**, *42*, 5480.
- (79) Gartner, Z. J.; Grubina, R.; Calderone, C. T.; Liu, D. R. *Angew. Chem., Int. Ed* **2003**, *42*, 1370.
- (80) Kuijpers, B. H.; Groothuys, S.; Keereweer, A. B.; Quaedflieg, P. J.; Blaauw, R. H.; van Delft, F. L.; Rutjes, F. P. *Org. Lett.* **2004**, *6*, 3123–3126.
- (81) Doerner, S.; Westermann, B. *Chem. Commun.* **2005**, 2852.
- (82) Malow, M.; Wehrstedt, K. D.; Neuenfeld, S. *Tetrahedron Lett.* **2007**, *48*, 1233.
- (83) Luxenhofer, R.; Jordan, R. *Macromolecules* **2006**, *39*, 3509.
- (84) Li, Y.; Huffman, J. C.; Flood, A. H. *Chem. Commun* **2007**, 2692.
- (85) Teyssot, M.-L.; Nauton, L.; Canet, J.-L.; Federico, C.; Chevry, A.; Gautier, A. *Eur. J. Org. Chem* **2010**, 3507–3515.
- (86) Moitra, N.; Moreau, J. J. E.; Cattoën, X.; Wong Chi Man, M. *Chem. Commun.* **2010**, *46*, 8416–8418.
- (87) Golas, P. L.; Tsarevsky, N. V.; Sumerlin, B. S.; Matyjaszewski, K. *Macromolecules* **2006**, *39*, 6451.
- (88) Schlossbauer, A.; Schaffert, D.; Kecht, J.; Wagner, E.; Bein, T. *J. Am. Chem. Soc.* **2008**, *130*, 12558–12559.
- (89) Patel, K.; Angelos, S.; Dichtel, W. R.; Coskun, A.; Yang, Y.-W.; Zink, J. I.; Stoddart, J. F. *J. Am. Chem. Soc.* **2008**, *130*, 2382–2383.
- (90) Malvi, B.; Sarkar, B. R.; Pati, D.; Mathew, R.; Ajithkumar, T. G.; Sen Gupta, S. *J. Mater. Chem.* **2009**, *19*, 1409–1416.
- (91) Nakazawa, J.; Stack, T. D. P. *J. Am. Chem. Soc.* **2008**, *130*, 14360–14361.
- (92) Nakazawa, J.; Smith, B. J.; Stack, T. D. P. *J. Am. Chem. Soc.* **2012**, *134*, 2750–2759.
- (93) Gao, J.; Zhang, X.; Xu, S.; Liu, J.; Tan, F.; Li, X.; Qu, Z.; Zhang, Y.; Quan, X. *Chem. Asian J.* **2014**, *9*, 908–914.

- (94) Vilà, N.; Ghanbaja, J.; Aubert, E.; Walcarius, A. *Angew. Chemie* **2014**, *53*, 2945–2950.
- (95) De Los Cobos, O.; Fousseret, B.; Lejeune, M.; Rossignol, F.; Dutreilh-Colas, M.; Carrion, C.; Boissière, C.; Ribot, F.; Sanchez, C.; Cattoën, X.; Wong Chi Man, M.; Durand, J.-O. *Chem. Mater.* **2012**, *24*, 4337–4342.
- (96) Cattoën, X.; Noureddine, A.; Croissant, J.; Moitra, N.; Bürglová, K.; Hodačová, J.; de los Cobos, O.; Lejeune, M.; Rossignol, F.; Toulemon, D.; Bégin-Colin, S.; Pichon, B. P.; Raehm, L.; Durand, J.-O.; Wong Chi Man, M. *J. Sol-Gel Sci. Technol.* **2014**, *70*, 245–253.
- (97) Yang, P.; Gai, S.; Lin, J. *Chem. Soc. Rev.* **2012**, *41*, 3679–3698.
- (98) Tarn, D.; Ashley, C. E.; Xue, M.; Carnes, E. C.; Zink, J. I.; Brinker, C. J. *Acc. Chem. Res.* **2013**, *46*, 792–801.
- (99) Dickschat, A. T.; Behrends, F.; Bühner, M.; Ren, J.; Weiß, M.; Eckert, H.; Studer, A. *Chem. -A Eur. J.* **2012**, *18*, 16689–16697.
- (100) Hoshikawa, Y.; Yabe, H.; Nomura, A.; Yamaki, T.; Shimojima, A.; Okubo, T. *Chem. Mater.* **2010**, *22*, 12–14.
- (101) Park, C.; Lee, K.; Kim, C. *Angew. Chem. Int. Ed.* **2009**, *48*, 1275–1278.
- (102) Park, C.; Kim, H.; Kim, S.; Kim, C. *J. Am. Chem. Soc.* **2009**, *131*, 16614–16615.
- (103) Chen, C.; Geng, J.; Pu, F.; Yang, X.; Ren, J.; Qu, X. *Angew. Chemie* **2011**, *50*, 882–886.
- (104) Ambrogio, M. W.; Pecorelli, T. A.; Patel, K.; Khashab, N. M.; Trabolsi, A.; Khatib, H. A.; Botros, Y. Y.; Zink, J. I.; Stoddart, J. F. *Org. Lett.* **2010**, *12*, 3304–3307.
- (105) Patel, K.; Angelos, S.; Dichtel, W. R.; Coskun, A.; Yang, Y.-W.; Zink, J. I.; Stoddart, F. J. *J. Am. Chem. Soc.* **2008**, *130*, 2382–2383.
- (106) Malvi, B.; Sen Gupta, S. *Chem. Commun.* **2012**, *48*, 7853–7855.
- (107) Malvi, B.; Panda, C.; Dhar, B. B.; Gupta, S. Sen. *Chem. Commun.* **2012**, *48*, 5289–5291.
- (108) De Los Cobos, O. Capteurs biologiques multifonctionnels (bio-puces) mis en forme par impression jet d'encre, Université de Limoges, 2013.
- (109) Gao, J.; Zhang, X.; Xu, S.; Tan, F.; Li, X.; Zhang, Y.; Qu, Z.; Quan, X.; Liu, J. *Chem. Eur. J.* **2014**, *20*, 1957–1963.
- (110) Moitra, N. Functional Hybrid Silicas: Alkaloid-Derived Materials for Organocatalysis; “click” Reactions in Sol-Gel Science, Ecole Nationale Supérieure de Chimie de Montpellier, 2011.

- (111) Bürglová, K. Nouvelle voie d'accès facile aux organosilanes précurseurs de matériaux hybrides par voie sol-gel, Ecole Nationale Supérieure de Chimie de Montpellier/ Institute of Chemical Technology in Prague, 2012.
- (112) Kesanli, B.; Lin, W. *Chem. Commun.* **2004**, 2284–2285.
- (113) Nozaki, C.; Lugmair, C. G.; Bell, A. T.; Tilley, T. D. *J. Am. Chem. Soc.* **2002**, *124*, 13194–13203.
- (114) Terry, T. J.; Dubois, G.; Murphy, A.; Stack, T. D. P. *Angew. Chemie* **2007**, *46*, 945–947.
- (115) Weitkamp, J.; Hunger, M.; Ryma, U. *Microporous Mesoporous Mater.* **2001**, *48*, 255–270.
- (116) Karimi, B.; Mobaraki, A.; Mirzaei, H. M.; Zareyee, D.; Vali, H. *Chem Cat Chem* **2014**, *6*, 212–219.
- (117) Nozawa, K.; Osono, C.; Sugawara, M. *Sensors Actuators, B Chem.* **2007**, *126*, 632–640.
- (118) Rebbin, V.; Schmidt, R.; Fröba, M. *Angew. Chemie* **2006**, *45*, 5210–5214.
- (119) Mercier, L.; Pinnavaia, T. J. *Adv. Mater.* **1997**, *9*, 500–503.
- (120) Schiel, J. E.; Mallik, R.; Soman, S.; Joseph, K. S.; Hage, D. S. *J. Sep. Sci.* **2006**, *29*, 719–737.
- (121) Li, J.; Qi, T.; Wang, L.; Liu, C.; Zhang, Y. *Mater. Lett.* **2007**, *61*, 3197–3200.
- (122) Lakhiari, H.; Legendre, E.; Muller, D.; Jozefonvicz, J. *J. Chromatogr. B Biomed. Sci. Appl.* **1995**, *664*, 163–173.
- (123) Yu, S.; Wong, T. K. S.; Pita, K.; Hu, X. *J. Vac. Sci. Technol., B* **2002**, *20*, 2036–2042.
- (124) Liong, M.; Lu, J.; Kovoichich, M.; Xia, T.; Ruehm, S. G.; Nel, A. E.; Tamanoi, F.; Zink, J. I. *ACS Nano* **2008**, *2*, 889–896.
- (125) PCT patents submitted.
- (126) El Hankari, S.; Motos-Pérez, B.; Hesemann, P.; Bouhaouss, A.; Moreau, J. J. E. *J. Mater. Chem.* **2011**, *21*, 6948–6955.
- (127) Nguyen, T. P.; Hesemann, P.; Linh Tran, T. M.; Moreau, J. J. E. *J. Mater. Chem.* **2010**, *20*, 3910–3917.
- (128) El Hankari, S.; Bouhaouss, A.; Hesemann, P. *Microporous Mesoporous Mater.* **2013**, *180*, 196–208.

- (129) Bürglová, K.; Nouredine, A.; Hadacova, J.; Toquer, G.; Cattoën, X.; Wong Chi Man, M. *Chem., A Eur. J.* **2014**, *20*.
- (130) Zhang, H.; Dunphy, D. R.; Jiang, X.; Meng, H.; Sun, B.; Tarn, D.; Xue, M.; Wang, X.; Lin, S.; Ji, Z.; Li, R.; Garcia, F. L.; Yang, J.; Kirk, M. L.; Xia, T.; Zink, J. I.; Nel, A.; Brinker, C. J. *J. Am. Chem. Soc.* **2012**, *134*, 15790–15804.
- (131) Monge-Marcet, A.; Pleixats, R.; Cattoën, X.; Wong Chi Man, M. *Catal. Sci. Technol.* **2011**, *1*, 1544–1563.
- (132) Zamboulis, A.; Moitra, N.; Moreau, J. J. E.; Cattoën, X.; Wong Chi Man, M. *J. Mater. Chem.* **2010**, *20*, 9322–9338.
- (133) Mehdi, A. *J. Mater. Chem.* **2010**, *20*, 9281–9286.
- (134) Coti, K. K.; Belowich, M. E.; Liong, M.; Ambrogio, M. W.; Lau, Y. A.; Khatib, H. A.; Zink, J. I.; Khashab, N. M.; Stoddart, J. F. *Nanoscale* **2009**, *1*, 16–39.
- (135) Croissant, J.; Cattoën, X.; Wong Chi Man, M.; Gallud, A.; Raehm, L.; Trens, P.; Maynadier, M.; Durand, J.-O. *Adv. Mater.* **2014**.
- (136) Abu-Reziq, R.; Avnir, D.; Blum, J. *Angew. Chem. Int. Ed.* **2002**, *41*, 4132–4134.
- (137) Hoffmann, F.; Cornelius, M.; Morell, J.; Fröba, M. *Angew. Chem. Int. Ed.* **2006**, *45*, 3216–3251.
- (138) Brunel, D.; Cauvel, A.; Di Renzo, F.; Fajula, F.; Fubini, B.; Onida, B.; Garrone, E. *New J. Chem.* **2000**, *24*, 807–813.
- (139) Sharma, K. K.; Anan, A.; Buckley, R. P.; Ouellette, W.; Asefa, T. *J. Am. Chem. Soc.* **2008**, *130*, 218–228.
- (140) Macquarrie, D. J. *Chem. Commun* **1996**, *16*.
- (141) Nakazawa, J.; Stack, T. D. P. *J. Am. Chem. Soc.* **2008**, *130*, 14360–14361.
- (142) Moitra, N.; Trens, P.; Raehm, L.; Durand, J.-O.; Cattoën, X.; Wong Chi Man, M. *J. Mater. Chem.* **2011**, *21*, 13476.
- (143) Meldal, M.; Tornøe, C. W. *Chem. Rev.* **2008**, *108*, 2952–3015.
- (144) Wong Chi Man, M.; Cattoën, X.; Moitra, N.; Bürglova, K.; Hodačová, J. Précurseurs Organosilanes Polysilylés Fonctionnalisables. FR 2992963, WO 2014006222.
- (145) Wong Chi Man, M.; Cattoën, X.; Bürglova, K.; Hodačová, J. Composés Organosilanes Polysilylés. FR 2992964, WO 2014006221.
- (146) Gregg, S. J.; Sing, K. S. W. *Adsorption, Surface Area and Porosity*; Academic P.; London, 1982.

- (147) Trens, P.; Denoyel, R.; Glez, J. C. *Colloids Surfaces A Physicochem. Eng. Asp.* **2004**, *245*, 93–98.
- (148) Thommes, M. *Chem. Ing. Tech* **2010**, *82*, 1059–1073.
- (149) Zhao, X. S.; Lu, G. Q.; Hu, X. *Microporous Mesoporous Mater.* **2000**, *41*, 37–47.
- (150) Yurchenko, G. R.; Matkovskii, A. K.; Mel'nik, I. V.; Dudarko, O. A.; Stolyarchuk, N. V.; Zub, Y. L.; Alonso, B. *Colloid J.* **2001**, *17*, 1119–1125.
- (151) Qian, B.; Jiang, H.; Sun, Y.; Long, Y. *Langmuir* **2001**, *17*, 1119–1125.
- (152) Rossi, P. F.; Busca, G.; Oliveri, G.; Vettor, A.; Milana, G. *Langmuir* **1992**, *8*, 104–108.
- (153) Gun'ko, V. M.; Yurchenko, G. R.; Turov, V. V.; Goncharuk, E. V.; Zarko, V. I.; Zabuga, A. G.; Matkovsky, A. K.; Oranska, O. I.; Leboda, R.; Skubiszewska-Zięba, J.; Janusz, W.; Phillips, G. J.; Mikhalovsky, S. V. *J. Colloid Interface Sci.* **2010**, *348*, 546–558.
- (154) Matsumoto, A.; Misran, H.; Tsutsumi, K. *Langmuir* **2004**, *20*, 7139–7145.
- (155) Melnyk, I. V.; Goncharyk, V. P.; Kozhara, L. I.; Yurchenko, G. R.; Matkovsky, A. K.; Zub, Y. L.; Alonso, B. *Microporous Mesoporous Mater.* **2013**, *153*, 171–177.
- (156) Tarasevich, Y. I.; Trofimchuk, A. K.; Legenchuk, A. V.; Ivanova, Z. G. *Colloid J.* **2004**, *66*, 78–83.
- (157) Hair, M. L.; Hertl, W. *J. Phys. Chem.* **1969**, *73*, 4269–&.
- (158) Ribeiro Carrott, M. M. L.; Candeias, A. J. E.; Carrott, P. J. M.; Ravikovitch, P. I.; Neimark, A. V.; Sequeira, A. D. *Microporous Mesoporous Mater.* **2001**, *47*, 323–337.
- (159) Rouquerol, F.; Rouquerol, J.; Sing, K. S. W. *Adsorption by porous and divided solids.*; Plenum Pre.; San Diego, 1999.
- (160) Trens, P.; Hudson, M. J.; Denoyel, R. *J. Mater. Chem.* **1998**, *8*, 2147–2152.
- (161) Olney, T. N.; Cann, N. M.; Cooper, G.; Brion, C. E. *Chem. Phys.* **1997**, *223*, 59–58.
- (162) Risau, W.; Flamme, I. *Annu. Rev. Cell Dev. Biol.* **1995**, *11*, 73–91.
- (163) Klein, C. *Science (80-.)*. **2008**, *321*, 1785–1787.
- (164) Gaudineau, B.; Fougère, M.; Guaddachi, F.; Lemoine, F.; de la Grange, P.; Jauliac, S. *J. Cell Sci.* **2012**, *125*, 4475–4486.
- (165) Anand, P.; Kunnumakkara, A. S. C.; Harikumar, K.; Tharakan, S.; OS, L.; Sung, B.; Aggarwal, B. *Pharm. Res.* **2008**, *25*, 2097–2116.

- (166) Ambrogio, M. W.; Thomas, C. R.; Zhao, Y.-L.; Zink, J. I.; Stoddart, J. F. *Acc. Chem. Res.* **2011**, *44*, 903–913.
- (167) Lee, J. E.; Lee, N.; Kim, T.; Kim, J.; Hyeon, T. *Acc. Chem. Res.* **2011**, *44*, 893–902.
- (168) Mortera, R.; Vivero-escoto, J.; Slowing, I. I.; Garrone, E.; Onida, B.; Victor, S.; Lin, Y. *Chem. Commun.* **2009**.
- (169) Tarn, D.; Ferris, D. P.; Barnes, J. C.; Ambrogio, M. W.; Stoddart, J. F.; Zink, J. I. *Nanoscale* **2014**, *6*, 3335–3343.
- (170) Vivero-escoto, J.; Slowing, I. I.; Trewyn, B. G.; Lin, V. S. *Small* **2010**, *6*, 1952–1967.
- (171) Barbé, C.; Bartlett, J.; Kong, L.; Finnie, K.; Lin, H. Q.; Larkin, M.; Calleja, S.; Bush, A.; Calleja, G. *Adv. Mater.* **2004**, *16*.
- (172) Lin, V. S.; Lai, C. Y.; Huang, J.; Song, S. A.; Xu, S. *J. Am. Chem. Soc.* **2001**, *123*, 11510–11511.
- (173) Conner, S. D.; Schmid, S. L. *Nature* **2003**, *422*, 37–44.
- (174) Chithrani, B. .; Ghazani, A. .; Chan, W. C. W. *Nanoscale Res. Lett.* **2006**, 662.
- (175) Argyo, C.; Weiss, V.; Bra, C.; Bein, T. *Chem. Mater.* **2014**, *26*, 435–451.
- (176) Yu, T.; Malugin, A.; Ghandehari, H. *ACS Nano* **2011**, *5*, 5717–5728.
- (177) Huang, X.; Li, L.; Liu, T.; Hao, N.; Liu, H.; Chen, D.; Tang, F. *ACS Nano* **2011**, *5*, 5390–5399.
- (178) Yu, T.; Greish, K.; McGill, L. D.; Ray, A.; Ghandehari, H. *ACS Nano* **2012**, *6*, 2289–2301.
- (179) Meng, H.; Yang, S.; Li, Z.; Xia, T.; Chen, J.; Ji, Z.; Zhang, H.; Wang, X.; Lin, S.; Huang, C.; Zhou, Z. H.; Zink, J. I.; Nel, A. E. *ACS Nano* **2011**, *5*, 4434–4447.
- (180) Slowing, I. I.; Wu, C.-W.; Vivero-Escoto, J. L.; Lin, V. S.-Y. *Small* **2009**, *5*, 57–62.
- (181) Nash, T.; Allison, A. C.; Harington, J. S. *Nature* **1966**, 259–261.
- (182) Maeda, H.; Sawa, T.; Konno, T. *J. Control. release* **2001**, *74*, 47–61.
- (183) Li, Z.; Barnes, J. C.; Bosoy, A.; Stoddart, J. F.; Zink, J. I. *Chem. Soc. Rev.* **2012**, *41*, 2590–2605.
- (184) Maeda, H.; Sawa, T.; Wu, J.; Matsumura, Y.; Hori, K. J. *J. Control. release* **2000**, 271.
- (185) Gottesman, M. .; Fojo, T.; Bates, S. E. *Nat. Rev. cancer* **2002**, *2*, 2489.

- (186) Mackowiak, S. A.; Schmidt, A.; Weiss, V.; Argyo, C.; von schirnding, C.; Bein, T.; Bräuchle, C. *Nanoscale Res. Lett.* **2013**, *13*, 2576–2583.
- (187) Petros, R. A.; DeSimone, J. M. *Nat. Rev. drug Discov.* **2010**, *9*, 615–627.
- (188) Rosenholm, J. M.; Meinander, A.; Peuhu, E.; Niemi, R.; Eriksson, J. E.; Sahlgren, C.; Lindén, M. *ACS Nano* **2009**, *3*, 197.
- (189) Zhang, Q.; Liu, F.; Nguyen, K. T.; Ma, X.; Wang, X. J.; Xing, B. G.; Zhao, Y. L. *Adv. Funct. Mater.* **2012**, *22*, 5144.
- (190) Pang, J. M.; Zhao, L. X.; Zhang, L. L.; Li, Z. H.; Luan, Y. X. *J. colloida interface Sci.* **2013**, *395*, 31.
- (191) Chen, D. Y.; Jiang, M. J.; Li, N. J.; Gu, H. W.; Xu, Q. F.; Ge, J. F.; Xia, X. W.; Lu, J. M. *J. Mater. Chem.* **2011**, *20*, 6422.
- (192) Wang, F.; Chen, X. L.; Zhao, Z. X.; Tang, S. H.; Huang, X. Q.; Lin, C. H.; Cai, C. B.; Zheng, N. F. *J. Mater. Chem.* **2011**, *21*, 11244.
- (193) Mamaeva, V.; Rosenholm, J. M.; Bate-Eya, L. T.; Bergman, L.; Peuhu, E.; Duchanoy, A.; Fortelius, L. E.; Landor, S.; Toivola, D. M.; Linden, M.; Sahlgren, C. *Mol. Ther.* **2011**, *19*, 1538–1546.
- (194) Zhou, C. F.; Kunzmann, A.; Rakonjac, M.; Fadeel, B.; Garcia-Bennett, A. *nanomedicine* **2013**, *7*, 327.
- (195) Fan, J. Q.; Fang, G.; Wang, X. D.; Zeng, F.; Xiang, Y. F.; Wu, S. Z. *Nanotechnology* **2011**, *22*.
- (196) Zhu, Y. F.; Fang, Y.; Kaskel, S. *J. Phys. Chem. C* **2010**, *114*, 16832.
- (197) Brevet, D.; Gary-Bobo, M.; Raehm, L.; Richeter, S.; Hocine, O.; Amro, K.; Looock, B.; Couleaud, P.; Frochot, C.; Morère, A.; Maillard, P.; Garcia, M.; Durand, J. O. *Chem. Commun.* **2009**, *12*, 1475.
- (198) Gary-Bobo, M.; Hocine, O.; Brevet, D.; Maynadier, M.; Raehm, L.; Richeter, S.; Charasson, V.; Looock, B.; Morere, A.; Maillard, P.; Garcia, M.; Durand, J. O. *Int. J. Pharmacol.* **2012**, *423*, 509.
- (199) Chen, Z. W.; Li, Z. H.; Lin, Y. H.; Yin, M. L.; Ren, J. S.; Qu, X. G. *Chem. Eur. J.* **2013**, *19*, 1778.
- (200) Omidian, H.; Park, K. *J. Drug Deliv. Sci. Technol.* **2008**, *18*, 83–93.
- (201) Guardado-Alvarez, T. M.; Sudha Devi, L.; Russell, M. M.; Schwartz, B. J.; Zink, J. I. *J. Am. Chem. Soc.* **2013**, *135*, 14000–14003.
- (202) Croissant, J.; Zink, J. I. *J. Am. Chem. Soc.* **2012**, *134*, 7268–31.

- (203) Tarn, D.; Xue, M.; Zink, J. I. *Inorg. Chem.* **2013**, *52*, 2044–2049.
- (204) Mortera, R.; Vivero-Escoto, J.; Slowing, I. I.; Garrone, E.; Onida, B.; Lin, V. S.-Y. *Chem. Commun.* **2009**, 3219–3221.
- (205) Xue, M.; Zink, J. I. *J. Phys. Chem. Lett.* **2014**, *5*, 839–842.
- (206) Croissant, J.; Zink, J. I. *J. Am. Chem. Soc.* **2012**, *134*, 7628–7631.
- (207) Guardado-Alvarez, T. M.; Sudha Devi, L.; Russell, M. M.; Schwartz, B. J.; Zink, J. I. *J. Am. Chem. Soc.* **2013**, *135*, 14000–14003.
- (208) Choi, E.; Lu, J.; Tamanoi, F.; Zink, J. I. *Z. Anorg. allg. Chemi.* **2014**, *640*, 588–594.
- (209) Liong, M.; Angelos, S.; Choi, E.; Patel, K.; Stoddart, J. F.; Zink, J. I. *J. Mater. Chem.* **2009**, *19*, 6251–6257.
- (210) Guardado-Alvarez, T. M.; Devi, L. S.; Vabre, J.-M.; Pecorelli, T. A.; Schwartz, B. J.; Durand, J.-O.; Mongin, O.; Blanchard-Desce, M.; Zink, J. I. *Nanoscale* **2014**, *6*, 4652–4658.
- (211) Angelos, S.; Liong, M.; Choi, E.; Zink, J. I. *Chem. Eng. J.* **2008**, *137*, 4–13.
- (212) Angelos, S.; Choi, E.; Vögtle, F.; De Cola, L.; Zink, J. I. *J. Phys. Chem. Lett.* **2007**, *111*, 6589–6592.
- (213) Dong, J.; Zink, J. I. *ACS Nano* **2014**, *8*, 5199–5207.
- (214) Ferris, D. P.; Zhao, Y. L.; Khashab, N. M.; Khatib, H. A.; Stoddart, J. F.; Zink, J. I. *J. Am. Chem. Soc.* **2009**, *131*, 1686–1688.
- (215) Zhao, Y. L.; Li, Z. X.; Kabehie, S.; Botros, Y. Y.; Stoddart, J. F.; Zink, J. I. *J. Am. Chem. Soc.* **2010**, *132*, 13016–13025.
- (216) Meng, H. A.; Xue, M.; Xia, T. A.; Zhao, Y. L.; Tamanoi, F.; Stoddart, J. F.; Zink, J. I.; Nel, A. E. *J. Am. Chem. Soc.* **2010**, *132*, 12690–12697.
- (217) Du, L.; Liao, S. J.; Khatib, H. A.; Stoddart, J. F.; Zink, J. I. *J. Am. Chem. Soc.* **2009**, *131*, 15136–15142.
- (218) Wang, C.; Li, Z. X.; Cao, D.; Zhao, Y. L.; Gaines, J. W.; Bozdemir, O. A.; Ambrogio, M. W.; Frascioni, M.; Botros, Y. Y.; Zink, J. I.; Stoddart, J. F. *Angew. Chem. Int. Ed. Engl.* **2012**, *51*, 5460–5465.
- (219) Liu, J. S.; Du, X. Z.; Zhang, X. F. *Chem. Eur. J.* **2011**, *17*, 810.
- (220) Angelos, S.; Khashab, N. M.; Yang, Y. W.; Trabolsi, A.; Khatib, H. A.; Stoddart, J. F.; Zink, J. I. *J. Am. Chem. Soc.* **2009**, *131*, 12912–12914.
- (221) Liu, J. S.; Du, X. Z. *J. Mater. Chem.* **2010**, *20*, 3642.

- (222) Patel, K.; Angelos, S.; Dichtel, W. R.; Coskun, A.; Yang, Y. W.; Zink, J. I.; Stoddart, J. F. *J. Am. Chem. Soc.* **2008**, *130*, 2382–2383.
- (223) Khashab, N. M.; Belowich, M. E.; Trabolsi, A.; Friedman, D. C.; Valente, C.; Lau, Y. N.; Khatib, H. A.; Zink, J. I.; Stoddart, J. F. *Chem. Commun.* **2009**, *36*, 5371.
- (224) Climent, E.; Martinez-Máñez, R.; Sancenón, F.; Marcos, M. D.; Soto, J.; Maquieira, A.; Amoros, P. *Angew. Chemie* **2010**, *49*, 7281–7283.
- (225) He, D. G.; He, X. X.; Wang, K. M.; Chen, M. A.; Cao, J.; Zhao, Y. X. *J. Mater. Chem.* **2012**, *22*, 14715.
- (226) Ruiz-Hernandez, E.; Baeza, A.; Vallet-Regi, M. *ACS Nano* **2011**, *5*, 1259–1266.
- (227) Popat, A.; Liu, J.; Lu, G. Q.; Qiao, S. Z. *J. Mater. Chem.* **2012**, *22*, 11173–11178.
- (228) Deng, Z. W.; Zhen, Z. P.; Hu, X. X.; Wu, S. L.; Xu, Z. S.; Chu, P. K. *Biomaterials* **2011**, *32*, 4976.
- (229) Chen, F.; Zhu, Y. C. *Microporous Mesoporous Mater.* **2012**, *150*, 83–89.
- (230) Liu, R.; Zhao, X.; Wu, T.; Feng, P. Y. *J. Am. Chem. Soc.* **2008**, *130*, 14418–14419.
- (231) Hu, X. X.; Hao, X. H.; Wu, Y.; Zhang, J. C.; Zhang, X. N.; Wang, P. C.; Zou, G. Z.; Liang, X. J. *J. Mater. Chem. B* **2013**, *1*, 1109.
- (232) Chang, B. S.; Chen, D.; Wang, Y.; Chen, Y. Z.; Jiao, Y. F.; Sha, X. Y.; Yang, W. L. *Chem. Mater.* **2013**, *25*, 574–585.
- (233) Chen, F.; Zhu, Y. C. *Nano Lett.* **2013**, *13*, 1047.
- (234) Mackowiak, S. A.; Schmidt, A.; Weiss, V.; Argyo, C.; von Schirnding, C.; Bein, T.; Bräuchle, C. *Nano Lett.* **2013**, *13*, 2576–2583.
- (235) Schlossbauer, A.; Sauer, A. M.; Cauda, V.; Schmidt, A.; Engelke, H.; Rothbauer, U.; Zolghadr, K.; Leonhardt, H.; Bräuchle, C.; Bein, T. *Adv. Healthc. Mater* **2012**, *1*, 316–320.
- (236) Fang, W. J.; Yang, J.; Gong, J. W.; Zheng, N. F. *Adv. Funct. Mater.* **2011**, *22*, 842–848.
- (237) Gao, C. B.; Zheng, H. Q.; Xing, L.; Shu, M. H.; Che, S. N. *Chem. Mater.* **2010**, *22*, 5437.
- (238) Ma, Y. H.; Zhou, L.; Zheng, H. Q.; Xing, L.; Li, C. G.; Cui, J. H.; Che, S. A. *J. Mater. Chem.* **2011**, *21*, 9483–9486.
- (239) Mendez, J.; Monteagudo, A.; Griebenow, K. *Bioconjugate Chem.* **2012**, *22*, 842.

- (240) Sauer, A. M.; Schlossbauer, A.; Ruthardt, N.; Cauda, V.; Bein, T.; Bräuchle, C. *Nano Lett.* **2010**, *10*, 3684–3691.
- (241) Choi, E.; Lu, J.; Tamanoi, F.; Zink, J. I. *Z. anorg. allg. Chem.* **2014**.
- (242) Angelos, S.; Choi, E.; Vögtle, F.; De Cola, L.; Zink, J. I. *Chem. Eng. J.* **2008**, *137*, 4–13.
- (243) Hartley, G. S. *Nature* **1937**, *140*, 281.
- (244) Deloncle, R. Dendrimeres phosphores a motifs azobenzene : Vers des nanomateriaux photoadaptatifs, Université Paul Sabatier Toulouse 3, 2007, pp. 18–22.
- (245) Rau, H. *Photochromism: Molecules and systems.*; 1990; p. 165.
- (246) Rau, H.; Lüddecke, J. *J. Am. Chem. Soc.* **1982**, *104*, 1616.
- (247) Monti, S.; Orlandi, G.; Palmieri, P. *Chem. Phys.* **1982**, *71*, 87–99.
- (248) Zimmerman, G.; Chow, L.-Y.; Paik, U.-J. *J. Am. Chem. Soc.* **1958**, *80*, 3258–3531.
- (249) Sierocki, P.; Maas, H.; Dragut, P.; Richardt, G.; Vögtle, F.; De Cola, L.; Brouwer, F. A. M.; Zink, J. I. *J. Phys. Chem. B* **2006**, *110*, 24390–24398.
- (250) Croissant, J.; Maynadier, M.; Gallud, A.; Peindy N'Dongo, H.; Nyalosaso, J. L.; Derrien, G.; Charnay, C.; Durand, J.-O.; Raehm, L.; Serein-Spirau, F.; Cheminet, N.; Jarroson, T.; Mongin, O.; Blanchard-Desce, M.; Gary-Bobo, M.; Garcia, M.; Lu, J.; Tamanoi, F.; Tarn, D.; Guardado-Alvarez, T. M.; Zink, J. I. *Angew. Chem. Int. Ed.* **2013**, *125*, 14058–14062.
- (251) Forster, T. H. In *10th Spiers Memorial Lecture Transfer Mechanisms of Electronic Excitation*; 1959; pp. 7–17.
- (252) Albani, R. J. *Principles and Applications of Fluorescence Spectroscopy.*; BlackWell Publishing, 2007.
- (253) Tokmakoff, A. In *Förster Resonance Energy Transfer*; 2008; Vol. 321, pp. 4–8.
- (254) Shirdel, J. Photo-Physical Characterization of Flavin-Pyrene-Phenothiazine Molecular Photonic Complexes., Universität Regensburg, 2007.
- (255) Wan, P.; Shukla, D. *Am. Chem. Soc.* **1989**, *93*, 571–584.
- (256) Shizuka, H. *Am. Chem. Soc.* **1985**, 141–147.
- (257) Cramer, F.; Hettler, H. *Naturwissenschaften* **1967**, *24*, 49–54.
- (258) Trens, P.; Tanchoux, N.; Papineschi, P.-M.; Maldonado, D.; di Renzo, F.; Fajula, F. *Microporous Mesoporous Mater.* **2005**, *86*, 354–363.

- (259) Tanchoux, N.; Trens, P.; Maldonado, D. *Colloids Surfaces, A* **2004**, *246*, 1–8.
- (260) Van Allen, D.; Venkataraman, D. *J. Org. Chem.* **2003**, *68*, 4590–4593.
- (261) Zheng, H.; McDonald, R.; Hall, D. G. *Chem. -A Eur. J.* **2010**, *16*, 5454–5460.
- (262) Brunet, E.; Juanes, O.; Jiménez, L.; Rodríguez-Ubis, J. C. *Tetrahedron Lett.* **2009**, *50*, 5361–5363.
- (263) Bolzati, C.; Cavazza-Ceccato, M.; Agostini, S.; Refosco, F.; Yamamichi, Y.; Tokunaga, S.; Carta, D.; Salvarese, N.; Bernardini, D.; Bandoli, G. *Bioconjug. Chem.* **2010**, *21*, 928–939.
- (264) Lu, X.; Bittman, R. *J. Org. Chem.* **2005**, *70*, 4746–4750.
- (265) Hynes, M. J.; Maurer, J. A. *Angew. Chemie* **2012**, *51*, 2151–2154.
- (266) Campbell-Verduyn, L. S.; Mirfeizi, L.; Dierckx, R. A.; Elsinga, P. H.; Feringa, B. L. *Chem. Commun.* **2009**, 2139–2141.
- (267) Dakshinamoorthy, D.; Lewis, S. P.; Cavazza, M. P.; Hoover, A. M.; Iwig, D. F.; Damodaran, K.; Mathers, R. T. *Green Chem.* **2014**, *16*, 1774–1783.
- (268) Sayed, S. Y.; Bayat, A.; Kondratenko, M.; Leroux, Y.; Hapiot, P.; McCreery, R. L. *J. Am. Chem. Soc.* **2013**, *135*, 12972–12975.
- (269) Banerjee, S.; Vidya, V. M.; Savyasachi, A. J.; Maitra, U. *J. Mater. Chem* **2011**, *21*, 14696.
- (270) Kubitschke, J.; Näther, C.; Herges, R. *European J. Org. Chem.* **2010**, *2010*, 5041–5055.
- (271) Gogoll, A. *J. org. Chem.* **2001**, 4165–4169.
- (272) Zhang, H.; Cai, Z.; Sun, Y.; Yu, F.; Chen, Y.; Sun, B. *J. Biomed. Mater. Res.* **2012**, *100*, 2441–2449.
- (273) Banerjee, S.; Veale, E. B.; Phelan, C. M.; Murphy, S. A.; Tocci, G. M.; Gillespie, L. J.; Frimannsson, D. O.; Kelly, J. M.; Gunnlaugsson, T. *Chem. Soc. Rev.* **2013**, *42*, 1601–1618.
- (274) Park, S. Y.; Yoon, J. H.; Hong, C. S.; Souane, R.; Kim, J. S.; Matthews, S. E.; Vicens, J. *J. Org. Chem.* **2008**, *73*, 8212–8218.
- (275) Dinges, J.; Albert, D. H.; Arnold, L. D.; Ashworth, K. L.; Akritopoulou-Zanze, I.; Bousquet, P. F.; Bouska, J. J.; Cunha, G. a; Davidsen, S. K.; Diaz, G. J.; Djuric, S. W.; Gasiecki, A. F.; Gintant, G. a; Gracias, V. J.; Harris, C. M.; Houseman, K. a; Hutchins, C. W.; Johnson, E. F.; Li, H.; Marcotte, P. a; Martin, R. L.; Michaelides, M. R.; Nyein, M.; Sowin, T. J.; Su, Z.; Tapang, P. H.; Xia, Z.; Zhang, H. Q. *J. Med. Chem.* **2007**, *50*, 2011–2029.

Abstract:

The present work aims to develop a reliable methodology of functionalization for silica hybrid materials made by sol-gel process using the *Click* Chemistry (CuAAC). This transformation can be highly useful in materials science thanks to its very high conversion and the excellent functional group tolerance. In this prospect, we have synthesized fully clickable bridged silsesquioxanes and periodic mesoporous organosilica that have shown high extents of *click* grafting. CuAAC was then used for tailoring the surface of bridged silsesquioxane by a fine-tuning of hydrophilic/lipophilic balance. Finally, the CuAAC methodology was applied on the mesoporous silica nanoparticles in order to make new generation of nanomachines by anchoring independent (nanoimpeller/targeting agent) or communicating moieties (FRET donor/acceptor, photoacid/proton receptor) aiming at conferring important features such as pore gating, tumor targeting and tracking

Keywords: click chemistry, PMOs, bridged silsesquioxane, surface modification, mesoporous silica nanoparticles, controlled delivery.

Résumé :

Nous visons dans ce travail de thèse à développer une méthodologie de fonctionnalisation par chimie click de matériaux à base de silice hybrides synthétisés par voie sol-gel. La réaction *click* (CuAAC) offre une tolérance exceptionnelle pour les fonctions organiques en plus d'un taux de fonctionnalisation très élevé. Dans cette optique, nous avons mis en œuvre en premier lieu des matériaux *clickables* à base d'organosilice pure (organosilice à mésoporosité périodique (PMO) et silsesquioxanes pontés (BS)) qui ont montré un taux quantitatif de greffage par CuAAC. Nous avons ensuite utilisé cette particularité pour contrôler les propriétés de surface des BS en modifiant le caractère hydrophile/lipophile. Dans le second axe de travail, nous nous intéressons à l'apport de la chimie *click* dans la modification de nanoparticules mésoporeuses de silice multifonctionnelles, dites mécanisées, pour des systèmes à délivrance contrôlée de principe actif. Nous avons incorporé par réaction CuAAC des fonctions indépendantes (nanopropulseur/agent de ciblage) ou communicantes (fluoropores, photoacide/récepteur pH-sensible) pour la formation d'une nouvelle génération de nanomachines.

Mots-clés : Chimie Click, PMOs, silsesquioxane ponté, modification de surface, nanoparticules mésoporeuses de silice, délivrance contrôlée.

